Transactions of the ASME

EDITORIAL STAFF
Editor, J. J. JAKLITSCH, JR.
Production Editor
CORNELIA MONAHAN
Editorial Production Assistant
BETH DARCHI

FLUIDS ENGINEERING DIVISION
Technical Editor
FRANK M. WHITE (1981)
Executive Secretary
L. T. NELSON (1981)
Calendar Editor
M. F. ACKERSON

Associate Editors
Fluid Machinery
H. JAMES HERRING (1981)
BUDUGUR LAKSHMINARAYANA (1983)
Fluid Measurements
BHARATAN R. PATEL (1983)
Fluid Mechanics
RICHARD A. BAJURA (1980)
OWEN M. GRIFFIN (1981)
BRIAN E. LAUNDER (1981)
WILLIAM G. TIEDERMAN (1981)
Fluid Transients
DAVID C. WIGGERT (1980)
Polyphase Flow
CLAYTON T. CROWE (1980)
ROBERT L. STREET (1981)
Review Articles
KENNETH E. HICKMAN (1981)

FOREIGN CORRESPONDENTS
Europe and Russia
JACQUES CHAUVIN
Europe and Russia
JOHN H. HORLOCK
India and Middle East
ARUN PRASAD
Japan and China
YASUTOSHI SENOO

POLICY BOARD, COMMUNICATIONS
Chairman and Vice-President
I. BERMAN

Members-at-Large
M. J. RABINS
J. E. ORTLOFF
J. W. LOCKE
W. J. WARREN

Policy Board Representatives
Basic Engineering, F. LANDIS
General Engineering,
A. A. SEIREG
Industry, R. K. HAMPTON
Power, R. E. REDER
Research, G. P. COOPER
Codes and Stds., L. L. ELDER
Computer Technology Com.,
A. A. SEIREG
Nom. Com. Rep., S. P. ROGACKI

Business Staff
345 E. 47th St.
New York, N. Y. 10017
(212)644-7789
Mng. Dir., Pub., C. O. SANDERSON

OFFICERS OF THE ASME
President, D. N. ZWIEP
Exec. Dir. Sec'y,
ROGERS B. FINCH
Treasurer, ROBERT A. BENNETT

The Journal of Fluids Engineering (USPS 278-480) is edited and published quarterly at the offices of The American Society of Mechanical Engineers, United Engineering Center, 345 E. 47th St., New York, N. Y. 10017. Cable Address, "Mechaneer," New York. **Second-class** postage paid at New York, N.Y., and at additional mailing office. **CHANGES OF ADDRESS** must be received at Society headquarters seven weeks before *they are to be effective. Please send* old label and new address. **PRICES:** To members, $25.00, annually: to nonmembers, $50.00. Single copies, $15.00 each. Add $1.50 for postage to countries outside the United States and Canada. **STATEMENT** from By-Laws. The Society shall not be responsible for statements or opinions advanced in papers or . . . printed in its publications (B13, Par. 4).

INDEXED by the Engineering Index, Inc.

Journal of Fluids Engineering

Published Quarterly by The American Society of Mechanical Engineers

VOLUME 102 • NUMBER 2 • JUNE 1980

Announcements and Special Notices

REVIEW—Axial Compressor Stall Phenomena

E. M. Greitzer

Associate Professor,
Department of Aeronautics and Astronautics,
Massachusetts Institute of Technology,
Cambridge, Mass. 02139

Stall in compressors can be associated with the initiation of several types of fluid dynamic instabilities. These instabilities and the different phenomena, surge and rotating stall, which result from them, are discussed in this paper. Assessment is made of the various methods of predicting the onset of compressor and/or compression system instability, such as empirical correlations, linearized stability analyses, and numerical unsteady flow calculation procedures. Factors which affect the compressor stall point, in particular inlet flow distortion, are reviewed, and the techniques which are used to predict the loss in stall margin due to these factors are described. The influence of rotor casing treatment (grooves) on increasing compressor flow range is examined. Compressor and compression system behavior subsequent to the onset of stall is surveyed, with particular reference to the problem of engine recovery from a stalled condition. The distinction between surge and rotating stall is emphasized because of the very different consequences on recoverability. The structure of the compressor flow field during rotating stall is examined, and the prediction of compressor performance in rotating stall, including stall/unstall hysteresis, is described.

Introduction

In normal operation of a compressor, the flow is nominally steady and axisymmetric, apart from the blade to blade pressure variations and the small scale unsteadiness associated with the moving pressure and velocity fields of the rotors (or impellers). However, if the performance map of a compressor is plotted in the usual form shown in Fig. 1, as pressure ratio versus mass flow for different rotational speeds,[1] a line can be defined which is commonly referred to as the stall line (or surge line) and which divides the map into two regions. To the left of the line, the flow is no longer steady. Large oscillations of the mass flow rate may occur (called *surge*) or severe self-induced circumferential flow distortions may rotate around the annulus (*rotating stall*), or a combination of both phenomena may appear.

Rotating stall induces large vibratory stresses in the blading of compressors and is therefore often unacceptable for structural reasons. In addition, there can be a large drop in performance associated with this flow regime (efficiencies below twenty per cent can be seen in the literature) [1][2] so that overall gas turbine engine cycles may not be self-sustained. In an engine the greatly decreased mass flow through the system can also cause turbine overtemperatures. Surge can be intolerable from the point of view of system operation and can also lead to high blade and casing stress levels [2]. Thus, no matter which type of instability appears when the stall line is crossed, the stall line generally represents a limit to the useful operation of the machine and is therefore to be avoided.

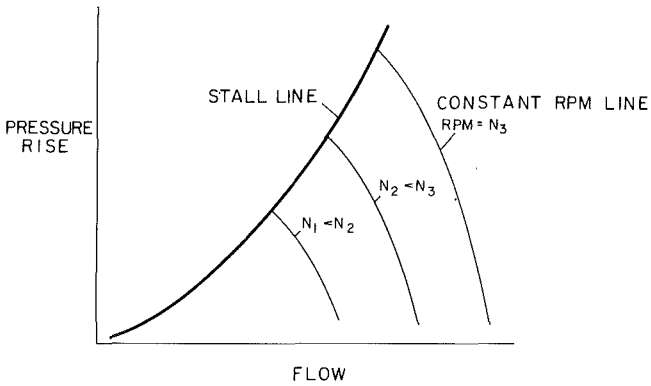

Fig. 1 Compressor performance map

The position of the stall line is a matter of great concern to the designer, and considerable effort is frequently expended to ensure that there is sufficient margin between the stall line and the operating line. Even if this is done, there are still certain situations under which stall will occur, such as rotor speed transients, flow distortions, and nonsteady inlet and exit flow pulsations. Thus, the problem of *recovery from a stall condition* also becomes extremely important.

Because of this the overall topic to be described can be separated, at least conceptually, into two main parts: (1) examination of the basic fluid mechanics associated with the *onset* of the instabilities that lead to rotating stall and/or surge, including such aspects as the impact of inlet distortion, effects of downstream system components on compressor stability, and stability enhancement, and (2) behavior *subsequent* to the onset of this initial instability including large

[1] Actually, corrected flow versus corrected speed.
[2] Numbers in brackets denote references.

Contributed by the Fluids Engineering Division for publication in the JOURNAL OF FLUIDS ENGINEERING. Manuscript received by the Fluids Engineering Division, September 17, 1979.

amplitude system transients, limit cycle surge oscillations, structure of the rotating stall flow field, and the effect of stall/unstall hysteresis on system recovery from rotating stall.

The choices of subjects to be covered in a survey of this type will reflect, to some extent, the background of the author. The present author's experience is mainly with aircraft engine turbomachinery. This review is therefore focused on the fluid mechanics of axial compressor stall, although it should be emphasized that many of the ideas (especially those concerning system behavior) can be applied to centrifugal compression systems as well.

Fluid Dynamic Instabilities in Compressors and Compression Systems

We can start this section by describing in a bit more detail the types of phenomena associated with instabilities in compression systems which arise due to the presence of stall. Looked at from the point of view of the individual diffusing passages in the compressor, stall generally implies separation of the flow from one or more of the passage walls. However, compressor blade rows consist of many of these diffusing passages in parallel, so that phenomena can occur which do not happen with a single airfoil or diffusing passage. One of the most striking of these is rotating stall. This is a flow regime in which one or more "stall cells" propagate around the circumference of the compressor with a constant rotational speed, usually between twenty and seventy percent of the rotor speed. In the cells the blades are very severely stalled. Typically there is negligible net through-flow, with areas of local reverse flow, in these regions. The cells can range from covering only part of the span (either at the root or at the tip) and being only a few blades in angular width, to covering the full span and extending over more than 180 degrees of the compressor annulus. It is this latter situation which most commonly occurs in multistage compressors at speeds near design and which is most serious. The part span stall of the front stages of multistage compressors at low speed attracted a large amount of interest in earlier years, but generally has much less severe consequences and is hence not of primary concern.

The basic explanation of the mechanism associated with the onset of stall propagation was first given by Emmons [3] and can be summarized as follows. Consider a row of axial compressor blades operating at a high angle of attack, such as is shown in Fig. 2. Suppose that there is a nonuniformity in the inlet flow such that a locally higher angle of attack is produced on blade B which is enough to stall it. If this happens, the flow can separate from the suction surface of the blade so that a substantial flow blockage occurs in the channel between B and C. This blockage causes a diversion of the inlet flow away from blade B and towards C and A (as shown by the arrows), resulting in an increased angle of attack on C and a reduced angle of attack on A. Since C was on the verge of stall before, it will now tend to stall, whereas the reduced angle of attack on A will inhibit its tendencies to stall. The stall will thus propagate along the blade row in the direction shown, and under suitable conditions it can grow to a fully developed cell covering half the flow annulus or more. In this fully developed regime, the flow at any local position is quite unsteady; however the annulus averaged mass flow is steady with the stall cells serving only to redistribute this flow.

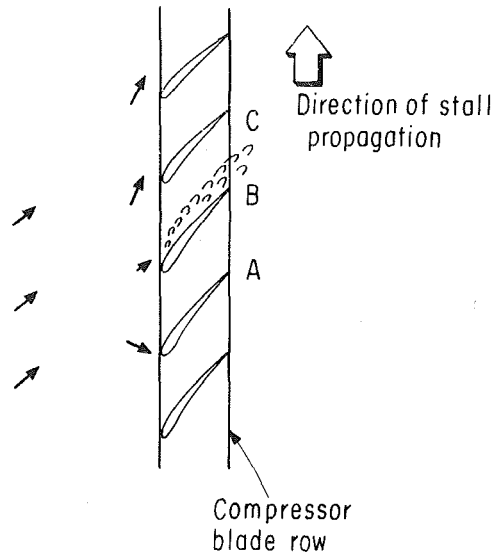

Fig. 2 Physical mechanism for inception of rotating stall

The onset of rotating stall is thus associated with an instability which arises due to the stall of the compressor blade passages.[3] For the overall compression system, this can be regarded as a localized instability. However, a more global *system* instability can also occur, leading to *surge*. In contrast to the behavior during rotating stall, the annulus averaged mass flow and the system pressure rise during surge undergo

[3] The point of stall can, however, be affected by other closely coupled components in the system as described below.

Nomenclature

a = speed of sound
A_c = compressor flow-through area
b = blade chord
B = nondimensional stability parameter; $B = \frac{U}{2\omega L_c} = \frac{U}{2a}\sqrt{\frac{V_p}{A_c L_c}}$
C_x = axial velocity
$\bar{C}_x$ = mean axial velocity
C_x' = nonuniformity in axial velocity
L_c = effective length of compressor
$\dot{m}$ = mass flow
$N/\sqrt{\theta}$ = rotor corrected speed
P = static pressure
P_T = total pressure
ΔP = pressure change across compressor
ΔP_{stage} = pressure rise per stage
δP_T = total pressure distortion
Q = inlet dynamic pressure
R = compressor mean radius
U = rotor speed at midspan
V_p = plenum volume
W = relative velocity
β = relative flow angle
λ = stall cell blockage
ϕ = axial velocity parameter; $\phi = C_x/U$
ϕ^* = design value of axial velocity parameter
$\bar{\phi}_{\text{cessation}}$ = value of annulus averaged axial velocity parameter at full-span stall cessation
ϕ_u = (local) value of ϕ in unstalled region of compressor
θ = circumferential coordinate
ρ = density
ψ_{TS} = pressure rise parameter; $\psi_{TS} = \frac{P_{\text{exit}} - P_{\text{inlet}}}{\rho U^2}$
ω = Helmholtz resonator frequency; $\omega = a\sqrt{\frac{A_c}{V_p L_c}}$

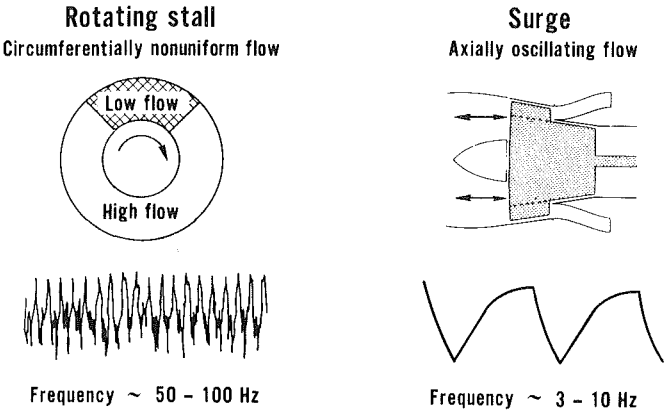

Fig. 3 Modes of system response resulting from stall

large amplitude oscillations. The frequencies of these oscillations are generally at least an order of magnitude below those associated with passage of a rotating stall cell and depend on the parameters of the entire system. In addition, during the surge cycles the instantaneous mass flow through the compressor changes from values at which (in steady state operation) the compressor would be free from stall, to values at which one would find rotating stall or totally reversed flow. Because of the low frequency of the oscillations, the compressor can pass in and out of these flow regimes in an approximately quasi-steady manner.[4]

The two types of instability are indicated schematically in Fig. 3. Sketches of the transient signatures that would be given by typical high response instrumentation, such as a hot wire at the compressor inlet for the rotating stall situation and a pressure probe in the combustor (or other volume downstream of the compressor) for the surge cycles, are also indicated in the figure. Rough magnitudes of the time scales associated with the different phenomena (in an aircraft gas turbine context) are shown as well. It is to be emphasized that although the illustration indicates the phenomena only in this particular context, these instabilities are inherent in pumping systems involving all types of turbomachines.

The two phenomena (surge and rotating stall) are seen to be quite distinct. However, they are not unrelated, since often the occurrence of the local instability (associated with the onset of rotating stall) can trigger the more global type of system instability (leading to surge). Thus one has to consider the possibilities of either type of instability and develop methods for their prediction. We will examine the techniques which have been applied to prediction of rotating stall first.

Prediction of the Onset of Rotating Stall

Correlations for Stall Inception. As noted, a key problem for the designer is the prediction of the point at which stall occurs. This problem has been attacked by many investigators at several quite different levels of approach. The most empirical are the correlations that have been developed for stall onset. The basic concept is to find a parameter (or parameters) which correlates the onset of stall[5] for a number of different blade geometries, compressor designs, etc. In a design procedure for a low hub-tip ratio fan, for example, the parameter could be applied at different span locations along the blading, using the local flow conditions generated by use of one of the many axisymmetric compressor flow field calculations, to see whether any section would be operating under too adverse a condition, while for a multistage compressor the parameter might be applied only on a meanline or averaged basis.

Several of the early correlations of this sort are described by Horlock [5], but one of the well-known examples of this type of approach, which is still much in use, is the work of Leiblein [6]. He developed a parameter which he called the diffusion factor (or D-factor). This was related to the adverse pressure gradient to which the boundary layer on the suction surface of the airfoil was subjected. The D-factor was defined by Leiblein as

$$D = 1 - \frac{W_2}{W_1} + \frac{\Delta W_\theta}{2\sigma W_1}$$

where W_1 is the inlet relative velocity, W_2 is the exit relative velocity, ΔW_θ is the change in circumferential velocity component and σ is the solidity.

It was found that the total pressure loss correlates quite well with D, and, based on Leiblein's cascade results, one can see a rather sharp rise in loss occur as D is increased past a value of roughly 0.6. This can therefore be taken as a *very approximate* criterion for the onset of stall in a cascade (see also [7] for further work using this approach). Although much of the work done by Leiblein was based on two-dimensional cascades, the use of the D-factor has been carried over to axial as well as to centrifugal compressors [8]. Features such as the differences between the flows in a cascade and the flows at the tips of axial compressor rotors, for example, are "recognized" by noting that different limiting values of the D-factor are used for the rotor tips than for other sections.

The correlations based on D-factor, as well as other improved correlations for the stall point, have been intensively investigated by the aircraft engine companies. Virtually all of this information, however, is held as proprietary and there is very little in the open literature, particularly as regards multistage compressors and transonic fans. Several features that are significant, however, are that the "limiting" D-factor, or other loading parameter, (i.e., the value at onset of stall) tends to increase as the aspect ratio and/or the non-dimensional tip clearance[6] decreases. An example of the first of these trends, as presented by Smith [9], is given in Fig. 4 which shows nondimensional stage pressure rise versus flow coefficient from two compressors with aspect ratios of 1.96 and 5. The two compressors each have four stages and the same non-dimensional tip clearance[6]. The lower aspect ratio compressor has a higher pressure rise per stage at the stall point, and stalls at a lower flow rate. Similar results have been found by Fligg [10]. Effects of tip clearance are also illustrated in the above mentioned paper by Smith [9] as well as in [11] and [12].

There are several other factors such as Reynolds number, tolerances and deterioration etc., that can also have an effect on the stall point. These are also accounted for in practice by using correlations, and they will not be discussed here save for the remarks that there can be a substantial loss in stall margin as the blade Reynolds number drops below roughly 100,000.

Although the use of correlations such as D-factor may appear to be an overly simple approach, it is one that is, at present, in common usage for multistage axial compressors. A recent example of such an approach can be found in [13]. More theoretical approaches have not yet led to the definition of stall point with additional precision, but this is not to say that the correlative procedures are all that is needed to put this

[4] In view of this behavior E. S. Taylor [4] has paraphrased P. T. Barnum to describe the distinction between surge and rotating stall, respectively: "You can operate a compressor to stall all of the blades some of the time, or to stall some of the blades all of the time."

[5] Defined here as the condition at which the steady axisymmetric flow becomes unstable.

[6] Tip clearance/staggered spacing.

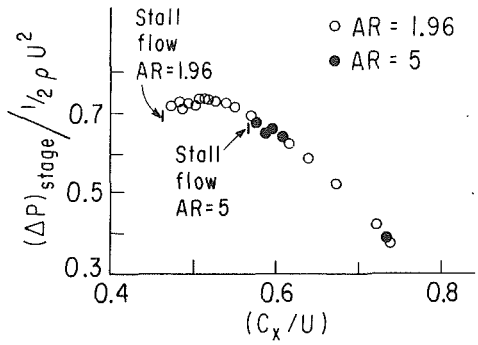

Fig. 4 Performance of high and low aspect ratio compressors (data of Smith [9])

problem to rest. Indeed, a comment in an overview of this topic by a representative of one of the engine companies states flatly "we still cannot predict accurately the onset of engine instability" [14]. (However, it should be recognized that requirements for stall prediction in aircraft gas turbine engines may be quite stringent compared to those in other areas of axial compressor usage.)

Although it is important to mention these correlations, and to give several relevant references, the main emphasis in this review is on the fluid dynamic phenomena associated with compressor stall, and the correlative procedures do not really provide insight into this aspect. Therefore we now consider approaches to the stall prediction problem, which are tied more closely to the flow instabilities occurring in the compressor. These can be divided into two types: linearized (small disturbance) stability analyses for predicting the *onset* of rotating stall, and nonlinear treatments which follow the growth of small perturbations to a fully developed (finite amplitude) state.

Stability Analyses for Rotating Stall Onset. The first of the linearized stability analyses was by Emmons [3], who investigated the conditions under which a small amplitude, circumferentially nonuniform, two-dimensional flow perturbation in a cascade would grow. Since then there have been many extensions of this investigation, of which two recent examples are the papers by Nenni and Ludwig [15] and by Fabri [16]. An excellent summary of the earlier work is given by Emmons, Rockett, and Kronauer [17] and a comprehensive bibliography up to 1967 has been compiled by Fabri [18]. A useful overall introduction to the topic is given by Stenning [19].

In these analyses a small amplitude perturbation is superimposed on a given mean operating condition of the compressor or cascade. The linearized equations of motion are solved to yield the forms of the flow perturbations in regions upstream and downstream of the compressor blade row (cascade). The wavelength of the flow nonuniformities is taken to be much larger than the blade pitch (as is experimentally found to be the case) so that an actuator disk[7] model of the cascade can be used. Suitable matching conditions are applied across the cascade to link the flow quantities upstream and downstream. In general the conditions used (for the two-dimensional case) have been continuity of mass across the cascade, an inlet/exit flow angle relation, and an inlet angle/total pressure loss relation, although some investigators have found it more convenient to work in terms of circulation and shed vorticity [15] rather than total pressure. From this procedure one can determine the eigenvalues of the system of equations which define the stability of the flow field, or one can examine the growth in time of an initially prescribed small perturbation (for times until the disturbances become too large for the linearized theory to apply).

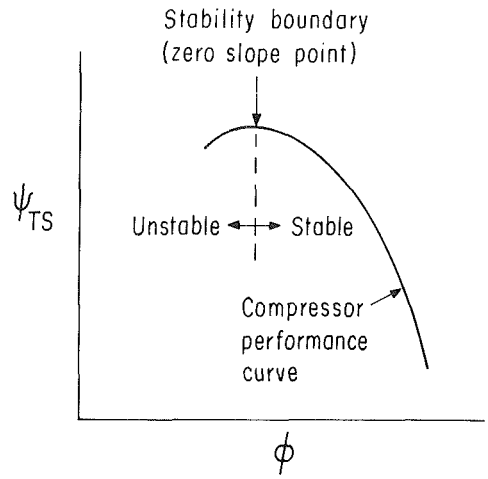

Fig. 5 Onset of compressor flow instability (rotating stall inception point)

These calculations yield results in terms of the critical *slope* of a function such as the mean compressor performance curve, or cascade loss curve, etc. at which the axisymmetric flow becomes unstable. However, these slopes are extremely difficult to obtain accurately, especially for the cases of greatest interest—multistage compressors or transonic fans—and this is a major reason for the relatively little usage of these methods by designers. In other words, if one wishes to use one of the instability calculations as a predictive tool, one must be able to predict the *slopes* of the compressor constant speed characteristic at off-design conditions, and, at present, this cannot be done with an adequate degree of precision.

Putting aside this difficulty, there is still the question of how well existing stability criteria describe the onset of rotating stall. As an example let us consider one of the best known of the (two-dimensional) criteria, due initially to Dunham [20], which states that rotating stall inception will occur at the peak (zero slope point) of the exit static pressure minus inlet total pressure compressor characteristic. This is illustrated schematically in Fig. 5. In this figure the horizontal axis is axial velocity parameter, ϕ, $(=C_x/U)$, and the vertical axis is nondimensional pressure rise, $\psi_{TS} = ([P_{exit} - (P_T)_{inlet}]/\rho U^2)$.

This criterion, which has also been derived by other investigators, has been applied with some success and does appear to furnish a rough "rule of thumb." However, counter examples in which it does not hold can readily be found. As illustration of this, Fig. 6 shows data from a representative sample of low speed multistage compressors.[8]

Curves V, VI, and VII do appear to show approximately zero slope (within the accuracy of the data), but curves I-IV have a negative (i.e., stable) slope right up to the stall points. This situation, where there does not appear to be a zero slope region of the compressor characteristic, is even more apparent in high speed multistage compressor data. (The author has not seen any multistage data in which the converse is true—i.e., in which operation significantly on the positive slope part of the characteristic is found.)

Having said this, however, it should be emphasized that in the opinion of this author these types of stability calculations can still be useful. This is true on several counts, not the least of which is that they provide an overall physical un-

[7] Defined as a representation of a blade row as a plane across which the mass flow is continuous but the total pressure, circumferential velocity, pressure, etc. can be discontinuous.

[8] Three Stage Compressors: I, II, V, VII, [21]; IV [22]; VI [23]; Four Stage compressor III, [24].

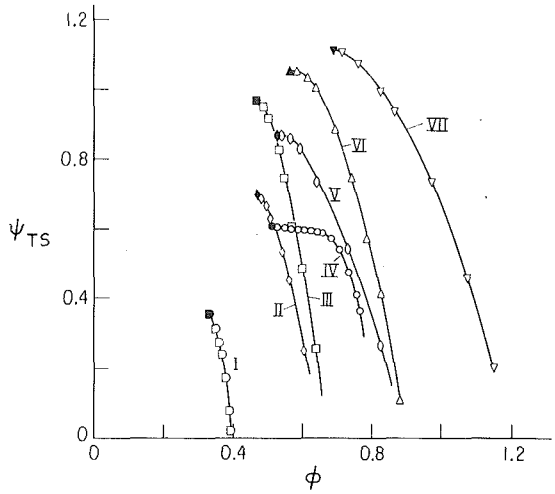

Fig. 6 Multistage compressor performance (low speed rigs); references identified in footnote 8

derstanding of the breakdown of the axisymmetric flow in axial pumps or compressors.

An important advantage of the stability analyses is that they can be used to show effects that correlations do not predict. One of these effects is the coupling, or interaction, between blade rows, between different compressor spools, or between a compressor and components downstream in the compression system. Such coupling is much stronger with asymmetric flows than in the axisymmetric situation. This feature, which is central to the understanding of nonaxisymmetric flows in compressors, occurs because of the much larger length scales of the flow nonuniformities than in the axisymmetric situation. Specifically, it is the "single lobed" (i.e., one per circumference) flow perturbation which appears to be of most practical interest in multistage compressors. For disturbances of this type the relevant length over which adjoining rows can be considered to interact is of the order of the radius of the machine. Thus, adjacent blade rows, or even the two spools of a gas turbine engine, can be considered to be closely coupled as far as circumferentially nonuniform flow is concerned, and, as emphasized by Dunham [20], it is not correct to analyze the stability of one row in a compressor without considering the influence of the other rows. This coupling can be taken into account by the stability analyses and although, as stated, they may not be quantitatively precise, they can still give valuable guidance as to when row-row, spool-spool, etc., interactions will be important.

Nonlinear Investigations of Rotating Stall Onset and Growth. Although the linearized analyses have, in the past, been used to try to predict some of the features of fully developed rotating stall, it has become clear that in this flow regime the stall cells are definitely not small perturbations and linear analysis is inapplicable. Thus this type of investigation is only useful for the problem of stall inception, and to follow the subsequent development of the rotating stall, one must use a nonlinear model. This has been done by Takata and Nagano [25], as well as by Orner [26]. These models use time marching techniques to determine whether a small disturbance will grow or decay by calculating the development of the flow to some eventual steady-state solution. This could consist of a flow with a large amplitude disturbance propagating around the compressor, which is taken to be indicative of compressor operation in rotating stall.

So far these calculations have only been applied to an isolated rotor or to a single stage. (It should be noted that these procedures can give no more information than the linearized stability analyses in regard to stall inception in a

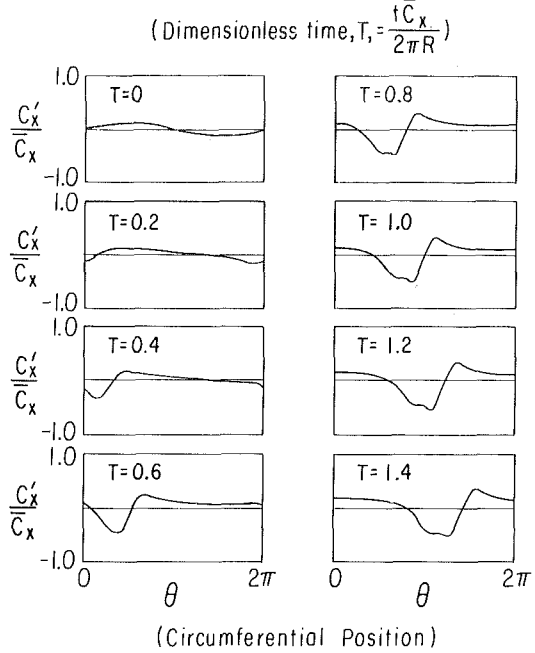

Fig. 7 Growth of small disturbance (calculations of Takata and Nagano [25])

uniform flow. However, they do seem to offer potential for assessing the effect of inlet distortion on stall inception, as is discussed below.) An example of the results of this type of calculation for an isolated rotor is given in Fig. 7 taken from Takata [25]. The figures show the normalized axial velocity nonuniformity, $C_x'/\bar{C}_x$, versus circumferential position, θ, at different nondimensional times, T, = (time • $\bar{C}_x$)/$2\pi R$. It can be seen that the initial sinusoidal perturbation grows into a large amplitude disturbance which propagates round the circumference.

Calculations of this type can show some of the features of rotating stall such as the hysteresis in the stall/unstall process. Other aspects, however, do not appear to be modeled very well, and a general comment on these nonlinear models is that, in spite of their complexity, many of the central features of the fully developed stalled flow may not yet be represented. For example, the present calculation procedures are either two-dimensional, assume that the flow occurs along axisymmetric stream surfaces so that flows perpendicular to these surfaces are supposed zero, or only include three-dimensionality in a potential flow representation. Experiments, however, indicate that strong radial flows can occur. In addition, the models of unsteady blade row performance that are used are quite rudimentary. They are essentially one-dimensional and rely heavily on extrapolation of the loss and turning characteristics (to the negative flow regime according to the experimental measurements). Further, the calculations are carried out with a constant mass flow, whereas in the actual situation the mass flow will change (along a throttle line) as the flow develops from unstalled to fully developed rotating stall. In addition, the steepness of the downstream throttle characteristics can also have significant effect [27]. In view of the path dependent behavior shown by some features of rotating stall (i.e., the hysteresis) it may be that these latter aspects should also be taken into account.

Because of the above, the author feels that while it is useful to pursue calculations of this type, they should be closely compared with experimental data to assess the effects of the assumptions. For example, one result of these calculations which is not satisfactorily explained is that for an isolated rotor the number of cells that appears from the calculation is equal to the number of lobes in the initial perturbation,

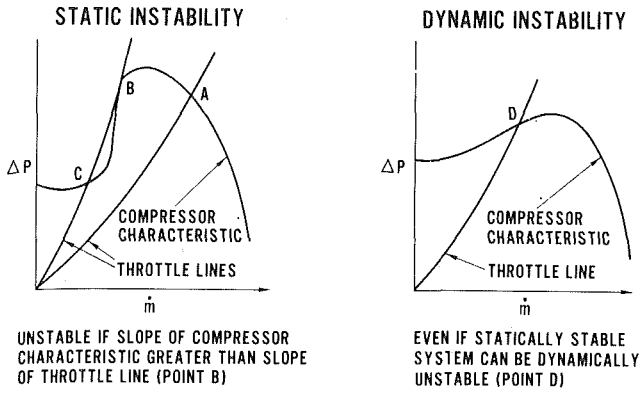

Fig. 8 Types of compression system instability

whereas tests with isolated rotors have shown that the number of cells is rather a function of the overall mass flow through the stage [28].

Overall Compression System Instability

We have so far discussed the prediction procedures for the inception of rotating stall in a compressor with uniform inlet flow, and we can now examine the criteria for the onset of the more global type of instability leading to surge. This is a system phenomenon and one in which, in contrast to rotating stall, the compressor appears to participate in an essentially one-dimensional manner.

We can sketch briefly the basic mechanism for compression system instability. The simplest view of this, and one that is found in many texts, can be derived with reference to a system consisting of a compressor and downstream throttle. The operating point of the "system" is the intersection of the compressor and the throttle pressure-flow characteristic curves. From considerations of the pressure rise through the compressor and the drop through the throttle it can be shown that the system will become unstable when the slope of the compressor pressure rise curve is steeper than the slope of the throttle curve [29].

This *static stability* argument is illustrated on the left of Fig. 8. For a small perturbation in mass flow (a decrease, say), if the system is operating at point A a pressure imbalance will arise to cause fluid accelerations that return the system to operation at the initial point. Point A is thus a stable operating point. At point B, however, where the throttle line is tangent to the compressor characteristic, the pressure forces associated with a small decrease in mass flow will cause the system to depart further from the initial operating point, so that point B is an unstable operating point.

This criterion is, however, too simple to describe the real phenomenon, since it only considers the static stability of the system. In fact it is generally the *dynamic stability* criteria which are violated first.[9] Thus as indicated on the right side of the figure a compression system can be statically stable (according to the foregoing slope criterion) and still exhibit instability.

[9] The terms dynamic and static instability can be made more quantitative by the following illustration. Consider a simple second order system described by the equation

$$\frac{d^2x}{dt^2} + 2\alpha\frac{dx}{dt} + \beta x = 0$$

where α and β are constants of the system. If $\beta > \alpha^2$, the condition for instability is simply $\alpha < 0$, but, independently of α, instability will occur if $\beta < 0$. It is usual to denote these two types of instability as dynamic and static respectively. Static stability ($\beta > 0$) is a necessary but not sufficient condition for dynamic stability.

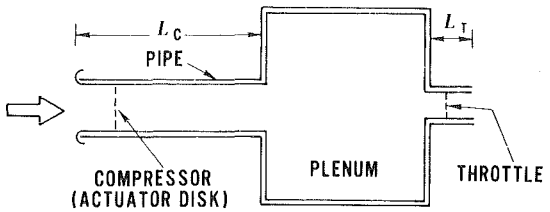

Fig. 9 Equivalent compression system for stability analysis

The basic analysis of the dynamic system stability was also by Emmons, et al. [3], who treated a lumped parameter system similar to that shown in Fig. 9. This consisted of a compressor operating in a duct of small flow through area, a plenum volume (where the flow had no appreciable kinetic energy), and a downstream throttle. Basic criteria were developed for the stability of this system. Since then other investigators have looked at extensions of this problem to predict the system instability point. Although there are differences between the various analyses, the general result that emerges is that the system will be unstable near the peak of the (constant speed) pressure rise/mass flow characteristic, at some slightly positively sloped point, which is generally well before the simple static stability criterion is violated [19].

Although the calculation of this system stability point can readily be carried out, once again we encounter a situation where the critical parameters are the slopes of the steady-state (uniform flow) compressor speed lines at the stall point and, as stated, there is difficulty in predicting these.

We have discussed the two types of instability, and it is useful to now relate them. The global (system) instability is a basically one-dimensional phenomenon, involving an overall, annulus averaged, (in some sense) compressor performance curve. For typical volumes, lengths, and throttle characteristics this must generally be slightly positively sloped for system instability to occur. We have also seen that the axisymmetric flow through a compressor can be unstable to two- (or three-) dimensional infinitesimal disturbances, and that this local instability marks the inception of rotating stall. However, the onset of this rotating stall is very often associated with a precipitous drop in the overall ("one-dimensional") pressure rise mass flow curve of compressor performance. In other words, the inception of rotating stall can lead to a situation where the instantaneous compressor operating point is on a steeply positively sloped part of the characteristic, with a consequent violation of the dynamic and/or the static instability criteria. In this sense, the onset of the local compressor instability can trigger the more global compression system instability. Because of this, the compressor designer does not generally differentiate between the two modes as far as the applications of the stall correlations are concerned.

Multi-Element Stability Models. Up to now the discussion of compression system stability has been based on viewing the compressor as a single element. However under some circumstances this can be too simple, since there can be differences between the mass flow perturbations at the front of the compressor and those at the rear due to compressibility. Thus, different investigators have extended the overall lumped parameter analysis and modeled the compressor in a stage by stage (or even row by row) method, with separate volumes and actuator disks for each stage. Mass, momentum, and energy balances are written for each of the stages. Examples of such investigations are references [30]-[34], and a discussion and comparison of some of the basic models can be found in [31].

The determination of the instability point for these models can be found either by solving for the eigenvalues or by

(digital) simulation of the system transients. In addition these models can explore the effects of pulsations that are imposed on the compression system. However, as with the simpler models, "the compressor stability boundary is strongly influenced by the stage characteristics. The overall results are thus dependent on the accuracy of the stage characteristics . . ." [34]. Hence the ability to predict the *slopes* of the steady-state (uniform-flow) compressor speed lines *at the stall* point is a key item in the successful use of these techniques.

Inlet Distortion Effects on Stall Inception

The discussion so far has been confined to stability predictions with a uniform inlet flow, but critical situations for stall are often those in which an inlet nonuniformity or distortion is imposed on the compressor. For an aircraft engine, for example, distortions can arise from inlet separations, armament firing, aircraft maneuvers, or take off in cross wind. In any event, if we consider a compressor operating in nonuniform flow at the same overall mass flow rate as one in a uniform flow, it is clear that in the former case some parts of the blading will be working at more unfavorable conditions than in the latter, and that some sections of the blading will be closer to the stall point. The overall effect of distortion is therefore to degrade the overall performance of the machine and, in particular, to decrease the stall free range of operation. Since the effects of distortion on compressor stall onset can be substantial, it is useful to discuss the general fluid mechanics of compressor operation with nonuniform flow.

In the investigations that have been carried out on the effect of inlet distortions, the flow nonuniformities are commonly divided into radially varying steady-state, circumferentially varying steady-state, and unsteady distortions. In reality the distortions encountered are combinations of two or possibly all three of these types, but significant progress has been made using the above simplifications since, in many situations, the principal loss in stall margin can be regarded as due to one of the three. For example, during changes of aircraft attitude the inlet distortion may vary significantly with time over a time scale of the order of tenths of seconds or longer, which is many times longer than the time for a fluid particle to move through the compressor. The distortion can therefore be considered as if it were steady-state. In analyzing the response of an axial flow compressor to an inlet flow distortion, it is also essential to recognize the strong interaction that exists between the compressor and the distorted flow field. Put another way, the compressor does not passively accept the distortion but plays an active role in determining the velocity distribution that will occur at the compressor face, which is what the individual compressor airfoils actually respond to.

We will very briefly discuss the pure radial distortion first. Typically this is analyzed using the axisymmetric procedures that have been developed for a uniform inlet flow, i.e., the distortion is essentially viewed as an off-design situation. (In doing this, one comment that can be made is that distortions encountered in practice can have substantially more severe gradients than do flows that arise solely from off-design operation. Hence, the calculations may have to be carried out using stations within the blade rows as well as at inlet and exit). The criteria that would then be applied to predict the onset of stall are based on the correlations referred to earlier. Therefore this type of distortion really does introduce any new phenomena from those mentioned previously, and we will not discuss it further.

With circumferential distortion, however, the asymmetry of the flow does introduce a new element into the fluid dynamic analysis of the compressor behavior. There has been a large amount of work on this topic. Much of it has been carried out treating the distortion as a small amplitude perturbation and using a linearized approach. Such an analysis can give very useful physical insight as well as quantitative information about the performance of the compressor in a circumferentially nonuniform flow. In particular it is able to show clearly the role of the various design parameters and operating conditions on distortion transfer, [10] to demonstrate the manner in which the upstream velocity field due to the distortion is substantially modified by the compressor, and to motivate the basic length rules for scaling the overall flow phenomena. Excellent examples of analyses of this type are the papers by Plourde and Stenning [35], Dunham [20], or Stenning [36], and these are recommended as an introduction to the field. (See also [37] for an extension of the basic ideas to compressible flow.)

From the point of view of *stability* prediction, however, the analysis of inlet distortion as a small perturbation can give no information as to the effect of inlet distortion on stability. This is because, in a linear system, the steady imposed distortion and the self-excited propagating perturbation (rotating stall) do not interact (i.e., the interaction is second order and thus not included in a linear analysis). We will therefore concentrate on those approaches which do attempt to assess the loss in stability due to inlet distortion. As in the uniform inlet flow situation, the approaches again range from correlations to more basic analyses.

The most empirical approach makes use of so-called "distortion indices" to describe the stability degradation to be expected from inlet distortion. The indices are based on the inlet total pressure distribution, and are a way to quantify the effects of a given total pressure pattern. For a given engine (or compressor) a correlation will be built up by testing with different types of inlet distortion to give the maximum distortion that can be tolerated at a given corrected speed. Once this is done the stability margin can be assessed in various other situations by converting the total pressure distortion in that case into an equivalent distortion index.

Much effort has been spent on these correlations for engines and they have been developed to take into account the fact that the distortions in general have a radial distribution to them as well as can contain a reasonable amount of unsteadiness. Descriptions of the basic methodology are given by Hercock and Williams [38] and by Collins [39], which also contains a list of other references on the subject. We will not discuss these correlations much further although there is one point which should be mentioned. There are situations in which the inlet total pressure distortion can be varying with time so that the instantaneous distortion factor undergoes very rapid changes. It is found in these situations that disturbances which have a time duration of less than *roughly* a rotor revolution have little effect on compressor stability [39]. Thus, for these higher frequency distortions, the unsteady response of the compressor appears to be beneficial as regards the onset of instability. We will discuss this important point further below.

At a somewhat more fundamental level of assessing compressor stability with inlet distortion are the so-called parallel comperessor model and its extensions. Descriptions of the basic ideas and assumption of this model are given by Reid [40], Stenning [36], and Mokelke [41]. The approach is to view a compressor operating in a circumferentially nonuniform flow as two compressors operating "in parallel" with each performing at a condition corresponding to the local value of mass flow. If the flow geometry downstream of the compressor is a constant area annulus, and the flow angle from the last stator is constant around the circumference, the two compressors can be taken to have the same exit *static* pressure. In addition, because there is very small opportunity

[10] The ratio of total pressure distortion at the exit to that at the inlet.

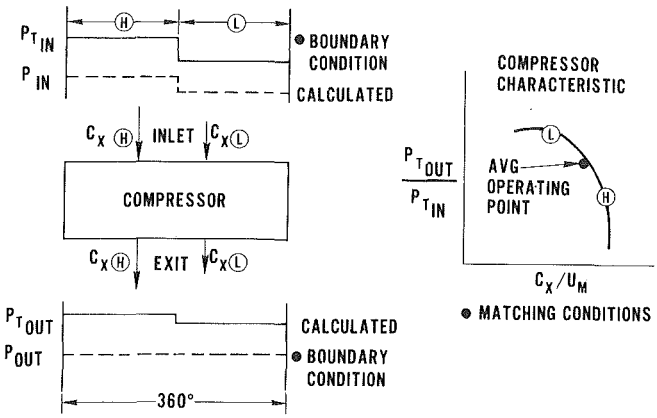

Fig. 10 Circumferential distortion analysis calculation procedure for 180 degree distortion

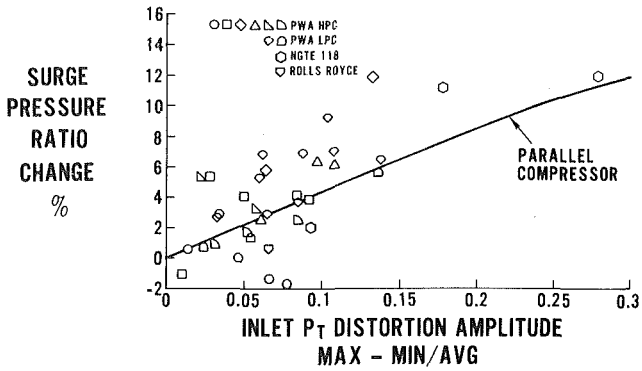

Fig. 11 Sensitivity to 180 degree circumferential distortion [45]

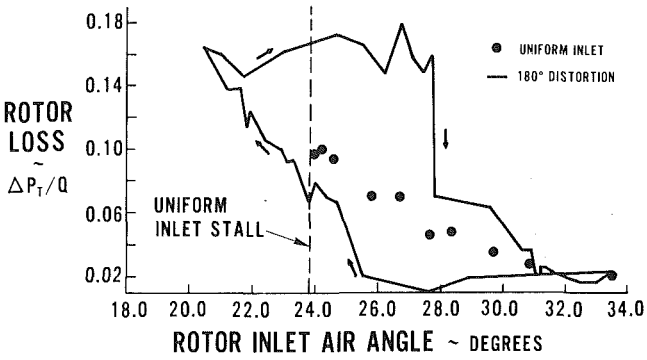

Fig. 12 Unsteady rotor response [45]

for circumferential cross flows within the compressor, the mass flow distribution at inlet and exit can be taken to be the same — i.e., there is no mixing of the flow in the two "segments" of the compressor. The overall mass flow, the two boundary conditions of specified local inlet total pressure distribution and constant exit static pressure, plus the idea that each segment is performing at some local point on the uniform flow characteristic, are enough to define the local mass flow distribution at the compressor inlet and thus the distorted flow performance. A schematic of this procedure is shown in Fig. 10 for a 180 degree square wave distortion in inlet total pressure. The model is not restricted to small amplitude nonuniformities, so effects due to the curvature of the compressor characteristic can be included. It should be noted that these models are also capable of treating inlet total temperature distortions as well as total pressure [41], [42].

In order to predict the stall point, however, some additional criterion must be invoked since the parallel compressor model is steady-state. The simplest is that the onset of rotating stall will occur when the flow in the low velocity region (point L in Fig. 10) is reduced to a level at which the machine will stall in a uniform flow. This concept, plus the basic parallel compressor ideas, leads one to the general design philosophy that steep speedlines are desired for distortion tolerant compressors [43], [44].

A comparison of the predictions of this model with test data is shown in Fig. 11, which presents the loss in stall pressure ratio as a function of the amplitude of the total pressure distortion, for 180 degree "square wave" distortions [45]. The solid line is the theoretical prediction given by the basic parallel compressor theory. It can be seen that although the model gives reasonable qualitative trends, on a quantitative basis the predictions leave considerable scope for improvement.

For a distortion of smaller extent this discrepancy is increased. For these distortions the theory predicts that there will be a greater loss in stall margin (compared to the uniform flow case) than is observed with the 180 degree distortion. (This is because the circumferential segment with the lowest axial velocity is assumed to be responsible for the stall, whereas the stall pressure ratio and flow are calculated as the average.) Experimental results are in substantial disagreement with this, however, since it is found that distortions of small circumferential extent have little effect on stall line.

The reason for this, and one of the major defects of the basic parallel compressor theory, appears to be associated with the assumption that the performance of the compressor can be described by the quasi-steady application of the local uniform flow performance curve. However, with a circumferential distortion, the rotor passes through a spatially nonuniform flow field and thus sees an unsteady flow. The response of the rotor can be considerably different than that predicted by a quasi-steady analysis, especially near the stall point. As one example of this, Fig. 12 shows the (relative) total pressure loss coefficient for a rotor operating in a 180 degree distortion [45]. The horizontal axis is inlet flow angle (measured from the tangential direction, so that decreasing β_1 means increasing angle of attack) and the vertical axis is the rotor total pressure loss coefficient. It can be seen that the loss coefficient exhibits an unsteady "loop" as a function of inlet angle as the rotor moves through the distortion. The values obtained in a uniform flow test of the rotor are also shown and it can be seen that there are substantial differences between the steady and unsteady performance.

A further very important point which is illustrated by this figure is that with distortion the rotor is operating transiently at a flow angle that is beyond the uniform flow stall point. That is, excursions to higher angles of attack (i.e., lower flow rates) than could be tolerated with a uniform flow can be tolerated locally (transiently) in the distorted case. This is in direct contrast to the hypothesis used in the basic parallel compressor model for defining the stall point, and the unsteady response appears to be an important feature to include in developing predictive methods for circumferential inlet distortion.

There are several different approaches to doing this. In the first, the idea of a critical angle of distortion has been developed [38], [40], [44]. This is essentially an angular extent of distortion below which "further loss of stall pressure ratio for a given distortion intensity is negligible" [40]. Thus, the procedure is to base the inlet distortion intensity on the average total pressure in a sector, of the extent of the critical angle, surrounding the lowest pressure. This constitutes an extension of the basic parallel compressor stall line hypothesis to account for unsteady response. However, it is necessary to evaluate the critical angle for each individual compressor, and quite different values have been reported in the literature [43]. In an alternative approach [45], a one-dimensional model of the unsteady rotor response is incorporated in a multisegment

parallel compressor model (roughly thirty segments are used). This model can have some segments operating at flows below the uniform flow stall point.

Better prediction of stall than with the basic model can be achieved using such approaches. As an example, the use of one of these methods (the multisegment parallel compressor analysis) for prediction of the distorted flow stall line in a two spool turbofan engine is described by Braithwaite and Soeder [42]. It should be emphasized, however, that adequate definition of the uniform flow performance curve (including stall point) is a prerequisite for successful use of any of these methods.

The third class of studies of the problem of compressor stability in a distorted flow is the numerical solution of the time dependent nonlinear inviscid equations of motion. These describe the flow field from a specified initial state to a final "steady-state solution" similar to that described earlier with the uniform inlet flow. As with the uniform flow situation the analyses can either predict a steady flow or a large amplitude propagating disturbance, which is now modulated by the presence of the inlet total pressure distortion. They can therefore give an indication of the stability point of the distorted flow. So far these have been applied to single rows or stages and have not really been thoroughly assessed against experimental data. A good example of this approach is the work by Adamczyk [46], which has been extended to the compressible flow regime by Pandolfi and Colasurdo [47].

Again, one of the main limitations is the modeling of the dynamic blade row performance, especially at flows near and below the uniform flow stall point. There is not space in this review to discuss some of the various experimental and theoretical approaches to investigating unsteady blade row response. However, several useful review articles on unsteady flows have appeared recently and the interested reader is referred to these [48–50]. (In addition, one novel approach to obtaining data at flows below the stall flow is that described in [51].)

Compressor-Component Coupling. As stated previously, if one considers the behavior of compressors in asymmetric flow, the general conclusion that emerges is that for the type of flow nonuniformities which have the greatest effect on stability, namely those with a circumferential length scale of the order of the circumference of the compressor (i.e., a "one lobed" type of pattern with a strong first Fourier component), the compressor and the downstream components must be viewed as closely coupled. Hence the distorted flow performance of the compressor can be quite dependent on the downstream component.

An example of this is given in Fig. 13, which shows both predictions and experimental data from several research compressor experiments [23]. The data are from three different tests with an inlet circumferential total pressure distortion. In these tests the only thing that was altered was the exit section, one test being conducted with an annular exit nozzle downstream of the compressor, another with a constant area annulus exit section, and the third with an annular exit diffuser downstream of the compressor. The vertical axis shows the compressor distortion transfer, which is the ratio of the magnitude of the total pressure nonuniformity at exit to that at inlet, for the three different exit sections. It can be seen that the presence of different downstream ducts has a substantial effect on the compressor performance in distorted flow. This is quite contrary to the usual experience in axisymmetric flow where, for a given flow rate, the performance of an upstream component is only weakly affected by downstream conditions. Note that the results shown in the figure were obtained with downstream components that are all relatively passive fluid mechanical devices. With another

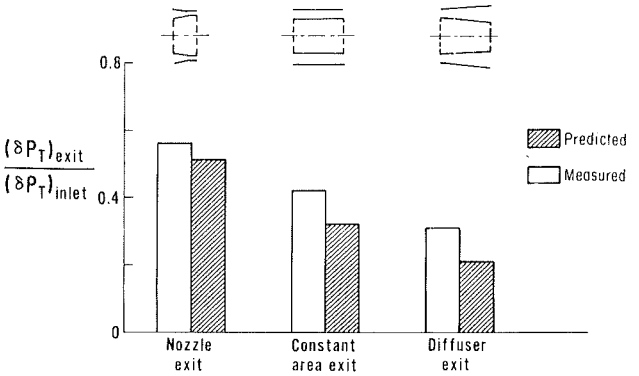

Fig. 13 Effect of downstream components on distortion transfer [23]

compressor downstream, as is usually the case in a modern multi-spool gas turbine engine, the effect of the coupling can be expected to be much stronger.

Coupled Compressor-Diffuser Flow Instability and Diffuser Instability. The above discussion of the coupling between a compressor and a downstream component furnishes a useful introduction to another aspect of the onset of instability in compression systems. Consider the compressor stability boundary for a nominally uniform inlet flow condition, i.e., the inception point of rotating stall. This occurs when conditions are such that a *circumferentially nonuniform* flow perturbation in the compressor annulus can grow. Based on the previous section, it might be expected that this point could be affected by components downstream of the compressor, since the downstream boundary condition on the flow perturbation is altered. The quantitative extent of changes in stability boundary is of course dependent not only on the nature of the downstream component, but on the circumferential length scale of the flow perturbation, since this also determines how closely the compressor and the downstream component are coupled [52]. For many situations of practical interest the predominant mode of instability occurs with a one-lobed type of disturbance so that the relevant axial distance within which there can be a strong interaction between components is on the order of the mean radius of the machine.[11]

This generally means that, in terms of the stability boundary, the compressor is *not* isolated from the influence of downstream components. More detailed analytic and experimental studies of this phenomenon bear out this general conclusion [53]. As noted before this has important application in analysis of two spool compression engines. It also emphasizes again that one cannot analyze the stability of a single row in a multistage compressor *by itself* as a guide to the compressor stability, but must include the other stages both upstream and downstream.

This type of interaction between the pumping element and the downstream components also can be strongly manifested in centrifugal compressors. In these situations the diffusers (vaned or vaneless) can be not only the cause of premature compressor stall, but can themselves exhibit rotating stall [54, 55]. In modern high pressure ratio centrifugal compressors, in fact, the initiation of system surge has been postulated to be linked to the instabilities in the diffuser [56].

A Digression on Unsteady Response. We have discussed the fact that the compressor blading responds in an unsteady manner, and that this departure from quasi-steady behavior appears to be quite significant near stall. However, there is a

[11] In other words, the coupling can only be neglected for axial separations that are significantly greater than this.

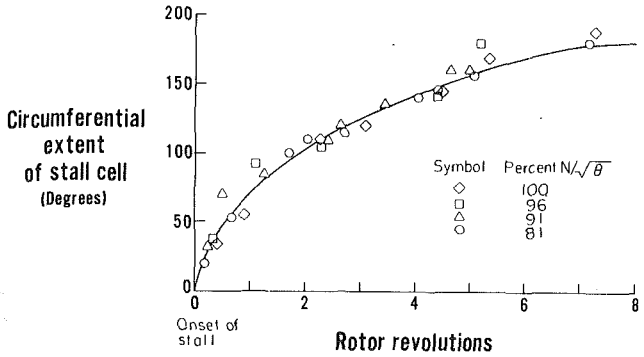

Fig. 14 Circumferential growth of stalled region (three stage compressor) [57]

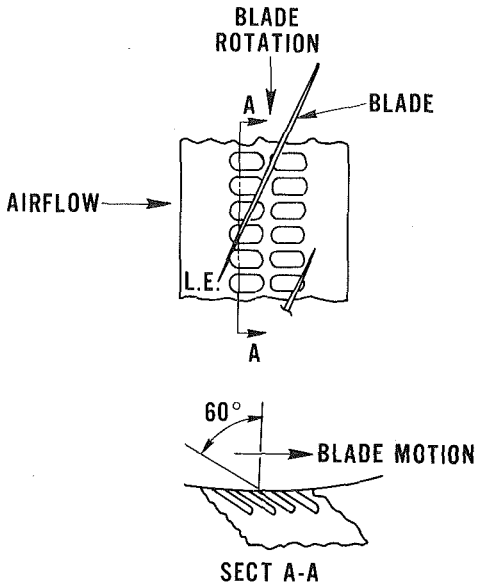

Fig. 15 Axial skewed groove casing treatment

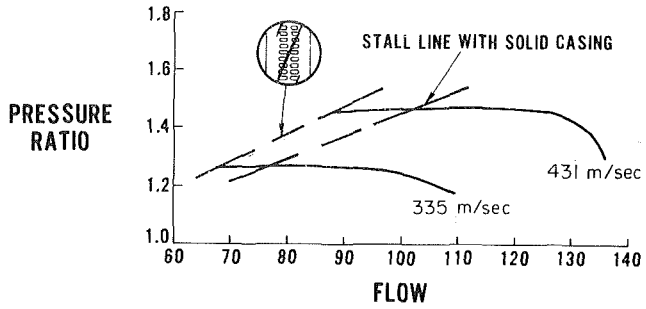

Fig. 16 Stall margin increase due to casing treatment [43]; flow in lbm/s

larger scale aspect of the unsteadiness which is also associated with the onset of rotating stall.

The time scale that one would tend to associate with *blade* unsteady response is on the order of b/W where b is the blade chord and W is the relative velocity. However let us consider the time scale that characterizes the transformation of an axisymmetric flow to the severely nonuniform one of rotating stall. A representative time scale might now be the disturbance wavelength (e.g., the mean circumference of the machine) divided by the through flow velocity. This is the time scale used in Fig. 7 and is much longer than that based on blade unsteady response. A qualitative physical argument for this scaling can be made by noting that the change from unstalled to stalled flow involves the shedding of blade circulation of the same sign over a significant circumferential extent of the flow annulus. The flow will only approach a "fully developed" state when this shed vorticity has been convected downstream some distance on the order of the disturbance wavelength.

These rough considerations imply that for a given machine the stall cell growth time might scale with axial velocity (or since C_x/U is approximately constant at stall, with rotor speed) and circumference. This has been found to be the case in one of the few instances where data is available, as shown in Fig. 14. This response of the overall flow field is therefore likely to occur on a time scale an order of magnitude or more longer than that associated with the individual blades. The compressor performance (pressure rise, torque) during a stall transient may therefore differ substantially from the steady state performance. This facet of unsteady response, which may be quite important in the application of one-dimensional compression system models, for example, is another of the features of the stall process that are at present not well understood, and on which there is little data.

Stability Enhancement Using Rotor Casing Treatment

We have described some of the various types of instability, commented on the criteria for determining their onset, and discussed the adverse effects of inlet distortion on stall inception. However, another area which is of interest concerns techniques for enhancing the stability margin of a turbomachine. The most straightforward of these is to achieve the needed stability margin by matching the compression system below its peak efficiency point (in effect setting the match point so that the compressor blading has incidences and pressure rises far below the maximum). Although this would provide an increase in airfoil incidence range between the operating line and the stability limit, it would also lead to decreased efficiency on the (down-rated) operating line, which is generally unacceptable.

One solution to this problem is the use of so-called "rotor casing treatment" to improve the stability of compressors. This casing treatment consists of grooves or perforations over the tips of the rotors in an axial compressor or located on the shroud in a centrifugal machine. Numerous investigations of these types of configuration have been carried out under widely varying flow conditions (e.g., references [58-65]), and these have demonstrated that the range of usefulness of these casing configurations extends from compressor operation in basically incompressible flow (relative Mach numbers of roughly 0.15) to the supersonic flow regime (relative Mach numbers of 1.5). A schematic of one of the more successful of these casing configurations is shown in Fig. 15. These grooves are known as axial skewed grooves. A typical improvement in stall line brought about by use of these grooves is shown in Fig. 16 for a transonic axial fan. It is to be noted that far larger improvements have been seen and that casing treatment has also been used to inhibit instability in centrifugal compressors [66, 67].

Although the basic mechanism of operation of the casing treatment has not yet been fully elucidated, some important points have emerged. If we refer back to the description of the onset of rotating stall, it is apparent that for the axisymmetric flow to become unstable the blade passages must be operating at a condition such that they have the capacity to generate large blockages for small changes in inlet conditions. What is found, however, is that the level of blockage in the rotor passages can be greatly decreased due to the presence of these grooves. As an example of this, Fig. 17 shows data taken just downstream of an axial compressor rotor [68]. The measured quantity is the nondimensional relative frame total pressure loss across the rotor, i.e., the total pressure loss measured (by

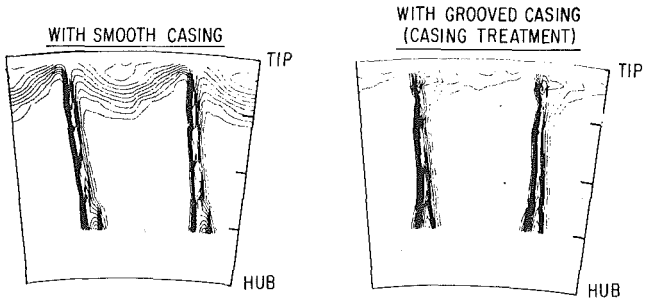

Fig. 17 Rotor exit total pressure loss contours near stall [68]

a probe rotating with the rotor) in a coordinate system fixed to the rotating blades. Data are shown for both solid wall and casing treatment, at a mass flow rate near the stall limit of the solid wall configuration. In this instance the onset of rotating stall appeared to be associated with a large blockage created near the end wall of the blade passage. The contours are increments of 0.05 in relative total pressure loss across the rotor divided by inlet dynamic pressure. It can be seen that with the casing treatment there is a much smaller region of low total pressure fluid and hence a greatly decreased blockage in the blade passage. One would therefore expect that the tendency towards rotating stall would also be greatly suppressed and the stable flow range of the machine extended with the grooved casing, which indeed was found to be the case.

These general ideas concerning the effect of the grooved casing on the flow blockage in the rotor passage can in fact be taken somewhat further. As described previously, the basic physical picture presented for the onset of rotating stall is one that is dependent on the level of flow blockage in the blade passages. In many instances, however, one can make a useful distinction between those situations in which the large blockages are associated with the endwall boundary layer and those in which the major part of the blockage is associated with the blade boundary layers away from the endwall. These two situations are referred to as wall stall and blade stall respectively.

Based on observations of widely varying effects of casing treatment on compressors exhibiting what appeared to be blade stall and those encountering wall stall, a series of experiments were carried out using two different rotor builds, one designed so that a blade stall was encountered, the other designed for a wall stall [68]. The rotors were tested both with and without casing treatment. It was found that the casing treatment markedly improved the stall range for the wall stall rotor (compared to the solid wall). In contrast, the blade stall rotor showed little change in stall point when the casing treatment was used. These experimental findings are consistent with the hypothesis that casing treatment is likely to be effective only in a situation in which a wall stall exists, and thus furnish one general guideline for its use.

The experimental results mentioned have shown some of the effects of the casing treatment on the overall flow field, but as stated, the mechanism of operation is still unknown. Different hypotheses have emerged but none is able to explain all the experimental results satisfactorily. As one example, several investigations have invoked the concept of a radial flow through the porous casing, and calculations carried out including this idea in the basic models for predicting rotating stall onset do show the possibility of a stabilizing influence of these radial flows [58], [65]. However, it should be noted that the analyses are based on the wavelength of the flow perturbations being much larger than the blade gap (i.e., treating the flow in the blade row on a passage averaged basis). While such radial flows can occur in situations where there is a plenum or external flow path, or where compressibility is important, experiments carried out using closed groove configurations at low speeds (where there can be no average radial flow into the casing over a sizeable fraction of the circumference) have also found substantial increases in stall margin. Thus while the "radial relief" idea may be important in some aspects of the problem it does not seem to be one of the most critical features.

In contrast to this passage average approach, it may be more useful to examine the flow in the grooves on a smaller scale, i.e., on a blade to blade basis. In particular consider the axial skewed groove configuration shown in Fig. 15. Note that there will in general be a higher static pressure over the rear part of the grooves than over the front part. One would therefore expect that fluid would be forced down into the groove at the rear and up as a jet at the front end. Such flows have been observed by Takata et al., who measured jet velocities that were comparable with free stream velocities [58]. In the frame of reference attached to the blade these jets have very high velocities (in a direction toward the pressure side of the blades). The flow in and out of the grooves is thus a potent device for the transfer of momentum between the moving wall and the low momentum flow in the boundary layer, thus increasing its total pressure (in the relative frame) and decreasing the blockage. In this connection it is relevant to note that data presented in [59] (from a compressor which was run with an axial skewed groove casing treatment) showed local blade surface pressures near the rotor tip that were higher than the relative total pressure. These overall considerations, however, have not yet been developed in a quantitative manner, and substantially more investigation is needed of the interaction between the flow in the grooves and that in the endwall region.

Although casing treatment is a potent remedy in increasing stall range, it should be emphasized that it is *not* a panacea. It has been found that those known treatments which have the most success in improving stall range generally have some penalty in efficiency associated with them. This situation gives a strong motivation to understand the basic fluid mechanics of operation of casing treatment in order to enable one to design optimum treatment configurations.

There are also situations in which casing treatment is unlikely to be successful. One has already been identified in the discussion of wall stall and blade stall, and a more obvious instance is when the stall occurs at the *hub*. In this situation, the flow shift towards the tip region, due to the casing treatment, can actually decrease the stall margin, since it will aggravate the hub stall condition. Finally, there can be mechanical and manufacturing difficulties associated with casing treatment usage in production engines. Designers have therefore been reluctant to adopt casing treatment as a standard item.

Behavior Subsequent to Instability Initiation

We have, until this point, been concerned primarily with the phenomena associated with the onset of instability. Another very important problem is associated with the behavior subsequent to the onset of instability, where one of two modes of system response, corresponding to surge or rotating stall, can be exhibited (see Fig. 3). For a system that goes directly into rotating stall, the transient behavior after the initial instability consists of a rapid decrease in pressure rise and flow, with eventual establishment of a new stable equilibrium point (in rotating stall) at a greatly reduced flow and pressure ratio. In surge, on the other hand, there is no new equilibrium point and both the mass flow and pressure rise undergo large amplitude oscillations.

For an aircraft gas turbine engine, a key requirement is recovery from stalled conditions once instability occurs. In this connection, therefore, it is important to note that even

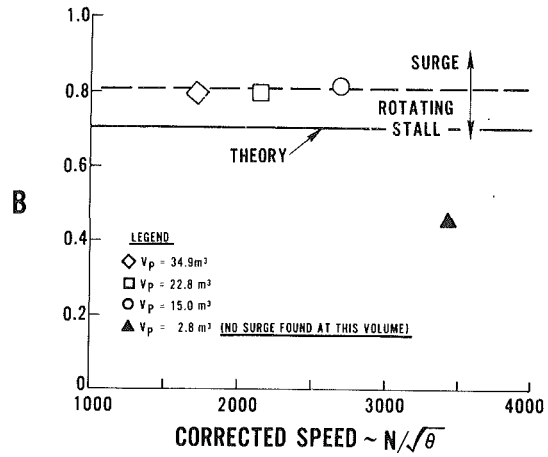

Fig. 18 Surge/rotating stall boundary for different plenum volumes [22]

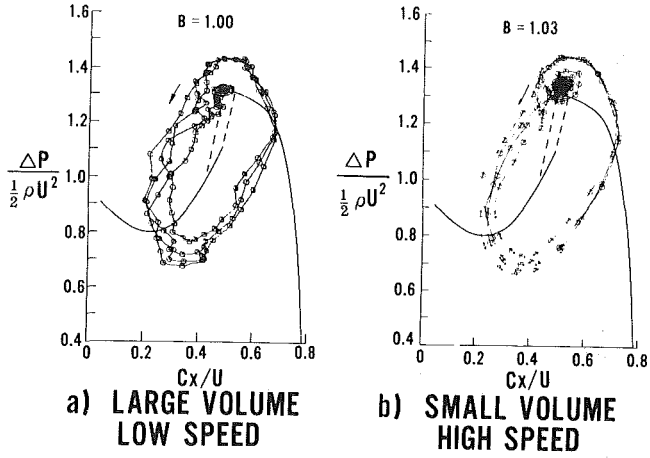

Fig. 19 Dependence of system response on B parameter [22]

though surge may be associated with severe transient stresses due to the large amplitude flow variations, the engine does operate in an unstalled condition over part of the surge cycle. Because of this, one is able to open bleed valves or make other changes that will have an effect on bringing the system out of surge. In contrast to this, rotating stall, and in particular the full span, large extent rotating stall which is characteristic of a multistage compressor, can be very difficult to recover from, as will be discussed in detail below. Therefore it is the surge mode that is much more favorable for recovery in systems such as aircraft gas turbine engines and is hence the more desirable one.

On the other hand, for an industrial centrifugal compressor or pump, it may be that operation in rotating stall (if one *must* encounter some sort of instability at some point in the operating range) can be tolerated, and that throttle movement is wide enough so that recovery is readily achieved. In this situation it may be that the often violent oscillations that occur during surge make this the less desirable of the two modes. Whatever the situation, however, it is apparent that an important question is whether a given pumping system will exhibit large amplitude oscillations of mass flow and pressure ratio (surge), or whether the system will operate in rotating stall where the annulus average mass flow and pressure ratio are essentially steady, but are greatly reduced from the pre-stall values.

To answer this, one must analyze the nonlinear system behavior. This was done by Greitzer [57] using the Helmholtz resonator type of compression system model introduced by Emmons (for the linear case) and pictured in Fig. 9. The analysis shows that for a given compression system i.e., specified compressor characteristic, plenum volume, compressor length, etc., there is an important nondimensional parameter on which the system response depends. This parameter is denoted as B:

$$B = \frac{U}{2\omega L_c}$$

where ω is the Helmholtz resonator frequency of the system, L_c is an "effective length" of the compressor duct, and U is the rotor speed. If we insert the definition of ω we can define B in terms of geometric and physical system parameters as

$$B = \frac{U}{2a}\sqrt{\frac{V_p}{A_c L_c}}$$

where a is the speed of sound, A_c is the compressor flow-through area and V_p is the plenum volume. For a given compressor characteristic there is a critical value of B which determines whether the mode of instability will be surge or rotating stall. Systems with B above the critical value (e.g., speeds above a critical value) will exhibit surge oscillations, while those having B lower than the critical (speeds below the critical value) will undergo an initial transient to the (annulus averaged) steady flow and pressure rise associated with operation in rotating stall.

Experimental evaluation of this concept is shown in Fig. 18, in which data is presented for a three stage compressor that was run with several different downstream volumes [22]. The horizontal axis is corrected speed and the vertical axis is the B parameter. The open symbols mark the experimental values of B at which the change-over from rotating stall to surge occurred for the different volumes tested. (The solid point indicates the highest value of B that could be obtained with the smallest volume used.) The regions in which one encounters surge (B above the critical value) or rotating stall (B below critical) as the mode of instability are also indicated. It can be seen that the prediction of a constant B as the boundary between surge and rotating stall is well borne out, although the value at which the change occurs is somewhat above that predicted by the theory. (It should be again emphasized that the value of 0.8 is for this particular compressor.)

Although it is necessary to carry out the calculations for any specific case, some motivation for this general result may be gained by the following qualitative physical arguments. Notice that we can write B as

$$B = \frac{(\rho U^2/2)A_c}{\rho U \omega L_c A_c}.$$

For a given compressor, the numerator, which is proportional to the magnitude of the pressure difference across the duct ($P_{\text{plenum}} - P_{\text{atmospheric}}$), represents the driving force for the acceleration of the fluid in the duct. If we consider oscillations that are essentially sinusoidal in character, the order of magnitude of the inertial forces that arise because of these local fluid accelerations will be given by the product of the fluid density, ρ, the frequency of the oscillations, ω, the amplitude of the axial velocity fluctuation and the volume of the fluid in the duct, $L_c A_c$. Hence if we assume that the axial velocity fluctuation is a specified fraction of the mean wheel speed the magnitude of these inertial forces will be proportional to the denominator. The ratio of the two forces (pressure to inertial) is therefore proportional to B. Thus as B is increased, for example by increasing the rotor speed, a fixed percent amplitude of the compressor axial velocity oscillations will result in inertial forces that are relatively smaller and

smaller compared to the driving force due to the pressure differential. The capability to accelerate the fluid in the duct is thus increased as B increases. Hence as B becomes larger one would expect greater excursions in axial velocity and thus a general trend toward surge rather than rotating stall, and this is in accord with the experimental results.

The B parameter is useful not only in defining the boundary between surge and rotating stall but also as a guide to the scaling of the overall transient behavior of a compression system. In other words, for the same value of B, a compression system should exhibit the same transient behavior, regardless of whether this value has been obtained using a large volume and a low speed or a small volume and a high speed. Figure 19 shows a comparison of the measured transient response for two systems at approximately the same value of B, one with a large volume and low speed and one with a small volume and high speed, with the value of B high enough such that surge occurred [22]. The figures show the instantaneous annulus averaged axial flow parametr (C_x/U) versus nondimensional system pressure rise, i.e., the instantaneous system operating point. The steady-state compressor curves are also shown for reference. As can be seen the two surge cycles show extremely similar behavior, emphasizing the influence of B as the relevant nondimensional parameter for the phenomena under study. Although this figure does not show overall flow reversal, it should be emphasized that with high pressure ratio multistage compressors, periods of reversed flow during the surge cycle are to be expected.

We have said that the question of whether surge or rotating stall will occur is not only dependent on B but upon the compressor characteristic. A basic attempt to take into account one aspect of this, the number of stages (N) leads to the use of NB as the relevant parameter for scaling rather than B. The motivation for this is that for N identical stages and a given value of B the pressure rise will be approximately proportional to N, so that the ratio of pressure to inertia forces will increase as the number of stages. There is thus a strong trend toward lower values of B needed to encounter surge, rather than rotating stall, as the number of stages and overall pressure rise of the machine is increased.

Physical Mechanism for Compression System Oscillations. We have described the necessity for certain system parameters to be of a specified magnitude in order to encounter surge. One other aspect concerns the position of the compressor operating point in order to have surge cycles. In particular, in order for a surge cycle oscillation to occur, the compressor slope must be positive over some part of the surge cycle. The physical mechanism associated with this can be seen by considering a compression system undergoing oscillation about a mean operating point. Since dissipation is occurring due to the presence of the throttle, there must be energy put into the system to maintain this oscillation, and the only source available to do this is the compressor. Thus let us examine the mass flow and pressure rise perturbation through the compressor. These are shown in Fig. 20 which presents the *perturbations* in mass flow ($\dot{m}$) and pressure rise (ΔP) through the compressor, plotted versus time over a period of one cycle. The product of the two, $\delta\dot{m} \times \delta\Delta p$, which is proportional to the net *excess* (over the steady state value) of production of mechanical energy is also shown.

In the case of a positive slope it is found that favorable conditions for the energy addition occur since high mass flow rate and high rate of mechanical energy addition (in the form of pressure rise) go together. As shown in the figure the product of the two is positive definite over the whole cycle. Thus the net amount of mechanical energy that the compressor puts into the flow will be higher than if the system

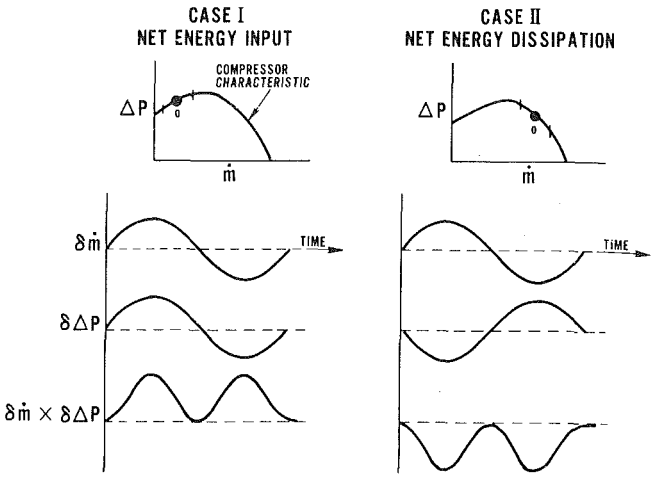

Fig. 20 Physical mechanism for surge oscillations

were in steady operation at the mean flow rate. (In a similar fashion the net dissipation due to the throttle will also be higher than if the system were in steady operation.) When the net energy input over a cycle balances the dissipation, a periodic oscillation can be maintained. In the case of an operating point on the negatively sloped region, as shown in the right-hand side of the figure, the compressor actually puts in less mechanical energy over a cycle than in steady operation, (since high mass flow is associated with low energy addition, and conversely) and no oscillations are possible. To summarize, (surge) oscillations are possible only when the mechanical energy input from the compressor is greater during the oscillatory flow than during a mean (steady) flow, and this can occur only if the characteristic is somewhere positively sloped so that high mass flow and high mechanical energy input per unit mass go together.

We have discussed some of the physical features of surge, and we now turn to examination of the other consequence of compressor instability - rotating stall. We will look at some of the overall features of this regime, then discuss some of the measurements on the structure of the flow field that have been carried out, and then examine a basic method for predicting compressor performance in rotating stall - particularly as regards the extent of the stall/unstall hysteresis loops.

General Features of Rotating Stall in Axial Compressors

Flow Regimes. It is useful first to describe the flow regimes encountered during compressor operation in rotating stall and to relate them to the changes in compressor performance that can be expected. Let us consider a hypothetical compressor, of, say, three stages, and examine the performance curves plotted in the form of ψ_{TS} versus ϕ, where ψ_{TS} = (exit static pressure - inlet total pressure)/ρU^2, and $\phi = C_x/U$. Two possibilities are shown in Fig. 21(a) and 21(b), which can be regarded as being representative of data from a number of actual compressor tests. Figure 21(a) shows a compressor whose performance curve is either continuous or has only a small discontinuity in pressure rise (a few percent) at the stall point, A. This behavior, where there is a very gradual drop in delivery pressure (or often no drop) at the inception of stall, is associated with the compressor operating with one or more stall cells that do not cover the total height of the annulus. This is known as part span stall, and an indication of a typical configuration is shown in the figure where we see two regions of severely retarded flow, i.e., two stall cells, at the tip. It is of course not always true that the cells appear at the tip; they can

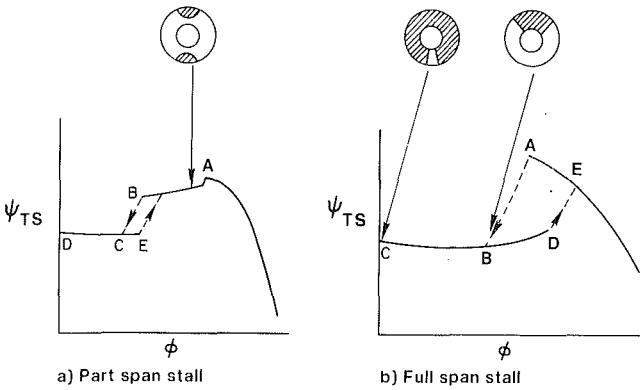

Fig. 21 Compressor characteristics showing rotating stall regimes

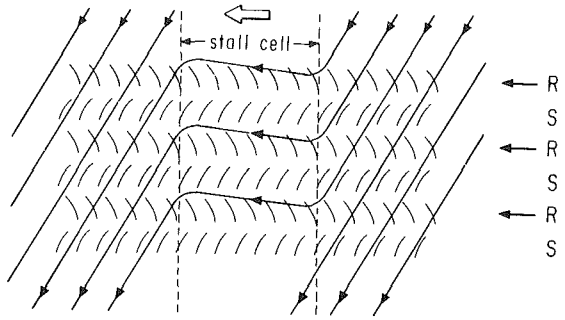

Fig. 22 Sketch of stall cell structure (drawn in absolute reference frame)

also be found at the hub, and the picture should just be regarded as giving one typical possibility.

Part span stalls are also often seen during low speed operation of multistage high pressure ratio compressors. Under these conditions, which can occur to the right of (i.e., below) the stall line shown in Fig. 1, there can be severe mismatching between the front and rear of the compressor, and the overall characteristic may thus still be quite negatively sloped.

As the throttle is closed from the stall point, and the mass flow through the compressor illustrated in Fig. 21(*a*) is further decreased, the performance curve can exhibit a large discontinuity where the pressure rise and mass flow jump to significantly reduced values; this occurs from point B to C on the figure. This jump is associated with a change in the type of stall. At point C there is one single cell, occupying a sizable fraction of the annulus and extending over the full annulus height. This regime is known as full span stall. Further throttling causes this cell to increase in size with the delivery pressure remaining relatively constant from point C to D. As the mass flow approaches zero, the stall cell can grow to fill the annulus so that the flow can become basically axisymmetric with the pressure rise often dropping off slightly. If we were to once again open the throttle, we would find that the mass flow at which the compressor left the *full span* stall regime, point E, was different from that at which it entered. However, this *hysteresis* is usually negligible for the onset and cessation of *part span* stall.

If we examine Fig. 21(*b*) we see a somewhat different picture. The large discontinuity in pressure rise and flow now occurs right at the stall limit (point A). The sharp drop in both these quantities as the operating point jumps from point A to point B in this figure is associated with the compressor going directly into single-cell, full span stall, as indicated schematically. Further throttling causes the stall cell area to grow, although it may not reach 100 percent of the annulus area even at zero mass flow through the compressor, with the pressure rise being relatively constant from point B to "shutoff" at point C. If one opens the throttle it is found that there is a substantial hysteresis between the onset and the cessation of stall, in that the throttle area has to be increased to a significantly larger value than that associated with stall onset, in order for the machine to unstall. It is in fact this large hysteresis which is responsible for the difficulty in recovering from a stalled condition.[12]

The two types of behavior at the stall limit point shown in Fig. 21(*a*) and 21(*b*) have also been termed progressive and abrupt stall respectively. This aptly describes the stall in terms of changes in the compressor output, since the former is associated with a relatively minor deterioration of the compressor performance from the unstalled state, but the latter can cause severe reductions in performance. On a fluid mechanical basis the occurrence of these different types of behavior is due to operation in different regimes of rotating stall. In order to predict the compressor performance subsequent to the onset of stall it is therefore important to be able to predict which type of rotating stall, part span or full span, will occur at the stall limit, since this is directly related to the occurrence and size of the hysteresis region.

Structure of the Stalled Flow Field. There have been many experimental investigations of the features of the flow fields associated with compressor performance in rotating stall. These have included flow visualization [69], studies of the three-dimensional velocity field [70, 71], as well as the use of instrumented blades to measure the time varying forces on the blades [72, 73].

Just as in the theoretical treatments of stall and stall inception, much of the detailed experimental work considers isolated rotors. However, it has become apparent that the constraints on the flow field in a multistage machine are quite different from those in an isolated rotor. For this reason we will concentrate here on one of the few investigations of rotating stall in a multistage environment, which was by Day and Cumpsty [21]. They used an ensemble averaging technique which was triggered on each passage of the stall cell so that they could average the results of many revolutions of the cell to provide detailed definition of stall cell properties. Their investigations were carried out on several different three stage compressors having quite different design values of axial velocity parameter, $(C_x/U)^*$, so the effect of this important parameter could be clearly seen.

Their paper, which addressed the full span stall problem, shows that in most cases the flow in the compressor can be divided into distinct areas of stalled and unstalled flow. To a reasonable approximation the flow in the unstalled area behaves as it would if there were no stall cell at all. In the stall cells the fluid velocities ahead of the rotors were near blade speed and in the direction of rotation, while behind the rotor the velocities were much lower. The axial velocities in the cells were small compared with either blade speed or the unstalled axial velocity; their precise magnitude and direction, however, varied from compressor to compressor. In addition it was emphasized that the full span stall cell extends *axially* through the compressor. The basic reason for this is that the axial spacing between blades is quite small compared to the width of the stall cell. Since a mass flow defect (which is what a stall cell is) in the front of the compressor can only be "filled in" by circumferential cross flows between the blade rows, the close spacing means that this defect will extend straight through the compressor (this is the same concept that is used in the modeling of circumferential distortion).

[12] This hysteresis between stall and unstall has, in the past, been held responsible for the existence of surge cycle oscillations. This is not correct and hysteresis in fact *inhibits* the occurrence of the surge cycles.

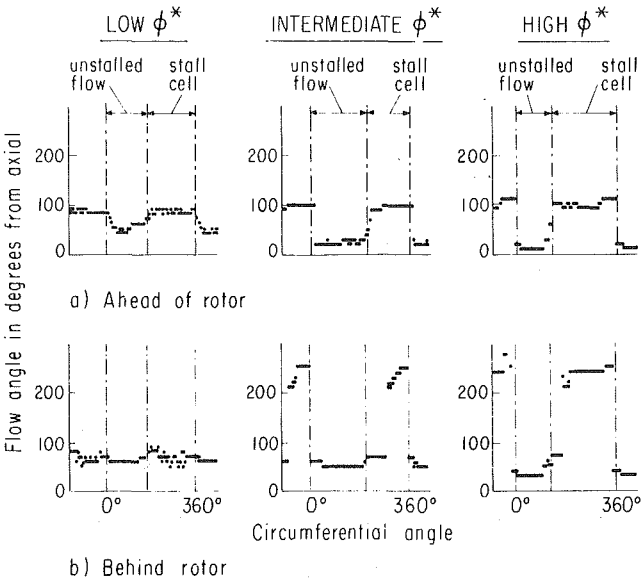

Fig. 23 Flow deflection measurements in three compressor builds [21]

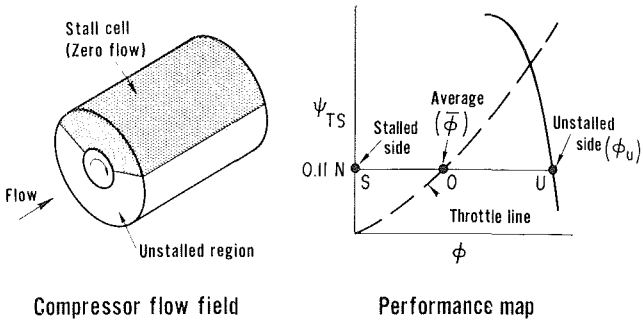

Fig. 24 Compressor operation in rotating stall

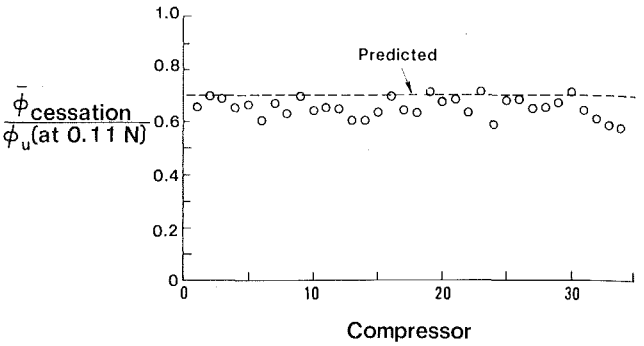

Fig. 25 Correlation for $\bar{\phi}$ at cessation of full span stall [27]; numbers on horizontal axis refer to individual compressors

Day and Cumpsty emphasize that the stall cell is very different from the wake of a bluff body, as many previous investigators have assumed. If this were the case, then in a coordinate system fixed to the cell the edges of the cell would coincide with the steady streamlines in the unstalled flow surrounding the wake. Such a description has been proposed by Rannie [74], for example, and has also been used as a model by Fabri for an isolated rotor [18]. The measurements, however, show clearly that were this to occur the cell would need to be helical, whereas it is essentially axial. The picture that emerges, therefore, of the instantaneous streamlines as viewed in an absolute coordinate system is shown in Fig. 22. There is, in fact, mass transport *across* the cell boundaries, so that fluid that was in the unstalled region (with a high axial velocity) is violently decelerated as it enters the cell, whereas particles which were in the cell are accelerated at the cell edges as they enter the unstalled flow. Therefore it should be emphasized that the "wake" models of stall cell flow cannot be applied to the single or multistage compressor situation.

Some idea of the magnitude of the changes in flow angle that can occur is shown in Fig. 23 which shows the circumferential distribution of flow angle (measured from axial) ahead of and behind the first rotor in a three stage compressor. The measurements were made at a radial location two thirds of the span from the hub. Data is shown from three builds — a low $(C_x/U)^*$ compressor, one with an intermediate value, and one with a high value. It can be seen that the stall cell flow is predominantly circumferential ahead of the rotor. Although not shown, this pattern is repeated stage-by-stage through the machine. In addition, because of the high values of swirl velocity, the centrifugal effects in the blade passages are very important. It is therefore suggested that analyses which do not model these effects may be more applicable to prediction of rotating stall in stationary rather than rotating blade rows.

Another important conclusion that was stressed in [21] is that "although the flow in a single stage build shows similarities with that in a multistage configuration of the same blading, the finer details of the flow are sufficiently different to preclude the extrapolation of single stage data to multistage configuration." The thesis by Day [24] discusses in detail these differences between the rotating stall behavior of isolated rotors (on which many previous investigations were focussed) and multistage compressors.

The emphasis in this discussion of rotating stall has been on the full span, large extent type, because this is the type which has the most severe effects on compressor performance, especially as far as the stall/unstall hysteresis. However, with regard to rotating stall in fans and single stage compressors (where part span stall is likely to be encountered) there have also been investigations of the part span stall regime [75], including one study of the stalled flow in a transonic compressor stage [76].

Prediction of Compressor Performance in Rotating Stall. The prediction of the compressor flow regimes in rotating stall is important for several reasons. One consideration can be that the speed and number of stall cells determine the forcing frequency for blade vibration and it is desirable to design the blades such that no resonance occurs. However, a very much more pressing consideration is that of stall *recovery,* i.e., the prediction of overall performance including the hysteresis loop.

In an approach to this problem Day, Greitzer, and Cumpsty [27] developed a correlation to predict stalled flow performance. The correlation is based on a heuristic fluid dynamic model of the compressor flow field in rotating stall. The compressor is divided into a stalled and unstalled zone analogous to the concept developed for inlet distortion. The stall cell is modeled by a zone of zero flow, and in the unstalled part of the flow the compressor is assumed to operate at a point on the unstalled performance curve. The situation is shown in Fig. 24 where we see the stalled "zone" of the compressor at S and the unstalled zone at the same pressure rise at U, with the mean operating point defined by the intersection of the horizontal line from S to U and the throttle curve at 0. This model is applied in conjunction with two experimental observations: 1) (following an observation originally due to McKenzie [77]) the nondimensional inlet total to exit static pressure rise per stage in rotating stall is constant *independent of the unstalled performance*, ($\psi_{TS} = 0.11N$ in stall, where N is the number of stages), 2) there is a critical value of stall cell blockage, λ, (i.e., extent of annulus covered by the cell) below which *full span* stall cannot exist,

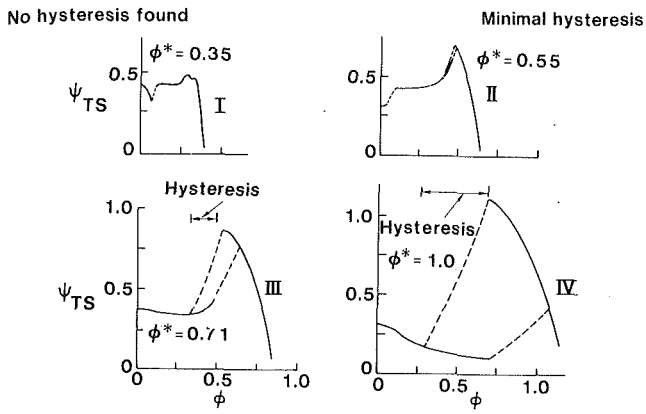

Fig. 26 Effect of ϕ^* (design C_x/U) on stall/unstall hysteresis (three stage compressors) [27]

(λ_{crit} = 0.3). Using these, one can make predictions about whether a given compressor will exhibit full span or part span stall as well as about the extent of the hysteresis loop.

To understand the central idea of the model, consider a compressor operating in the full span stall regime. To recover, we must open the throttle. Referring to Fig. 24, this would move point 0 to the right (points S and U remain fixed) as more of the annulus becomes unstalled and the blockage decreases. When the critical value of blockage is reached (at 0.3) full span stall can no longer exist and the compressor comes out of rotating stall. Since the blockage can be directly related to the ratio SO/SU, which is just $\bar{\phi}/\phi_{\text{unstalled}}$, by

$$\bar{\phi}/\phi_{\text{unstalled}} = 1 - \lambda,$$

we can obtain a formula for the value of $\bar{\phi}$ at stall cessation if we know the level of the horizontal line $\bar{SU}$, since this picks out $\phi_{\text{unstalled}}$ on the (known) unstalled part of the compressor characteristic. As stated, from experimental observations this can be placed at a level of $0.11N$ where N is the number of stages. Since the critical value of blockage at which the full span stall ceases is 0.3 we have, for stall cessation

$$\frac{\bar{\phi}_{\text{cessation}}}{\phi_{\text{unstalled at } 0.11N}} = 0.7$$

This correlation is shown in Fig. 25. Data are presented from thirty-four different single and (mostly) multistage low speed compressors. It can be seen that the correlation furnishes a very useful method for predicting stall cessation.

Using this basic procedure, parametric studies can be carried out to determine the effect of different design parameters on stall performance. As shown in [27], two important parameters are $(C_x/U)^*$ (design value of axial velocity parameter) and number of stages. For a given design value of C_x/U the larger the number of stages the larger the size of the stall/unstall hysteresis. However, a more potent effect is the value of $(C_x/U)^*$; the higher the value for a given number of stages the larger the size of the stall/unstall hysteresis loop. Experimental evidence to support this idea is shown in Fig. 26 which presents data for four different three stage compressors with different values of $(C_x/U)^*$. At the lowest value of $(C_x/U)^*$ (curve I) no hysteresis could be found. As we examine curves II, III, and IV which have increasing values of $(C_x/U)^*$ we find an increase in the extent of hysteresis.

The procedure described in [27] also addresses the question of whether a given machine will exhibit part span stall or full span stall at the stall onset. Only one aspect of this will be pointed out here—namely that the same machine can develop either part span or full span stall and "the widely held view that part span and full span are the modes for low and high hub tip ratio machines is either wrong or else is a gross oversimplification" [21].

Research Needs and Suggestions for Future Work

We can now review those areas which the author thinks are fruitful to pursue. On the general topic of stall prediction in a uniform flow, there appears to be little more to be gained from purely two-dimensional linearized treatments, but three-dimensional aspects of stall inception are subjects on which work is needed. In particular, questions such as the impact of wall stall versus blade stall on the stall point, as well as stall onset in low hub/tip radius ratio compressors, have not been really resolved. Approaches that are based on treating the blade row or rows as a "black box," however, will still have to contend with the capability of present axisymmetric flow calculation procedures to predict the slopes of the uniform flow speedlines or loss characteristics near stall. Because of this it may well be that a numerical treatment of the flow in the blade passage region would be of considerable use here in clarifying how the blockage changes with small changes in incidence angle near the stall point.

For distorted flows there is also potential for research. To the present author, it seems that a disproportionate effort has gone into the relatively straightforward tasks of solving the inviscid flow equations outside of the blade row, while the simple models that are in use for the fluid dyamics *in* the blade row are those that were presented by Emmons [3] and Stenning [69] approximately twenty-five years ago. In fact, one still has to essentially sketch that part of the loss and turning characteristics associated with large angles of attack. Thus, the author feels that more effort should be spent concentrating on the more difficult problem of understanding the unsteady rotor response in the heavily loaded (near stall) regime. Probably both experimental and numerical investigations will be needed for this.

There is, in addition, a need to develop better stability criteria in the case of distorted inlet flows. As one example, it would be useful to attempt to formulate the linearized stability problem for a situation where the "mean flow" is a steady finite inlet distortion. Such an analysis might give some additional insight into the basic fluid mechanics of the onset of instability with the inlet distortion.

Although not discussed in the review, it should be noted that there are distortions that are characterized by large variations in inlet flow angles rather than by nonuniformities in total pressure. The inlet vortex (or ground vortex) is an important example of this type of distortion, which can have a significant effect on stability [78]. At present no theory exists to adequately describe this type of inlet nonuniformity.

On stability enhancement using casing treatment, there is considerable scope for useful work. As stated, the mechanism(s?) by which the treatment decreases the passage blockage is (are) still unclear and there is a need for both theoretical and experimental work on this topic.

There are also important areas which are associated with the behavior subsequent to the onset of the initial instability. More accurate models are needed to predict the local details of the surge phenomenon in multistage compressors. This is important from an aeroelastic standpoint as well as from purely aerodynamic grounds.

Prediction of the features of rotating stall in multistage compressors is also needed. We can discuss first the overall performance characteristic. The data reported in [27] and the subsequent discussion by Harman [79] seem to bear out the hypothesis that the inlet total to exit static pressure rise in rotating stall is roughly constant per stage independent of unstalled performance, but there is no understanding of why this occurs. Further, even though the pressure rise is independent of the unstalled performance, the torque does

depend strongly on details of stall behavior related to compressor design parameters, and this is not understood. Investigation of these "global" properties should be pursued since they directly affect the hysteresis phenomenon and hence the recoverability of the compressor. A further facet of this topic is that for aircraft engines which have two or more spools, it is extremely important to understand the interactions between the high and low pressure compressors and their effect on stalled flow performance.

The central features of the stall cell structure also are not well modeled at present. Work is being carried out on this topic, but present models are still rudimentary, compared to the experimentally measured details of the flow. Here again an important facet seems to be the complex three-dimensional, separated unsteady flow in the blade passages. The blade row models in use for the calculation procedures are essentially the same as those used for the inlet distortion problem, however they are now being extrapolated even further (to the negative flow regime). Again, the author feels that more attention should be paid to the blade row characteristics, particularly in view of Takata's comment that the nonlinearities in the equations of motion do not seem to have an important role in determining the wave shape, disturbance amplitude, etc., but rather that these aspects are believed to be determined chiefly through the nonlinear effects due to the blade row characteristic [25].

Work also is needed in the area of overall compression system modeling, particularly for high pressure ratio multistage compressors. Systems which include two streams and two spools (i.e., turbofans) are an important application of this work. In this context, it should be noted that some of the transients associated with surge in modern gas turbine compressors can be on the same time scale as rotor rotation, or particle flow-through time. Under such conditions the compressor response can be far from a quasi-steady one. This is true for transients both from unstalled to negative flow as well as from negative flow to unstalled. Thus (again) if one wants to do significantly better than present models, the effort should be in trying to understand the overall unsteady performance of the blading.

As a summation, it is interesting to refer to a survey paper on aircraft engines written by Hawthorne over twenty years ago [80]. He stated: "Stall propagation is undoubtedly a phenomenon of the greatest importance to the engine aerodyamics and is one in which our understanding is still in the preliminary stage." It should be apparent from this review that the author agrees completely with the first part of this statement. As to the latter part, although much has been achieved, it should also be apparent that understanding, if not quite preliminary, is still far from complete.

Acknowledgment

In the preparation of this review the author has been helped by a number of people. In particular, however, he would like to acknowledge Dr. N. A. Cumpsty (who found time to pause at M. I. T. during his journeys between Cambridge University and Caltech) and Mr. R. S. Mazzawy of Pratt & Whitney Aircraft, both of whom suggested clarifications and improvements to the several versions of the paper. The comments of Dr. C. S. Tan (of M. I. T.), and Messrs. J. P. Nikkanen and B. A. Robideau (of P & W) are also appreciated. This work was carried out under the sponsorship of NASA Lewis Research Center Grant NSG 3208.

References

1 Iura, T., and Rannie, W. D., "Experimental Investigations of Propagating Stall in Axial-Flow Compressors," ASME *Transactions*, Apr. 1954, pp. 463–471.

2 Mazzawy, R. S., "Surge Induced Structural Loads in Gas Turbines," ASME Paper 79-GT-91, 1979.

3 Emmons, H. W., Pearson, C. E., and Grant, H. P., "Compressor Surge and Stall Propagation," ASME *Transactions*, Vol. 27, Apr. 1955, pp. 455–469.

4 Taylor, E. S., "Evolution of the Jet Engine," *Astronautics and Aeronautics*, Vol. 8, 1970, pp. 64–72.

5 Horlock, J. H., *Axial Flow Compressors*, Chapter 3, "Two Dimensional Cascades, Experimental Work," Krieger Publishers, 1973.

6 Leiblein, S., "Experimental Flow in Two Dimensional Cascades," Chapter VI in *Aerodynamic Design of Axial Flow Compressors*, NASA SP-36, 1965.

7 Leiblein, S., "Loss and Stall Analysis of Compressor Cascades," ASME *Journal of Basic Engineering*, Vol. 81, Sept. 1959, pp. 387–400.

8 Rodgers, C., "A Diffusion Factor Correlation for Centrifugal Impeller Stalling," ASME *Journal of Engineering for Power*, Vol. 100, Oct. 1978, pp. 592–603.

9 Smith, L. H., Jr., "Casing Boundary Layers in Multistage Axial Flow Compressors," in *Flow Research on Blading*, edited by L. S. Dzung, Elsevier Publishing Co., 1970.

10 Fligg, J. A., "Tests of a Low Speed Three-Stage Axial Flow Compressor at Aspect Ratios of One, Two and Four," AIAA Paper 66-613, AIAA Second Propulsion Joint Specialist Conference, 1966.

11 Smith, L. H., "The Effect of Tip Clearance on the Peak Pressure Rise of Axial Flow Fans and Compressors," ASME Symposium on Stall, 1958.

12 McNair, R. E., "Tip Clearance Effects on Stalling Pressure Rise in Axial Flow Compressors," ASME Symposium on Compressor Stall, Surge, and System Response, 1960.

13 Howell, A. R., and Calvert, W. J., "A New Stage Stacking Technique for Axial-Flow Compressor Performance Prediction," ASME *Journal of Engineering for Power*, Vol. 100, Oct. 1978, pp. 698–703.

14 Mikolajczak, A. A., "Introduction" to *Unsteady Flows in Jet Engines*, Project Squid/AFOSR/UARL Workshop at United Aircraft Research Laboratories, ed. by F. O. Carta, 1974.

15 Nenni, J. P., and Ludwig, G. R., "A Theory to Predict the Inception of Rotating Stall in Axial Flow Compressors," AIAA Paper 74-528, AIAA 7th Fluid and Plasma Dynamics Conference, 1974.

16 Fabri, J., "Growth of a Perturbation in an Axial Flow Compressor," ASME Paper 78-GT-30, 1978.

17 Emmons, H. W., Kronauer, R. E., and Rockett, J. A., "A Survey of Stall Propagation — Experiment and Theory," ASME *Journal of Basic Engineering*, Vol. 81, Sept. 1959, pp. 409–416.

18 Fabri, J., "Rotating Stall in Axial Flow Compressors," *Internal Aerodynamics (Turbomachinery)*, Institution of Mechanical Engineers, 1967.

19 Stenning, A. H., "Rotating Stall and Surge," Chapter 15 in *Fluid Dynamics of Turbomachinery*, ASME Lecture Course, Iowa State University, 1973.

20 Dunham, J., "Non Axisymmetric Flows in Axial Flow Compressors," Mechanical Engineering Sciences Monograph No. 3, Institution of Mechanical Engineers, 1963.

21 Day, I. J., and Cumpsty, N. A., "The Measurement and Interpretation of Flow within Rotating Stall Cells in Axial Compressors," *Journal of Mechanical Engineering Sciences*, Vol. 20, 1978, pp. 101–114.

22 Greitzer, E. M., "Surge and Rotating Stall in Axial Flow Compressors. Part II: Experimental Results and Comparisons with Theory," ASME *Journal of Engineering for Power*, Vol. 98, Apr. 1978, pp. 199–217.

23 Greitzer, E. M., Mazzawy, R. S., and Fulkerson, D. A., "Flow Field Coupling Between Compression System Components in Asymmetric Flow," ASME *Journal of Engineering for Power*, Vol. 100, Jan. 1978, pp. 66–72.

24 Day, I. J., "Axial Compressor Stall," Ph.D. thesis, Cambridge University Engineering Department, 1976.

25 Takata, H., and Nagano, S., "Nonlinear Analysis of Rotating Stall," ASME Paper 72-GT-3, 1972.

26 Orner, N., "Rotating Stall in Axial Flow Compressors," Von Karman Institute Lecture Series, "Unsteady Flow in Turbomachines," 1979, Brussels, Belgium.

27 Day, I. J., Greitzer, E. M., and Cumpsty, N. A., "Prediction of Compressor Performance in Rotating Stall," ASME *Journal of Engineering for Power*, Vol. 100, Jan. 1978, pp. 1–14.

28 Montgomery, S. R., and Braun, J. J., "Investigation of Rotating Stall in a Single Stage Axial Compressor," NACA Technical Note TN3823, 1957.

29 Hill, P. G., and Peterson, C. R., *Mechanics and Thermodynamics of Propulsion*, Addison-Wesley Publishers, 1965.

30 Tesch, W. A., Steenken, W. G., "J85 Clean Inlet Flow and Parallel Compressor Models," NASA Contractor Report CR-134978, Mar. 1976.

31 Corbett, A. G., and Elder, R. L., "Stability of an Axial Flow Compressor with Steady Inlet Conditions," *Journal of Mechanical Engineering Science*, Vol. 16, No. 6, 1975.

32 Corbett, A. G., and Elder, R. L., "Mathematical Modeling of Compressor Stability in Steady and Unsteady Flow Conditions," in *Unsteady Phenomena in Turbomachinery*, AGARD CP-177, 1976.

33 Jansen, W., and Swarden, M. C., "Compressor Sensitivity to Transient and Distorted Transient Flows," AIAA paper 71-670, 1971.

34 Willoh, R. G., and Seldner, K., "Multistage Compressor Simulation Applied to the Prediction of Axial Flow Instabilities," NASA TMX-1880, 1960.

35 Plourde, G. A., and Stenning, A. A., "Attenuation of Circumferential Inlet Distortion in Multistage Axial Compressors," *Journal of Aircraft*, Vol. 5, No. 3, 1968.

36 Stenning, A. A., "Inlet Distortion Effects in Axial Compressors," Chapter 14 in *Fluid Dynamics of Turbomachinery*, ASME Lecture Course, Iowa State University, 1973.

37 Mokelke, A., "The Prediction of Steady, Circumferential Pressure and Temperature Distortions in Multistage Axial Flow Compressors," ASME Paper 79-GT-184.

38 Hercock, R. G., and Williams, D. D., "Aerodynamic Response," in *Distortion Induced Engine Instability*, AGARD Lecture Series, No. 72, 1974.

39 Collins, T. P., "Engine Stability," Chapter 21, in *The Aerothermodynamics of Aircraft Gas Turbine Engines*, edited by G. Oates, AFAPL-TR-78-52, 1978.

40 Reid, C., "The Response of Axial Flow Compressors to Intake Flow Distortion," ASME Paper 69-GT-29, 1969 ASME Gas Turbine Conference.

41 Mokelke, H., "Prediction Methods," in *Distortion Induced Engine Instability*, AGARD Lecture Series, No. 72, 1974.

42 Braithwaite, W. M., and Soeder, R. H., "Combined Pressure and Temperature Distortion Effects on Internal Flow of a Turbofan Engineer," Paper presented at AIAA/SAE, 15th Joint Propulsion Specialists Conference, 1979.

43 Mikolajczak, A. A., and Pfeffer, A. M., "Methods to Increase Engine Stability and Tolerance to Distortion," in *Distortion Induced Engine Instability*, AGARD Lecture Series, No. 72, 1974.

44 Williams, D. D., and Yost, J. O., "Some Aspects of Inlet-Engine Flow Compatability," *Aeronautical Journal*, Sept. 1973, pp. 483-492.

45 Mazzawy, R. S., "Multiple Segment Parallel Compressor Model," ASME *Journal of Engineering for Power*, Vol. 99, Apr. 1977, pp. 288-296.

46 Adamczyk, J. J., "Unsteady Fluid Dynamic Response of an Isolated Rotor with Distorted Inflow," AIAA Paper 74-49, 1974.

47 Pandolfi, M., and Colasurdo, "Numerical Investigations on the Generation and Development of Rotating Stalls," ASME Paper 78-WA/GT-5.

48 McCroskey, W. J., "Some Current Research in Unsteady Fluid Dynamics," ASME JOURNAL OF FLUIDS ENGINEERING, Vol. 99, Mar. 1977, pp. 8-38.

49 Platzer, M. F., "Unsteady Flows in Turbomachines — A Review of Current Developments," from *Unsteady Aerodyamics*, AGARD CP-227, 1977.

50 Telionis, D. P., "Review – Unsteady Boundary Layers, Separated and Attached," ASME JOURNAL OF FLUIDS ENGINEERING, Vol. 101, Mar. 1979, pp. 29-43.

51 Nagano, S., Machida, Y., and Takata, H., "Dynamic Performance of Stalled Blade Rows," Japan Soc. of Mech. Eng. Paper #JSME 11, presented at Tokyo Joint Int. Gas Turbine Conf., Tokyo, Japan, Oct. 1971.

52 Greitzer, E. M., and Griswold, H. R., "Compressor Diffuser Interaction with Circumferential Flow Distortion," *Journal Mechanical Engineering Science*, Vol. 18, Feb. 1976, pp. 25-43.

53 Greitzer, E. M., "Coupled Compressor-Diffuser Flow Instability," *J. Aircraft*, Vol. 14, Mar. 1977, pp. 233-238.

54 Jansen, W., "Rotating Stall in Radial Vaneless Diffusers," *ASME Journal of Basic Engineering*, Vol. 86, Dec. 1964, pp. 750-758.

55 Abdelhamid, A. N., and Bertrand, J., "Distinctions between Two Types of Self-Excited Gas Oscillations in Radial Vaneless Diffusers," ASME Paper 79-GT-58, 1979.

56 Toyama, K., Runstadler, P. W., and Dean, R. C., "An Experimental Study of Surge in Centrifugal Compressors," ASME JOURNAL OF FLUIDS ENGINEERING, Vol. 99, Mar. 1977, pp. 115-129.

57 Greitzer, E. M., "Surge and Rotating Stall in Axial Flow Compressors. Part I: Theoretical Compression System Model," ASME *Journal of Engineering for Power*, Vol. 98, Apr. 1976, pp. 190-198.

58 Takata, H., and Tsukuda, Y., "Study on the Mechanism of Stall Margin Improvement of Casing Treatment," ASME Paper 75-GT-13, ASME Gas Turbine Conference, Mar. 1975.

59 Prince, D. C., Jr., Wisler, D. C., and Hilvers, D. E., "Study of Casing Treatment Stall Margin Improvement Phenomena," NASA CR-134552, Mar. 1974.

60 Osborn, W. M., Lewis, G. W., Jr., and Heidelberg, L. J., "Effect of Several Porous Casing Treatments on Stall Limit and on Overall Performance of an Axial-Flow Compressor Rotor," NASA TN D-6537, Nov. 1971.

61 Moore, R. D., Kovich, G., and Blade, R. J., "Effect of Casing Treatment on Overall and Blade-Element Performance of a Compressor Rotor," NASA TN D-6538, Nov. 1971.

62 Fabri, J., and Reboux, J., "Effect of Outer Casing Treatment on Stall Margin of a Supersonic Rotating Cascade," ASME Paper 75-GT-95, ASME Gas Turbine Conference, Mar. 1975.

63 Tesch, W. A., "Evaluation of Range and Distortion Tolerance for High Mach Number Transonic Fan Stages, Task IV Stage Data and Performance Report for Casing Treatment Investigations, Volume I," NASA CR-72862, May 1971.

64 Bailey, E. E., "Effect of Grooved Casing Treatment on the Flow Range Capability of a Single-Stage Axial Flow Compressor," NASA TM X-2459, Jan. 1972.

65 Horlock, J. H., and Lakhwani, C. M., "Propagating Stall in Compressors with Porous Walls," ASME Paper 75-GT-59, 1975.

66 Amann, C. A., Nordensen, G. E., and Skellenger, G. D., "Casing Modification for Increasing the Surge Margin of a Centrifugal Compressor in an Automotive Turbine Engine," ASME *Journal of Engineering for Power*, Vol. 97, July 1975, pp. 329-336.

67 Jansen, W., Presentation at Panel on Centrifugal Compressor Efficiency Improvement, ASME Gas Turbine Conference, 1979.

68 Greitzer, E. M., Nikkanen, J. P., Haddad, D. E., Mazzawy, R. S., and Joslyn, H. D., "A Fundamental Criterion for the Application of Rotor Casing Treatment," ASME JOURNAL OF FLUIDS ENGINEERING, Vol. 101, June 1979, pp. 237-244.

69 Stenning, A. H., and Kriebel, "Stall Propagation in a Cascade of Airfoils," *Trans. ASME*, Vol. 80, May 1958, pp. 777-790.

70 Dunham, J., "Observations of Stall Cells in a Single Stage Compressor," Aeronautical Research Council, C. P. 589, 1961.

71 Tanaka, S., and Murata, S., "On the Partial Flow Rate Performance of Axial Flow Compressor and Rotating Stall, First and Second Reports," *Bulletin of the J.S.M.E.*, Vol. 18, No. 117, Mar. 1975.

72 Sexton, M. R., O'Brien, W. F., and Moses, H. L., "An On-Rotor Investigation of Rotating Stall in an Axial Flow Compressor," in *Unsteady Phenomena in Turbomachinery*, AGARD CP-177, 1976.

73 Cossar, B. F. J., Moffat, W. C., and Peacock, R. E., "Compressor Rotating Stall in Uniform and Non-Uniform Flow," unpublished report, Cranfield Inst. of Technology, 1979.

74 Rannie, W. D., "The Axial Compressor Stage," Part F in *Aerodynamics of Turbines and Compressors*, edited by W. R. Hawthorne, Princeton University Press, 1964.

75 Breugelmans, "Flow Measurements in a Rotating Stall cell," from Von Karman Institute Lecture Series, "Unsteady Flow in Turbomachines," Brussels, Belgium, 1979.

76 Bartlett, F., and Greitzer, E. M., "Stalled Flow Performance of a Single Stage Transonic Compressor," M.I.T. Gas Turbine and Plasma Dynamics Laboratory Report 144, Dec. 1978.

77 McKenzie, A., Private Communication.

78 Motycka, D. L., "Ground Vortex - Limit to Engine/Reverser Operation," ASME *Journal of Engineering for Power*, Vol. 98, Apr. 1976, pp. 258-264.

79 Harman, J. W., "Discussion" (on the paper "Prediction of Compressor Performance in Rotating Stall,") ASME *Journal of Engineering for Power*, Vol. 100, Jan. 1978, pp. 13-14.

80 Hawthorne, W. R., "Some Aerodynamic Problems of Aircraft Engines," *Journal of Aeronautical Sciences*, Vol. 24, Oct. 1957, pp. 713-730.

Peter Freymuth
Department of Aerospace Engineering Sciences,
University of Colorado,
Boulder, Colo. 80309

REVIEW: A Bibliography of Thermal Anemometry

Editor's Foreword: The material which follows is an excerpt from the TSI Technical Paper, "A Bibliography of Thermal Anemometry" by Dr. Freymuth. The complete paper was published in the *TSI Quarterly* (Vol. 4, Issue 4, Nov./Dec. 1978 and addenda appeared in Vol. 5, 1979, Issue 1, Feb./Mar. and Issue 4, Nov./Dec.), a journal of TSI, Inc., St. Paul, Minn. This bibliography was recommended for publication in the *Journal of Fluids Engineering* because of its scope and value to researchers who employ thermal anemometers. It is not listed by many of the indexing services employed by fluids engineers. By publishing this excerpt, the *Journal* seeks to make the availability of the bibliography more widely known. The complete paper of 26 pages cannot be included here. However, the Technical Editor has placed a copy on file with the Engineering Societies Library, 345 E. 47th St., New York, N. Y. 10017. Copies may be obtained from this Library or from TSI, Inc., P.O. Box 43394, St. Paul, Minn., 55164. The excerpt below includes all of the narrative text of the original paper, but only the 1977 and 1978 bibliography listing, which serve as examples of the form of the bibliography. The earliest paper cited in the complete bibliography dates back to 1817!

I Introduction

Thermal anemometry is primarily the technique of velocity measurement in fluid flows by means of thermal sensors. The thermal measurement of other flow properties like temperature, density, composition, etc., is also considered part of thermal anemometry.

There exist excellent reviews of the field (Burgers 1931; Kovasznay 1954, 1959, 1965; Hinze 1959, 1975; Corrsin 1963; Bradshaw 1971; Sandborn 1972; Comte-Bellot 1976, 1977). These reviews list only a small fraction of the available literature in order to avoid confusion and to serve as primary guides into the field of thermal anemometry.

In contrast we aim at a rather comprehensive bibliography of thermal anemometry which is intended as a secondary guide for the specialist in this field, as a time saving device in locating and selecting references for a specialized research project; as a device for the assessment of new work in the light of the existing body of literature; and as an aid in avoiding unnecesary duplication of efforts.

Prior to compilation of the bibliography it was decided to exclude papers which only use the technique without contributing to it and to exclude papers which do not contribute directly (for instance, the invention of the transistor contributes indirectly to the technique, and is of course not included in this bibliography). However, borderline cases exist. An exception to the above policy is made in including papers concerned with heat transfer from sensors in fluids at rest, since this represents a limiting case of thermal anemometry. This exception pushes the earliest reference back to 1817 (Dulong et Petit).

Thermal anemometry proper can be traced to the last two decades of the nineteenth century (Ser 1888; Weber 1894; Oberbeck 1895) and has since undergone vigorous development. Efforts are scattered over many countries, journals and reports. The entire body of literature of thermal anemometry consists of about 1400 papers to this date, with about 200 of them published prior to 1950.

A bibliography of this magnitude can only be effective if it is properly organized for easy access to specialized information. Future updating of incomplete or erroneous information and adding of future papers must be simple. Compactness is another virtue.

The classification scheme which has been adopted is by year of publication and by alphabetical order of authors within each year. On the left margin there appears a two digit identification number within each year. At the right margin each reference includes at least one and maximally two subject index numbers which indicate the subject areas of strongest contribution and relevance of the paper.

The subject index numbers are two-digit numbers with the first digit indicating a major research area of thermal anemometry and the second digit indicating a subfield within a major area. The subject index number key is presented at the end of this section.

The classification scheme adopted should facilitate identification of a paper by year of publication and identification number. It should facilitate access to the historical development of thermal anemometry (chronological order), access to particular authors (alphabetical order of authors within each year), access to titles and sources (separate columns are provided for titles and sources), and access to various subject areas (subject index number).

In this way, a separate chronological index, author index, subject index, etc., are unnecessary. Excerpting of frequently needed materials is left to the reader.

Key to Subject Index Numbers

0 General Information

0 0 Books on heat transfer and fluid mechanics most often referred to in thermal anemometry

0 1 Monographs, introductions, reviews, bibliographies, histories, proceedings on thermal anemometry

0 2 Catalogs, manuals, bulletins, devoted substantially to thermal anemometry

1 Design, use and operation of thermal anemometers

1 0 Design of constant temperatue anemometers

1 1 Design of resistance thermometers for flow measurements

1 2 Design of constant current anemometers
1 3 Operational procedures
1 4 Linearization
1 5 Data processing, data evaluation

2 Dynamics of thermal anemometers

2 0 Linear dynamics of constant temperature anemometers
2 1 Nonlinear dynamics of constant temperature anemometers
2 2 Dynamics of resistance thermometers for flow measurements
2 3 Linear dynamics of constant current anemometers
2 4 Nonlinear dynamics of constant current anemometers
2 5 Direct testing of the dynamics of thermal anemometers and resistance thermometers, dynamic determination of sensitivity
2 6 Electronic testing of the dynamics of thermal anemometers and resistance thermometers
2 7 Signal to noise ratio of thermal anemometers

3 Thermal sensors

3 0 Design, manufacturing, maintenance, mechanical strength of thermal sensors
3 1 Simple probes
3 2 Probes with several sensor elements and probe arrays
3 3 Special probes (wake sensing probes, flush mounted probes, aspirating probes and others)
3 4 Wire probes
3 5 Film, split-film, cooled film probes, coated wires and films
3 6 Thermistor, transistor, thermocouple probes
3 7 Spacial resolution of thermal sensors and probe interference; local heat transfer and fluid mechanics
3 8 Theoretical fluid mechanics and heat transfer applied to thermal sensors

4 Sensitivity, calibration and measurements in gaseous flow

4 0 Zero velocity (free convection)
4 1 Very low speed flow (mixed convection, oscillating probes)
4 2 Low speed (incompressible) flow
4 3 High speed (compressible) and low density (molecular) flow
4 4 Directional sensitivity, three dimensional flow, high intensity turbulence, end losses and other corrections
4 5 Temperature measurement, temperature compensation (nonisothermal gaseous flow)
4 6 High temperature flow
4 7 Heterogeneous gas mixtures
4 8 Novel applications, combinations, and comparison with other techniques

5 Sensitivity, calibration and measurements in liquid flow

5 0 Water, oil and similar liquid flow
5 1 Liquid metal flow
5 2 Blood flow, biomedical anemometry, and non-Newtonian liquids
5 3 Temperature measurement, temperature compensation (nonisothermal liquid flow)
5 4 Two phase flow
5 5 Novel applications, combinations and comparison with other techniques

NO.	AUTHOR(S)	TITLE 1977	SOURCE	INDEX NO.
1	Acrivlellis, M.	Hot-wire measurements in flows of low and high turbulence intensity	Disa information No 22, 15-20	44
2	Acrivlellis, M. Ahmed, M.	Finding the spatial flow field by means of hot-wire anemometry	Disa information No 22, 21-28 (see Wigeland et al.)	44
3	Antonini, G. Guiffant, G. Perrot, P.	The effect of transverse oscillations on heat transfer from a horizontal hot-wire to a liquid	Int. J. Heat Mass Transfer 20,88-92	50
4	Antonini, G. Guiffant, G. Perrot, P. Azad, R. S.	The use of holography for direct visualization of thermal distribution around hot-wires in a liquid under dynamic conditions	Disa Information No 21,28-32 (Reichert et al.)	50
5	Bank, N Gauvin, W. H. Beguier, C.	Inclined hot-wire response equations for a flow field having a dominant tangential velocity component	Can.J.Chem.Eng. 55,516 (see Rey et al.)	44
6	Bennet, J. C.	Measurement of periodic flow in rotating machinery	AIAA 10th Fluid & Plasmadynamic Conference, June 27-29 770-713	48 36
7	Bremhorst, K. Krebs, L. Gilmore, D. B. Bullock, K. J.	The frequency response of hot-wire anemometer sensors to heating current fluctuations	Int. J. Heat and Mass Transfer 20, 315-322 (see McConachie et al.)	22 23
8	Comte-Bellot, G.	The physical background for hot-film anemometry	Proc. Symp. Turbulence in Liquids, Rolla 1975 1-13	01 21
9	Comte-Bellot, G.	Hot-wire and hot-film anemometers	Measurement of Unsteady Fluid Dynamic Phenomena, Hemisphere Pub. Corp. 123-162	01
10	Dahm, A. Vagt, J. D.	Entwicklund und Herstellung interferenzarmer Hitzdrahtsonden	Hermann-Foettinger Institut Report No. 01177	30 37

NO.	AUTHOR(S)	TITLE	SOURCE	INDEX NO.
	Dahm, A.		(see Vagt et al.)	
11	Delhaye, J. M. Galaup, J. P.	Hot-film anemometry in air-water flow	Proc. Symp. Turbulence in Liquids, Rolla 1975 83-90	54
	Dobbins, R. A.		(see Eklund et al.)	
12	Drubka, R. E. Tan-atichat, J. Nagib, H. B.	Analysis of temperature compensating circuits for hot-wires and hot-films	Disa information No. 22, 5-14	45
13	Drubka, R. E. Nagib, H. M. Tan-atichat, J.	On temperature and yaw dependence of hot-wires	ITT Fluids and Heat Transfer Report R77-1 Illinois Institute of Technology	45 44
14	Durst, F. Ermshaus, R.	Hot-wire wake sensors for simultaneious two-dimensional velocity measurements	Proc. 17th Congress Int. Assoc. for Hydraulic Research, 623-630	44 33
15	Durst, F.	Hot-wire and laser-Doppler techniques in turbulence research	Univ. Karlsruhe Rept. SFB80/EM/119	48
16	Eklund, T. I. Dobbins, R. A.	Application of the hot-wire anemometer to temperature measurement in transient gas flow	Int. J. Heat Mass Transfer 20, 1051-1058	45
	Ermshaus, R.		(see Durst et al.)	
	Eyler, L. L.		(see Flaherty et al.)	
17	Fairall, C. W. Schacner, G.	Frequency response of hot-wire used for atmospheric turbulence measurements in the marine environment	Rev. Sci. Instrum. 48, 12-17	42 30
18	Fattahi, B. Hsu, C. T.	Feasibility of the use of three-dimensional anemometers in a simulated tornado flow measurement	J. Physics E: Sci. Instrum 10, 73-79	48
19	Fiedler, H. Mensing, P.	Eine Methode zur Kompensation des Temeratureinflusses bei Hitzdrahtmessungen	Z. Flugwiss. Weltraumforsch. 1, 81-86	45
20	Fingerson, L. M.	Phase shift of constant temperature anemometer	TSI News, summer 1977, 7-8	20
	Fingerson, L. M.		(see Freymuth et al.)	
21	Flaherty, T. W. Eyler, L. L. Sesonske, A.	Non-isothermal mercury pipe flow turbulent characteristics	Proc. Symp. Turbulence in Liquids, Rolla, 1975 26-31	53
22	Freymuth, P.	Frequency response and electronic testing for constant-temperature hot-wire anemometers	J. Phys. E. 10, 705-710	20 26
23	Freymuth, P.	Further investigation of the non-linear theory for constant-temperature hot-wire anemometers	J. Phys. E. 10, 710-713 (also SQUID Workshop Turbulence in internal Flows, Hemisphere Publ. Corp.)	21
24	Freymuth, P. Fingerson, L. M.	Electronic testing of frequency response for thermal anemometers	TSI Quarterly 3, Nov. Dec. 5-12	26
25	Froebel, E. Vogt, J. D.	Mess-und Auswerteverfahren von Hitzdrahtsignalen mit dem Turbulenzgradmesser TGM III der DFVLR	Deutsche Luft-und Raumfaht, Forschungsbericht DLR-FB 77-61	15
26	Gai, S. I.	Calibration and use of hot wire probes for steady state measurements in low density flows	Waerme-und Stoffuebertragung 10, 107-115	43
	Galaup, J. P.		(see Delhaye et al.)	
27	Gaulier, C.	Measurement of air velocity by means of a triple hot-wire probe	Disa Information No. 21, 16-20	32
	Gilmore, D. B.		(see Bremhorst et al.)	
	Guiffant, G.		(see Antonini et al.)	
28	Hojstrup, J. Rasmussen, K. Larsen, S. E.	Dynamic calibration of temperature wires in moving air	Disa Information No. 21,33	25
29	Horstman, C. C. Rose, W. C. Hsu, C. T.	Hot-wire anemometry in transonic flow	AIAA J. 15, 395-401	43
			(see Fattahi et al.)	
30	Humphrey, R. L.	Liquid turbulence and its measurement	Proc. Symp. Turbulence in Liquids, Rolla 1975, 103-115	50 01
31	Jagadeesan, T. R.	Study of air motion in a compres-	Society of Automotive	48

NO.	AUTHOR(S)	TITLE	SOURCE	INDEX NO.
	Murthy, B. S.	sion ignition engine cylinder	Engineers, Feb. 18-Mar. 4	
	Klages, H.	Beitraege zur experimentellen Untersuchug und Anwendung von Heissfilmsonden	Max-Planck-Institut fuer Stroemungsforschung, Bericht Nr. 14/1977, Goettingen	35
	Krebs, L.		(see Bremhorst et al.)	
	Larsen, S. E.		(see Hojstrup et al.)	
	Logan, E.		(see Siuru et al.)	
	Lu, S. S.	The dynamic response of the constant temperature hot wire anemometer	Bulletin of the College of Engineering, National Taiwan Univ., No. 22 65-76	20
32	Lueck, R. G. Hertzman, O. Osborn, T. R.	The spectral response of of thermistors	Deep-Sea Research 24, 951-970 Pergamon Press	53
33	McConachie, P. J. Bullock, K. J.	Simultaneous measurement of longitudinal velocity and temperature fluctuations with a single wire in non-isothermal flow	Proc. Symp. Turbulence in Liquids, Rolla 1975, 14-25	45
34	Meier, H. U.	Measuring techniques for compressible turbulent boundary layers	Deutsche-Forschungs- und Veruchsamstalt fuer Luft-und Raumfaht Report DLR-FB77-49	43
	Mensing, P.		(see Fiedler et al.)	
	Murthy, B. S.		(see Jagadeesan et al.)	
	Nagib, H. M.		(see Drubka et al.)	
	Nagib, H. M.		(see Wigeland et al.)	
35	Nall, B. H.	Use of a hot-wire anemometer as a particle velocity detector in standing sound waves	Rev. Sci. Instrum. 48, 449-453	48
	Perrot, P.		(see Antonini et al.)	
36	Perry, A. E.	The time response of an aspirating probe in gas sampling	J. Phys. E. 10,898-902	47
	Gaviglio, J. Dussauge, J. P.	On reduction of errors arising in hot-wire anemometry of thin turbulent shear layers	N.B.S. Special Publication 484; Symposium on flow in open channels and closed conduts, Gaithersburg, Md.	44
	Rasmussen, K.		(see Hojstrup et al.)	
37	Reichert, J. K. Azad, R. S.	Wall shear stress measurement with a hot film in a variable temperature flow	Rev. Sci. Instrum. 48, 341-345	45
38	Rey, C. Beguier, C.	On the use of a three parallel wire probe	Disa Information No. 21, 11-15	32
39	Richards, B.E. (editor)	Measurement of unsteady fluid dynamic phenomena (book)	Hemisphere Publishing Corporation	01
	Sandborn, V. A.	Laboratory instrumentation in turulence measurements	Handbook of Turbulence; Frost, Moulden Editors, Plenum Press, 315-368	01
	Schacher, G.		(see Fairall et al.)	
	Sesonske, A.		(see Flaherty et al.)	
	Shaukatullah, H. Gebhart, B.	Hot-film anemometer calibration and use in fluids at varying background temperature	Letters Heat and Mass Transfer 4, 309	53
40	Siebert, W.	A method to determine the components of mean velocity and Reynolds sensor in water flows using single wire hot film probes	Proc. 17th Congress Int. Assoc. for Hydraulic Research, 631	50
41	Siuru, W. D. Logan, E.	Use of a slanting hot-wire to make measurements in an artificially roughened tube	Disa Information No. 21, 5-10	33
42	Tan-atichat, J.		(see Drubka et al.)	
	Vagt, J. D.		(see Froebel et al.)	
43	Vagt, J. D. Dahm, A.	Bemerkungen zur Herstellung und zum Einsatz von Hitzdrahtsonden im Stroemungslabor	Deutsche Luft-und Raumfaht, Report DLR-FB 77-16, 271-276	30
	Vagt, J. D.		(see Dahm et al.)	
44	Voss-Spilker, P.	Flow measurements in two-phase diffusive flow	Disa information No. 22, 34-38	54

NO.	AUTHOR(S)	TITLE	SOURCE	INDEX NO.
45	Wigeland, R. A. Ahmed, M. Nagib, H. M.	Vorticity measurements using calibrated vane-vorticity indicators and comparison with x-wire data	AIAA Paper No. 77-720 AIAA 10th Fluid and Plasma Dynamics Conference, Albuquerque	48
		1978		
1	Acrivlellis, M.	An improved method for determining the flow field of multi-dimensional flows of any turbulence intensity	DISA Information 23, 11-16	44 15
2	Acrivlellis, M.	Flow field dependence on hot-wire probe cooling law and probe adjustment	DISA Information 23, 17-23	44
3	Aggarwal, J. K.	A directionally insensitive thin-film shear stress gauge	J. Phys. E. 11, 349-352	33
4	Bandyopadhyay, P.	Combined smoke visualization and hot-wire anemometry in turbulent boundary layers	Structure asnd Mechanisms of Turbulence I Lecture Notes in Physics 75, 205-221	48
5	Betrand, J. I. Conderc, J. P.	Hot-film calibration in liquids	DISA Information 23, 28-32	50
6	Bremhorst, K.	Response to stream temperature perturbations at higher frequencies of finite aspect ratio hot-wire anemometers	J. Phys. E. 11, 812-814	45 44
7	Bremhorst, K. Gilmore, D. B.	Influence of end conduction on the sensitivity to stream temperature fluctuations of a hot-wire	Int. J. Heat Mass Transfer 21, 145-154	45 44
	Budny, R. S.		anemometer (see Keffer et al.)	
8	Burkhardt, W. M. Falco, R. E. Butler, G. A.	Response of hot-wire anemometry in flows visualized by an oil fog	Am. Phys. Soc. Bulletin 23, 995 (see Francis et al.)	30 54
9	Coles, D. Wadcock, A. J.	Flying-hot-wire study of two-dimensional mean flow past a NACA 4412 airfoil at maximum lift	Am. Phys. Soc. Bulletin 23, 991	48
	Davis, M. R.	Hot wire anemometer response in flow with acoustic disturbances	J. Sound and Vibration 56, 565,570	43
	Disa	Proceedings of the dynamic flow conference 1978—Dynamic measurements in unsteady flow	Printed in Denmark April 1979. The details of the Proceedings will be listed under 1979 at a later date	01
	Falco, R. E. Finnigan, J. J.		(see Burkhardt et al.) (see Mulhearn et al.)	
10	Fabris, G.	Probe and method for simultaneous measurement of instantaneous temperature and three velocity components in turbulent flow	Rev. Sci. Instrum. 49. 654-664	45 44
	Foss, F. J.	Transverse vorticity measurements	Final Report, NASA Grant NGR-23-004-091 (revised 1979)	32 15
	Francis, M. S.		(see Keese et al.)	
11	Francis, M. S. Kennedy, D. A. Butler, G. A.	Technique for the measurement of spatial vorticity distributions	Rev. Sci. Instrum. 49, 617-623	15
12	Freymuth, P.	A comparative study of the signal-to-noise ratio for hot-film and hot-wire anemometers	J. Phys. E. 11, 915-918	27
13	Freymuth, P.	Extension of the nonlinear theory to constant-temperature hot-film anemometers	TSI Quarterly, Aug/Sept 3-6	21
14	Freymuth, P.	Theory of frequency optimization for hot-film anemometers	J. Phys. E. 11, 177-179	20
15	Freymuth, P.	Supplement on electronic testing of frequency response for thermal anemometers	TSI Quarterly 4, May/June p. 2	26
16	Freymuth, P.	A bibliography of thermal anemometry	TSI Quarterly 4, Issue 4	01
	Friehe, C. A. Gasser, R.	Raumluftgeschwindigkeits-Messeinrichtung fuer Klimatechische Labors	(see Lenschow, et al.) HLH 29, 345-346	41

NO.	AUTHOR(S)	TITLE	SOURCE	INDEX NO.
	Gaviglio, J.	Sur le methodes de l'anemometrie par fil chaud des ecoulements turbulents compressibles des gaz	J. de Mechanique appliquee 2, 449-498	43 01
17	Hah, C. Lakshiminarayana, B. Ho, Chih-ming Hoffman, P. H.	Effect of rotation on a rotating hot-wire sensor	J. Phys. E. 11, 999-1001 (see Wygnanski et al.) (see Smits et al.)	44
18	Hussain, A. K. M. F. Zaman, K.S.M.Q. Kawall, J. K.	The free shear layer tone phenomenon and probe interference	J. Fluid Mech. 87, 349-383 (see Kuffer et al.)	
19	Keesee, J. E. Francis, M. S. Lang, J. D.	A technique for vorticity measurement in unsteady flow	AIAA paper No. 78-801	15
20	Keffer, J. F. Budny, R. S. Kawall, J. G. Kennedy, D. A.	Digital technique for the simultaneous measurement of velocity and temperature	Rev. Sci. Instrum. 49, 1343-1346 (see Francis et al.)	
21	Ko, C. L. McLaughlin, D. K. Troutt, T. R. Lang, J. D. LaRue, J. C.	Supersonic hot-wire fluctuation data analysis with a conduction end-loss correction	J. Phys. E 11, 488-494 (see Keesee et al.) (see Lenschow et al.)	43
22	Lenschow, D. H. Friehe, C. A. LaRue, J. C.	The development of an airborne hot-wire anemometer system	Preprint Vol. Fourth Symp on Meteorological Observations and Instrumentation 463-466	48
	Larsen, S. E. Rasmussen, K. R.	Comment on: Measurement of air velocity by means of a triple hot-wire probe (with a reply by Gaullier, C.)	DISA Information 23, 4-5	35
	Lu, S. S.	A study of the constant-temperature hot-wire anemometer	Nat'l. Sci Council Monthly, 6, No. 1 February (in Chinese) (see Ko et al.) (see Swearingen et al.)	26 20
	McLaughlin, D. K. McLaughlin, D. K. Millon, F. Paranthoen, P. Trinite, M.	Influence des echanges thermiques entre le capteur et ses supports sur la mesure des fluctuations de temperature dans un ecoulement turbulent	Int. J. Heat Mass Transfer, 21, 1-6	44 45
23	Mojola, O. O.	The effects of orientation of hot-wire probe body in turbulent shear flows	DISA Information 23, 24-27	37
24	Mulhearn, P. J. Finnigan, J. J.	A simple device for dynamic testing of x-configuration hot-wire anemometer probes	J. Phys. E. 11, 679-681	25
25	Parsons, J. R. Mulligan, J. C.	Measurement of the properties of liquids and gases using a transient hot-wire technique	Rev. Sci. Instrum, 49, 1460-1463	56
	Perry, A. E. Polyakov, A. F. Shindin, S. A.	Peculiarities of hot-wire measurements of mean velocity and temperature in the wall vicinity	(see Smits et al.) Heat and Mass Transfer, Pergamon Press, 53-58	48 44 45
26	Pratt, R. L. Bowsher, J. M.	A simple technique for the calibration of hot-wire anemometers at low aire velocities	DISA Information 23, 33-34	41
27	Remke, K.	Some remarks on the response of hot-wire and hot-film probes to passage through an air-water interface	J. Phys. E. 11, 94-96	54
	Schacher, G. E. Fairall, C. W.	Producing small scale temperature fluctuations in an air stream	Rev. Sci. Instru. Vol. 49, pp. 1432-1434	25 45
28	Smits, A. J. Perry, A. E. Hoffmann, P. H.	The response to temperature fluctuations of a constant-current hot-wire anemometer	J. Phys. E. 11, 909-914	
29	Swearingen, J. D. McLaughlin, D. K. Troutt, T. R.	Crossed hot-wire measurements in low to moderate Reynolds number supersonic jets	Am. Phys. Soc. Bull. 23, 1016	43
30	Tavoularis, S.	A circuit for the measurement of	J. Phys. E. 11, 21-24	45

NO.	AUTHOR(S)	TITLE	SOURCE	INDEX NO.
		instantaneous temperature in heated turbulent flows		
	Troutt, T. R.		(see Ko et al.)	
	Troutt, T.		(see Swearingen et al.)	
	Wadcock, A. J.		(see Coles et al.)	
31	Wygnanski, I. Ho, Chih-ming Zaman, K. B. M. Q.	Note on the prong configuration of an x-array hot-wire probe	Rev. Sci. Instrum, 49, 865-866 (see Hussain et al.)	37

II. Some Observations and Remarks

The development of thermal anemometry seems to have peaked in 1968 with 85 papers and is slowly tapering off (39 papers in 1977), but is still very vigorous. This development may reflet the maturing of the field as well as diversion of efforts to the complementary field of laser anemometry.

A fair amount of redundancy is characteristic for the field of thermal anemometry. Whether this is necessary or regrettable is not clear to this author.

Some surprises of interest to this author were encountered during work on the bibliography which are shared in the closing remarks of this section:

Measurements of velocity and temperatures in flows developed parallel but often separately. They can be traced to the last part of the ninteenth century, i.e., crude attempts by Oberbeck (1895) and Weber (1894) for velocity and Hall (1891) and Callendar and Nicholson (1897) for temperature. Thermal inertia of velocity probes was first considered by Retschy (1912) and of temperature probes by Petersen (1913). Benson and Brundrett (1962) give a historical survey of temperature measurements in flows.

A forerunner of the split-film probe (Olin, 1970) was devised by Huguenard, et al. (1924) by locating two wires along a larger cylinder and utilizing the directional sensitivity of this arrangement.

A step-up transformer for hot-wire signal amplification was used as early as 1926 by Tyler and in the same year Gupta reported the first electronic amplification of hot-wire signals.

The constant temperature anemometer was invented by Morris (1912) and the first constant temperture anemometer with automatic feedback control was designed by Hill, Hargood-Ash and Griffiths in 1921 (and commercially sold!). Since electronic amplifiers were not available at that time, an electro-mechanical feedback mechanism was devised.

Electronic square wave testing of constant current anemometers was pioneered by Ziegler in 1931, and Fig. 1 shows over-, under-, and proper frequency compensation as depicted in Ziegler's paper.

Although Ziegler invented the first constant temperature anemometer with electronic feedback in 1934, square wave testing of this device seems to have arrived rather late in 1960 when Staritz first mentions it.

Biomedical thermal anemometry seems to go back to 1933 when Gibbs used a heated thermocouple probe for the measurement of blood flow.

The idea of using probe shaking as a method for frequency response evaluation and for dynamic calibration of sensor sensitivity is not new. It was practiced by Salter and Raymer (1934) and by Simmons (1939).

Let us jump from these early developments into the immediate past.

Comte-Bellot in her 1976 review mentions the need to investigate parametric excitation of harmonics in resistance thermometers induced by large velocity fluctuations. As it turns out, Mikhailov had considered this problem in 1965, two years after Corrsin had considered parametric excitation for the constant current anemometer. Mikhailov's results are not quite correct but the error can easily be repaired. It can be

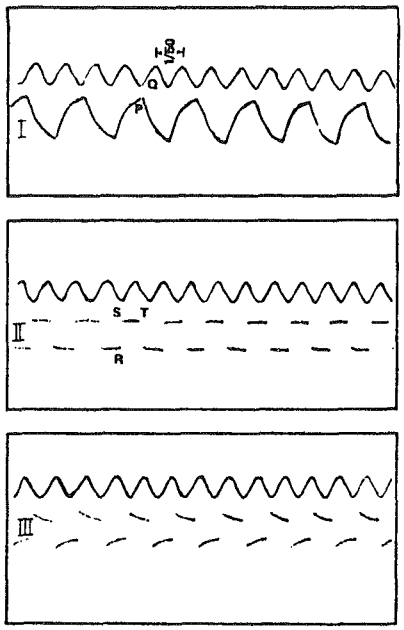

Fig. 1 Illustration of proper frequency compensation from the paper by Ziegler (1931). I: under-compensation, II: proper compensation, III: over-compensation

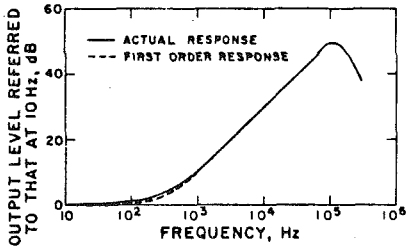

Fig. 2 Sine wave test for a hot wire in constant temperature mode in still air (from Freymuth and Fingerson, 1977) and first order response (dotted line). The first order response curve has been aligned to coincide with the linear range of the actual response

shown that parametric excitation in resistance thermometers is less serious than in constant current anemometers which is the main result.

Let us finally consider a most recent paper by Bremhorst, Krebs and Gilmore (1977) where they show that thin wire resistance thermometers exhibit peculiar deviations from a first order dynamic response at low velocities and rather low frequencies. This effect reflects the heat conduction from the wire into the wire supports of finite heat capacity. Since a constant temperature anemometer exhibits just the inverse dynamic response during sine wave testing as a resistance thermometer when exposed to temperature fluctuations (Freymuth, 1969), one may search for this effect in previously reported sine wave tests (Freymuth and Fingerson, 1977) for constant temperature anemometers. The effect indeed can be

identified in these tests as is shown in Fig. 2. In Fig. 2, the sine wave test for a hot-wire exposed to still air is shown (from Fig. 4 in Freymuth and Fingerson, 1977). Furthermore, the response has been drawn which one would expect from a first order wire response (dashed line). The effect clearly shows up. At a velocity of 30 ft/sec (Fig. 5 of Freymuth and Fingerson, 1977), the effect was too weak for positive identification which also agrees with the experience by Bremhorst, et al. For cylindrical hot films (Figs. 6 and 7 in Freymuth and Fingerson, 1977), the effect also could not be identified despite the fact that the aspect ratio of the film is low. The reason for this finding is presumably the low thermal conductivity of the film substrate material in conjunction with its high thermal inertia.

III Acknowledgments and Requests for Cooperation

Supply of requested information by the following authors is gratefully acknowledged:
D. Bechert, E. Berger, P. Bradshaw, K. Bremhorst, J. M. Burers, S. Corrsin, F. Durst, L. M. Fingerson, F. N. Frenkiel, C. A. Friehe, M. Herbeck, R. L. Humphrey, L. S. G. Kovasznay, V. A. Sandborn, J. Way.

In compiling the bibliography, deliberate use has been made of the bibliographical materials contained in the papers listed. Without this "passive cooperation" by all authors, the compilation of the bibliography would have been an impossible task.

TSI Incorporated, St. Paul, Minnesota, U.S.A. is acknowledged for its contribution in supporting the compilation of this bibliography, which first appeared in the *TSI Quarterly*, November/December 1978 issue, and for permitting its publication in the "Journal of Fluids Engineering." TSI Incorporated develops and manufactures instruments for measurements in Aerosol and Fluid Mechanics Research.

M. Kiya
Associate Professor.

M. Arie
Professor.

K. Koshikawa
Graduate Student.

Department of Mechanical Engineering,
Hokkaido University,
Sapporo 060, Japan

An Analysis of Uniform Shear Flow Past a Porous Plate Attached to a Plane Surface

The wake-source model of Koo and James was extended to the case of a two-dimensional porous plate attached to a plane surface along which a turbulent boundary layer developed. The approaching stream is replaced by a uniform shear flow of linearly-varying velocity profile such that the height of the plate is much smaller than the boundary-layer thickness. The theory requires as input the pressure-drop coefficient of the porous plate and the boundary-layer velocity profile at an appropriate location upstream of the plate.

1 Introduction

There are numerous practical situations in which flow passes partly through and partly around a porous body; common examples of such bodies are fish nets, snow fences, natural and artificial wind breaks, and slotted injection disks in oil-combustion chambers, which are used to create a low-velocity zone suitable for ignition. The porous body can also be regarded as an artificial feature designed to protect certain industrial activities against the wind, or pedestrians from the flow around buildings in whose precincts they are forced to venture. It is typical of the lattice framework used for many steel structures. A review of the flow past screens was recently written by Laws and Livesey [1]. Graham [2] treated a turbulent flow past a porous plate in order to calculate the fluctuating drag of the lattice structures.

In any of the above applications, one of the most fundamental problems may be to clarify the flow field in the near wake of a porous body in terms of its geometrical shape such as porosity, and the properties of the approaching flow. Castro's measurement [3] of the wake of a porous plate in uniform stream of a wind tunnel revealed the existence of a recirculating bubble which detached from the body and moved downstream as the porosity is increased. The presence of the bubble can be regarded as a consequence of the failure of the air in the wake to provide enough fluid for entrainment for the shear layers that spring from the edges of the plate. As the porosity increases, more fluid is made available and the deficit in the balance with entrainment is not made evident until the shear layers have extended further downstream. When the porosity is sufficiently large, the bubble disappears altogether. Exactly the same qualitative feature of the bubble was also observed in the authors' own laboratory in the wake of a porous plate attached to a solid surface along which a turbulent boundary layer developed.

In order to predict the development of flow in the wake of the porous plate, together with the detached bubble if any, an accurate determination of the quantity of fluid which has passed through the plate will be required at the outset. The theory presented by Koo and James [4] can be used to determine this quantity. In their model, an inviscid incompressible fluid is assumed and the porous plate is replaced by a source distribution. The stream function is adjusted to give the correct mass and momentum flow across the plate.

In the present paper, the wake-source model of Koo and James [4] will be extended to the flow past a porous plate attached to a solid plane surface. Since the boundary layer developing along the surface contains a rather large velocity gradient in the normal direction, it is important to incorporate into the theory the nonuniform velocity profile upstream of the porous plate. The velocity profile in a turbulent boundary layer is approximately proportional to the normal distance raised to some power – a power-law variation. However, a theoretical analysis of the flow pattern around the porous plate will include prohibitive complexity in the case of shear flow of nonlinear velocity profile even when an inviscid incompressible fluid is assumed. The main difficulty is the nonlinearity of the governing equation, i.e.

$$\Delta\psi = -\zeta(\psi) \tag{1}$$

where ψ is the stream function, Δ the Laplacian operator and ζ denotes the vorticity which is generally a nonlinear function of ψ. This situation may necessarily lead to a certain simplification of the approaching flow to such an extent that an analytical treatment becomes possible. A uniform shear flow which has a constant vorticity will be assumed in the present analysis. In this case, equation (1) reduces to

$$\Delta\psi = -\zeta_0 \tag{2}$$

where ζ_0 is the constant vorticity. Although the uniform shear flow will probably a very rough approximation to actual turbulent boundary layers, the authors are of the opinion that such an analysis has a considerable significance as a first step to estimate the effects of the nonuniformity of the approaching stream.

Koo and James [4] suggested that their theory could treat the case of a nonuniform upstream velocity distribution. As may be evident from the foregoing discussion, their method in

Contributed by the Fluids Engineering Division for publication in the JOURNAL OF FLUIDS ENGINEERING. Manuscript received by the Fluids Engineering Division, July 13, 1978.

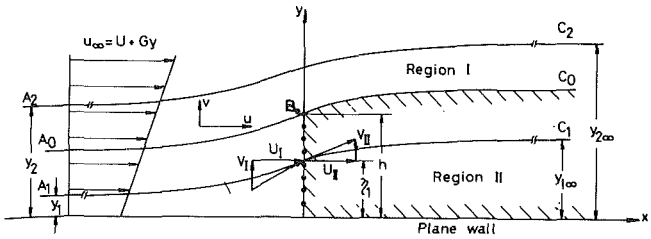

Fig. 1 Definition sketch of the problem

its original form, i.e., the representation of the porous plate by a source distribution, can be extended only to the case of a uniform shear flow which has a constant vorticity. In order to be able to treat a nonuniform approaching flow other than a uniform shear flow, one must probably make some appropriate assumptions, such as a small perturbation from the original flow.

2 Mathematical Formulation of the Model

As shown in Fig. 1, x and y are Cartesian coordinates along and normal to the plane surface and the corresponding velocity components are denoted by u and v. In view of the aforementioned assumption, the velocity profile at infinitely large distances from the porous plate is described by

$$(u_\infty, v_\infty) = (U + Gy, 0) \tag{3}$$

where U is the slip velocity at infinity on the x axis and G denotes the velocity gradient. The values of U and G must be determined in terms of the boundary-layer velocity profile at an appropriate location upstream of the plate. The stream function which yields the velocity components of equation (3) is

$$\psi_\infty = \int_0^y u_\infty dy = Uy + (1/2)Gy^2 \tag{4}$$

When the uniform shear flow is disturbed by two-dimensional disturbances described by a stream function ψ', the stream function ψ of the total flow field is simply written by

$$\psi = \psi_\infty + \psi' \tag{5}$$

Since the vorticity in the original inviscid stream, which is $-G$, is constant, Kelvin's law of conservation of vorticity requires that the disturbance stream function ψ' should satisfy the Laplace equation $\Delta\psi' = 0$ in the region outside the wake of the plate. This situation implies that the flow field outside the wake can be treated by means of the well-established potential flow theory. In the wake region, the flow will not generally have a constant vorticity because of nonuniform energy losses along the porous plate. In what follows, the regions of flow outside and inside the wake will be designated as I and II, respectively.

In order to represent the displacement effect of the wake in region I, the porous plate is replaced by a continuous distribution of sources. Let the source strength per unit length of the plate be denoted by $Q(\eta)$ at $y = \eta$, where $0 \leqq \eta \leqq h$, h being the height of the plate. The boundary condition that the vertical velocity component must vanish on the x axis can be satisfied by arranging image sources of the same strength at $y = -\eta$. The complex potential function of the entire source system then becomes

$$W_Q = (2\pi)^{-1} \int_0^h Q(\eta) \log(z^2 + \eta^2) d\eta \tag{6}$$

in which $z = x + iy$ and $i = (-1)^{-1/2}$. The sum of two flows given by equations (4) and (6) yields the stream function

$$\psi = \psi_\infty + \mathrm{Im}(W_Q) \tag{7}$$

where Im means the imaginary part. The velocity components are

$$u(x, y) = U + Gy + \frac{1}{\pi} \int_0^h Q(\eta) \frac{x(x^2 + y^2 + \eta^2)}{[x^2 + (y-\eta)^2][x^2 + (y+\eta)^2]} d\eta \tag{8a}$$

$$v(x, y) = \frac{1}{\pi} \int_0^h Q(\eta) \frac{y(x^2 + y^2 - \eta^2)}{[x^2 + (y-\eta)^2][x^2 + (y+\eta)^2]} d\eta \tag{8b}$$

The essense of the technique of Koo and James [4] is to set ψ_I equal to ψ in region I and then require that the streamline pattern for ψ_{II} is the same as that for ψ in region II; that is, one requires that $u_{II}/v_{II} = u/v$ in region II. This stipulation is satisfied by putting $\psi_{II} = B(\psi)\psi$, where B is a function of ψ, because one has

$$u_{II} = \partial\psi_{II}/\partial y = Eu \tag{9a}$$

$$v_{II} = -\partial\psi_{II}/\partial x = Ev \tag{9b}$$

in which $E = B + \psi\,(dB/d\psi)$. The factors B and E may be interpreted as attenuation functions for the stream function and velocity components in region II. The unknowns in the present problem are thus the source-strength distribution $Q(y)$ and the attenuation factor B or E. These two unknowns can be determined by satisfying the mass and energy balances across the porous plate.

Nomenclature

B = attenuation factor for stream function in wake
d = diameter of rod
E = attenuation factor for velocity in wake
G = vertical velocity gradient of shear flow
h = height of porous plate
i = $(-1)^{1/2}$
K = pressure-drop coefficient of porous plate
l = distance between centers of consecutive rods
p_I, p_{II} = pressure immediately upstream and downstream of porous plate
$p_1, p_{1\infty}$ = infinitely windward and leeward pressures on streamline A_1C_1
$p_2, p_{2\infty}$ = infinitely windward and leeward pressures on streamline A_2C_2
Q = strength of source
Q_m, Q_{m+1} = m-th and $(m+1)$-th approximations to Q
R = integral defined by equation (23)
u, v = longitudinal and vertical velocity components
$u_1, u_{1\infty}$ = infinitely windward and leeward velocities along streamline A_1C_1
$u_2, u_{2\infty}$ = infinitely windward and leeward velocities along streamline A_2C_2
u_∞, v_∞ = longitudinal and vertical velocity components of shear flow

A streamline which is located at $y = y_1$ infinitely upstream is assumed to cross the porous plate at the height of $y = \eta_1$, as shown in Fig. 1. The velocity components and pressure immediately upstream and downstream of the plate at $y = \eta_1$ are designated as U_I, V_I, p_I and U_{II}, V_{II}, p_{II} respectively. The requirement that the mass flux should be continuous across the plate yields

$$U_I = U_{II} \tag{10}$$

because an incompressible fluid is considered in the present analysis. The pressure drop across the plate can be expressed by the dimensionless pressure-drop coefficient K, which is assumed to be known, in the form

$$p_I - p_{II} = K\left(\frac{1}{2}\rho U_I^2\right) \tag{11}$$

where ρ is the density of fluid. The coefficient K is a function of the porosity β and the Reynolds number R_d which is based on the approaching flow velocity and the rod diameter if the porous bodies are single rows of parallel rods at right angles to the flow. K decreases with R_d until $R_d > 250$, after which point K is a function of β only (Laws and Livesey [1]). In the framework of this theory, the coefficient K can be allowed to vary as a function of the coordinate along the plate.

It should be noted that this theory cannot satisfy the deflection condition of the streamlines at the plate because its inclusion would overspecify the problem for E and Q. A relation between the attenuation factor E and the deflection coefficient, which is defined as the ratio of the tangential velocity after the plate and that before, is given in Koo and James [4]. Moreover, the static pressure is discontinuous across the dividing streamline B_0C_0 (see Fig. 1). According to Koo and James [4], however, the discontinuity in pressure is small enough to be neglected. A more refined model could be constructed by adding a vortex distribution to the source distribution along the porous plate. Since Koo and James [4] found that the improvement in accuracy was generally very small, the neglect of a vortex distribution would be justified.

The height of the streamline A_1C_1 at the infinitely leeward positon will be written as $y_{1\infty}$. Let the velocities and pressures at the locations $(-\infty, y_1)$ and $(+\infty, y_{1\infty})$ be denoted by u_1, p_1 and $u_{1\infty}$, $p_{1\infty}$. The Bernoulli equations on the two segments of the streamline A_1C_1, which lie in regions I and II, yield

$$p_1 - p_{1\infty} + \frac{1}{2}\rho(u_1^2 - u_{1\infty}^2) = p_I - p_{II} + \frac{1}{2}\rho(V_I^2 - V_{II}^2) \tag{12}$$

in which $u_1 = U + Gy_1$ and $u_{1\infty} = E(U + Gy_{1\infty})$. Since the longitudinal velocity components induced by the source distribution are $-Q(\eta_1)/2$ and $Q(\eta_1)/2$ immediately upstream and downstream of the plate, U_I and U_{II} can be expressed as

$$U_I = U + G\eta_1 - (1/2)Q(\eta_1) \tag{13a}$$

$$U_{II} = E\{U + G\eta_1 + (1/2)Q(\eta_1)\} \tag{13b}$$

The lateral velocity components V_I and V_{II} are obtained by setting $x = 0$ in equations (8b) and (9b)

$$V_I = \pi^{-1}\int_0^h Q(\eta)\eta_1(\eta_1^2 - \eta^2)^{-2}d\eta \tag{14a}$$

$$V_{II} = E\pi^{-1}\int_0^h Q(\eta)\eta_1(\eta_1^2 - \eta^2)^{-2}d\eta \tag{14b}$$

By applying the Bernoulli theorem to a streamline A_2C_2 which does not meet the porous plate (see Fig. 1), one obtains

$$p_2 + (1/2)\rho u_2^2 = p_{2\infty} + (1/2)\rho u_{2\infty}^2 \tag{15}$$

where u_2, p_2 and $u_{2\infty}$, $p_{2\infty}$ are the velocity and pressure on the same streamline infinitely windward and leeward locations. If the heights of the streamline A_2C_2 at $x = -\infty$ and $+\infty$ are designated by y_2 and $y_{2\infty}$, one has $u_2 = U + Gy_2$ and $u_{2\infty} = U + Gy_{2\infty}$.

The conservation of mass flux across the porous plate, which is applied to the region between the x axis and the streamline A_1C_1, yields

$$\left(Uy_{1\infty} + \frac{1}{2}Gy_{1\infty}^2\right) - \left(Uy_1 + \frac{1}{2}Gy_1^2\right) = \int_0^{\eta_1} Q(y)\,dy \tag{16a}$$

In the same manner, one obtains for the region enclosed by the x axis and the streamline A_2C_2

$$\left(Uy_{2\infty} + \frac{1}{2}Gy_{2\infty}^2\right) - \left(Uy_2 + \frac{1}{2}Gy_2^2\right) = \int_0^h Q(y)\,dy \tag{16b}$$

By utilizing equation (16b), equation (15) is reduced to

$$p_2 - p_{2\infty} = \rho G\int_0^h Q(y)\,dy \tag{17a}$$

Since the streamlines are parallel to the x axis at $x \to +\infty$, there is no pressure difference between regions I and II there, viz. $p_{1\infty} = p_{2\infty}$. Equation (17$a$) then yields

$$p_1 - p_{1\infty} = \rho G\int_0^h Q(y)\,dy \tag{17b}$$

Nomenclature (cont.)

u_{II}, v_{II} = longitudinal and vertical velocity components in region II
u_b = velocity of boundary layer at matching position
u_{th} = theoretical velocity at matching position
U = slip velocity of shear flow at infinity
U_0 = reference velocity
U_I, V_I = longitudinal and vertical velocity components immediately upstream of porous plate
U_{II}, V_{II} = longitudinal and vertical velocity components immediately downstream of porous plate
W_Q = complex potential function of source distribution
x, y = longitudinal and vertical coordinates
$y_1, y_{1\infty}$ = infinitely windward and leeward heights of streamline A_1C_1
$y_2, y_{2\infty}$ = infinitely windward and leeward heights of streamline A_2C_2
z = complex variable = $x + iy$
β = porosity of porous plate = $(l - d)/l$
Δ = Laplacian operator = $\partial^2/\partial x^2 + \partial^2/\partial y^2$
η, η_1 = coordinate along porous plate
ρ = density of fluid
ψ = stream function
ψ_I, ψ_{II} = stream function in regions I and II
ψ' = disturbance stream function
ζ = vorticity
ζ_1 = constant vorticity

because $p_1 \equiv p_2$. This equation shows that a source of strength, say Q_T, immersed in the uniform flow will induce a pressure drop equivalent to $\rho G Q_T$ between infinitely windward and leeward positions.

Substitution of equations (11) and (17*b*) into equation (12) now gives

$$KU_I^2 = 2G\int_0^h Q(y)\,dy + (u_I^2 - u_{I\infty}^2) + (V_{II}^2 - V_I^2) \tag{18}$$

Since the velocities U_1, V_1 and V_{11} are functions of η_1 while u_1 and $u_{1\infty}$ are expressed in terms of y_1 and $y_{1\infty}$, it is necessary to rewrite the latter velocities as functions of η_1. The result is

$$u_I^2 - u_{I\infty}^2 = (1-E^2)(U+G\eta_1)^2 - (1+E^2)G\int_0^\eta Q(y)\,dy \tag{19}$$

The attenuation function E is expressed as a function of $Q(\eta_1)$ by combining equations (10) and (13), namely

$$E = \left\{U+G\eta_1 - \frac{1}{2}Q(\eta_1)\right\} \Big/ \left\{U+G\eta_1 + \frac{1}{2}Q(\eta_1)\right\} \tag{20}$$

By substituting equations (14), (19) and (20) into equation (18) and rearranging the terms, one obtains

$$K\left\{(U+Gy)^2 - \frac{1}{4}[Q(y)]^2\right\}^2$$
$$= \left\{U+Gy+\frac{1}{2}Q(y)\right\}^2 \times 2G\int_0^h Q(\eta)\,d\eta$$
$$-\left\{(U+Gy)^2 + \frac{1}{4}[Q(y)]^2\right\} \times 2G\int_0^y Q(\eta)\,d\eta$$
$$+2Q(y)\,(U+Gy)\left\{(U+Gy)^2 - \left[\int_0^h \frac{Q(\eta)}{\pi} y(y^2-\eta^2)^{-2}\,d\eta\right]^2\right\} \tag{21}$$

in which the variable η_1 has been written as y without any loss of generality. An appropriate solution of equation (21) will yield the source-strength distribution $Q(y)$ $(0 \leqq y \leqq h)$, and the velocity field in the neighborhood of the porous plate can thus be calculated from equation (8) in region I and from equation (9) in region II.

A general solution of equation (21) does not seem feasible because of its nonlinearity, and consequently a numerical technique should be devised to solve this equation. Since the second and third terms on the right-hand side of equation (21) contain G as a multiplicative factor, these terms can be deleted from this equation to obtain a first-order approximate solution in cases where Gh is much smaller than U. If Gh is of the same order of magnitude as U, an iterative procedure may be employed in which a sufficiently small value of Gh is assumed at first to get a solution and then, by increasing Gh by a small amount, another solution is obtained on the basis of the first solution. By repeating this procedure, one can obtain the source-strength distribution for a required combination of U and G. If $Q_m(y)$ denotes the mth approximate solution for $Q(y)$, the $(m+1)$-th approximation $Q_{m+1}(y)$ can be calculated from

$$K\left\{(U+Gy)^2 - \frac{1}{4}[Q_{m+1}(y)]^2\right\}^2 - 2(U+Gy)^3 Q_{m+1}(y)$$
$$= \left\{U+Gy+\frac{1}{2}Q_m(y)\right\}^2 \times 2G\int_0^h Q_m(\eta)\,d\eta$$
$$-\left\{(U+Gy)^2 + \frac{1}{4}[Q_m(y)]^2\right\} \times 2G\int_0^y Q_m(\eta)\,d\eta$$
$$-2Q_m(y)\,(U+Gy)\left[\int_0^h \frac{Q_m(\eta)}{\pi} y(y^2-\eta^2)^{-2}\,d\eta\right]^2 \tag{22}$$

3 Numerical Calculation and Comparison With Experiment

In order to assess the accuracy and range of validity of the mathematical model, a comparison is made between the theory and a measurement of the velocity field in the vicinity of the porous plate. A series of experiments is in progress in the authors' laboratory to clarify the flow field downstream of porous bodies immersed in turbulent boundary layers. In these experiments, the drag force acting on several porous plates is also measured. The results will be published elsewhere in due time.

A porous plate of the height h = 2.97 cm was a two-dimensional grid of parallel circular rods of diameter d = 0.125 cm at right angles to the approaching stream. The mean distance l between the centers of consecutive rods was 0.158 cm and thus the porosity of the plate is

$$\beta = (l-d)/l = 0.209$$

The porous plate was attached to the floor of an air tunnel whose test section is 0.5 m high, 0.5 m wide and 6.0 m long. Therefore, the blockage-area ratio is less than 6 percent. In order to realize a thick turbulent boundary layer, a tripping rod of 3.0 cm diameter was installed on the tunnel floor 1.13 m upstream of the plate. The reference velocity U_0 was measured in a uniform-flow region above the plate and was maintained at U_0 = 26.0 m/s. The velocity distribution upstream of the plate was measured by a Pitot-static tube which was consisted of a flattened total-head tube with an opening 0.15 cm wide and 0.05 cm high and a static tube of 0.12 cm diameter. The measurement of velocity in the wake region was made by the use of a 180 deg Pitot cylinder which is fully described by Arie [5] and Arie and Rouse [6].

The pressure-drop coefficient K may generally be a function of the coordinate along the plate. However, since exact variation of K along the plate is not known to the authors, K is tentatively assumed to be constant and equal to

$$K = (1-\beta)/\beta^2 = 18.11$$

which is valid for two-dimensional grids of parallel rods spanning the entire cross section of the flow (Owen and Zienkiewicz [7]).

As mentioned previously, the values of U and G must be determined on the basis of the boundary-layer velocity profile at an appropriate position upstream of the porous plate, which will hereafter be designated as the matching position. Since the present model implicitly assumes that the flow in the vicinity of the plate is characterized by a rapid distortion during which the effect of viscosity does not have enough time to manifest itself, the matching position should be chosen to satisfy this requirement. An appropriate matching position may be a function of Reynolds number. However, an exact criterion upon which the matching position is to be determined is not included within the framework of the present inviscid theory. In the following calculation, the matching position was selected rather arbitrarily at the location $2.2h$ upstream of the plate. The procedure to determine U and G is as follows:

(i) A uniform shear flow $U + Gy$ is obtained by applying the least-squares method to the boundary-layer velocity profile in the range $0 < y \leqq h$ at the matching position. This shear flow is tentatively employed as the approaching flow infinitely upstream of the plate. Since the turbulent boundary layer has large transverse velocity gradient in the immediate neighborhood of the solid surface, the velocity there should not be included in the process to determine the shear flow in the interest of better representation of the overall velocity

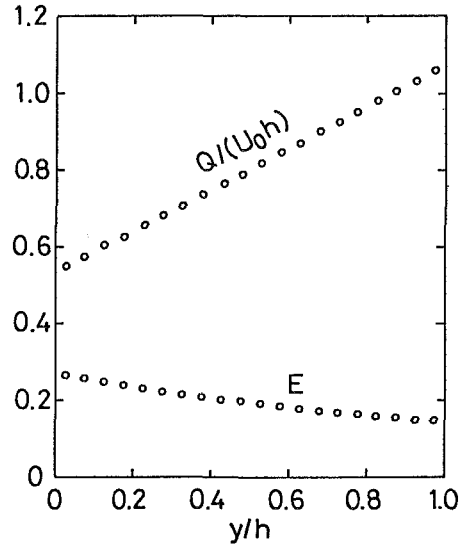

Fig. 2 Calculated distribution of source strength Q and attenuation factor E

profile in the range $0 < y \leqq h$. In a particular example considered here, the velocity in the region $y \geqq 0.05$ cm was employed.

(ii) The source-strength distribution $Q(y)$, which was determined on the basis of the approaching flow just described, is utilized to calculate the velocity profile at the matching position. The calculated velocity profile was found to have almost the same mean shear in the region $0 < y \leqq h$ as that of the approaching shear flow (see Fig. 3(a)). Therefore, an optimum value of U can be obtained by requiring that the integral

$$R = \int_0^h |u_{\text{th}}(y) - u_b(y)|\, dy \tag{23}$$

should attain a minimum value at the matching position. Here, $u_{\text{th}}(y)$ is the calculated velocity profile and $u_b(y)$ denotes that in the turbulent boundary layer.

The approaching shear flow finally determined by this procedure is

$$u_\infty = U_0\{0.467 + 0.247(y/h)\} \tag{24}$$

The source-strength distribution $Q(y)$ was solved for twenty values of y with the last term of equation (22) neglected for the sake of simplicity. The results are shown in Fig. 2 as plots of Q and E versus y. The calculated and experimental velocity distributions are compared at a few locations upstream and downstream of the plate. The calculated velocity profiles at the locations $x/h = -2.2$ and -1.1 are in reasonable agreement with the measured ones in the range $0 < y/h < 1$. The approaching shear flow given by equation (24) is also included in Fig. 3(a) in order to show that, despite a marked retardation of flow in front of the plate, the transverse velocity gradient at the matching position ($x/h = -2.2$) is practically the same as that of the approaching flow in the above range of y. Because of the very assumption of the uniform shear flow, the theoretical velocity profiles deviate markedly from the experimental ones in the vicinity of the wall and in the region beyond $y/h = 1.0$. This feature is one of the shortcomings of the present model.

The theoretical velocity distribution is compared with the experiment in Fig. 3(b) at the location $x/h = 1.0$. Since the solution of the source strength increases very closely in proportion to y, the resulting velocity profile is rather flat in the wake region. On the other hand, the measurement shows a complicated profile with a maximum at about $x/h = 0.5$.

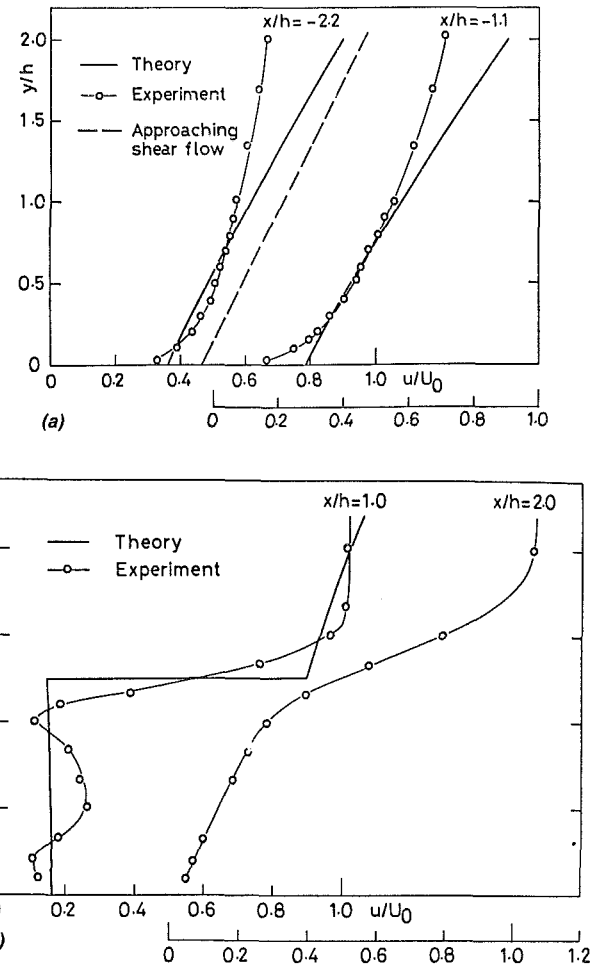

Fig. 3 Predicted and experimental velocity profiles at *(a)* windward locations and *(b)* leeward locations. The broken line in *(a)* shows the theoretical velocity profile of uniform shear flow infinitely upstream of the porous plate, which is determined in the manner described in the text. This shear flow yields the velocity profile at the matching position ($x/h = -2.2$), which is expressed as a solid line labelled as "theory." On the basis of observed fluctuations of velocity head during measurement, the uncertainty of u/U_0 is estimated to be less than 1 percent in the region upstream of the plate and about 7 percent in the region downstream of it owing to high intensity of turbulence. In both figures *(a)* and *(b)*, the abscissa is the distance and the error negligible.

Nevertheless, the average velocity in the wake is predicted within an error less than 15 percent. The complex variation of the measured profile at $x/h = 1.0$ might be attributed to a probable nonuniformity of the pressure-drop coefficient K along the plate. The experimental velocity distribution at $x/h = 2.0$, which is also shown in Fig. 3(b), was not compared with the theory because of significant diffusion of the shear layer at this position.

Since the numerical calculation was performed by ignoring the vertical velocity components at the plate, i.e. V_{II}^2 and V_{I}^2 in equation (18), the effect of these terms on the shape of the velocity profile in the wake should be mentioned. The authors are aware of the fact that the neglect of these terms will not be justified near the edges of the plate because the terms usually become infinite there. The numerical calculation by Koo and James [4] (Fig. 9 of their paper) shows that the inclusion of these terms yields a dip in velocity at the edge of the wake. However, even for the case of a large solidity such as $K = 16$, which is near to $K = 18.11$ in the present case, their calculation shows that the minimum velocity at the dip amounts to 75 percent of a rather uniform velocity over most of the wake region. It should be noted that this is a minor

concern because this part of the flow is a mixing layer for a real fluid, in which the velocity profile is continuous and not abrupt as shown in Fig. 3 (*b*).

The discontinuity of velocity across the dividing streamline is unavoidable in any inviscid analysis. However, since the shape of the dividing streamline can be predicted by the present theory, it may be possible to construct more realistic velocity profiles in the wake by taking into account the turbulent diffusion of the shear layer, perhaps by means of the boundary-layer type of approximation. This will be left for a future study.

4 Conclusions

It appears that the present extension of the wake-source model of Koo and James [4] approximately represents the near-flow field around and through a two-dimensional porous plate attached to a solid surface along which a turbulent boundary layer has developed. Since the approaching stream is replaced by a uniform shear flow of linearly-varying velocity profile, the height of the plate must be much smaller than the boundary-layer thickness in order to expect a reasonable prediction from the theory. This condition may be well satisfied in the case of snow fences and natural or artificial wind breaks. The theory requires as input the pressure-drop coefficient and the boundary-layer velocity profile at an appropriate position upstream of the porous plate. A procedure to determine an optimum shear flow on the basis of the measured velocity profile was also proposed.

Acknowledgments

The authors express their sincere thanks to Mr. T. Yamazaki and Mr. T. Sampo for their skillful assistance in constructing the experimental apparatus.

References

1 Laws, E. M., and Livesey, J. L., "Flow through Screens," *Ann. Rev. Fluid Mech.*, Vol. 10, 1978, pp. 247–266.

2 Graham, J. M. R., "Turbulent Flow Past a Porous Plate," *J. Fluid Mech.*, Vol. 73, Part 3, 1976, pp. 556–591.

3 Castro, I. P., "Wake Characteristics of Two-Dimensional Perforated Plates Normal to an Air-Stream," *J. Fluid Mech.*, Vol. 46, Part 3, 1971, pp. 599–609.

4 Koo, J.-K. and James, D. F., "Fluid Flow Around and Through a Screen," *J. Fluid Mech.*, Vol. 60, Part 3, 1973, pp. 513–538.

5 Arie, M., "Characteristics of Two-Dimensional Flow behind a Normal Plate in Contact with a Boundary on Half Plane," *Memoirs of the Faculty of Engineering*, Hokkaido University, Vol. 10, No. 2, 1956, pp. 211–310.

6 Arie, M. and Rouse, H., "Experiments on Two-Dimensional Flow Over a Normal Wall," *J. Fluid Mech.*, Vol. 2, Part 2, 1956, pp. 129–141.

7 Owen, P. R., and Zienkiewicz, K. H., "Production of Uniform Shear Flow in a Wind Tunnel," *J. Fluid Mech.*, Vol. 2, Part 6, 1957, pp. 521–531.

M. Kiya
Associate Professor.

M. Arie
Professor.

H. Tamura
Instructor.

H. Mori
Graduate Student.

Department of Mechanical Engineering,
Hokkaido University,
Sapporo 060, Japan

Vortex Shedding From Two Circular Cylinders in Staggered Arrangement

The frequency of vortex shedding from two circular cylinders of the same diameter in staggered arrangement is experimentally investigated at a Reynolds number of 1.58×10^4. This Reynolds number is within the range where the flow around a circular cylinder is relatively insensitive to Reynolds number changes. The results are summarized in several figures from which one can obtain the Strouhal number of vortex shedding for all arrangements within distances between their centers less than 5 diameters.

1 Introduction

Fluid-dynamic interaction between two circular cylinders immersed in a stream is of fundamental importance in fluids engineering. Twin chimney stacks, off-shore structures in high seas, twin-conductor transmission lines, heat-exchanger tubes can be mentioned among others. Zdravkovich [1] critically reviewed investigations in this category up to early half of 1977. He noted that one of the most neglected features of the interference flow was, and still is, the measurements of vortex shedding from two cylinders in staggered arrangement. Available data to Zdravkovich [1], and also to the authors, were those measured by Hori [2] and Ishigai, et al., [3] in the immediate subcritical Reynolds-number range. These data, however, covered only a narrow range of the staggered arrangement, thus showing that further experiments should be performed to establish the vortex-shedding characteristics of two circular cylinders in staggered arrangement.

The present paper describes the results of an experimental investigation which was made to clarify the frequency of vortex shedding from two circular cylinders of the same diameter for a rather wide range of staggered arrangement. The major part of the investigation was carried out at a Reynolds number of 1.58×10^4 and this is within the range where the flow around a circular cylinder is relatively insensitive to Reynolds-number changes. Although this Reynolds number may be lower than that relevant to practical situations mentioned above, the present experiment can clarify some of the fundamental nature of the interference between two cylinders in a uniform stream.

2 Experimental Apparatus

The experiment was conducted in a wind tunnel of the open-return type with a test section 0.2 m high, 0.4 m wide, and 1.0 m long. The roof of the tunnel was made of a acrylicresin sheet 0.3 cm thick which could be shaped from outside of the tunnel to yield zero pressure gradient in the streamwise direction. Two brass cylinders of diameter 0.955 cm spanned the wind tunnel vertically, thus having a length-to-radius ratio of 20.9. The center of a pair of the two cylinders was located at the position 0.3 m downstream of the entrance of the test section, where the time-averaged velocity was uniform to the accuracy of 98 percent except the boundary layers along the walls. The thickness of the boundary layers was less than 2 cm. The time-averaged velocity distribution was detected by the traverse of a Pitot-static tube and the resulting dynamic pressure was read on a Betz manometer. The freestream turbulence level measured at this position by a constant-temperature hot-wire anemometer was about 0.8 percent at the velocity of 24.5 m/s, which was the velocity employed in the present experiment.

The two cylinders were mounted on an acrylicresin turn table of diameter 8 cm which was made flush with the floor of the tunnel. Since the center of the rotation of the turn table was made to coincide with the center of a pair of the two cylinders (see Fig. 1), the rotation of the turn table could produce a rather wide range of staggered arrangement with the distance between the cylinders changed systematically. The distance (denoted by δd) was varied in the range from $1.0d$ to $5.5d$, d being the diameter of the cylinders. A definition sketch of two cylinders in a stream is shown in Fig. 1. An acrylicresin distance piece 0.2 cm thick was screwed onto the top of the cylinders to ensure a required distance between them. The uncertainty in the distance was determined to be 0.02 cm at most by direct measurement along their span by means of a dial gauge. Moreover, the angle α (see Fig. 1) was changed from 0 to 180 deg with the interval of 15 deg, the uncertainty in α being negligible.

The frequency of vortex shedding from the cylinders was determined on the basis of the velocity fluctuation in the wake of each cylinder, which was detected by a constant-temperature hot-wire anemometer. The hot-wire probe was mounted on a traversing mechanism outside the tunnel test section through carefully sealed slits in one of the vertical side

Contributed by the Fluids Engineering Division for publication in the JOURNAL OF FLUIDS ENGINEERING. Manuscript received by the Fluids Engineeing Division, May 16, 1979.

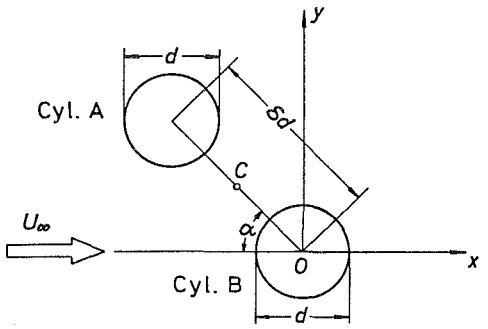

Fig. 1 Definition sketch. *C* denotes the center of turn table onto which the pair of two cylinders are mounted.

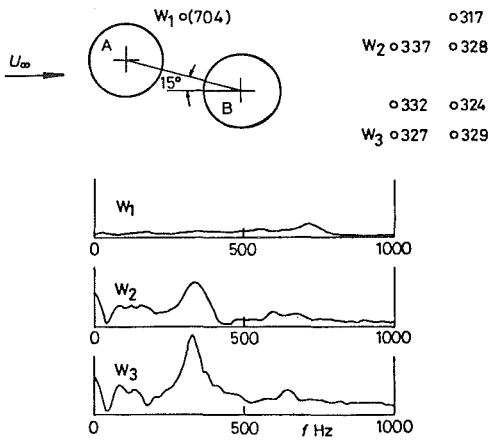

Fig. 2 Vortex-shedding frequency and power spectra of fluctuating velocity at several locations downstream of two circular cylinders. The vertical scale of the spectra is linear arbitrary scale. Numbers imply the vortex-shedding frequency in Hz. Number in the parentheses indicates the frequency at which the spectrum peak is low and broad. α = 15 deg, δ = 2.0, U_∞ = 24.5 m/s, d = 0.955 cm, Re = 1.58 × 10^4.

walls. The detection of the velocity fluctuation was made in the mid-span plane on both sides of the wake of each cylinder and a few diameters downstream of their center. Since one is mainly interested in the frequency of fluctuating forces acting on the cylinders owing to the periodic vortex shedding from them, the velocity fluctuation should be detected as near as possible to the cylinders. The frequency of the velocity fluctuation corresponding to the periodic vortex shedding was determined by processing the hot-wire signal by means of SAICOR 42A correlator and SAICOR 472 Fourier transformer.

The positions where the vortex-shedding frequency was measured are illustrated in Figs. 2–4 for the cases of α = 15, 45, and 75 deg, with the nondimensional distance between the cylinders being maintained to be δ = 2.0. It should be noted that the cylinder *B* (see Fig. 1) is equivalent to the cylinder *A* for which the angle α is read as 180 deg - α. Sketches of power spectrum of fluctuating velocity at a few positions, and the vortex shedding frequencies determined therefrom, are also

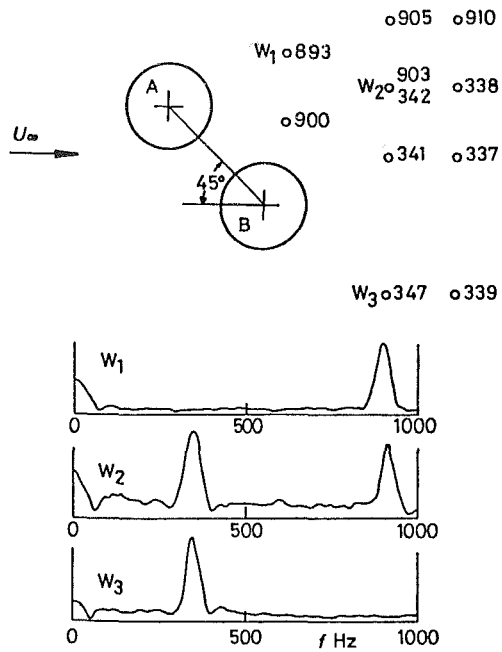

Fig. 3 Vortex-shedding frequency and power spectra of fluctuating velocity at several locations downstream of two circular cylinders. α = 45 deg. The values of other parameters are the same as in Fig. 2. For further informations, see the caption of Fig. 2.

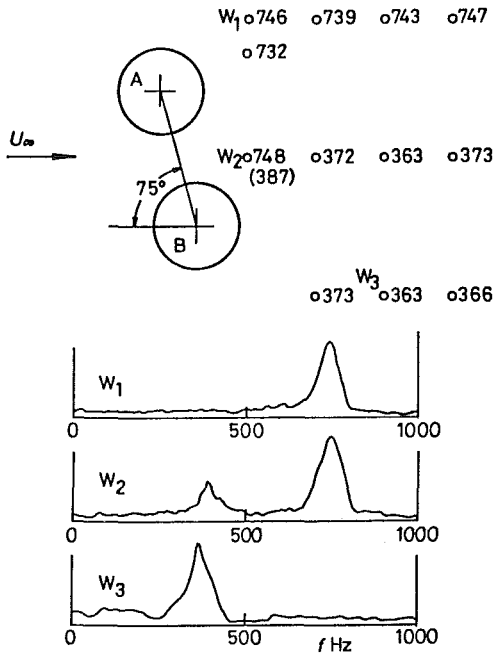

Fig. 4 Vortex-shedding frequency and power spectra of fluctuating velocity at several locations downstream of two circular cylinders. α = 75 deg, The values of other parameters are the same as in Fig. 2. For further informations, see the caption of Fig. 2.

Nomenclature

d = diameter of cylinders
f = frequency of vortex shedding
Re = Reynolds number = $U_\infty d/\nu$
St = Strouhal number = fd/U_∞
U_∞ = free-stream velocity
x, y = Cartesian coordinate system (see Fig. 1)
α = angle between free-stream direction and a plane including axes of two cylinders
δ = distance between the center of two cylinders nondimensionalized by diameter of cylinders
ν = kinematic viscosity of fluid

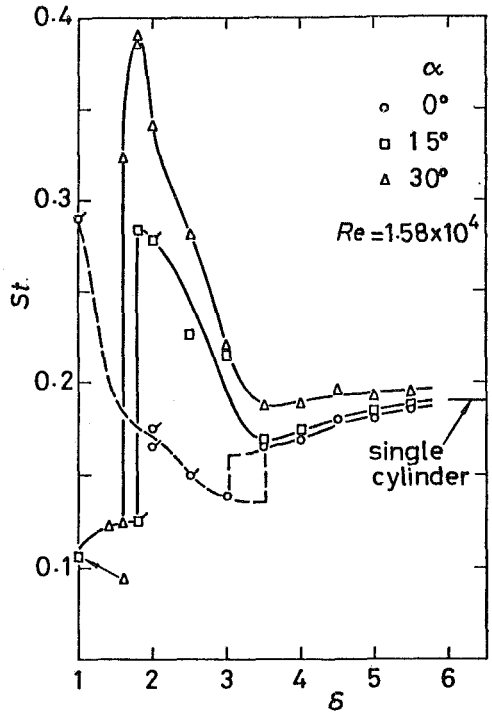

Fig. 5 Strouhal number plotted against the nondimensional distance δ. The uncertainty in St is ± 0.007 and that in δ is ± 0.02. α = 0, 15, and 30 deg. Re = 1.58×10^4. Possible range of the critical spacing for which the shear layers separated from the upstream cylinder reattach to the downstream cylinder is expressed by a rectangle enclosed by broken lines. The curve for α = 0 deg is shown by a broken line in the range $1.0 < \delta < 3.0$ in order to emphasize the weak velocity fluctuations.

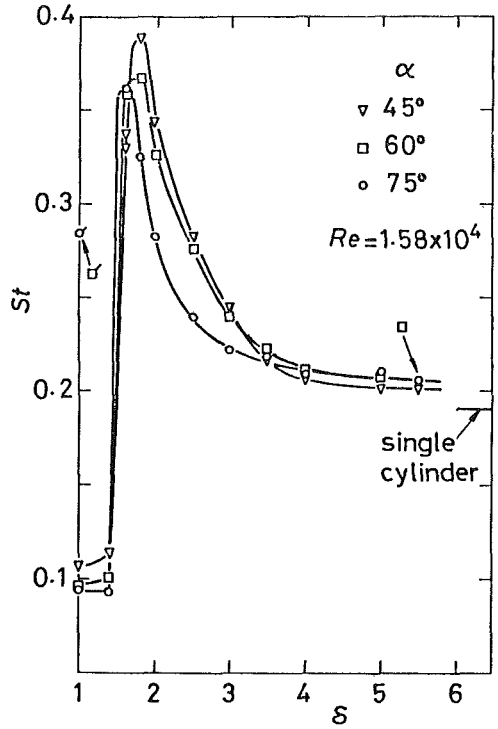

Fig. 6 Strouhal number plotted against the nondimensional distance δ. α = 45, 60, and 75 deg. For further informations, see the caption of Fig. 5.

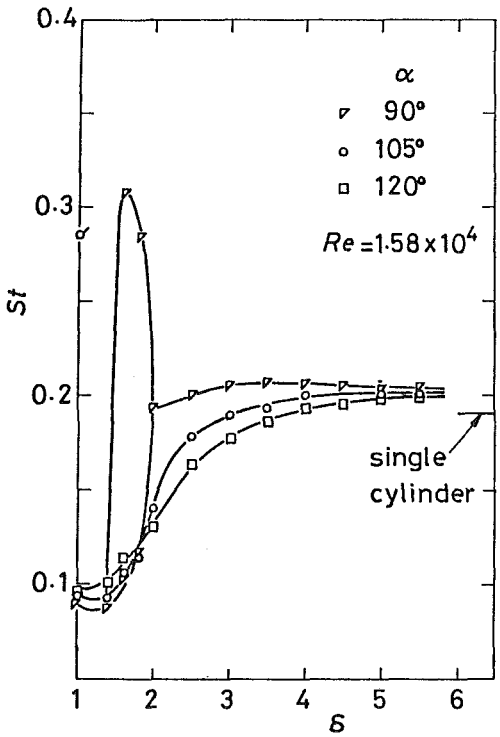

Fig. 7 Strouhal number plotted against the nondimensional distance δ. α = 90, 105, and 120 deg. For further informations, see the caption of Fig. 5.

included in Figs. 2–4. The spectrum labelled as W_1 in Fig. 2 shows that the energy of fluctuating velocity is generally low and the strength of vortices shed with the frequency f = 704 Hz, where the spectrum shows a low and broad maximum, is very weak. Moreover, the spectra labelled as W_2 in Figs. 3 and 4 will provide examples in which two-vortex shedding frequencies exist simultaneously. One of the two frequencies corresponds to the vortex shedding from a particular cylinder and the other frequency to that from another cylinder.

Finally, a single cylinder occupied 2.4 percent of the area of the tunnel test section and, according to the blockage correction method of Maskell [4], the corrected value of the Strouhal number would be almost 1.4 percent lower than that measured on the basis of the effective increment in the dynamic pressure of the undisturbed stream. With the two cylinders in the tunnel, at certain arrangement of them, marked interference of their wakes was found and it was not thought possible to correct accurately for the effects of blockage. Therefore the results are presented uncorrected.

3 Results and Discussion

For the purpose of simplicity, the description of the experimental results will be made with reference to Fig. 1, in which the cylinder B is tentatively assumed to be fixed, and thus the two parameters α and δ suffice to determine the arrangement of the two cylinders. Tandem arrangement occurs when α = 0 and 180 deg while the side-by-side arrangement corresponds to α = 90 and 270 deg. All other values of α represent staggered arrangement. In view of the geometrical symmetry, the experiment was performed in the range α = 0 deg ~ 180 deg. Moreover, it may be noted that the cylinder A is an upstream cylinder for 0 deg $< \alpha <$ 90 deg while it becomes a downstream cylinder for 90 $< \alpha <$ 180 deg.

The Strouhal number St of vortex shedding from the cylinder A is summarized in Figs. 5–8 as a function of the nondimensional separation δ for each angular position α.

3.1 Tandem Arrangement (α = 0 and 180 deg). There is no distinct vortex shedding detectable behind the upstream

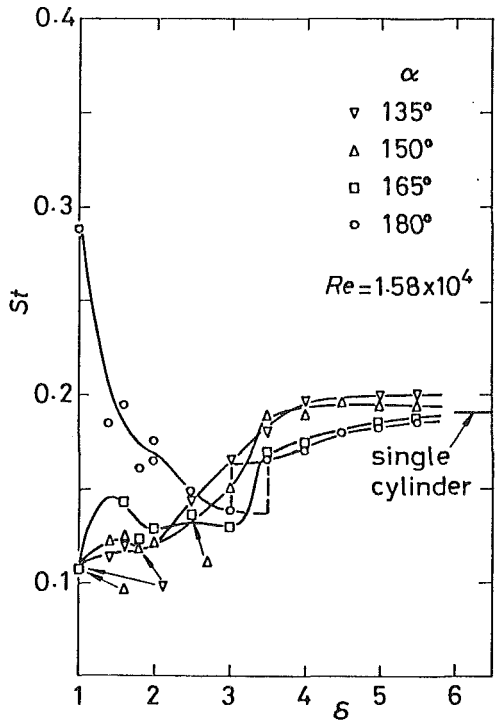

Fig. 8 Strouhal number plotted against the nondimensional distance δ. α = 135, 150, 165, and 180 deg. For further informations, see the caption of Fig. 5.

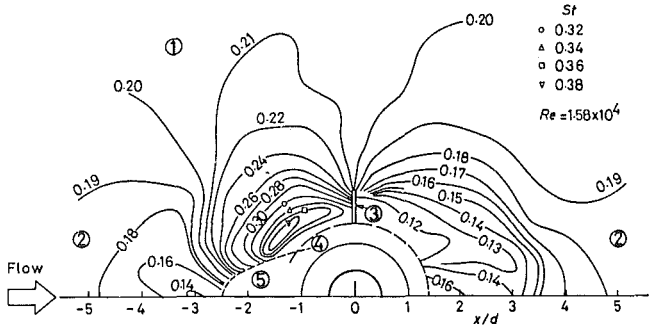

Fig. 9 Interference Strouhal number for all arrangements. Re = 1.58 × 10^4. The uncertainties in abscissa and ordinate are ±0.4 for $\delta > 3.0$ and ±0.2 for $\delta < 3.0$. The curves corresponding to St = 0.19 are taken as the boundaries between regions ① and ②. The boundary between regions ④ and ⑤ is not clear in the present experiment.

cylinder (α = 0 deg) up to δ = 3.0, as will be seen in Fig. 5. The flagged data points plotted in the range $1 \leqq \delta \leqq 3.0$ indicate the frequency at which a low and broad spectrum peak appears in the same manner as the spectrum labelled as W_1 in Fig. 2. No distinct vortices were found, however, in the photographs of flow taken by Ishigai et al., [3] when $\delta < 3.0$. The weak spectrum peaks should thus be considered as the result of a velocity fluctuation induced behind the upstream cylinder by the periodic vortex shedding from the downstream cylinder. This supposition is supported by the fact that the Strouhal numbers corresponding to the weak spectrum peaks are in good agreement with those for the downstream cylinder (α = 180 deg), see Figs. 5 and 8. Even in the case of δ = 1.0, where the cylinders are in contact, a rather distinct spectrum peak is observed in the immediate downstream of the shoulder of the upstream cylinder.

Beyond the spacing $\delta \simeq 3.0$, the vortex shedding suddenly becomes distinct and its frequency soon reaches the value found behind the single cylinder. This feature can be interpreted by the fact that, for spacings less than $\delta \simeq 3.0$, the shear layers which separate from the upstream cylinder reattach to the downstream one and this inhibits the vortex shedding from the upstream cylinder. Ishigai, et al., [3] observed, at the Reynolds number of 8000, that this critical spacing is $\delta \simeq 3.8$ and a sudden jump of the Strouhal number occurs at that spacing. The data taken by Okajima [5] at transcritical Reynolds numbers show that the critical spacing is also $\delta \simeq 3.8$. In the present experiment, the critical spacing is thought to exist in the range $3.0 \leqq \delta \leqq 3.5$, see Fig. 5.
Fig.5.

As seen in Fig. 8, the vortex shedding was detected in the whole range of spacings behind the downstream cylinder. Its Strouhal number continuously decreases in the range $1.0 \leqq \delta \leqq 3.0$ from a value (0.288) well above the Strouhal number for a single cylinder down to values well below it. The scatter of data in the range $1.4 \leqq \delta \leqq 2.0$ should be attributed to experimental errors because the errors are estimated to be ±0.007 for St. Beyond $\delta \simeq 3.0$ up to a spacing of $\delta \simeq 6.0$, the Strouhal number seems to continuously increase. According to the data shown in Fig. 6 of Zdravkovich [1], the Strouhal number which has approached the value found for a single cylinder will decrease again beyond $\delta \simeq 8.0$.

The same figure of Zdravkovich [1] shows that a sudden jump of the Strouhal number for the downstream cylinder occurs at the critical spacing beyond which the shear layers separated from the upstream cylinder begin to interact each other to produce a periodic vortex shedding. Thus commencement of the vortex shedding behind the upstream cylinder strongly affects and synchronizes the vortex shedding from the downstream cylinder. As will be seen in Fig. 8, the jump of the Strouhal number seems to exist also in the present experiment. As mentioned previously, it can only be said that the critical spacing exists in the range $3.0 \leqq \delta \leqq 3.5$, owing to the absence of data within this range of δ. This situation is shown in Figs. 5 and 8 by a rectangle enclosed by the broken lines. Moreover the St ~ δ curve for α = 0 deg (see Fig. 5) is also shown by a broken line in the range $1.0 \leqq \delta \leqq 3.0$ in order to emphasize the weak velocity fluctuation there.

3.2 Side-By-Side Arrangement (α = 90 deg). This case has been treated by a number of investigators, Spivack [6], Hori [2], Bearman and Wadcock [7], Ishigai, et al., [3], Quadflieg [8], among others. The most prominent feature in this arrangement is bistable nature of vortex shedding from both cylinders: for transverse spacings less than 2*d*, two different frequencies are recorded in both wakes as shown in Fig. 7. The upper frequency disappears for spacings less than about 1.4*d* and only the lower one continues down to the cylinders in contact. It is now well established that, when the nondimensional spacings exist in the range $1.4 < \delta < 2.0$, the gap flow between the cylinders is biased to one side. Consequently, wide and narrow wakes are formed behind the cylinders, the wider wake corresponding to lower frequency of vortex sheddig while the narrower wake to higher frequency. The biased flow in the gap is bistable and intermittently changes over downwards and upwards, thus producing the branching of the St ~ δ curve in the range $1.4 < \delta < 2.0$. When δ is less than 1.4, the gap flow between the cylinders becomes very weak and as a result the pair of the cylinders behaves as a single body. The result is a single frequency of vortex shedding, which is approximately a half of the frequency for the single circular cylinder. For all transverse spacings greater than 2*d*, there exists a single frequency in both wakes which, when reduced to the Strouhal number, is approximately the same as for the single cylinder.

3.3 Staggered Arrangement. First of all, consider the case of 0 deg < α < 90 deg in which the cylinder *A* behaves as an upstream cylinder (see Figs. 5 and 6). Since, in this configuration of the cylinders, the gap flow is always biased to

the side of the cylinder A, the width of the wake immediately behind the cylinder A becomes much smaller than that behind the cylinder B. Actual occurrence of this flow pattern is well demonstrated by a flow-visualization technique, see Ishigai, et al., [3]. The biased gap flow thus yields a frequency of vortex shedding from the cylinder A much higher than that from the cylinder B. The Strouhal number of the cylinder A seems to attain a maximum value of about 0.39 at $\delta \simeq 1.8$ in the range $\alpha = 30$ deg $\sim$ 45 deg to the extent of the present experiment. In view of the biased gap flow described just above, this fact suggests that a maximum deflection of the gap flow, which may imply the narrowest wake behind the cylinder A, occurs for this particular configuration of the two cylinders.

At a certain critical spacing, which is somewhere in the neighborhood of $1.5d$ and slightly depends on the angle α, the Strouhal number suddenly drops down to values of about 0.1. For spacings less than critical, the gap flow becomes very weak so that the pair of the cylinders behaves as if it were a single body. Beyond the spacing corresponding to the maximum Strouhal number, the Strouhal number decreases rather rapidly in a monotonic way to the value of the single cylinder, for the angle of $\alpha = 45$ deg $\sim$ 75 deg. However, for smaller angles (see Fig. 5), the Strouhal number seems to approach the value found for the single cylinder after passing a minimum value, as the nondimensional distance δ increases. It may be noted that the St $\sim \delta$ curve for $\alpha = 15$ deg is almost identical to that for $\alpha = 0$ (tandem arrangement) in the range $\delta \geqq 3.0$.

As soon as the cylinder A becomes the downstream cylinder, i.e., 90 deg $< \alpha <$ 180 deg, its Strouhal number becomes lower than that of the single cylinder, see Figs. 7 and 8. Distinct vortex shedding always exists behind the cylinder A in this arrangement. Different behavior of the St $\sim \delta$ curves for $\alpha = 165$ and 180 deg in the range $\delta \leqq 3.0$ again indicates a rather large change in the flow pattern accompanied by a rather small change in the geometrical configuration: the Strouhal number increases with decreasing δ for $\alpha = 180$ deg while that for $\alpha = 165$ deg remains substantially constant. For spacings larger than $3.0d$, the St $\sim \delta$ curves for the two angles are almost coincident. The different behavior of the St $\sim \delta$ curves in the region $\delta < 3.0$ should be attributed to whether or not the gap flow is significant.

Finally, it may be noted that, as far as the present experiment is concerned, the bistable vortex shedding was observed only in the case of $\alpha = 90$ deg. Hence the bistable side-by-side arrangement represents a transition from the upstream and the downstream stagger.

3.4 Interference Strouhal Number for All Arrangements. The experimental results described above are summarized in a single figure, i.e., Fig. 9, in which the curves of constant Strouhal numbers are drawn by linear interpolation between the measured values of the Strouhal number. All possible arrangements of the two cylinders can be classified into several regions by taking into account whether the Strouhal number is greater or less than that for the single cylinder, whether or not the vortex shedding occurs from the cylinder A, etc. The cylinder A can be situated in the following five regions:

(1) Region where the Strouhal number is higher than that for the single cylinder.

(2) Region where the Strouhal number is less than that for the single cylinder.

(3) Region where the bistable vortex shedding occurs.

(4) Region where the pair of the cylinders behaves as a single body with regard to the vortex shedding.

(5) Region where weak or no vortex shedding occurs.

In Fig. 9, these regions are denoted by ①, ②, ③, ④ and ⑤ respectively. The boundary between regions ① and ② is taken as the lines corresponding to St = 0.19 because values of the Strouhal number between 0.18 and 0.20 are recognized as typical at the Reynolds number Re = 1.58×10^4 of the present experiment. Region ④ is a concentric one between $\delta = 1.0$ and 1.4 in which the Strouhal number for the cylinder A is about 0.12 for 0 deg $< \alpha \leqq 45$ deg and 135 deg $\leqq \alpha <$ 180 deg and about 0.09 for 60 deg $\leqq \alpha \leqq 120$ deg, as seen in Figs. 5–8. To the extent of the present experiment, it is difficult to draw lines of constant Strouhal number in region ④ because of very complex nature of the distribution of the data points there.

One of the prominent features of Fig. 9 is that an island of high Strouhal number exists in front of the cylinder B. Very narrow region ③ of the bistable vortex shedding sharply separates regions ① and ②. The width of that region was not determined by the present experiment. Accordingly, when the pair of the cylinders takes arrangements in the vicinity of the bistable vortex shedding, very small change in the direction of the oncoming stream can bring about large change in the frequency of vortex shedding from the cylinders, thus producing complex fluctuating forces induced by the vortex shedding. It may be noted that the boundary between regions ④ and ⑤ is not clear in the present experiment.

The curves compiled in Figs. 5–9 will probably be affected by the Reynolds number. It is hoped that the nature of vortex shedding from the cylinders in staggered arrangement will quantitatively clarified over a sufficiently wide range of the Reynolds number, especially in the supercritical regime.

4 Conclusions

The frequency of vortex shedding from two circular cylinders of the same diameter in staggered arrangement has experimentally been investigated at a Reynolds number 1.58×10^4. The results are summarized in several figures from which one can obtain the Strouhal number of vortex shedding for all arrangements within distances between their centers less than 5 diameters. The results of the present investigation may be summarized as follows:

1 When the distances between the cylinders are less than about 1.4 diameters, the pair of the cylinders behaves as a single body with regard to the vortex shedding.

2 The bistable side-by-side arrangement represents a transition from the upstream to the downstream stagger with regard to one of the two cylinders. This transition brings about a large change in the Strouhal number for the cylinder.

3 There exists an islandlike region in which the Strouhal number for the upstream cylinder is much higher than that for the single cylinder.

4 The Strouhal number for the downstream cylinder is generally lower than that for the single cylinder except the case where the distance between the cylinders is less than about $1.4d$ in tandem arrangement.

5 The gap flow between the cylinders is biased to the side of the upstream cylinder, thus forming a much narrower wake behind the upstream cylinder than that behind the downstream cylinder. Narrower wakes corrspond to higher Strouhal number and wider wakes to lower Strouhal number.

Acknowledgments

The present work was supported by Grant-in-Aid for Scientific Research from the Ministry of Education, Science and Culture (Japan). The authors are indebted to Mr. T. Yamazaki and Mr. T. Sampo for their skillful assistance in the construction of the experimental apparatus, and to Dr. Y. Suzuki for the discussion on the experimental results.

References

1 Zdravkovich, M. M., "Review of Flow Interference Between Two Circular Cylinders in Various Arrangements," ASME JOURNAL OF FLUIDS ENGINEERING, Vol. 99, No. 4, 1977, pp. 618–633.

2 Hori, E., "Experiments on Flow Around a Pair of Parallel Circular Cylinders," *Proc. 9th Japan National Congress for Applied Mech.*, Tokyo, 1959, pp. 231–234.

3 Ishigai, S., Nishikawa, E., Nishimura, K., and Cho, K., "Experimental Study of Structure of Gas Flow in Tube Banks with Tube Axes Normal to Flow (Part 1, Kármán Vortex Flow Around Two Tubes at Various Spacings)," *Bulletin of the Japan Society of Mechanical Engineers,* Vol. 15, No. 86, 1972, pp. 949–956.

4 Maskell, E. C., "A Theory of the Blockage Effects on Bluff Bodies and Stalled Wings in a Closed Wind Tunnel," Aeronautical Research Council Reports and Memoranda, No. 3400, 1965.

5 Okajima, A., "Flow Around Two Tandem Circular Cylinders at Very High Reynolds Numbers," *Bulletin of the Japan Society of Mechanical Engineers,* Vol. 22, No. 166, 1974, pp. 504–511.

6 Spivack, H. M., "Vortex Frequency and Flow Pattern in the Wake of Two Parallel Cylinders at Varied Spacings Normal to an Air Stream," *Journal of Aeronautical Sciences,* Vol. 13, 1946, pp. 289–297.

7 Bearman, P. W., and Wadcock, A. J., "The Interaction Between a Pair of Circular Cylinders Normal to a Stream," *Journal of Fluid Mechanics,* Vol. 61, Part 3, 1973, pp. 499–511.

8 Quadflieg, H., "Wirbelinduzierte Belastungen eines Zylinderpaares in inkompressibler Strömung bei grossen Reynoldszahlen," *Forsch. Ing.-Wes.*, Vol. 43, No. 1, 1977, pp. 9–18.

References

1 Zdravkovich, M. M., "Review of Flow Interference Between Two Circular Cylinders in Various Arrangements," ASME JOURNAL OF FLUIDS ENGINEERING, Vol. 99, No. 4, 1977, pp. 618-633.

2 Hori, E., "Experiments on Flow Around a Pair of Parallel Circular Cylinders," *Proc. 9th Japan National Congress for Applied Mech.*, Tokyo, 1959, pp. 231-234.

3 Ishigai, S., Nishikawa, E., Nishimura, K., and Cho, K., "Experimental Study of Structure of Gas Flow in Tube Banks with Tube Axes Normal to Flow (Part 1, Kármán Vortex Flow Around Two Tubes at Various Spacings)," *Bulletin of the Japan Society of Mechanical Engineers*, Vol. 15, No. 86, 1972, pp. 949-956.

4 Maskell, E. C., "A Theory of the Blockage Effects on Bluff Bodies and Stalled Wings in a Closed Wind Tunnel," Aeronautical Research Council Reports and Memoranda, No. 3400, 1965.

5 Okajima, A., "Flow Around Two Tandem Circular Cylinders at Very High Reynolds Numbers," *Bulletin of the Japan Society of Mechanical Engineers*, Vol. 22, No. 166, 1974, pp. 504-511.

6 Spivack, H. M., "Vortex Frequency and Flow Pattern in the Wake of Two Parallel Cylinders at Varied Spacings Normal to an Air Stream," *Journal of Aeronautical Sciences*, Vol. 13, 1946, pp. 289-297.

7 Bearman, P. W., and Wadcock, A. J., "The Interaction Between a Pair of Circular Cylinders Normal to a Stream," *Journal of Fluid Mechanics*, Vol. 61, Part 3, 1973, pp. 499-511.

8 Quadflieg, H., "Wirbelinduzierte Belastungen eines Zylinderpaares in inkompressibler Strömung bei grossen Reynoldszahlen," *Forsch. Ing.-Wes.*, Vol. 43, No. 1, 1977, pp. 9-18.

DISCUSSION

M. M. Zdravkovich[1]

The Sapporo's school of Fluid Mechanics founded by Professor Arie is to be congratulated for the new measurements that are particularly useful and timely in confirming and advancing our understanding of the flow interference caused by two cylinders in cross flow. Series of 'unexpected discontinuities' as I called them some years ago [9] reappeared so convincingly in the Sapporo's paper, that they may be called the expected discontinuities in Strouhal number values.

The extensive measurements carried out by the authors covered systematically all in-line, side-by-side and staggered arrangements from the two cylinders being in contact up to five diameters apart at an intermediate subcritical Reynolds number. The latter was correctly chosen to be sufficiently low in order to avoid a transitional regime for the downstream cylinder by the turbulent wake of the upstream one. The Strouhal number, which is known to be almost magically constant throughout the subcritical range of Reynolds numbers for the single cylinder, appeared strongly affected by the interference between the two cylinders and their wakes. The authors found that the Strouhal number varied from being as low as 0.08 to as high as 0.38. The previous measurements by Ishigai et al., at Re = 8×10^3 quoted as reference [3] by the authors, reported that the increase of the Strouhal number was above 0.8 for some close arrangements. The comment by the authors on possible reasons for such a drastic increase will be valuable.

The authors proposed a classification of Strouhal number regions for all tested arrangements of two cylinders. Such a plot as given in Fig. 9 has a great value for practical applicatons. The bistable side-by-side arrangements are clearly shown as a boundary between high and low Strouhal numbers. The change of flow pattern at the critical spacing in tandem arrangement, which had had even more drastic effect on the Strouhal number, was not shown in Fig. 9. The discontinuous jumps of the Strouhal number appeared beyond any shade of doubt in Figs. 5 and 6. They occurred when the upstream cylinder was sufficiently near to the downstream one so that the intense gap flow ceased. This discontinuity did not occur, however, when the downstream cylinder approached the upstream one as clearly evident in Figs. 7 and 8 except for α = 90, 180 and possibly 165 deg. These two distinct features of the interference between the two cylinders were concealed in Fig. 9 within regions 4 and 5.

An attempt to show these discontinuities by using the data measured by the authors is shown in Fig. 10. When the upstream cylinder approaches the downstream one in the tandem arrangement, the vortex shedding ceases behind the former and a discontinuous drop occurs on the latter. The

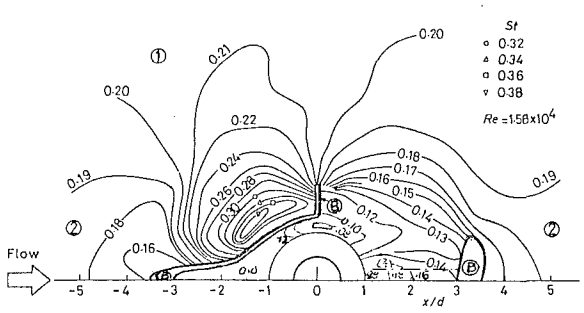

Fig. 10

authors put forward a right argument that a weak and wide band peak found in the spectrum was caused by the vortex shedding behind the downstream cylinder. This argument can be extended further and the tandem arrangement could be taken as a "single body," which appears more streamlined, when the cylinders are nearer to one another until finally they really become the single body when they are in contact. The result is a narrow wake and the Strouhal number reaching 0.28, as seen in Fig. 8. Hence, it appears that physically there is only one region bounded by a discontinuity denoted by a double line to indicate the bistable behavior. The boundary extends over upstream staggered arrangements and presumably reaches the bistable side-by-side discontinuity.

The discontinuities in the Strouhal number were not found at α = 105, 120, 135 and 150 deg according to Figs. 7 and 8. Hence it may be expected that low Strouhal number region extends up to the δ = 1. There is a jump for α = 165 and 180 deg around $3 < \delta < 3.5$ and this is depicted in Fig. 10 as a closed bistable region B within which a jump in Strouhal number may occur from 0.14 to 0.16.

The chain-dotted line represents the position of the downstream cylinder producing maximum lift coefficient at Re = 6.1×10^4 (see reference [1] given by the authors). It was found (1) that the gap flow ceased suddenly below that line and it is not known how this will affect vortex shedding. The frequency measured by the authors was only along α = 165 and 180 and hence the lines drawn in Fig. 10 are conjectural and denoted with (?).

I will be grateful to the authors for their comments on my reinterpretation of their classification, which I took the liberty to do without having the numerical values of the Strouhal numbers.

Additional Reference

9 M. M. Zdravkovich and D. L. Pridden, "Interference Between Two Circular Cylinders; Series of Unexpected Discontinuities," *J. of Industrial Aerodynamics*, Vol. 2, 1977, pp 255-270.

[1] College of Engineering, University of Salford, Salford, U.K.

SEIKAN ISHIGAI[2] and EIICHI NISHIKAWA.[3] The authors are to be congratulated for their measurements with precisely defined cylinder locations whose slight errors have serious effects on the corresponding Strouhal numbers. Previous works by the discussers employed mildly heated cylinders for the purpose of visualizing the flow. The authors' paper expands the Reynolds number to 1.58×10^4 and the flow field is strictly isothermal. The discussers are glad to see that our previous results are substantially reconfirmed. We would like to know the authors' opinion on the following four points:

1. The experimental result on the tandem arrangement as given in Fig. 5 seems to suggest that the Region (5) in Fig. 9 should be expanded to include $x/d = -3 \sim -3.5$. Please see also the point 3 on this discussion.

2. The highest Strouhal number obtained by the authors is 0.39 whereas still higher values were reported [10] by the discussers, for example, 0.61 for $\delta = 1.21$ and $\alpha = 56$ deg. This point is in the Region (4) in which the authors say that the pair of cylinders behaves as a single body with regard to the vortex shedding and consequently such a high Strouhal number reported by the discussers is impossible. However, our previous report [10] has a photograph Fig. 5-*g* which clearly indicates vortex sheddings at the point mentioned above. For such point as this, the wake, i.e., the vortex formation region, is extremely narrow, and, consequently, the vortex formation detection by means of velocity measurement would be very difficult unless the point of vortex existence is known beforehand. This is one reason why the discussers employed the flow visualization method first and then the velocity fluctuation measuring method for finding the Strouhal number at the predetermined points. It is felt that higher Strouhal numbers are to be found in some points whose δ and α are included in the Region (4) of the authors.

3. Figs. (*c*) and (*g*) in Fig. 5 of the paper [10] by discussers indicate that in some cases, the wake of the ahead cylinder A is certainly absorbed by the free shear layer of the rear cylinder B, but the cylinder A does generate vortices. This fact is the basis of the discussers' opinion that the vortex generation is not a good criteria for determining the region in which the two cylinders behave as a single body.

The relation between the drag coefficient C_d and the vortex frequency has been the subject of many investigations, among which Bearman's report [11] seems to be the most reliable. Bearman's relation can serve as the criteria for determining the existence of the interaction of two tubes. The discussers propose to define three domains relative to the mutual interaction as follows:

I. The two cylinders can be treated as a single body if the total of the two C_d's and the Strouhal number of the Cylinder B satisfies the relation given by Bearman. (This region is equivalent to Region (4) and (5) of the authors.)

II. Other cases than I and II (Regions (4) and (5) by the authors.)

III. The two cylinders are mutually independent if each cylinder satisfies Bearman's relation.

The three domains are as given in Fig. 11 of the discussion. We agree with the authors on the subdivision of the Domain II.

4. The result [12] of our further study on more complicated cases of tube nests is reproduced in Fig. 12 of this discussion. The flow pattern map is divided into numerous fields.

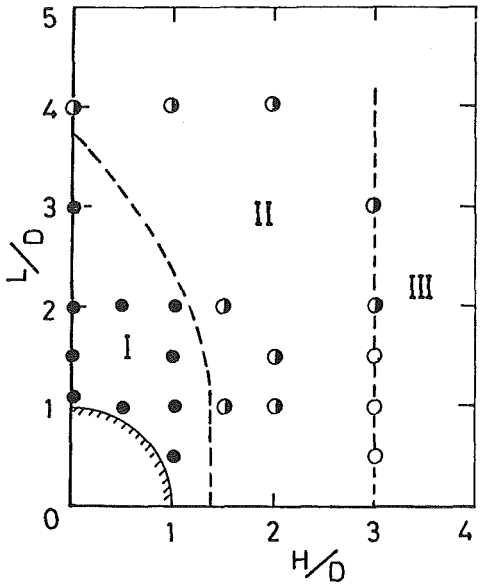

Fig. 11 Classification of the interference of tube pairs, I: Region where the tube pair behaves as a single body, II: Intermediate interference region; III: Region where each tube behaves as a single body

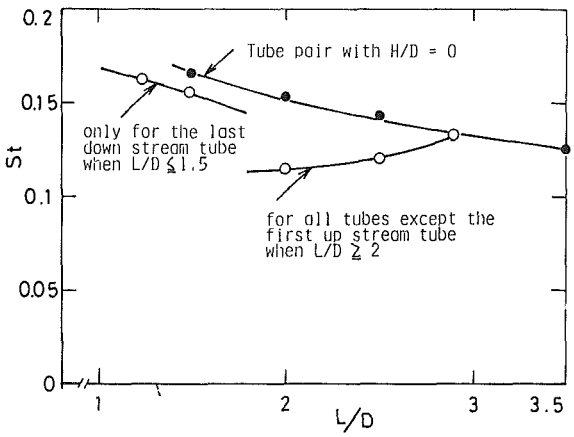

Fig. 12 Strouhal numbers plotted against *L/D* for single-column tube bank

However, all of them are the results of various combinations of flow patterns for two tubes. The authors' paper is therefore an important first step into the more complicated cases of tube nests.

Additional References

10 Ishigai, S., Nishikawa, E., Nishimura, K., and Cho, K., "Experimental Study of Structure of Gas Flow in Tube Banks with Tube Axes Normal to Flow (Part 1, Karman Vortex Flow around Two Tubes at Various Spacings)," *Bulletin of the Japan Society of Mechanical Engineers,* Vol. 15, No. 86, 1972, pp. 949–956.

11 Bearman, P. W., "On Vortex Street Wakes," *Journal of Fluid Mechanics,* Vol. 28, 1967, pp. 625–641.

12 Ishigai, S., and Nishikawa, E., "Experimental Study of Structure of Gas Flow in Tube Banks with Tube Axes Normal to Flow (Part 2, On the Structure of Gas Flow in Single-Column, Single-Row, and Double-Row Tube Banks)," *Bulletin of the Japan Society of Mechanical Engineers,* Vol. 18, No. 119, 1975, pp. 528–535.

13 Ishigai, S., Nishikawa, E., and Yagi, E., "Structure of Gas Flow and Vibration in Tube Banks with Tube Axes Normal to Flow," International Symposium on Marine Engineering TOKYO '73, 1973, Paper No. 153.

14 Nishikawa, E. and Ishigai, S., "Structure and Pressure Drop of Gas Flow in Tube Banks with Tube Axes Normal to Flow," *Transactions of the Japan Society of Mechanical Engineers,* Vol. 43, No. 373, pp. 3310–3319 (in Japanese).

[2]Professor, Department of Mechanical Engineering, Osaka University, Osaka, Japan.

[3]Associate Professor, Kobe University of Mercantile Marine, Kobe, Japan.

Authors' Closure

The authors are grateful to Dr. Zdravkovich and Professors Ishigai and Nishikawa for their thoughtful and valuable comments.

Dr. Zdravkovich's first comment is concerned with the rather large difference in the maximum Strouhal numbers measured by the authors and by Professor Ishigai et al. Since the same concern is also aroused by Professors Ishigai and Nishikawa in their discussion to the present paper, it will be considered later in the authors' discussion 2 to their comments.

The authors generally agree to Dr. Zdravkovich's reinterpretation of Strouhal number regions, which are shown in Fig. 10. Taking into account his comments, we have also modified Fig. 9 and the results are given in Fig. 13. Main differences between Figs. 10 and 13 are as follows:

(i) The bistable regions are denoted by ③ in Fig. 13 whereas they are designated as Ⓑ in Fig. 10.

(ii) In Fig. 13, the region ⑤ of no vortex shedding from the cylinder A is assumed to be a narrow region whose boundary is indicated by a dotted line. The dotted line is conceptual and hence denoted with the question mark (?). In order to exactly locate this boundary of region ⑤, detailed measurements of the Strouhal number should be performed in the range 0 deg $< \alpha <$ 15 deg.

(iii) Although Dr. Zdravkovich suggests some equi-St lines in region ④ of Fig. 9, the authors feel that it is very difficult to draw such lines in this region. Since the Strouhal number remains fairly constant (0.09 ~ 0.12) here, it may be more appropriate to define a single region ④, which is shown in Fig. 13 in a revised form.

(iv) The equi-St lines below the chain-dotted line of Fig. 10 are a little modified in Fig. 13 on the basis of the numerical data of the Strouhal number. The authors agree to Dr. Zdravkovich's suggestion that the chain-dotted line below which the gap flow suddenly ceases may also correspond to a boundary of sudden change in the Strouhal number of the downstream cylinder. However, its exact location cannot be determined from the present experiment in which no measurements were made in the range 165 deg $< \alpha <$ 180 deg.

The points raised by Professors Ishigai and Nishikawa are discussed as follows:

1. The discussers' conjecture is correct. The revised version of Fig. 9 is given in Fig. 13.

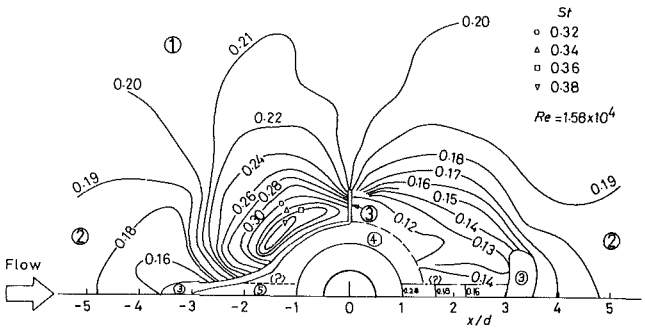

Fig. 13

2. In the present experiment, the measurement of the vortex-shedding frequency was made at every 15 degrees of α and was not detailed enough to clarify the nature of interaction of the two cylinders in close proximity. If much smaller intervals of α and δ were employed, the higher Strouhal number which is quoted by the discusser might have been detected. It may also be possible that the gap flow between the two cylinders in close proximity depends on the Reynolds number, which leads to different vortex formation region of the cylinder A and thus different Strouhal number.

3. The new criterion proposed by the discussers seems to be reasonable in itself. The authors are not sure about whether Figs. 5(c) and (g) of the discussers' reference [10] actually indicate definite vortex shedding from the cylinder A, although the discussers say that the vortex shedding does exist. To the authors' eyes, the two cylinders in these arrangements, especially Fig. 2(c) of reference [10], seem to behave as a little larger single body. The power spectrum peak of the velocity fluctuation associated with the vortex shedding of the cylinder A, if any, is supposed to be much less than that for the cylinder B. Accordingly, it may not necessarily be inappropriate to define a region in which the two cylinders behave as a single body with regard to the vortex shedding.

4. The authors agree to the discussers' opinion that the present paper yields an important first step to understand more complicated flows past tube nests.

Finally, the authors with Dr. Zdravkovich and Professors Ishigai and Nishikawa in that it is necessary to pursue the subject matter further, especially with detailed and careful experiments on the interaction of the two cylinders in close proximity.

Combined Simultaneous Flow Visualization/Hot-Wire Anemometry for the Study of Turbulent Flows

R. E. Falco
Department of Mechanical Engineering,
Michigan State University,
East Lansing, Mich. 48824

The measurement of coherent motions in turbulent and unsteady flows is discussed. A technique which discriminates these motions based upon the patterns they create by scattering light from a fog of tiny oil drops is described. It is shown that hot-wire anemometry can be used in this oil fog so that hot-wire data can be conditionally sampled to the visual patterns, giving directly interpretable measures of the importance of the selected features. The three-dimensionality of the coherent motions can also be directly accounted for, using mutually orthogonal sheets of light. Results of step flows, and zero and favorable pressure gradient flows are described.

Introduction

An important aspect of the study of nonsteady fluid dynamics is the class of flows which are describable by a set of averaged quantities which are steady, but whose flow fields are changing from instant to instant. Turbulent flows which are statistically steady constitute the largest class of such flows. Although the classical understanding of the fluctuations which occur in turbulent flows suggested that they should be thought of as part of a random process which could best be described by statistical formulations based on long time averages, thus ignoring the specific contributions of individual fluctuations, our current understanding suggests that there exist classes of coherent motions imbedded in the turbulent flow which may cause the important fluctuations, and that every attempt should be made to locate and characterize these structures. Following this stage, information about their formation and evolution is necessary.

Because these coherent motions are three-dimensional, appear to occur randomly, and will be in different stages of evolution when observed, the task of characterizing them is very difficult. But the primary problem has been the detection of their presence [1, 2, 3, 4]. Several techniques have been used to detect coherent motions, but the most successful has been the use of a passive marking contaminant. This technique depends upon the constant reformation of concentration gradients which are largely the result of the transport of marker free fluid into the marked fluid and vice versa. The mechanism which transports the marked fluid is often an identifiable coherent motion. Thus a technique which can determine instantaneous marker concentration should be able to detect the coherent motions. However, because the motions have a three-dimensional character, identification should be made, at the minimum, over a two-dimensional surface. Furthermore, if a coherent pattern in two dimensions can be observed to evolve, then the detection scheme can be said to have successfully identified a feature of interest. These criterion can be met by a marker whose patterns can be examined visually in selected planes throughout the flow field. Once located, the availability of an accurate quantitative measuring technique to record the structure of the motion is highly desirable. The technique of combining oil fog visualization and hot-wire anemometry embodies all of these features.

The paper first describes a new wind tunnel which allows continuous introduction of the marker. The tunnel represents an attempt to combine a flow visualization tunnel similar to the one designed by Dr. M. R. Head of Cambridge University, (in which several of the results to be presented were obtained) with the latest low turbulence wind tunnel design techniques, so as to allow high quality quantitative measurements to accompany visualization at both low and moderate speeds. A method of obtaining two sheets of light and photographing data seen within them is discussed next. Then the data acquisition system which allows simultaneous hot-wire information to be digitally recorded and synchronized with the motion pictures is discussed. This is followed by results showing the effects of operation of hot-wire anemometry in the oil fog marker. Having established the basic requirements of the technique, the immediate benefit of using a volume marking flow visualization technique using room lights is shown via example of the flow up a forward facing step. This is followed by a discussion of changes in turbulence structure in a nozzle type contraction where sheet lighting is essential. The purpose of examining these nonequilibrium flows is to show the immediate value of the technique for the study of complex engineering flows. Data on the three-dimensional aspects of coherent motions in equilibrium turbulent flows is then presented. This is followed by the results of experiments using combined flow visualization, hot-wire anemometry and marker detecting

Contributed by the Fluids Engineering Division for publication in the JOURNAL OF FLUIDS ENGINEERING. Manuscript received by the Fluids Engineering Division, July 11, 1978.

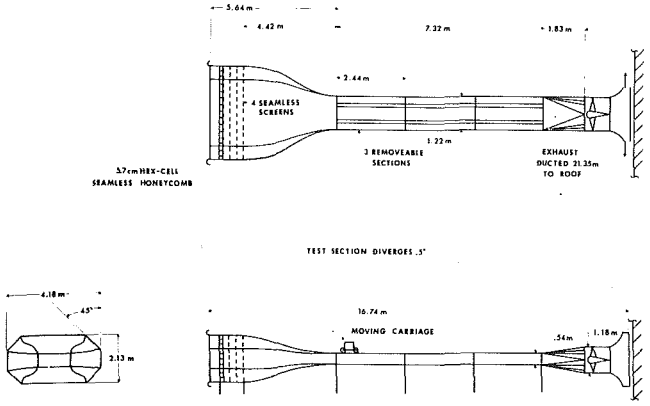

Fig. 1 Low turbulence boundary layer flow visualization tunnel capable of continuous use of oil fog marker

system which show the degree of coincidence between the marker and the edge of the turbulent boundary layer.

Experimental Apparatus

Wind Tunnel. A basic requirement of volume marking flow visualization techniques is the capability of continuously introducing the marker. Because it is desirable to have the marker fill a large part of the turbulent flow, the volume of contaminated air which must be removed is large. This removal is conveniently accomplished with an open return tunnel which exhausts to the atmosphere. The other requirements for the tunnel are similar to those of any other high quality wind tunnel, with the exception that it is desirable to operate at speeds as low as 0.4 m/s. Furthermore, because of the limitations of photographic techniques there is a need to achieve high Reynolds numbers by choosing as large a scale as possible, thus keeping the characteristic velocity as low as possible. Figure 1 shows the Michigan State University visualization tunnel. Air enters an octagonal entrance region, goes through a 4.8 mm Hex-cell seamless honeycomb, then through four seamless screens. The honeycomb/screen combination has been optimized following the suggestions of Loehrke and Nagib [5]. After passage through the screens a 13.6:1 contraction follows during which the geometry changes from octagonal to rectangular. The flow emerges into the 1.7 m by .75 m test section. The test section is 7.3 m long, and diverges slightly to maintain a constant pressure. Air and marker which are introduced in the test section then pass through a straight walled diffuser, through the axial fan, then through a second radial diffuser into a sealed room. Ducts lead from this room to the roof of the building where air is discharged into an unused air conditioning housing and eventually finds its way to the atmosphere.

The test section has a plexiglass top and side to permit lighting and photography. The top of each section is removable, permitting contractions for favorable pressure gradient studies or slots for adverse pressure gradient studies to be easily inserted. Rails along the top permit camera and light sources to follow the flow. A specially designed constant speed carriage drive will soon be added, allowing accurate estimates of the convection velocity of coherent motions to be obtained. The current arrangement allows speeds from .4 m/s to 8.8 m/s to be attained. Operation at even lower speeds is possible by inserting an additional honeycomb at the entrance to the working section. The free steam turbulence level is ≈ .14 percent at 7 m/s.

Marker and Lighting. The flow is made visible by introducing a fog of .5-5 μm oil droplets. The droplets are produced in a commercial "smoke generator" by forcing white mineral oil through capillary tubing which is heated. The oil vaporizes and is passed through a nozzle where it condenses into droplets. These are carburized and introduced into the flow. A suitable heat exchanger is used to cool the fog to ambient temperatures. Having filled the flow with marker, the user can choose the method of illumination. The marker is introduced into the flow through a row of holes which spans the tunnel width, using an overpressure small enough that the laminar boundary layer above the holes remains stable. The laminar boundary layer with the oil fog in the lower part was then tripped. The resulting turbulent boundary layer was almost completely filled with the oil fog. For many purposes use of a thin sheet of light which reveals a two-dimensional concentration map is appropriate. This is most easily achieved by spreading a laser beam over the field of interest using a cylindrical lens, scanners or rotating mirrors. It is not necessary to use a laser (see Fiedler and Head [6]), but the difficulty of achieving an intense, uniform, thin (≈ 2 mm) sheet with incandescent or flash discharge light sources is considerable. A 10 watt Argon-Ion laser is sufficient to photograph flows at 7 m/s.

Because turbulent flows are three-dimensional it is often necessary to know at what location through a coherent structure the light plane is slicing. A particularly important area of investigation, where three-dimensional information is needed, is the interaction between the wall region and the outer region of turbulent boundary layers, where information about the sub-layer spanwise structure must be correlated with outer layer structural information, which has been primarily studied in side views. For these purposes a crossed light sheet apparatus, which produces two mutually orthogonal sheets of light, is in general use in the facility. Simultaneous sheets are created by splitting the laser beam and routing the two resulting beams through beam spreaders, which are usually positioned so that mutually orthogonal sheets are created which intersect at some desired location within the flow field. Hot-wires are positioned in one or both light planes. Visual data from both light planes is recorded by a single camera. This requires directing the light via mirrors mounted outside the tunnel's plexiglass walls to the camera. Details of the split screen view are presented later.

Data Acquisition. Although visual information can by itself yield important information it is highly desirable to obtain detailed quantitative measurements of the coherent motions identified by the visual technique. This requires the

Nomenclature

E = volts
E_{RMS_s} = RMS voltage in oil fog
$E_{RMS_{NS}}$ = RMS voltage in clean air
$K = \frac{\nu}{U_\infty^2}\frac{dU_\infty}{dx}$
P = static pressure
R = resistance ratio
$R_{vv}(x,0,z,t)$ = space-time correlation of v
R_θ = momentum thickness
Reynolds number $= \frac{U_\infty \theta}{\nu}$
U_∞ = free stream velocity
u,v,w = instantaneous turbulent velocities in the x,y,z directions
u',v',w' = RMS values of u,v,w, respectively
x = coordinate along the wall
y = coordinate normal to the wall
z = spanwise coordinate
θ = momentum thickness
ν = kinematic viscosity

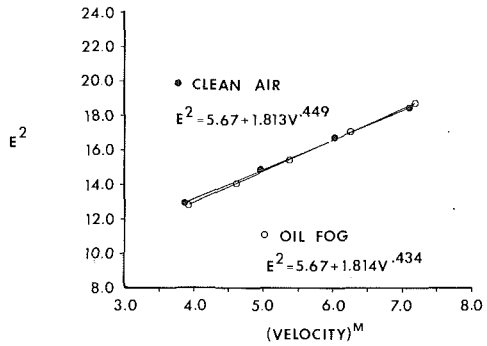

Fig. 2 Voltage velocity relations for wires operated in oil fog contaminated air and clean air. $R = 1.8$ in both cases

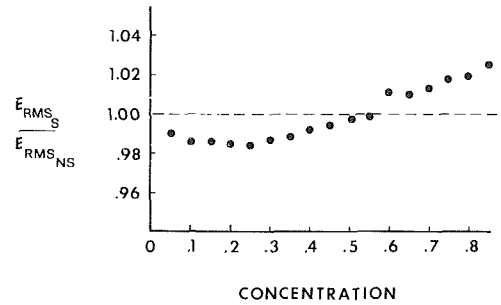

Fig. 3 The ratio of RMS voltage fluctuation due to the streamwise velocity component, in oil fog contaminated air, to that in clean air, versus concentration (arbitrary scale). $R = 1.8$, $U_\infty = 1.9$ m/s

simultaneous acquisition of visual and hot-wire anemometry data. An early method used by the author was to display the anemometry signals on a scope and photograph them while at the same time photographing the visual data using a split screen technique. However, this technique has the major disadvantage that the data must be digitized by hand, a slow and relatively inaccurate process. Furthermore, it was essentially confined to low speed experiments.

To overcome these deficiencies, we have designed and built a unique data acquisition system. A prerequisite for simultaneous acquisition of visual and hot-wire data is the ability to synchronize the two types of data. But an equally important factor is the necessity to store long records, which will have to be digitized at a high rate for high Reynolds number flows. Our constraint was the availability of a minicomputer with only 20K core storage. We desired to continuously store the signals from four hot-wire anemometers initially (and eight eventually), taken at $10kH_z$ for 10 s. This is the time required to expend 100 ft of film at 500 frames/s.

The need for long digital records results from the fact that the identification of coherent features in turbulent shear flows often requires inspection of hundreds of feet of shear layer thickness. This is not because they are rare events, but is due both to the three-dimensional nature of these features and to the additional randomness resulting from their finite lifetimes.

The system developed at MSU is capable of digitizing the signals from 4 wires at 20,000 Hz each or 8 wires at 10,000 Hz each with 12 bit resolution. These digitized data are continuously stored on a 23 million 16 bit word disk. Data which are simultaneously digitized from the hot-wire array are serially transferred from the A/D converter to a specially designed hard wire processor which has two parallel buffers. One of these is filled with data while data from the other are transferred to the disk. The need for the dual buffers arises because of the desire to continuously record the high rate data. They temporarily store data to avoid the gaps that would otherwise result from disk track change delays and rotational positioning times. Once the continuous record is stored on the disk, it is transferred in 8K blocks to a T1 960A minicomputer and stored on magnetic tape. These tapes are then processed on the MSU CYBER 750. A timing signal generated by the processor's clock is displayed across an LED array and photographed. The same signal is simultaneously transmitted to the disk. This allows future identification of stored signal data with the visual information.

Results

Effects of Oil Droplet Fog on Hot-Wire Operation. The capability of obtaining simultaneous flow visualization and hot-wire anemometry data depends upon the ability to use hot-wire anemometry in the oil fog environment. Since it is well known that dust can seriously affect hot-wire calibrations, trouble was expected when it was decided to try to operate a wire in an oil fog. The results of preliminary experiments indicated no change in calibrations at resistance ratio = 1.8 over a limited range of velocities. We have since performed careful experiments at several resistance ratios to determine the usable range of the technique. The results of calibrations in clean air and in smoke filled air at resistance ratios of 1.6, 1.8 and 2.0 showed that at all three resistance ratios the data taken in the oil fog can be fitted to the Collis and Williams [7] velocity-voltage relationship. We see from Fig. 2 that the effect of operation in the oil fog contaminated air is well within the experimental error of a three parameter least squares fit to the Collis and Williams relationship at $R = 1.8$. However, definite effects occur at both higher and lower resistance ratios. At $R = 2.0$ operation of the wire in smoke results in a decrease in sensitivity, with respect to its clean air response, while operation at $R = 1.6$ has the opposite effect. The opposite trends suggest a mechanism which involves the attainment of an "equilibrium" coating for certain oil properties and wire temperature. More detailed investigations are currently being performed to illuminate the mechanisms involved. One aspect of these investigations is the documentation of changes in the fluctuating response of the hot-wire anemometers. Figure 3 shows the ratio of RMS u (in contaminant)/RMS u (in clear air) versus relative concentration for $R = 1.8$. Over a wide range of concentrations, errors up to 4 percent occur. These results show that hot-wire anemometry can be operated in oil fog contaminated air. It should be noted that the relatively small loss in accuracy is less important in the study of coherent motions, where recording large fluctuations (which are often the order of 10-50 times the long time average) is the primary goal, than for the study of long time average statistics.

Examples of the Internal Coherency in Equilibrium and Nonequilibrium Flows. The plan of presentation of the flow data will be to indicate the importance of visual information, indicate how improved visual techniques can provide additional information, then going a step further, indicate the value of having hot-wire information to go with the data.

Separation at a Forward Facing Step. Visual information obtained from a volume marking technique can be very enlightening, even in the case of flows which have received a lot of attention. The flow patterns produced when two or three-dimensional obstacles are introduced into laminar or turbulent boundary layers are readily visualized using the smoke technique. The ability of the technique to instantaneously map the concentration distribution in prescribed planes of a three-dimensional region reveals details not obtainable before. Figure 4 shows the flow pattern which resulted from placing a two-dimensional "fence" onto a wall over which a laminar boundary layer was developing. The

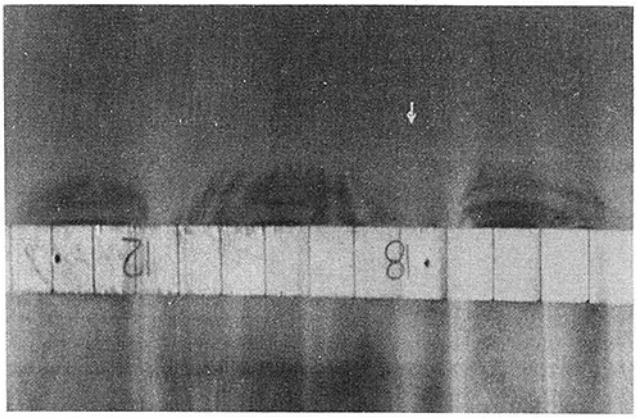

Fig. 4 Separation of a two-dimensional laminar boundary layer at a two-dimensional fence. The ratio of boundary layer thickness/step height is 2.5

fence was 1 cm high and the boundary layer thickness without the fence in place was approximately 2.5 cm. The fence spanned the tunnel (0.91 m) but the field of view is only the central 0.45 m. It can be clearly seen from the photographs that the flow separates in a three-dimensional manner and rearranges itself into a highly three-dimensional field. The laminar boundary layer was two-dimensional before the fence was placed on the wall. However, with the fence in place it has become three-dimensional far upstream of the separated region, as evidenced by the (high) ridges of denser smoke, and the lateral curvature of the streamlines. The separated region consists of "cells" of various sizes within which vortex tubes can be seen. The flow over the top of the fence is also highly three-dimensional, with most of the smoke filled boundary layer fluid going over in narrow streaks, which are seen to coincide with the boundaries of the cells, and which also appear to be continuations of the ridges found upstream of the separated region. This three-dimensionality is presumably the result of the amplification of existing spanwise variations, however, it was found to exist in three different wind tunnels, at least two of which had very uniform spanwise conditions and low free stream turbulence levels (results differed only quantitatively), suggesting that even very small variations can be highly amplified. Since small spanwise variations can't be completely removed from wind tunnel investigations (Bradshaw [8]) data interpreted under the assumption of two-dimensionality may have to be reexamined.

When the oncoming flow is a turbulent boundary layer, evidence of these cells can still be found, although they are fluctuating in position, size and number. The highly three-dimensional nature of this flow field hasn't received much attention, although a large number of experimental investigations of this flow have been performed (see Chang [9]). Several investigations have indicated "unusual" findings however. For example, Sandborn and Liu [10] found a fluctuating separation point position, and Bradshaw and Galea [11] found an increase in the low frequency content of the u spectra which they suggested was due to a "modulation of the displacement thickness and the separation position by the turbulent eddies." The visualization data suggests that the turbulent eddies interact with the three-dimensional cellular separated region in a strongly nonlinear manner resulting in, for example, the merging of two cells into one, etc.

The obvious advantages of simultaneous hot-wire measurements to gain an understanding of such complex flow fields do not need to be elaborated.

Strongly Accelerated Turbulent Boundary Layer. Another example of a flow which has received a lot of attention is the turbulent boundary layer which undergoes a strong favorable pressure gradient [12, 13, 14, 15, 16]. Despite attempts to uncover the physics behind the apparent relaminarization of the initially fully turbulent boundary layer, several important apparent contradictions remain. For example, for high values of the acceleration parameter K, in cases where K has been maintained constant long enough for the turbulent intensity u/U_∞ to decrease to low levels, it is well documented that the skin friction remains at levels appropriate for a low Reynolds number fully turbulent boundary layer [13, 14, 16]. Although the skin friction remains high, the entrainment rate goes down, and can be made to go to zero in constant K flows [16]. Furthermore, it has been observed [15, 16, 14] that the absolute values of the Reynolds stress increases as the flow goes through a contraction (although at an appreciably slower rate than the mean velocity). These facts strongly suggest that the normal coupling between the wall region and the outer region is changed by acceleration. This further suggests that both the outer and wall region structures should change. Little data on structural changes has so far been obtained. It has been firmly established [14] that the "law of the wall" breaks down for values of $K \gtrsim 10^{-6}$. In the inner region, Schraub and Kline [12], using a visual counting technique, indicated that the nondimensional spanwise spacing of the wall region streaky structure increases as K becomes more positive and the bursting frequency decreases. Simpson and Wallace [16], using probe techniques found suitable for fully turbulent boundary layer flows, clearly illustrated the difficulty of using them to obtain burst frequencies and sublayer scales even in constant K flows.

Outer region structural information has been obtained by Blackwelder and Kovasznay [15] and Simpson and Wallace [16]. Reference [15] presents spacetime correlations of the large eddy structure. They stay essentially the same in a rapidly accelerated flow in the region where $K \approx 4$, the major change being the absence of the pronounced negative regions found in the $R_{vv}(x,0,z,t)$ correlations. The R_{uv} correlations appeared more symmetric, but had maximum correlations of about the same levels as found in zero pressure gradient flows. Clearly, the large eddies of the outer region which are still strong, do not produce a sufficiently strong interaction of the type suggested by Laufer [2] and Falco [17] that occurs in zero pressure gradient flows, which results in a measurable perturbation in the wall region and new wall layer activity. This, then, appears to be a decoupling of the effects of the outer layers on the wall region, although we maintain very high wall shear stress levels. However, because the absolute values of the turbulent intensities and Reynolds stress increase in the outer region, some energizing mechanism is necessary, which appears to be different from the transport of low momentum fluid away from the wall; the mechanism which is essential to the maintenance of the Reynolds stress in constant pressure flows.

If we take the point of view that if we understand the coherent motions in a turbulent shear flow we will understand the essential features of the flow, it appears that experiments which determine the changes that take place in the coherent motions as the turbulent boundary layer undergoes the acceleration will shed light on the process of relaminarization.

Measurements and photographs were taken with the roof of the third section of the low speed tunnel in the Engineering Department, Cambridge University, removed, and replaced by a sheet of 3 mm plexiglass, shaped so as to provide a contraction ratio of either 3:1 or 6:1. Only the results obtained with the latter are briefly reported here. For this case the nondimensional pressure gradient is approximately a factor of two greater than the value usually considered necessary to produce laminarization.

Figure 5 shows the general configuration and positions

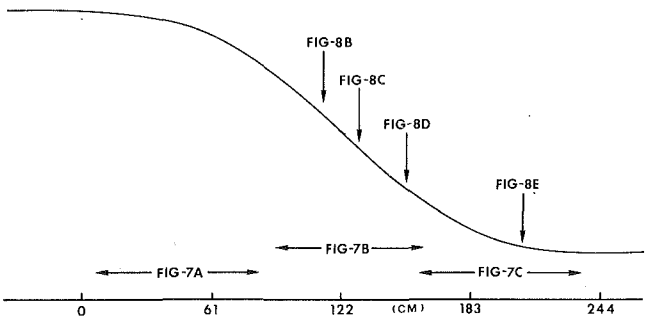

Fig. 5 Configuration of the 6:1 contraction used in the accelerated flow studies. The field of view of the side views shown in Fig. 7 and the location of the transverse views shown in Fig. 8 are indicated

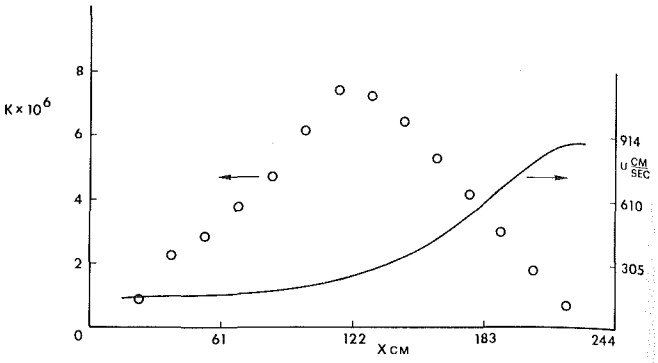

Fig. 6 The velocity distribution and the nondimensional pressure gradient versus distance along the contraction

covered by the photographs of Figs. 7 and 8. Figure 6 shows the velocity distribution, and the acceleration expressed by the nondimensional pressure gradient

$$K = -\frac{\nu}{U_\infty^3}\frac{dP}{dx} = \frac{\nu}{U_\infty^2}\frac{dU_\infty}{dx}.$$

Figure 7(*a*), (*b*), (*c*) shows longitudinal sections of the layer covering the length of the contraction (see Fig. 5). These photos were not taken simultaneously, but represent typical results from large numbers taken at each camera position. It is clear that the turbulence in the boundary layer undergoes a large change. Proceeding downstream, we see a progressive growth of the laminar coherent vortex motions until by the middle of the contraction they have become the largest scale features. Furthermore, new coherent vortex motions do not appear in these side views, with the result that there is much less fine scale turbulence. This increase in the scale of these eddies/boundary layer thickness occurring as R_θ decreases (see for example reference [15]) as we proceed down the contraction, is consistent with the changes found by Falco [18], (who called these coherent vortex motions "typical eddies"), with Reynolds number in zero pressure gradient flows. In fact, there is a generally remarkable similarity between the pictures in the left half of the region covered by Fig. 7(*b*) and very low Reynolds number constant pressure flow. In the downstream half of the contraction the most evident change is the stretching of the smoke marked boundary layer fluid. Associated with Fig. 7(*a*) and (*c*) is the increased spread of intermittency that is to be expected if new fine scale structure is not generated. Visual observations and motion pictures show that, in the later stages, there appears to be little turbulence in these side views. Thus, intermittency measurements made by measuring the light scattered from the smoke marked regions [16] must be carefully interpreted. (As we shall see later, ambiguities alsc are present in zero pressure gradient flows). By observing the flow field from the transverse view, significant additional information is added to the picture. The evolution of the structure in this view is shown in photographs of Fig. 8 which correspond to the positions indicated in Fig. 5. All sections in Fig. 8 span the tunnel, thus the changes in the scale of the smoke filled features are the result of the position in the contraction at which the photographs were taken, not subsequent difference in magnification. Figure 8(*a*) shows the structure of the zero pressure gradient layer at the tunnel station corresponding to the position of the center of the contraction (but, of course, before the contraction was placed in the tunnel) and represents the structure of the boundary layer before the contraction. Figure 8(*b*) and (*c*) illustrates the increasing scale of the "typical eddy" with respect to the depth of the layer, and the increasing depth of the intermittency. Figure 8(*c*) and

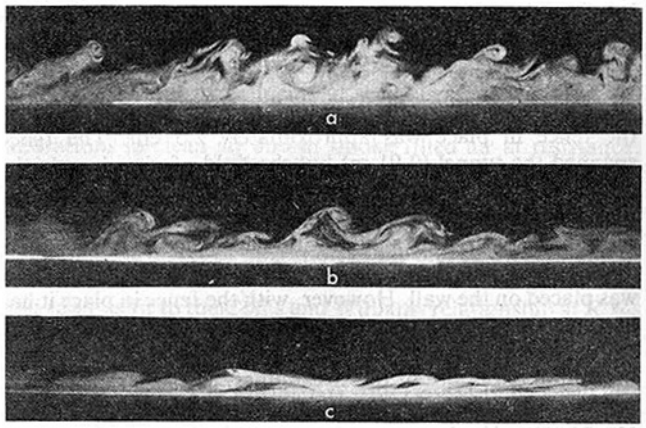

Fig. 7 Side views of a turbulent boundary layer undergoing a favorable pressure gradient. The locations of *a*, *b*, and *c* are indicated in Fig. 5

(*d*) conveys the impression that the stretching the boundary layer has undergone has concentrated and presumably intensified the existing regions of streamwise vorticity in the turbulent layer. Thus, it may be that when the layer has apparently reverted to the laminar form, as indicated by the mean velocity profiles, fairly intense concentrations of streamwise vorticity (see Fig. 8(*e*)) may yet exist in the outer part of the layer. This may be the mechanism which results in the increased Reynolds stress noted by Blackwelder and Kovasznay [15] in the outer part of a strongly accelerated layer. The visual investigation adds at least two important points to the physical picture of relaminarization. The first (shown in Fig. 7(*b*)) is that the large scale structure persists, even at values of $K > 7$ (this is consistent with the results of Blackwelder and Kovasznay [15]) and the intermittency is increased. It is in this region that the unexpected increase in wall shear stress occurs, although the law of the wall no longer holds and the sublayer bursting rate is found to have decreased even for significantly lower values of K. Second, the boundary layer in the later stages of the acceleration, where the mean velocity profile is laminar-like, has undergone a dramatic change in structure, its appearance being dominated by an array of large scale streamwise vortices. Although the amplification of streamwise vorticity by vortex stretching is expected, the organization into large scale vortices, the apparent strength, as well as the spanwise intermittency distribution, are unexpected, and strongly suggest that we are seeing the evolution of the large scale structure that existed upstream of the contraction. Clearly, quantitative information taken simultaneously with photographs such as these can effectively provide information about entrainment, transport and inner-outer layer interactions.

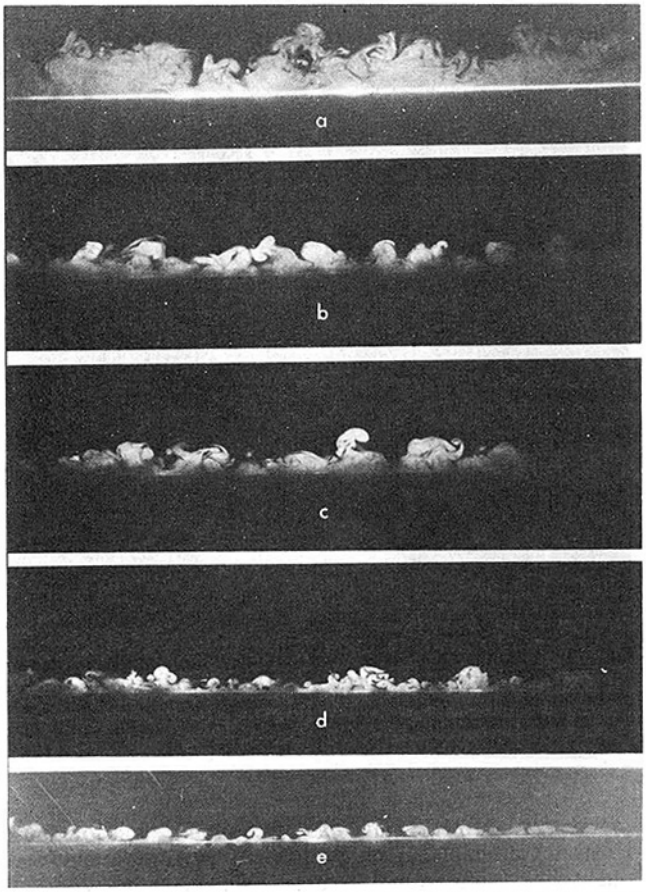

Fig. 8 Changes in the structure seen in the transverse view at various positions along the contraction, which are indicated in Fig. 5. (*a*) is the reference zero pressure gradient flow

Constant Pressure Turbulent Boundary Layer. The visual information provided by a turbulent bounday layer in constant pressure flow is equally enlightening. Most experiments reported to date that have tried to describe the equilibrium structure of the large eddies have relied upon visual and point information in a single plane, most often parallel to the flow and normal to the wall [17, 18, 19]. However, visual information indicates that even the large scale structure is strongly three-dimensional. Figure 9(*a*) shows a characteristic side view and Fig. 9(*b*) shows a characteristic plan view. The photos were not taken simultaneously (Fig. 9(*a*) and (*c*) were taken at Cambridge). Both figures are at low Reynolds number ($R_\theta \approx 700$). Figures 9(*c*) and 9(*d*) show similar data at higher Reynolds numbers ($R_\theta = 4{,}000$). Both Fig. 9(*b*) and 9(*d*) were taken at the half intermittency level ($y/\delta \approx .8$).

A large amount of information is revealed in these pictures. First, it is clear that both large and small scale coherent structures which exist within the zero pressure gradient turbulent boundary layer are strongly three-dimensional. At least two kinds of coherency are obvious. At the lower R_θ, laminar vortices of the type described above, which are a large fraction of the boundary layer thickness, dominate the outer region. At higher R_θ the large scale motions have complicated internal structures. It is clear from photos like these, and from motion pictures, that the role played by coherent motions may be Reynolds number dependent. The fact that the present technique uses air instead of a liquid, which permits a wide range of Reynolds numbers to be obtained, will allow Reynolds number effects, (which of course also appear in mean flow results, for example, in the breakdown of the "law of the wake"), to be studied. Using simultaneous hot-wire anemometry, these motions have been mapped and discussed for low Reynolds numbers (see Falco [17, 18]) when they appeared in a light plane oriented as in Fig. 9(*a*) or 9(*c*). At that time the strong three-dimensionality of the type evidenced in Fig. 9 (*b* and *d*) was not expected.

It is obvious from these photos that any technique which seeks to obtain convergent ensemble averaged signatures for

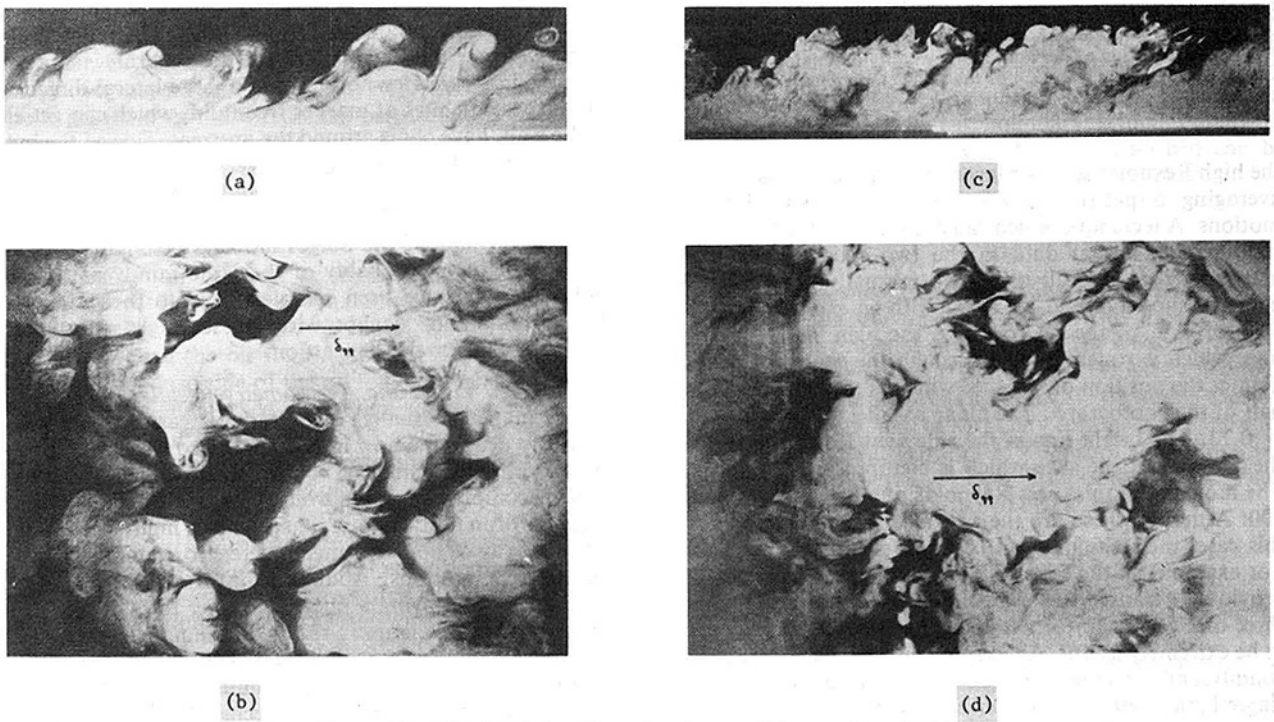

Fig. 9 Visualized turbulent boundary layers at low and moderate Reynolds numbers. Both (*a*) and (*b*) are at low Reynolds number ($R_\theta \approx 700$). (*a*) side view; (*b*) plan view with light plane at 0.8 of the boundary layer thickness. (*c*) and (*d*) show similar photos at moderate Reynolds number ($R_\theta = 4000$). Flow left to right

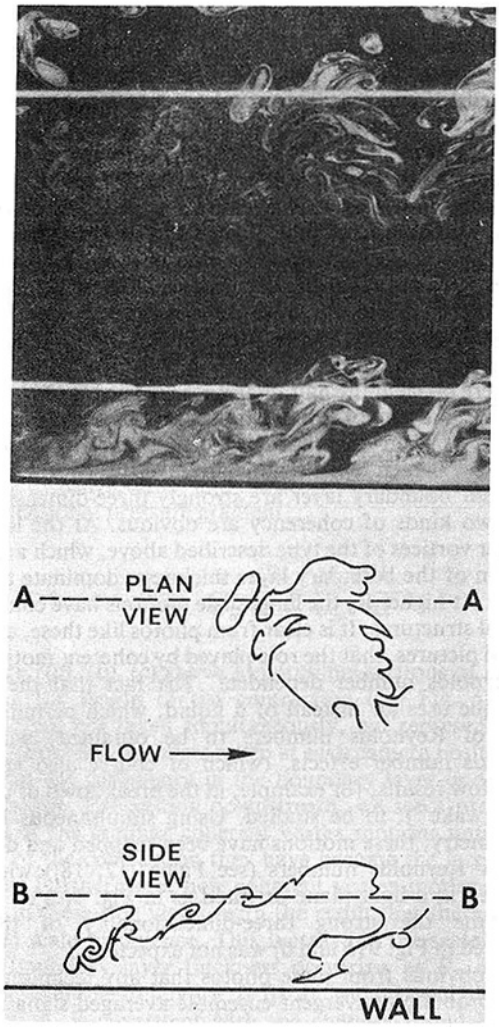

Fig. 10 Simultaneous views of a large eddy in a turbulent boundary layer, $R_\theta \approx 700$. Line A-A of the accompanying explanatory sketch represents the edge of the light plane which illuminates the side view. Line B-B represents the edge of the light plane which illuminates the plan view

the high Reynolds number large scale motions must refine the averaging to specific spanwise locations within the large scale motions. A technique which can accomplish this must provide simultaneous visual data in the two mutually orthogonal planes. An early result using two mutually orthogonal light planes is shown in Fig. 10, along with an explanatory sketch. The top half of the photo shows the plan view. The bright line, which is roughly going through the center of the eddy, defines the position of the slice which is pictured in the lower half of the photograph. The plane parallel to the wall is at $y/\delta = 0.73$. The bright line in the side view (lower half) defines the position of the slice which is pictured in the upper half. The momentum thickness Reynolds number is approximately 700. Although these are the two most interesting planes for this case, the technique can be adjusted to suit the problem. For example, in the favorable pressure gradient case a plane providing a transverse view would be informative. Qualitative three-dimensional information of this type has already proven to be extremely useful. An example is the interpretation of the conditionally sampled large eddy data of Falco [17]. Using a single light sheet and an x-wire, the signatures of large scale motions were conditionally sampled at $y^+ = 67$. The results showed that roughly half of these features had a zone averaged streamwise perturbation which was greater than the local mean velocity. The other half had a zone averaged

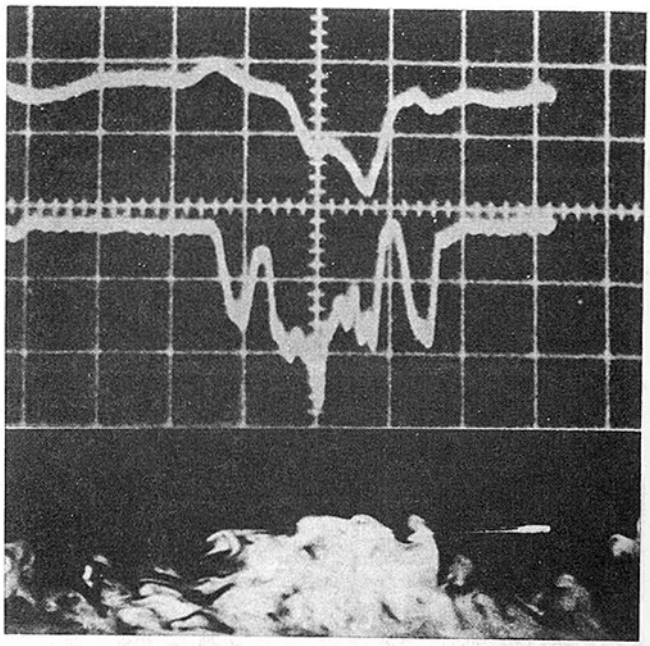

Fig. 11 Simultaneous visual, hot-wire, and concentration density information in a turbulent boundary layer at $R_\theta \approx 1200$. Top signal is u, lower signal is proportional to the oil fog concentration. The hot-wire can be seen intersecting the light plane which is parallel to the flow. Signals are scaled to the boundary layer photo.

momentum defect. This was unexpected, and obviously frustrates attempts to model these large eddies. However, qualitative results from the crossed light sheet studies revealed that these large bulges had a complex three-dimensional nature. By following the flow over the field of view, the evolution of oil fog concentration gradients in both side and plan views indicated that large scale inflows occurred which had a strong lateral component. Nychas, et al. [20] observed the streamwise components of these inflows. Thin crevices of marker free fluid, which appear to separate large scale motions in a side view, often have a large lateral dimension. Thus, these tongues of marker free fluid, which can get close to the wall, have come around the upstream side of the bulges with both wallward and lateral velocity components. This suggests that along the sides of the bulges high speed wallward moving fluid exists. Thus, the conditionally sampled results which show half of the bulges moving faster than the local mean velocity are probably of the same family as the other half, but may have been sampled close to their sides. Additional simultaneous hot wire crossed light data will be needed to confirm this suggestion.

Combined Visual and Anemometry Results. Once the flow field is mapped visually, quantitative measurements will be needed to determine how important the coherent motions are and how they are enhanced or weakened by the applied strain rates. A complete program would combine three-dimensional visual information photographed with a high speed camera with an array of hot-wire anemometers to quantitatively map the coherent motions. Additional information can also be obtained by employing a photomultiplier to map smoke/no-smoke boundary. Figure 11 shows an example of early results obtained at Cambridge with a single light plane, a u-wire and a photomultiplier tube. The photomultiplier is focused upon a spot just above the probe tip (a technique used in reference [6]), thus when oil fog which is in the light plane passes the wire, the photomultiplier responds. Using an x-wire and photomultiplier, this technique has been used to determine how closely the "edge" of the boundary layer coincides with

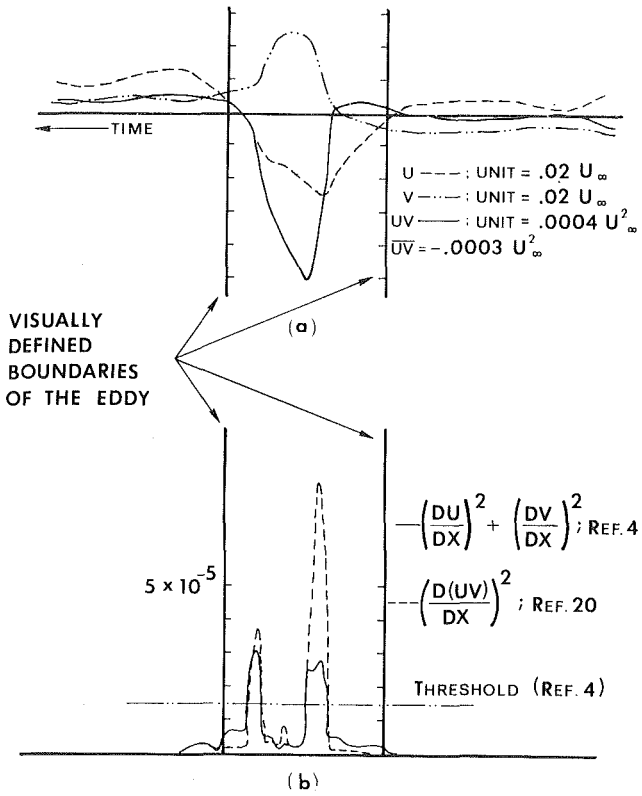

Fig. 12 Application of two turbulence detectors to a "typical eddy." (a) The u, v and uv signatures; (b) results of the detectors. The vertical lines represent the oil fog boundaries of the eddy. The threshold is the one used by Hedley and Keffer (4).

the smoke marked edge. Results indicate that a significant number of times during which smoke filled fluid passes the x-wire very little u or v of uv perturbation occurs. At other times, very large perturbations occur when the smoke passes over the wire. These times are often associated with the passage of a vortex like "typical eddy" [17]. When smoke free regions passed over the wire, small perturbations were often observed, even when the extent of these regions was large (see Fig. 11). Changes in u, v or uv signal levels associated with passage into or out of a marked region always occurred over a length scale which was large compared with the thickness of the marker boundary.

Thus, using an x-wire, a simple answer about the correspondence cannot be given. Physically, because the Schmidt number is $\approx$ 38,000, we expect vorticity to diffuse more rapidly than the oil fog, however, large perturbations were never found outside of the oil fog contaminated region, whereas regions of marked fluid were sometimes found to have essentially no perturbations associated with them. An attempt was made to quantify the correspondence by doing a detailed study of the output of two turbulence detector functions associated with the laminar vortex motions called "typical eddies" [17], which are defined by their oil fog marked boundaries. When a "typical eddy" passed over the x-wire, the u, v and uv signals were stored as well as the signal from a photomultiplier tube. The hot-wire signals were then processed to obtain the detector functions used by Antonia [21], and Hedley and Keffer [4].

Figure 12 shows the u, v and uv signals associated with a single "typical eddy" and the response of the two turbulent detectors. The vertical lines represent the smoke boundaries of the eddy. This response was characteristic of that found for the 56 eddies sampled. Both detectors acted similarly. They indicated that two turbulent regions existed, each of length approximately one-tenth of the length of the boundary defined by the oil fog. They both indicated that no turbulence existed in the center of the typical eddies, where the magnitude of the velocity fluctuations and instantaneous Reynolds stress was greatest. Their failure to indicate turbulence in the center of the eddies means that they cannot be used to check the ability of the smoke to define the "edge" of the boundary layer. However, a more important conclusion from these results is that turbulence detectors of the type used here cannot give reliable information about the frequency and duration of turbulence regions in the outer intermittent part of the turbulent boundary layers.

Conclusions

In conclusion, a technique has been presented which permits both qualitative and quantitative examination of features in unsteady or turbulent flow fields. By filling selected regions of flow field with an oil fog marker, then selecting an appropriate illumination technique, detailed structural features can be observed. Quantitative information from hot-wire anemometry can be obtained in the oil fog contaminated air. A technique has been described which allows long continuous records of high rate data to be obtained using a hard wire processor and a disk. The visual and anemometry data are synchronized by photographing a timing signal and simultaneously recording it on the disk. Data showing the effects of oil fog on hot-wire response indicated that the changes were small. Visual results showed the nature of the changes which occur when a turbulent boundary layer is strongly accelerated. Using mutually orthogonal sheets of light, some three-dimensional characteristics of coherent motions in equilibrium turbulent boundary layers were briefly discussed. The correspondence of the oil fog marked boundary of the layer with hot-wire signals showed the complex nature of the turbulent boundary. Direct comparison of the response of some turbulence detectors indicated their poor performance.

Most experiments to date have been performed at low Reynolds numbers. The system described will enable similar structural information to be obtained at Reynolds numbers high enough for asymptotic conditions to be approached in the outer region of turbulent boundary layers. Finally, it should be mentioned that the techniques described can be applied to all types of nonsteady and turbulent flows.

Acknowledgments

I wish to acknowledge the debt owed to Dr. M. R. Head. He generously made available the use of his unique smoke tunnel, obtained financial support enabling me to use it, and maintained an active interest in the work. Thanks are due to Mr. Wendel Burkhardt for his assistance in obtaining the hot-wire calibration data, and to Mr. Gary Newman for help with the simultaneous data. Portions of this work were supported by the Ministry of Defense, Great Britain, and by the Fluid Dynamics Program of the Office of Naval Research.

References

1 Blackwelder, R. F., and Kaplan, R. E., "On the Wall Structure of the Turbulent Boundary Layer," *J. Fluid Mech.*, Vol. 76, 1976, pp. 89–112.

2 Laufer, J., "New Trends in Experimental Turbulence Research," *Annual Review of Fluid Mechanics*, Vol. 7, 1975, pp. 307–326.

3 Bradshaw, P., and Murlis, J., "On the Measurement of Intermittency in Turbulent Flow," *Imp. Coll. Aero. Tech Note* 73-108, 1973.

4 Hedley, T. B., and Keffer, J. F., "Turbulent/Non-Turbulent Decisions in an Intermittent Flow," *J. Fluid Mech.*, Vol. 64, pp. 625–644.

5 Loehrke, R. I., and Nagib, H. M., "Control of Free Stream Turbulence by Means of Honeycombs: A Balance Between Suppression and Generation," ASME Paper No. 76-FE-2.

6 Fiedler, H., and Head, M. R., "Intermittency Measurements in the Turbulent Boundary Layer," *J. Fluid Mech.*, Vol. 25, 1966, pp. 719–735.

7 Collis, D. C., and Williams, M. J., "Two Dimensional Convection from Heated Wires," *J. Fluid Mech.*, Vol. 6, 1959, pp. 357–384.

8 Bradshaw, P., "The Effect of Wind Tunnel Screens on Nominally Two-Dimensional Boundary Layers," *J. Fluid Mech.*, Vol. 22, 1965, pp. 679–687.

9 Chang, P. K. *Separation of Flow*, Pergamon Press, New York, 1970.

10 Sandborn, V. A., and Liu, C. Y., "On Turbulent Boundary Layer Separation," *J. Fluid Mech.*, Vol. 32, 1968, pp. 293–304.

11 Bradshaw, P., and Galea, P. V., "Step-Induced Separation of a Turbulent Boundary Layer in Incompressible Flow," *J. Fluid Mech.*, Vol. 27, 1967, pp. 111–130.

12 Schraub, F. A., and Kline, S. J., "A Study of the Structure of the Turbulent Boundary With and Without Longitudinal Pressure Gradients," Stanford University, Mech. Engr. Dept. Rep. MD-12, 1965.

13 Badri Narayanan, M. A., and Ramjee, V., "On the Criteria for Reverse Transition in a Two-Dimensional Boundary Layer Flow," *J. Fluid Mech.*, Vol. 35, 1969, pp. 225–241.

14 Jones, W. P., and Launder, B. E., "Some Properties of Sink-Flow Turbulent Boundary Layers," *J. Fluid Mech.*, Vol. 56, 1972, pp. 337–351.

15 Blackwelder, R. F., and Kovasznay, L. S. G., "Large-Scale Motion of a Turbulent Boundary Layer During Relaminarization," *J. Fluid Mech.*, Vol. 53, 1972, pp. 61–83.

16 Simpson, R. L., and Wallace, D. B., "Laminarescent Turbulent Boundary Layers: Experiments on Sink Flows," SQUID Rep. SMU-1-PU, 1975.

17 Falco, R. E., "Coherent Motions in the Outer Region of Turbulent Boundary Layers," *Phy. Fluids*, Vol. 20, 1977, S124-S132.

18 Falco, R. E., "Some Comments on Turbulent Boundary Layer Structure Inferred from the Movements of a Passive Contaminant," AIAA Paper No. 74-99, 1974.

19 Kaplan, R. E., and Laufer, J., "The Intermittently Turbulent Region of the Boundary Layer," *Proc. 12th Int. Cong. Appl. Mech.*, Stanford, pp. 236–245.

20 Nychas, S. G., Hershey, H. C., and Brodkey, R. S., "A Visual Study of Turbulent Shear Flow," *J. Fluid Mech.*, Vol. 61, 1973, pp. 513–540.

21 Antonia, R. A., "Conditionally Sampled Measurements Near the Outer Edge of a Turbulent Boundary Layer," *J. Fluid Mech.*, Vol. 56, 1972, pp. 1–18.

Lower Mode Response of Circular Cylinders in Cross-Flow

W. W. Durgin
Associate Professor,
Mechanical Engineering.

P. A. March[1]
Lead Engineer,
Closed Conduit Flow Section.

Alden Research Laboratory,
Worcester Polytechnic Institute,
Holden, Mass. 01520

P. J. Lefebvre[2]
Graduate Research Assistant,
Worcester Polytechnic Institute,
Worcester, Mass.

Transverse amplitude responses of a circular cylinder in cross-flow were determined as a function of reduced velocities for a variety of spring constants and damping coefficients. Maxima were found at reduced velocities of 5 and 16, and were of comparable amplitude. The first resonance, designated the "fundamental mode," was due to normal vortex street excitation of the spring-mass system. The second resonance, designated the "lower mode," occurred when the natural frequency was approximately one-third of the normal vortex shedding frequency. By assuming that the driving force was sinusoidal, it was possible to evaluate the lift coefficients at resonance. Lift coefficients for the lower mode behaved similarly with amplitude ratio but were an order of magnitude lower than lift coefficients for the fundamental mode. A mechanism was used to oscillate the cylinder transversely at prescribed frequencies and amplitudes. Dominant wake frequencies were determined from a frequency analysis of the hot-wire signal for a range of velocities and a fixed frequency of oscillation. It was found that synchronization of the shedding frequency to the forcing frequency did not take place for the lower mode. The familiar "lock-in" region, or frequency synchronization over finite bandwidth, was observed for the fundamental mode only. Since the frequency associated with normal vortex shedding was not suppressed when oscillations took place in the lower mode, it would seem that a low frequency vortex street had not replaced the normal one. It is likely, then, that the spring-mounted cylinder responded subharmonically to the exciting force resulting from vortex shedding. In this regard, however, it was curious that subharmonic response was not found at a frequency ratio of 0.5 as it was at 0.33. A conceptual model, which incorporated features of both the low frequency vortex street and subharmonic response, was developed which accounted for lower mode response at a frequency ratio of 0.33 as well as the lack of response at 0.5.

Introduction

Circular cylinders exposed to cross-flow are known to experience aerodynamic excitation as a consequence of the trailing vortex street. When the shedding frequency is near the natural frequency of the mechanical system, lock-in to the latter takes place and vibrations of substantial amplitude can occur if damping is relatively small. For Reynolds numbers above 300, the phenomenon is characterized by a Strouhal number $S = f_s d/U \approx 0.2$, where the shedding frequency is nearly equal to the natural frequency $f_s \approx f_n$.

The recent review by King [1] provides a good introduction to the subject of oscillations induced by vortex shedding. Papers by Bishop and Hassan [2], Koopmann [3], Toebes and Ramamurthy [4], Jones [5], and Blevins [6], provide more detailed results, especially with regard to the synchronization of vortex shedding with lateral vibrations of circular cylinders. One notable feature of this phenomenon is that the force is directly related to the vortices which are shed alternately from each side of the cylinder with each pair of opposite signs causing one full force cycle. Another is that the ensuing cylinder oscillation substantially affects the vortex shedding process. Near resonance in the fundamental mode (designating phenomena taking place near S = 0.2), the shedding becomes highly organized, longitudinally, and the shedding frequency is entrained to the natural frequency of the spring-mass system. Mathematical models, incorporating essential features of the fluid and mechanical systems, have not been put forth by Hartlen and Currie [7], Skop and Griffin [8], and Iwan and Blevins [9].

Of particular relevance to the present investigation is the possibility of resonance in modes other than the fundamental mode. Various definitions of frequencies associated with the processes involved are defined as follows:

f_s = vortex shedding frequency
f_{so} = vortex shedding frequency for rigidly supported cylinder
f_n = natural frequency of mechanical system
f_f = frequency of mechanically forced cylinder motion

For the present purposes, the modes are defined as:

[1] Present Position: Mechanical Engineer, Tennessee Valley Authority, Norris, Tenn.
[2] Present Position: Product Engineer, Foxboro Company, Foxboro, Mass.

Contributed by the Fluids Engineering Division for publication in the JOURNAL OF FLUIDS ENGINEERING. Manuscript received by the Fluids Engineering Division, January 25, 1979.

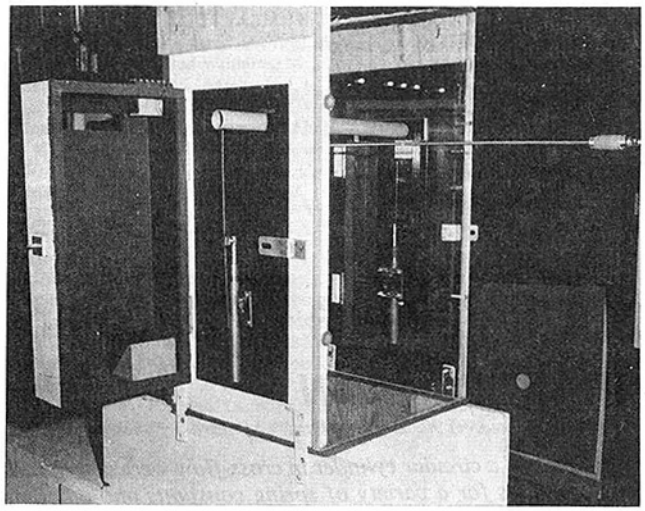

Fig. 1 Elastically mounted cylinder

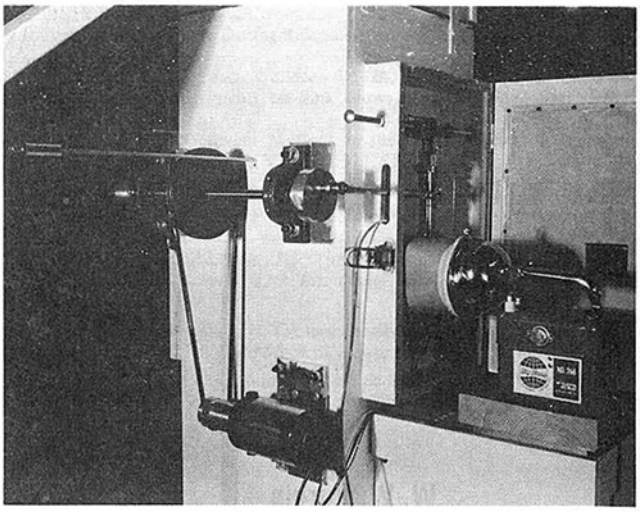

Fig. 2 Mechanically oscillated cylinder

Higher mode	$f_n > f_{so}$
Fundamental mode	$f_n = f_s = f_{so}\ (1 \pm \epsilon)$
Lower mode	$f_n < f_{so}$

where ϵ is small and is indicative of the synchronization bandwidth during fundamental mode lock-in. Bishop and Hassan [2] found response in the higher mode (frequency demultiplication, in their terminology) for mechanically oscillated cylinders. Time records of the force in linkage between the oscillation mechanism and the cylinder showed frequency components at $f_f/2$ and $f_f/3$ when the forcing frequency was approximately 2 and 3 times the shedding frequency, respectively. Although this conclusion seems clear from their representative force traces, quantitative evaluation using force measurements of this sort are difficult because of the large inertial contribution to the record.

Toebes [10], by examining hot-wire records of wake velocities behind cylinders undergoing mechanically forced oscillations, also found higher mode response at ratios of 2 and 3. Additionally, he observed lower mode response at a ratio of 0.5; that is, the vortex shedding frequency, f_{so}, was approximately twice the cylinder oscillation frequency.

Penzien [11] obtained records of strain from cantilever beams supporting cylinders which could vibrate laterally. While it is not possible to infer amplitude of motion from his published data, lower mode response can be observed for some test cases. The frequency ratio was, at times, near 0.33 although the results are not consistent. In addition, the lower mode response was occasionally larger than the fundamental response.

Lienhard and Liu [12] investigated the frequency of vortex shedding behind a mechanically oscillated cylinder and found indications of lock-in for both higher and lower modes as well as for the fundamental mode. Except for the fundamental mode, the locked-in regions were not distinct. One test series indicated lower mode response at a ratio of 0.55, while several showed the higher mode.

Quite by accident, Gowing [13], while investigating the possibility of using lock-in at the fundamental mode as a means of extracting work from a flowing fluid, discovered that his spring-mounted cylinder was vibrating with large amplitude at a frequency much lower than predicted for normal vortex shedding. The cylinder was mounted on a long, flexible leaf spring at its center and facing upstream in a wind tunnel. The apparatus was designed to produce large amplitude oscillation to facilitate the use of a simple electric generator. It was found that substantially greater oscillation could be maintained in the lower mode than in the fundamental mode, resulting in greater power extraction.

It was hypothesized that a vortex street of low frequency was either shed directly or formed quickly through coalesence. The latter has been demonstrated experimentally for evolving streets by Taneda [14], and Durgin and Karlsson [15] for single cylinders, while Thomas and Kraus [16] and Zdravkovich [17] made similar findings for multiple cylinder arrangements. Numerical studies by Acton [18] and Christiansen and Zabusky [19] have also exhibited coalesence. Additionally, Griffin and Votaw [20] examined the wakes of laterally vibrated cylinders using smoke visualization demonstrating vortex elongation which precedes vortex fission, although fission was not observed.

Alternatively, the observed response could have been caused by sub-harmonic response of the spring-cylinder system to excitation by the usual vortex street. Two different types of experiments were conducted to help clarify the nature of the observed lower mode response. In the first series of experiments, Stasaitis [21] utilized cylinders which were elastically supported in a manner similar to Gowing's [13]. The apparatus was used to document the phenomenon and explore the effect of various parameters. In the second series

Nomenclature

a = amplitude of cylinder motion
C_l = lift coefficient
d = cylinder diameter
f = frequency
f_s = vortex shedding frequency
f_{so} = frequency based on $S = 0.2$
f_n = natural frequency
f_f = frequency of mechanically forced cylinder motion
M = equivalent mass per unit length
P_f = spectral density as percent of area under spectrum
P_{fn} = spectral density at f_n
P_{fs} = spectral density at f_s
R = Reynolds number $= Ud/\nu$
S = Strouhal number $= fd/U$
t = time
U = free stream velocity
U_r = reduced velocity $= U/f_n d$
x = streamwise coordinate
y = lateral coordinate
δ_r = reduced damping
δ_s = logarithmic decrement of damping
ν = kinematic viscosity of fluid
ρ = fluid density
τ = time constant

Table 1 Parameters for free vibration tests (d = 2.48 cm)

Test No.	f_n (HZ)	U (m/sec)	τ (sec)	M (gm/cm)	δ_s	δ_r	R	U/fd	a/d	C_ℓ
1	8.4	3.41	7.9	0.303	0.0151	1.27	5690	16.4	0.230	0.014
2	9.0	3.50	7.6	0.302	0.0147	1.23	5790	15.6	0.184	0.011
3	9.5	3.75	6.8	0.301	0.0154	1.28	6250	15.9	0.196	0.012
4	10.0	3.78	5.6	0.301	0.0179	1.49	6300	15.2	0.191	0.014
5	10.7	4.15	5.4	0.299	0.0172	1.42	6860	15.6	0.159	0.011
6	11.5	4.51	5.2	0.298	0.0167	1.38	7520	15.9	0.180	0.012
7	13.6	5.36	4.8	0.295	0.0154	1.26	8940	15.9	0.145	0.009
8	16.5	6.16	3.2	0.292	0.0191	1.55	10260	15.2	0.129	0.010
9	19.4	7.38	1.2	0.291	0.0433	3.48	12300	15.4	0.103	0.017
10	8.1	3.05	8.2	0.304	0.0150	1.26	5080	15.2	0.159	0.010
11	7.7	3.23	8.4	0.285	0.0155	1.22	5390	17.0	0.134	0.008
12	6.7	2.74	9.6	0.288	0.0155	1.23	4570	16.4	0.123	0.008
13	5.7	2.07	10.9	0.291	0.0161	1.30	3460	14.7	0.097	0.006
18	15.5	6.43	3.2	0.281	0.0204	1.78	10720	16.7	0.104	0.009
19	12.2	4.88	5.0	0.285	0.0164	1.45	8130	16.1	0.212	0.015
20	10.1	4.27	5.4	0.288	0.0183	1.64	7110	17.0	0.155	0.012
21	8.1	3.26	7.4	0.292	0.0166	1.50	5440	16.1	0.165	0.012
22	11.5	4.79	5.6	0.280	0.0156	1.21	7980	16.7	0.214	0.013
23	8.2	3.54	8.2	0.285	0.0149	1.17	5890	17.5	0.212	0.012
24	6.1	2.53	10.2	0.290	0.0161	1.29	4220	16.7	0.120	0.008
Error	±0.5%	±0.5%	±1%	±0.5%	±1.5%	±2.8%	±0.9%	±1.4%	±3.4%	±9%

of experiments, Lefebvre [22] used a cylinder which was mechanically oscillated and observed the response of the wake in the range of interest.

Experimental Apparatus

This investigation utilized a vertical wind tunnel with a test section measuring 30 cm by 30 cm. The vertical orientation eliminated static deflection of the cylinders, which were mounted on flexible springs, Fig. 1. Air entered the tunnel through a rounded entrance and proceeded through the test section, a vaned elbow, blower, Venturi meter, and regulating valve. For the first series of experiments, rigid paper and plastic composite cylinders were attached to leaf springs mounted in telescoping clamps on the outside of the tunnel wall. The cylinders passed through slots in the walls so that approximately 3 cm on each end were not in the air stream. The slots and telescoping clamps were sealed from the room environment by hinged, air tight boxes. Both cantilever springs vibrated in unison in the fundamental mechanical mode. The frequency of the second mechanical mode was about 30 times the fundamental. Except for the side wall boundary layers, the flow in the test section was uniform within the resolution of the hot-wire. The turbulence intensity varied from 1.7 percent at the highest speed to 6.0 percent at the lowest speed.

To monitor cylinder oscillations, a photo cell was coupled to an amplifier and used to monitor the intensity of light modulated by a shield connected to the spring-cylinder combination. A digital counter was used to determine the frequency of oscillation, and the amplitude of oscillation was taken directly from a storage oscilloscope.

For the second series of experiments, the cylinder was mounted on a mechanism capable of imparting harmonic motion, as shown in Fig. 2. A crankshaft with adjustable stroke was driven through a rubber belt by a stepping motor with feedback speed control. The photo cell arrangement was again used to monitor cylinder motion.

Observation of wake velocities was made for both experimental series using a commercial hot-wire anemometer. For the experiments with forced cylinder oscillation, spectral analysis was performed by tape recording and digitally analyzing the signal on a computer system.

Results

Both measured and derived parameters for peak lower mode response of elastically mounted cylinders are listed in Table 1. Figure 3 shows the non-dimensional cylinder motion amplitude, a/d, versus the reduced velocity, $U_r = U/f_n d$ for six different natural frequencies, f_n. The fundamental mode response to vortex shedding is visible as the peaks near $U_r = 5$ (Strouhal number S = 0.2). The peak responses are generally somewhat smaller than those obtained by other investigators. The low values of damping and the treatment of the sidewalls probably contribute to this difference. In addition, the peak values are not entirely consistent with the reduced damping values. The reason for this behavior is not presently understood. Additional peaks are apparent near $U_r = 16$ and reflect substantial oscillatory response to the flowing stream. The reduced velocity at the secondary peak was essentially independent of Reynolds number over the range tested, as can be seen from Fig. 4. Values of the reduced damping, δ_r, were rather small because of the small cylinder mass.

Evidently, in the lower mode, the spring mounted cylinder experienced an exciting force at approximately one-third the normal vortex shedding frequency associated with the flow velocity. By assuming the exciting force to be sinusoidal, the lift coefficient for lower mode resonance could be evaluated. Blevins and Burton (23), for example, give the equation

$$C_l = \delta_r \frac{a}{d} \frac{(2\pi S)^2}{\pi} \tag{1}$$

where δ_r is the reduced damping

$$\delta_r = \frac{2M\delta_s}{\rho d^2} \tag{2}$$

The logarithmic decrement of damping, δ_s, was evaluated from vibration decay curves with no air flow, as indicated in Blevins [24]. These values were measured for only a single perturbation from equilibrium so that amplitude dependence was not investigated. The curves, however, appeared exponential. The mass per unit length, M, includes the cylinder mass, hydrodynamic mass, and a portion of the spring mass. Here, the Strouhal number is evaluated as the reciprocal of the reduced velocity, U_r. Figure 5 shows that the lift coefficient increased with amplitude over the experimental range in a manner comparable to that of the fundamental mode. The magnitudes, however, are an order of magnitude less than those associated with typical fundamental mode response.

In the second series of experiments, the 2.48 cm diameter cylinder was oscillated with an amplitude of $a/d = 0.175$ at a frequency of 10.1 Hz. The hot-wire probe was positioned at $x/d = 3.0$ and $y/d = 1.3$. Velocities at this location were found to provide relatively large power spectral density for both the forcing frequency and vortex shedding frequency over the range of velocities used. Signal analyses were performed such that the frequency range 0-51 Hz was spanned with a resolution of 0.1 Hz. A low pass filter with a roll-off of 18 db/octave set at 50 Hz was provided at the input of the A/D converter to eliminate foldover. The output spectra were normalized individually so that the highest peak always

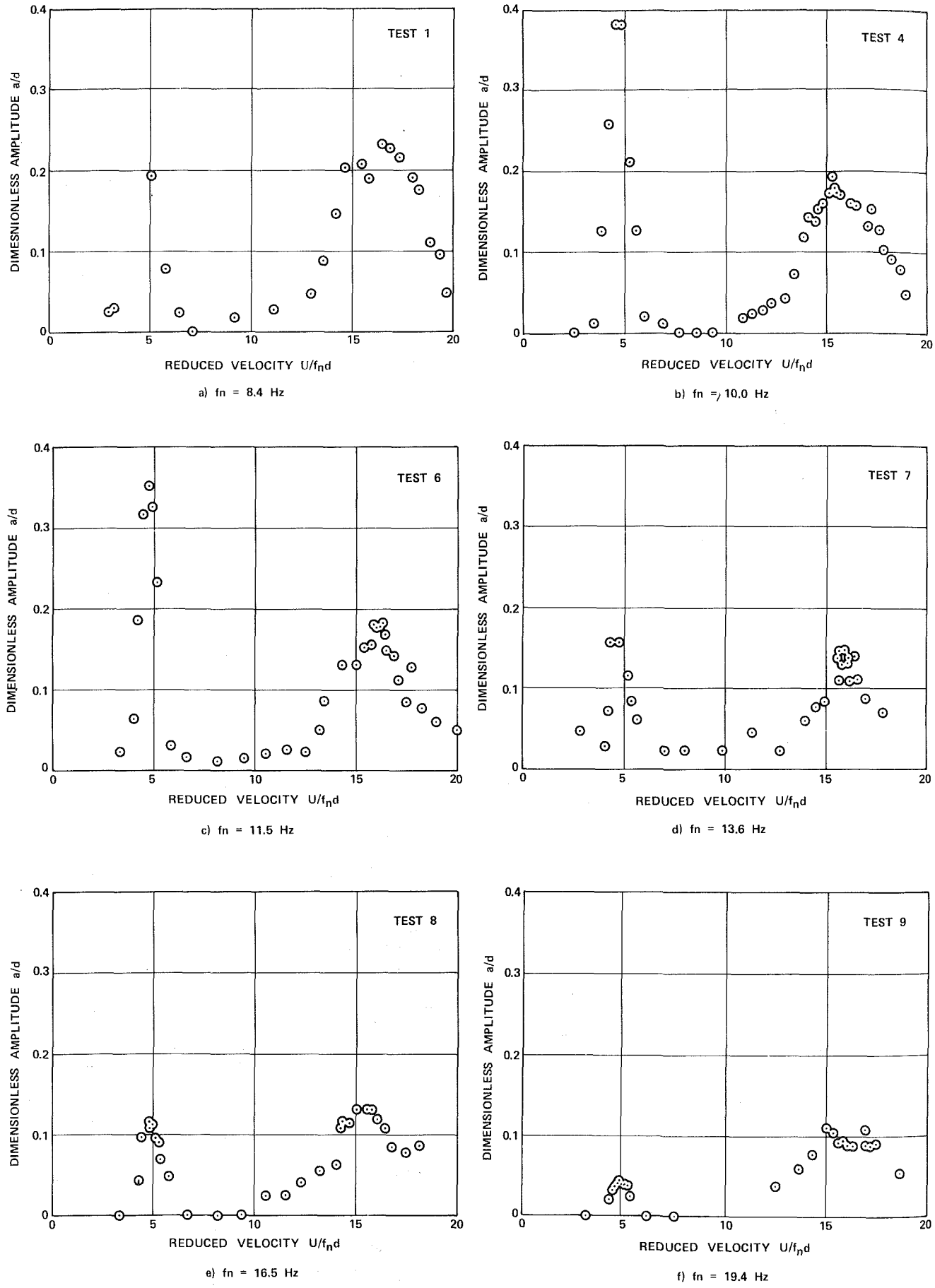

a) fn = 8.4 Hz

b) fn = 10.0 Hz

c) fn = 11.5 Hz

d) fn = 13.6 Hz

e) fn = 16.5 Hz

f) fn = 19.4 Hz

Fig. 3 Amplitude response of elastically mounted cylinders

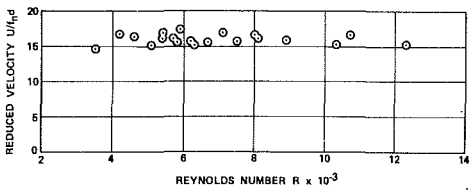

Fig. 4 Reduced velocity of lower mode response versus Reynolds number

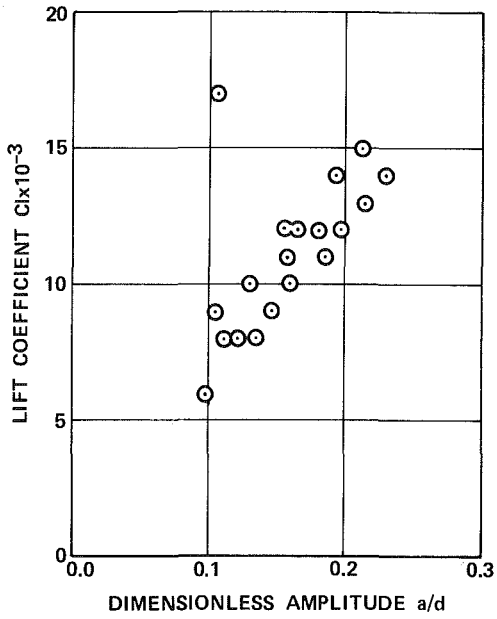

Fig. 5 Lower mode lift coefficient variation with amplitude

equalled full scale on the graphics screen. The value of the highest peak relative to the integral under the spectrum, P_f, was calculated as percent and is tabulated in Table 2 as either P_{fso} or P_{ff} as appropriate. The Reynolds number, R, and the frequency ratio, f_f/f_{so}, are also tabulated.

Figure 6 shows power spectra for various air velocities. In (*a*), the shedding frequency is less than the forcing frequency, and distinct peaks can be seen for each. Synchronization has been achieved in (*b*), and all energy is at 10.1 Hz. In (*c*), synchronization has been lost and the forcing frequency is less than the shedding frequency. For $f_f/f_{so} = 0.5$, (*d*), substantial energy can be found at both frequencies. In (*e*), the conditions of the freely vibrating cylinder are approached, and the energy at the forcing frequency is considerably less than at the shedding frequency. For conditions approximately the same as those for the freely vibrating case, (*f*), the energy at the forcing frequency is even smaller.

A total of 33 spectra were obtained for Reynolds numbers between 1318 and 8697. The results are summarized in Figure 7, where lock-in in the fundamental mode can be clearly seen. At frequency ratios $f_f/f_{so} = 0.5$ and 0.33, distinct lock-in was not achieved. Both frequencies were, however, clearly present above the fundamental mode lock-in region.

An error analysis based on direct propagation of estimated measurement inaccuracies was made. Maximum errors, in percents to be associated with derived quantities, are tabulated at the end of Tables 1 and 2.

Discussion

The spring mounted cylinder experienced excitation at $f_n/f_{so} = 0.33$. Although the lift coefficients were relatively small, the cylinders, nevertheless, experienced substantial

Table 2 Peaks in power spectra

	R	f_f/f_{so}	P_{fso} (%)	P_{ff} (%)
	1580	1.64	4.14	1.76
	2370	1.00	32.16	32.16
	4480	0.53	1.97	3.92
	4740	0.50	2.09	2.14
	6460	0.36	2.92	1.38
	7120	0.33	1.41	0.77
Error		±0.9%	±1.0%	±0.5%	±0.5%

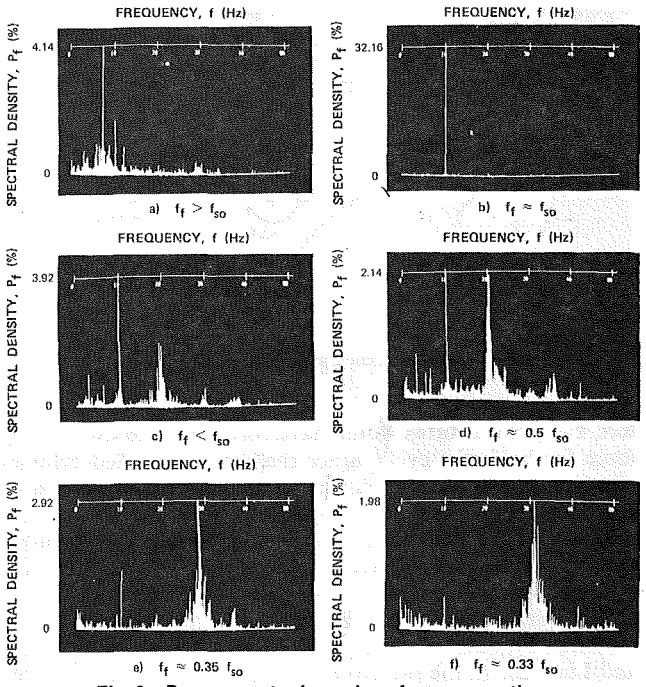

Fig. 6 Power spectra for various frequency ratios

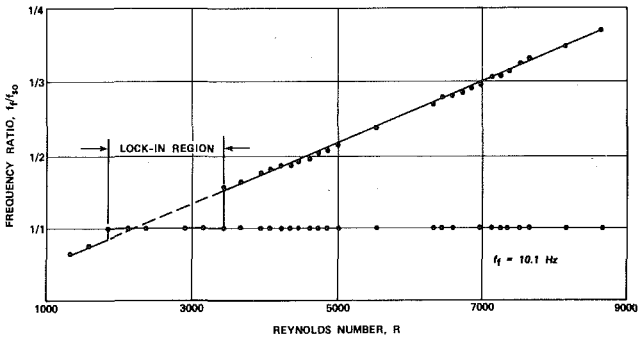

Fig. 7 Wake response for various free stream velocities

vibration amplitude. This response probably resulted from the low reduced damping used, which would explain why no other investigators have distinctly observed the phenomena. If the free oscillation and forced oscillation situations are fluid mechanically equivalent, then, under the hypothesis that a low frequency vortex street was formed, the shedding frequency should have been entrained to the forced oscillation frequency near $f_f/f_{so} = 0.33$. This was not found to be true and, in fact, most of the energy associated with fluctuating wake velocities was found at f_{so}.

The lower mode response could have been subharmonic excitation by the (higher) vortex shedding frequency. In ef-

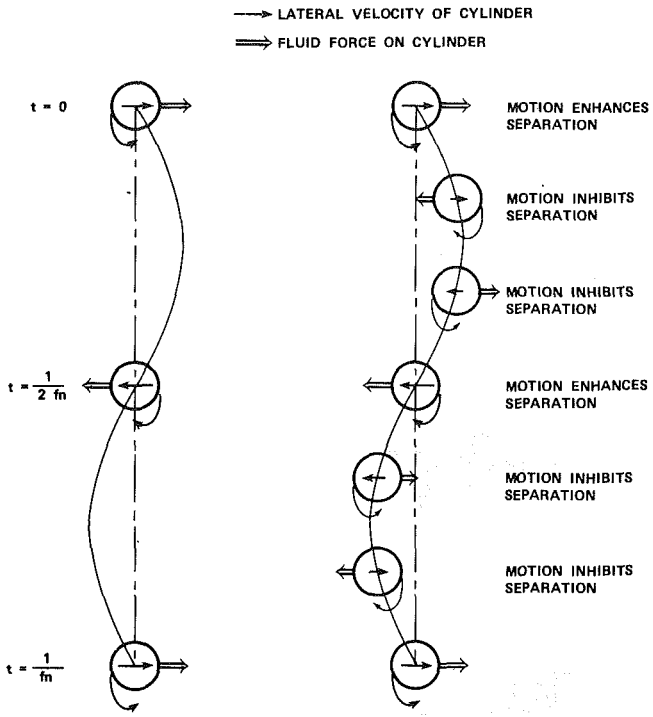

Fig. 8 Vortex shedding at $f_n \approx f_{so}$ and $f_n \approx f_{so}/3$

fect, every third vortex would have contributed to the exciting force for half of a cycle. Since the spring-mounted cylinder vibrated in two modes with an effective frequency ratio of approximately 5/16 = 0.31 (0.29 average by actual calculation for each test) rather than 0.33, the Strouhal number would have to have decreased from 0.21 to 0.19 over the Reynolds number range 1000 to 8000. This behavior was, in fact, verified using spectral analysis of the wake of a rigidly mounted cylinder. Similar behavior was found by Lienhard and Liu [12]. In the present case, the variation was probably due to the sidewall treatment and its effect on base pressure as well as the free stream turbulence variation with tunnel speed. More peculiarly, the spring-mounted cylinder did not respond at a frequency ratio $f_f/f_{so} = 0.50$ as found by Toebes [10] and Linenhard and Liu [12]. Effectively for this mode, every other shed vortex of the same sign would contribute to the exciting force for half of a cycle. The spectral analysis, however, for the cylinder undergoing forced oscillation near $f_f/f_{so} = 0.50$ indicated conditions similar to $f_f/f_{so} = 0.33$. So, explanation in terms of subharmonic response cannot be altogether consistent either.

A vortex shedding sequence which encompasses aspects of both the low frequency vortex street hypothesis and the subharmonic response hypothesis is depicted in Fig. 8. During fundamental mode response, which is shown for comparison, vortex shedding is enhanced by motion of the cylinder. The lateral velocity promotes separation causing a vortex to form. The resulting force thus bears the proper relationship to the velocity.

Basically, the same sequence can occur with two intervening vortices added. The extra vortices are located at positions in the cycle such that separation is inhibited, thus resulting in weaker vortices. The ensuing forces do not act in the direction of motion and thus tend to retard motion. However, under conditions of small damping, as in the present study, sufficient energy is put into each half-cycle by every third vortex to overcome damping and the retarding force of the intervening vortices. Velocity fluctuations in the wake would exhibit frequencies of f_{so} and $f_{so}/3$. It would seem that there is no possible arrangement which can result in a similar sequence at $f_{so}/2$. In this case, of course, equation (1) cannot estimate the lift coefficients. Ericsson [25] has extended this method of description to explain other lateral modes as well as in-line modes experimentally observed by Wootten, et al. [26] and King [1].

Conclusions

Lower mode response of elastically mounted cylinders near $f_n = f_{so}/3$ can occur providing damping is small. Synchronization over finite bandwidth (lock-in) was not observed, however.

Similar response was not found for $f_n = f_{so}/2$.

A conceptual model which combines some features of a low frequency vortex street with subharmonic response can be used to explain lower mode response and the difference in observed behavior at $f_{so}/2$ and $f_{so}/3$.

References

1 King, R., "A Review of Vortex Shedding Research and its Application," *Ocean Engineering,* Vol. 4, 1977, pp. 141–171.

2 Bishop, R. E. D., and Hassan, A. Y., "The Lift and Drag Forces on a Circular Cylinder Oscillating in a Flowing Fluid," *Proceedings of the Royal Society* (London), Series A, Vol. 277, 1964, pp. 51–75.

3 Koopmann, G. H., "The Vortex Wakes of Vibrating Cylinders at Low Reynolds Numbers," *Journal of Fluid Mechanics,* Vol. 28, Part 3, 1967, pp. 501–512.

4 Toebes, G. H., and Ramamurthy, A. S., "Fluidelastic Forces on Circular Cylinders," *Journal of the Engineering Mechanics Division,* Proceedings of the American Society of Civil Engineers, Vol. 93, EM 6, 1967, pp. 1–20.

5 Jones, G. W., "Unsteady Lift Forces Generated by Vortex Shedding About a Large, Stationary and Oscillating Cylinder at High Reynolds Numbers," ASME Paper No. 68-FE-36, 1968.

6 Blevins, R., "Vortex Induced Vibration of Circular Cylindrical Structures," ASME Paper No. 72-WA/FE-39, 1972.

7 Hartlen, R. T., and Currie, I. G., "Lift-Oscillator Model of Vortex-Induced Vibration," *Journal of Engineering Mechanics,* Proceedings of the American Society of Civil Engineers, Vol. 96, EM 5, 1970, pp. 577–591.

8 Skop, R. A., and Griffin, O. M., "An Heuristic Model for Determining Flow-Induced Vibrations of Offshore Structures," OTC 1843, Offshore Technology Conference, Dallas, Texas, 1973.

9 Iwan, W. D., and Blevins, R. D., "A Model for Vortex Induced Oscillation of Structures," ASME JOURNAL OF APPLIED MECHANICS, Vol. 96, 1974, pp. 581–586.

10 Toebes, G. H., "The Unsteady Flow and Wake Near an Oscillating Cylinder," ASME JOURNAL OF BASIC ENGINEERING, Vol. 91, No. 3, 1969, pp. 493–505.

11 Penzien, J., "Wind Induced Vibration of Cylindrical Structures," *Journal of the Engineering Mechanics Division,* Proceedings of the American Society of Civil Engineers, Vol. 83, EM1, Jan. 1957, pp. 1–17.

12 Lienhard, J. H., and Liu, L. W., "Locked-In Vortex Shedding Behind Oscillating Circular Cylinders, with Application to Transmission Lines," ASME Paper 67-FE-24, Presented at the Fluids Engineering Conference, Chicago, Illinois, May 8-11, 1967.

13 Gowing, S., "An Investigation of the Aeolian Converter as a Power Generator," Report prepared for NSF-URP GY 1180, Worcester Polytechnic Institute, 1974.

14 Taneda, S., "Downstream Development of the Wakes Behind Cylinders," *J. Phys. Soc. Japan,* Vol. 14, 1959, pp. 843–848.

15 Durgin, W. W., and Karlsson, S. K. F., "On the Phenomenon of Vortex Street Breakdown," *Journal of Fluid Mechanics,* Vol. 48, 1971, pp. 507–527

16 Thomas, D. G., and Kraus, K. A., "Interaction of Vortex Streets," *Journal of Applied Physics,* Vol. 35, No. 12, 1964.

17 Zdravkovich, M. M., "Smoke Observations of the Wake of a Group of Three Cylinders at Low Reynolds Number," *Journal of Fluid Mechanics,* Vol. 32, Part 2, 1968, pp. 339–351.

18 Acton, E., "The Modeling of Large Eddies in a Two-Dimensional Shear Layer," *Journal of Fluid Mechanics,* Vol. 76, Part 3, 1976, pp. 561–592.

19 Christiansen, J. P., and Zabusky, N. J., "Instability, Coalescence, and Fission of Finite-Area Vortex Structures," *Journal of Fluid Mechanics,* Vol. 61, Part 2, 1973, pp. 219–243.

20 Griffin, O. M., and Votaw, C. W., "The Vortex Street in the Wake of a Vibrating Cylinder," *Journal of Fluid Mechanics,* Vol. 51, Part 1, 1972, pp. 31–48.

21 Stasaitis, J. F., "The Interaction of Elastically Mounted Cylinders with Secondary Vortex Streets," M.S. thesis, Worcester Polytechnic Institute, 1976.

22 Lefebvre, P. J., "An Investigation of Primary and Secondary Vortex Street Lock-In," M.S. thesis, Worcester Polytechnic Institute, 1977.

23 Blevins, R. D., and Burton, T. E., "Fluid Forces Induced by Vortex Shedding," ASME JOURNAL OF FLUIDS ENGINEERING, Vol. 98, 1976, pp. 19–24.

24 Blevins, R. D., *Flow Induced Vibration,* Van Nostrand Reinhold Company, New York, 1977.

25 Ericsson, L. E., and Reding, J. P., "Vortex-Induced Asymmetric Loads on Slender Vehicles," Report LMSC-D630807, Lockheed Missiles and Space Company, Inc., Sunnyvale, Calif., Jan. 1979.

26 Wootton, L. R., Warner, M. H., and Cooper, D. H., "Some Aspects of the Oscillations of Full-Scale Piles," IAHR Symposium on Flow Induced Structural Vibrations, Karlsruhe, Germany, 1972.

25 Ericsson, L. E., and Reding, J. P., "Vortex-Induced Asymmetric Loads on Slender Vehicles," Report LMSC-D630807, Lockheed Missiles and Space Company, Inc., Sunnyvale, Calif., Jan. 1979.

26 Wootton, L. R., Warner, M. H., and Cooper, D. H., "Some Aspects of the Oscillations of Full-Scale Piles," IAHR Symposium on Flow Induced Structural Vibrations, Karlsruhe, Germany, 1972.

DISCUSSION

L. E. Ericsson.[3] The interesting results obtained by Durgin, et al. [27], for subharmonic response to Karman vortex shedding on a cylinder in crossflow are very much in agreement with the findings in a recently completed analysis of vortex-induced asymmetric loads [28]. In Fig. 1 the case $f = f_{v0}/2$ has been added to Fig. 8 of reference [27], to illustrate the effect of the translatory deflection. The situation in Fig. 1 is analogous to that existing for a pitching airfoil [29]. The moving wall has a wall-jet-like effect on the boundary layer development between stagnation and separation points. The downstream moving wall delays separation and causes a large overshoot of static lift maximum on a pitching airfoil [29]. The upstream moving wall effect is to promote separation. This adverse effect is even more powerful than the beneficial effect of the downstream moving wall, as is demonstrated by Swanson's results for a rotating cylinder [30]. Returning to Fig. 1 it can be seen that for $f = f_{v0}$ at each vortex shedding event, alternating between top and bottom sides of the cylinder, the upstream moving wall effect promotes separation, thus enhancing the vortex-induced transverse force and causing the observed strong translatory response of the cylinder to the Karman vortex shedding [27]. At $f = f_{v0}/2$, however, the translatory velocity-moving wall effect is zero for the vortex shedding events taking place at maximum deflection. And at zero deflection, where the moving wall effect is maximum, it alternates between enhancing and opposing the vortex shedding, explaining why no cylinder response to the vortex shedding was observed at this frequency [27]. Finally, for $f = f_{v0}/3$, the maximum moving wall effect obtained at zero

[3] Lockheed Missiles and Space Co., Inc., Sunnyvale, Claif.

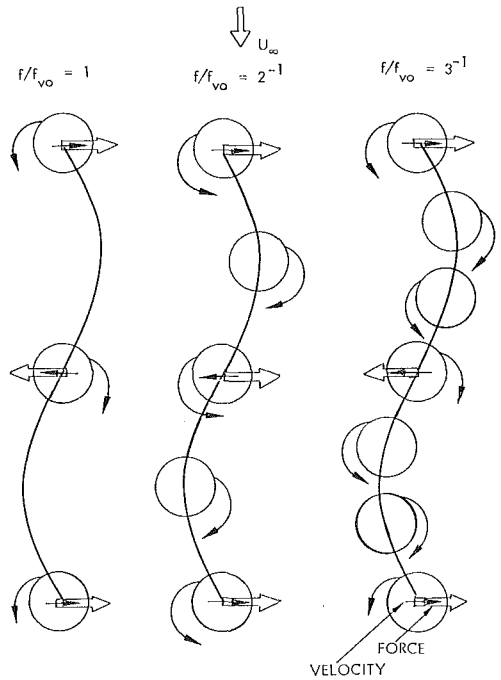

Fig. 1 Vortex shedding from translating cylinder at $f = f_{v0}$, $f = f_{v0}/2$ and $F = f_{v0}/3$

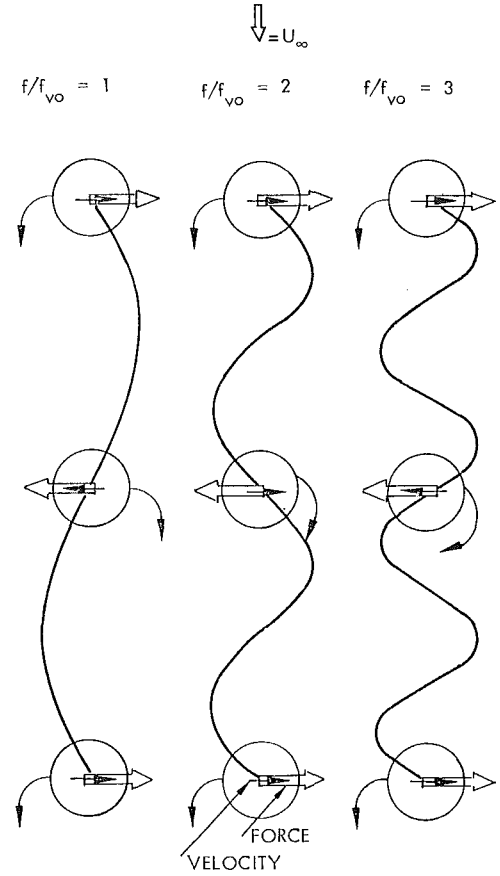

Fig. 2 Vortex shedding from translating cylinder at $f = f_{v0}$, $f = 2f_{v0}$ and $f = 3f_{v0}$

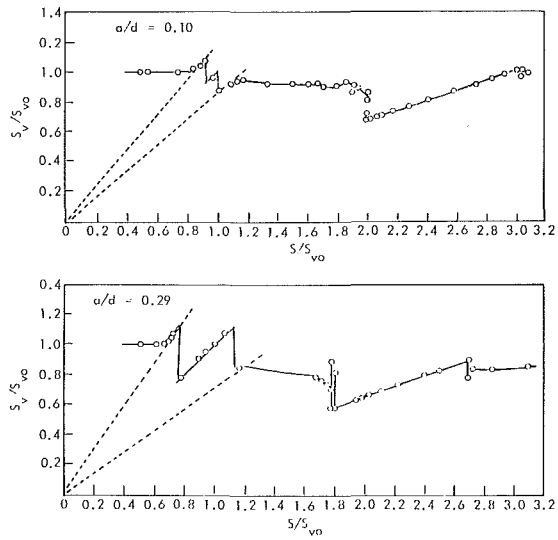

Fig. 3 Effect of translatory oscillation on cylinder vortex shedding

deflection always enhances the vortex shedding, as in the case of $f=f_{v0}$. For the intermediate pair of vortex shedding events occuring at near maximum deflection the translatory velocity with associated moving wall effect is very small. In addition, as was pointed out in reference [27], the (moving wall) effects are of opposite signs further diminishing the net effect of these two intermediate vortex shedding events at near maximum deflection.

Thus, one can see how the moving wall effect associated with the translatory oscillations can explain the observed subharmonic response at $f = f_{v0}/3$ and the absence of any response at $f = f_{v0}/2$. What about the superharmonic response? Figure 2 shows how in the case $f = 3\,f_{v0}$ every vortex shedding event is enhanced by the moving wall effect, whereas for $f = 2\,f_{v0}$ every other event is opposed by the translatory velocity effect. Thus, one would expect that locking-on of the vortex shedding phenomenon is possible at $f = f_{v0}$ and $f = 3\,f_{v0}$, but not for $f = 2\,f_{v0}$. This is exactly what the results obtained by Stansby [31] show (Fig. 3). There are lock-ins at $S_c = S_0$ and $S_c = 3\,S_0$, but no clear sign of locking-on at $S_c = 2\,S_0$.

Additional References

27 Durgin, W. W., March, P. A., and Lefebvre, P. J., "Lower Mode Response of Circular Cylinders in Cross Flows," ASME Winter Annual Meeting, San Francisco, Dec. 11–15, 1978, *Nonsteady Fluid Dynamics Volume*, pp. 193–200.

28 Ericsson, L. E., and Reding, J. P., "Vortex-Induced Asymmetric Loads on Slender Vehicles," Contract N60921-77C-0234, Report LMSC-D630807, Dec. 1978, Lockheed Missiles and Space Company, Sunnyvale, Calif.

29 Ericsson, L. E., and Reding, J. P., "Dynamic Stall Analysis in Light of Recent Numerical and Experimental Results," *Journal of Aircraft*, Vol. 13, No. 4, Apr. 1976, pp. 248–255. (Also AIAA Paper No. 75-26)

30 Swanson, W. M., "The Magnus Effect: A Summary of Investigations to Date," ASME *Journal of Basic Engineering*, Sept. 1961, pp. 461–470.

31 Stansby, P.K., "The Locking-on of Vortex Shedding due to Cross-Shear Vibration of Circular Cylinders in Uniform and Shear Flows," *Journal of Fluid Mechanics*, Vol. 74, Part 4, 1976, pp. 641–665.

C. Dalton
Department of Mechanical Engineering.

B. Chantranuvatana
Formerly Graduate Assistant.

Univ. of Houston,
Houston, Texas 77004

Pressure Distributions Around Circular Cylinders in Oscillating Flow

Oscillatory motion of a circular cylinder is studied from the viewpoint of the average pressure distribution on the cylinder. Effects of Reynolds number up to 40,000, period, and Keulegan and Carpenter number on the pressure distribution are examined. Results are explained in terms of vortex shedding and its relationship to period and Keulegan-Carpenter number. The effects of flow reversal, sweeping wake vortices back over the cylinder, are discussed.

Introduction

Numerous studies have examined the problem of determining the forces acting on a circular cylinder immersed in a uniform steady crossflow. The force description consists of a steady drag component, a fluctuating lift component at the vortex shedding frequency and an oscillating drag component at twice the vortex shedding frequency. The usual method of determining the drag (or lift) is by measuring the force on the cylinder instead of measuring independently the pressure and shear stress distributions. Measurement of the force is usually not direct, but involves measuring the force-induced strain. This is typically done with strain-gage transducers of varied type. Several of the more prominent studies which have used this technique are Fung [1], Bishop and Hassan [2], and Vickery [3]. All of these investigators applied the strain-gage method of determining the fluctuating lift and drag on cylinders immersed in an otherwise steady flow.

Since the total force is composed of both pressure and friction components, individual measurement of their average distributions also allows the drag to be determined. Achenbach [4] took this approach in determining the drag at Reynolds numbers up to 5×10^6. Achenbach's results agreed quite well with earlier studies that measured total drag; these results also provided a connection between previous subcritical and supercritical Reynolds number tests.

Frequently, the drag acting on a circular cylinder is determined by measuring the average pressure distribution around the circumference. This method yields only the pressure component of force. However, when the Reynolds number is greater than about 10^3, over 97 percent of the total drag is attributable to pressure drag. This value fluctuates somewhat at the transcritical region, according to Achenbach, but remains less than 97 percent up to a Reynolds number of 5×10^6. Since the pressure is the dominant mechanism of drag at high Reynolds numbers, a knowledge of its distribution is quite helpful in understanding the drag problem.

Several studies have considered the problem of drag determination from the viewpoint of measuring only the average pressure distribution around the cylinder circumference. Grove, et al., [5] measured the circumferential pressure distribution around a circular cylinder for (low) Reynolds numbers between 76 and 191. This was done using a manometer tap in the wall of the cylinder. Pressure distributions were related to wake characteristics to aid in the understanding of the drag problem.

Roshko [6] performed a series of experiments on circular cylinders at Reynolds numbers up to 8.4×10^6. His intent was to obtain additional drag data at high Reynolds numbers. The drag was measured by means of the average circumferential pressure distribution. The pressure measurements were made with taps at 10 deg intervals over half of the circumference.

Batham [7] conducted a series of tests on smooth and rough cylinders in a range of transcritical Reynolds numbers from 1.1×10^5 to 2.4×10^5. Batham's primary purpose was to examine the effects of surface roughness and freestream turbulence on the average pressure distribution. His results agreed closely with those of Achenbach for the same physical parameters.

One of the few studies on pressure distribution available in unsteady flow is the effort of Schwabe [8]. This study reported on the impulsive start from rest to constant velocity and the accompanying wake development. Schwabe did not actually measure the pressure, but calculated it from a detailed analysis of flow visualization pictures. He gave average pressure profiles at different dimensionless times during the impulsive start. At small times, the pressure profile still retained some similarity to the potential flow distribution. For larger times, the calculated pressures had characteristics that were similar to a steady flow past a cylinder.

Studies in unsteady approach flow have been concerned with direct measurement of the force using strain-gage transducers. Keulegan and Carpenter [9], Sarpkaya [10], and Dalton, et al., [11] are among many who have examined the problem of a cylinder immersed in a time-dependent flow field. The physical problem is the wave force on an offshore platform.

Keulegan and Carpenter, in a pioneering study, considered

Contributed by the Fluids Engineering Division and presented at the Fluids Engineering Conference, New Orleans, La., March 10-13, 1980, of THE AMERICAN SOCIETY OF MECHANICAL ENGINEERS. Manuscript received by the Fluids Engineering Division, February 23, 1979. Paper No. 80-FE-8.

a horizontal cylinder in a standing wave field. They measured the force on the cylinder with a dynamometer utilizing strain gages. Keulegan and Carpenter were interested in predicting the time-dependent force on the cylinder. From their experiments, they sought to determine Fourier-averaged drag and inertia coefficients as a function of the Reynolds number, based on maximum velocity, and the period parameter, UT_m/d, which is also based on maximum velocity. (The period parameter as defined by Keulegan and Carpenter is now known as the Keulegan-Carpenter number). The work of Keulegan and Carpenter led Sarpkaya [10] to consider the flow past a cylinder in terms of the Fourier-averaged coefficients. Sarpkaya has conducted extensive experiments on fixed cylinders in harmonic flow to measure both lift and drag. The approach taken was to compare the measured force to the "Morison equation" (see Sarpkaya [10] for a concise interpretation of the Morison equation). The purpose of the comparison is to obtain the Fourier-averaged drag and inertia coefficients over a wave cycle to facilitate the computation of wave forces. Dalton, et al., [11] have treated the wave force problem from the point of view of sinusoidally oscillating the cylinder in a fluid otherwise at rest. The purpose was not to calculate drag and inertia coefficients but to obtain a better understanding of the time dependence of the force description. Dimensionless force plots were presented showing the effects of positive and negative acceleration on the instantaneous force at a given velocity. The time-dependent wake due to the difference in positive and negative acceleration was noted to have a significant effect on the instantaneous force.

The aforementioned studies in [9, 10, 11] have all been concerned with force as determined from strain-gage measurements of either force or bending moment. The unsteady pressure distribution was not measured or observed in the course of these experiments.

A recent study considered the effect of an oscillation about a mean velocity in the flow past a circular cylinder. In this study, Hatfield and Morkovin [12] examined the unsteady pressure as the freestream oscillation frequency approached the vortex shedding frequency. Their objective was to examine the possible resonant coupling mechanisms between freestream oscillations and vortex shedding. The coupling was found to be insignificant. The pressure measurement technique is, however, of interest. The pressure signal is transmitted from an opening in the surface of the cylinder through flexible tubing to a remote Pitran pressure transducer. This transducer has a high sensitivity, flat frequency response to 50,000 Hz, and an output voltage linearly proportional to input pressure in a specified range. Since the transducer is remote, corrections had to be made for the frequency response of the flexible tubing.

An obvious gap in the study of time-dependent flow is in the development of the average pressure distribution in a sinusoidally oscillating flow field. The purpose of the present investigation was to examine this type of pressure distribution. Knowledge of the time-dependent pressure distribution could lead to a greater understanding of the oscillatory flow field and the resultant force description. The term "time-dependent average" pressure distribution needs defining. This term refers to the pressure distribution in a developing flow, but averaged over many cycles of the harmonic oscillation. Therefore, the present study was intended to examine the time-dependent average pressure distribution around a circular cylinder in an oscillatory flow field.

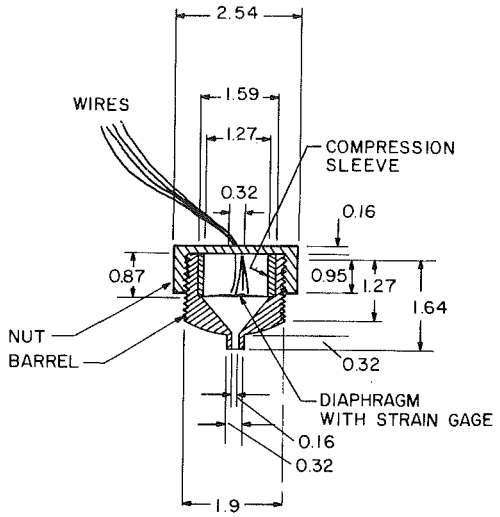

Fig. 1 Cross section of the pressure transducer (dimensions in cm)

Experimental Apparatus

These tests were conducted in a water tank in which the cylinder was oscillated in water which was otherwise at rest. The cylinder underwent a sinusoidal oscillation generated by a scotch-yoke mechanism. The tank is 0.61 m wide by 2.47 m long with a water depth of 0.43 m. The cylinder extended over the entire water depth with a clearance of 6 mm between the bottom of the cylinder and the bottom of the tank. The details of this experimental facility are described by Hamann and Dalton [13] and by Dalton, et al., [11] and will not be pursued further here.

The pressure transducer was developed especially for this investigation. The pressure transducer was mounted inside the cylinder with a small sensing port extending through the cylinder wall forming a smooth junction with the outside surface of the cylinder. The transducer is composed of a strain gage attached to a diaphragm mounted in a housing. A schematic of the transducer is shown in Fig. 1. The strain gages were BLH type FAES 4-44-35 S 13 with a resistance of 350.0 ohms in each leg. The diaphragm material was chosen to be aluminum and the diaphragm size was 0.127 mm thick and 12.7 mm in diameter. The strain gages were attached according to manufacturer's directions and were moisture-proofed with Gagekote.

Due to space limitations, only two pairs of transducers could be placed inside the test cylinder. Each pair consisted of an active transducer and a reference (dummy) transducer. The latter had its opening closed and was mounted in the same vertical position as the active transducer. Its function was to compensate for the inertia effect due to the oscillation of fluid inside the cavity of the transducer. The transducers were mounted flush with the outside wall of the cylinder and were held in place by means of specially made braces placed between the backs of the transducers and the adjacent inner wall

Nomenclature

a = amplitude of oscillation
C_p = pressure coefficient
d = cylinder diameter
KC = Keulegan-Carpenter number, $U_{max}T/d$
R = Reynolds number, UT/d
R_{max} = Reynolds number based on maximum velocity
T = period of oscillation
U = velocity
U_{max} = maximum velocity
θ = angle as measured from stagnation point
ω = circular frequency of oscillation

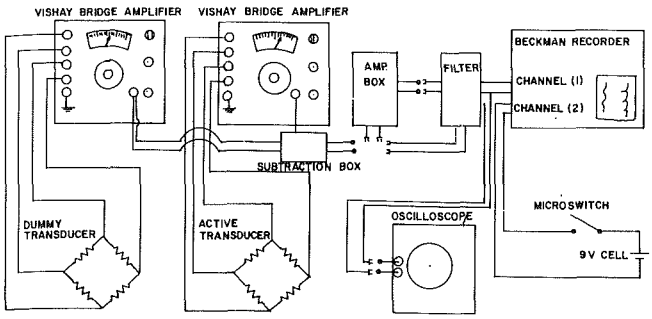

Fig. 2 Instrumentation block diagram

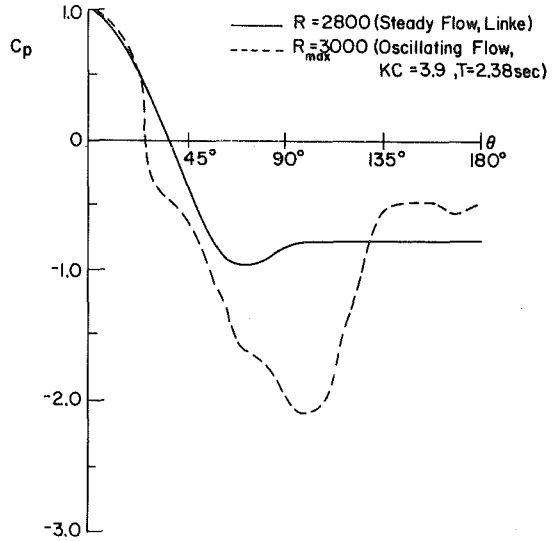

Fig. 3 Comparison of pressure coefficients in steady flow and oscillating flow (at maximum velocity) at approximately the same Reynolds number

of the cylinder. Mounting of the transducer required special attention due to the lack of space inside the cylinder. Epoxy and silicone rubber were applied to the outer surface of the pressure port openings. This procedure guarded against leakage of water into the cylinder which could have affected the wiring and moisture proofing material. The two pairs of transducers were located at 17.15 cm and 23.5 cm from the bottom of the cylinder and were 120 degrees apart. It was realized early in the study that an ordinary strain-gage lead wire could generate a fluctuating signal due to the movement of the wire (see Perry [14], p. 255). To eliminate this problem, a 4-lead shielded cable with 0.64 cm outside diameter was used. No disturbance of the signal was then observed.

The aluminum test cylinder was 4.1 cm in diameter. The upper end was rigidly attached to the mounting bracket on the scotch yoke assembly. The submerged part of the cylinder could be rotated about its vertical axis by means of a joint of 4 ball bearings. For the sake of simplicity in mounting of the transducers, the cylinder was built in three parts which were connected by sleeves and pins. Finally, the surface of the cylinder was polished and coated with spray paint for protection against corrosion.

The instrumentation package consisted of two Vishay bridge amplifiers, one for the active transducer and the other for the dummy, a two-channel thermal writing Beckman recorder, and a standby oscilloscope. This same instrumentation package has been described by Dalton, et al., [11].

A schematic diagram of the instrumentation is shown in Fig. 2. The signal from the dummy transducer was subtracted from the active transducer signal in the subtraction box. For low oscillations, the amplitude of the signal out of the subtraction box was quite small. A forty-gain amplifier was built to boost the signal level for these low oscillation cases. The signal was next passed through a ten-cycle notch filter. The filter was necessary to eliminate some friction noise, at approximately 10 Hz, which was due to the linear bearings of the scotch yoke mechanism. The filter had been built especially for this purpose based on observation, [11] and [13]. The output instrument was the Beckman recorder, which has a sensitivity selector which can be used to adjust the gain of the filter output.

The transducers were calibrated with a Meriam Instruments micromanometer, model 34FB2TM. This manometer has a high sensitivity over a pressure range of 0.025 mm to 25 cm of water pressure. Thus, a precise linear characteristic curve for each transducer was obtained.

Early in the investigation, it was found that, in the two pairs of transducers, higher output signals were given by the active of one and by the dummy of the other. This was due to the fact that the flexibilities were slightly different for the two diaphragms in a pair of transducers. To compensate for this difference, a variable resistor was placed in parallel between the output wires of the higher-output transducer. By proper adjustment of this resistor, the original higher characteristic curve could be made identical to the lower one.

Results

This study involves a developing boundary layer and wake. The characteristics of such a flow should be discussed prior to the interpretation of the time-dependent average pressure profiles. There have been several studies which have examined the flow characteristics of oscillatory flows. Sarpkaya [15] reported on the vortex formation and behavior during an oscillatory flow. The flow characteristics depend on the Keulegan-Carpenter number ($KC = U_{max} T/d$) as follows: As the cylinder moves in one direction, wake vortices are formed. For small values of KC (less than about 0.38) flow separation does not occur and no vortices form. For KC values up to about 5, a pair of wake vortices form but remain symmetrical and do not shed during motion in one direction. However, as the cylinder reverses direction, the pair of vortices move toward the cylinder and dissipate rapidly due to the increased relative velocity between the cylinder and fluid. As this occurs, a new pair of symmetric vortices forms in the new wake of the cylinder and the process is repeated.

For KC values between about 5 to 15, one vortex becomes larger than the other but conventional, alternate shedding does not yet occur. The vortices which have not yet broken away from their feeding layers before the flow reverses are only partially developed and are subject to the same rapid dissipation of energy mentioned earlier. The vortices that have been shed are swept past the cylinder thereby increasing the relative velocity and affecting the generation of new vortices in the new wake region. For values of KC greater than about 15, alternate shedding does occur. The number of vortices shed depends on both the KC value and the period of the oscillation.

This flow description is borne out by Heinzer and Dalton [16] who performed a flow visualization study of the oscillating cylinder problem. The observations by Sarpkaya were substantiated by these flow visualization studies. The formation and shedding of the vortices and their motion upon flow reversal was vividly demonstrated.

The developing average pressure distribution during an impulsive start of a circular cylinder from rest to a constant velocity is shown by Schwabe [8]. These results show that, as the boundary layer develops, the pressure adjusts from the initial potential flow distribution to the appropriate distribution for the given parameters.

The difference in steady flow and time-dependent average pressure distributions is shown in Fig. 3. The pressure-coefficient (C_p) plot for steady flow, by Linke [17] at a Reynolds number of 2800, shows the typical laminar boundary layer behavior. The measured oscillatory flow average pressure coefficient, shown at maximum velocity at a maximum Reynolds number of 3000, demonstrates the characteristics of the developing boundary layer. The cylinder has not moved sufficiently far (KC = 3.9 is much too small) for the steady flow pressure profile to be approximated. The difference between the two plots in Fig. 3 is aptly predicted by the preceding discussion. In fact, the irregularities in the first 80 deg of pressure coefficient plot for the oscillatory case can be explained by the motion of vortices past the cylinder upon flow reversal. This residual vorticity, being swept downstream, has influenced the upstream pressure.

The results to be presented are represented by the circumferential pressure-coefficient distributions from four sets of tests. Each set consisted of varying the oscillatory frequency through four values while holding the scotch-yoke oscillation amplitude constant. Table 1 gives a summary of the sequence of tests that were performed. All pressure coefficients are based on maximum velocity.

Typical average pressure coefficient plots are shown in Figs. 4 and 5. These typical plots show the variation of C_p with θ for four different situations: Maximum velocity, zero velocity and half-maximum velocity during acceleration and deceleration. Figure 4 shows the results for KC of 15.5, period of 3.84 s and a Reynolds number based on maximum velocity

Table 1 Parameters describing the test sequence

KC	period, T s	ω rad/s	R_{max} x10^{-3}
3.9	1.03	6.12	6.9
	1.36	4.62	5.2
	1.92	3.27	3.7
	2.38	2.65	3.0
7.73	1.02	6.13	13.8
	1.38	4.55	10.3
	2.72	2.31	5.2
	3.36	1.87	4.2
15.5	1.03	6.07	27.4
	1.44	4.36	19.7
	3.01	2.09	9.4
	3.84	1.63	7.4
23.2	1.07	5.86	39.6
	1.52	4.13	27.9
	3.06	2.05	13.9
	6.08	1.03	7.0

of 7400. This Reynolds number is well below the transition value of the laminar boundary layer. In spite of this, the maximum velocity plot of C_p versus θ appears similar to the steady flow turbulent boundary layer distribution. This is explained by the preceding discussion on the flow field development. The combined influence of vortices sweeping by the cylinder during flow reversal and the developing boundary layer both have affected the average pressure distribution. Also shown in Fig. 4 are pressure coefficient plots at a velocity of one-half maximum velocity, one case for accelerating flow and the other for decelerating. The accelerating flow should generate a larger force on the cylinder than the declerating flow. This is verified in Fig. 4 by the larger negative pressure distribution over the rear portion of the cylinder. At zero velocity, the pressure coefficient distribution does not produce zero force as would be expected for steady flow. The effect of the time-dependent wake accounts for the negative pressure distribution over the cylinder surface.

A higher Reynolds number case is shown in Fig. 5. The Reynolds number based on maximum velocity is 27,900, KC

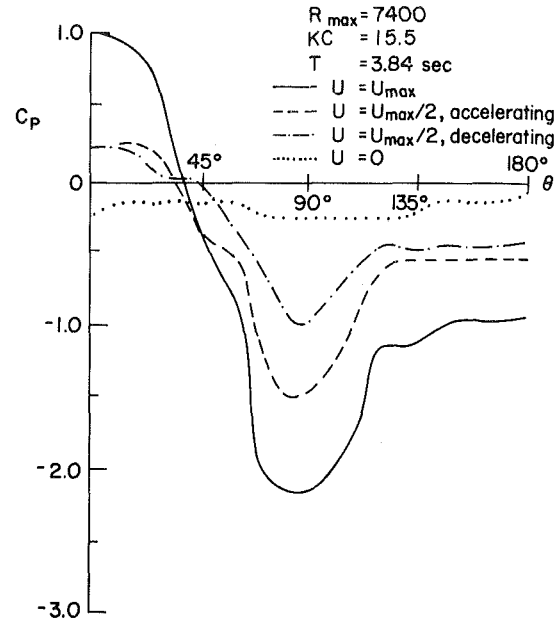

Fig. 4 Pressure coefficients at a Reynolds number of 7400, KC = 15.5 and T = 3.84 s. (Uncertainty interval on C_p is ±0.117.)

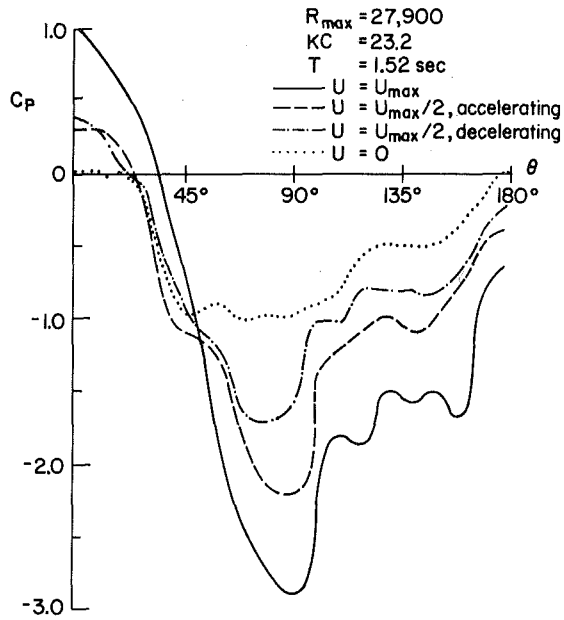

Fig. 5 Pressure coefficients at a Reynolds number of 27,900, KC = 23.2 and T = 1.52 s. (Uncertainty interval on C_p is ±0.075.)

is 23.2, and the period is 1.52 s. The same trends as noted for Fig. 4 are noted here for the maximum velocity and half-maximum velocity pressure coefficient plots. A notable difference is the larger negative value at maximum velocity. This is explained due to the smaller elapsed time (a period of 1.52 s as opposed to 3.84 s) in Fig. 4. In the smaller period test, the flow field did not have sufficient time to develop as contrasted to the larger period test. Another notable difference is in the zero velocity pressure coefficient distribution; its negative amplitude greatly exceeds that shown in Fig. 4. One means of explaining this difference is the larger KC value in the latter case (23.2 as compared to 15.5). For KC values this large, there would be several cycles of vortices shed during one half cycle of motion. The return motion of the cylinder occurs over a greater distance with a longer (in length) sequence of vortices available to be swept over the

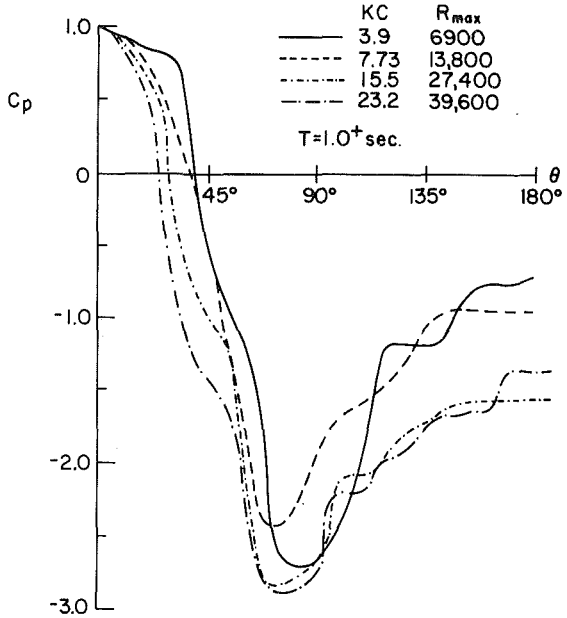

Fig. 6 Comparison of pressure coefficients at $T = 1$ s and varying KC (Maximum uncertainty interval on C_p is ± 0.051.)

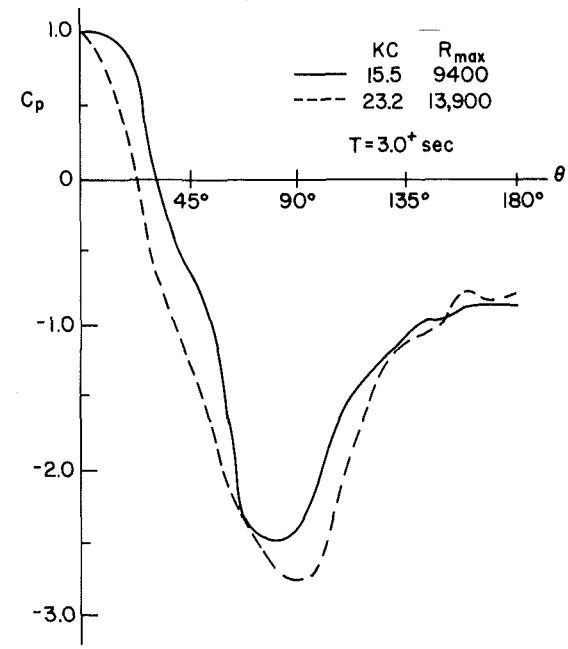

Fig. 7 Comparison of pressure coefficients at $T = 3$ s and varying KC. (Maximum uncertainty interval on C_p is ± 0.051.)

cylinder. In fact, this could also contribute to the greater negative pressure for the maximum velocity case.

A comparison of results available at essentially the same period (approximately 1 s) is available in Fig. 6. For the two lowest KC values, an established shedding process has not yet developed. For the two highest KC values, vortex shedding is more developed, especially at the higher KC value. The developed shedding pattern explains the larger negative wake pressure distributions for the two highest KC value cases. It is also noted in Fig. 6 that the pressure distribution on the forepart of the cylinder decreases with increasing KC. An explanation of this is that the wake vortices extend in extent as KC increases. As the longer sequence of vortices sweeps back over the cylinder when motion reverses, the relative velocity increases and the result is a lower pressure distribution on the forepart of the cylinder. This same observation can be made from Fig. 7, which is a comparison of two different KC maximum-velocity pressure plots at approximately a 3 s period. The larger KC value has a lower pressure on the forepart of the cylinder of the reasons just cited for Fig. 6.

Conclusions

An objective of this study was the examination of the average pressure distribution on an oscillating cylinder to obtain a better understanding of how the pressure is affected by the flow field. The presence of the wake vortices upon flow reversal was found to affect the pressure distribution in an understandable and predictable way. It was found that, for the small values of Keulegan-Carpenter number studied, the pressure distributions at maximum velocity did not closely match the steady flow pressure distributions. The KC value was found to affect the pressure distribution at a given period by causing the pressure on the forepart of the cylinder to decrease and the wake pressure to decrease as KC increases. The wake vortices affected the pressure distributions by increasing the relative velocity between cylinder and fluid. It is felt that these results add to the understanding of time-dependent flows and, ultimately, to wave forces on offshore structures.

This study, however, does not address the problem of the instantaneous pressure distribution around the oscillating cylinder. The asymmetry of the flow due to vortices, both fore and aft of the cylinder, and the effect on the instantaneous pressure distribution could not be determined from the experimental program that was conducted. Instead, the average pressure distribution, in the sense of Schwabe's study [8], was measured to identify the differences from the steady flow average pressure distribution. Measurement of the instantaneous pressure distribution in oscillatory flows is currently underway by the first author.

References

1 Fung, Y. C., "Fluctuating Lift and Drag Acting on a Cylinder in a Flow at Supercritical Reynolds Numbers," *J. Aerospace Sci.*, Vol. 27, 1960, p. 801.

2 Bishop, R. E. D., and Hassan, A. Y., "The Lift and Drag on a Circular Cylinder in a Flowing Fluid," *Proc. Roc. Soc. Lon.* A, Vol. 277, 1963, p. 32.

3 Vickery, B. J., "Fluctuating lift and drag on a long cylinder of square cross-section in a smooth and in a turbulent stream," *J. Fluid Mech.*, Vol. 25, 1966, p. 481.

4 Achenbach, E. "Distribution of Local Pressure and Skin Friction Around a Circular Cylinder in Cross-flow up to Re = 5×10^6," *J. Fluid Mech.*, Vol. 34, 1968, p. 625.

5 Grove, A. S., Shair, F. H., Peterson, E. E., and Acrivos, A., "An Experimental Investigation of the Steady Separated Flow Past a Circular Cylinder," *J. Fluid Mech.*, Vol. 19, 1964, p. 60.

6 Roshko, A., "Experiments on the Flow Past a Circular Cylinder at Very High Reynolds Numbers," *J. Fluid Mech.*, Vol. 10, 1961, p. 345.

7 Batham, J. P., "Pressure Distribution on Circular Cylinders at Critical Reynolds Numbers," *J. Fluid Mech.*, Vol. 57, 1973, p. 209.

8 Schwabe, M., "Pressure Distribution in Nonuniform Two-dimensional Flow," *Translation: Nat. Adv. Comm. Aero., Tech. Mem.*, No. 1039, Feb. 1935.

9 Keulegan, G. H., and Carpenter, L. H., "Forces on Cylinders and Plates in an Oscillating Fluid," *J. Res.*, NBS, Vol. 60, 1958, p. 423.

10 Sarpkaya, T., "Forces on Cylinders and Spheres in a Sinusoidally Oscillating Fluid," ASME *Journal of Applied Mechanics*, Vol. 42, 1975, p. 32.

11 Dalton, C., Hunt, J. P., and Hussain, A. K. M. F., "The Forces on a Cylinder Oscillating Sinusoidally in Water: Further Experiments," ASME *Journal of Pressure Vessels Technology*, Vol. 100, 1978, p. 297.

12 Hatfield, H. M., and Morkovin, M. V., "Effect of an Oscillating Free Stream on the Unsteady Pressure on a Circular Cylinder," ASME JOURNAL OF FLUIDS ENGINEERING, Vol. 95, 1973, p. 249.

13 Hamann, F. H., and Dalton, C., "The Forces on a Cylinder Oscillating Sinusoidally in Water," ASME *Journal of Engineering Industry*, Vol. 93, 1971, p. 1197.

14 Perry, C. C., and Lissner, H. R., *The Strain Gage Primer*, 2nd ed., McGraw-Hill, New York, 1962.

15 Sarpkaya, T., "In-Line and Transverse Forces on Cylinders in Oscillatory Flow at High Reynolds Numbers," *J. Ship Res.*, Vol. 21, 1977, p. 200.

16 Heinzer, A., and Dalton, C., "Wake Observations for Oscillating Cylinders," ASME *J. Basic Engineering*, Vol. 91, 1969, p. 850.

17 Linke, plot taken from M. V. Morkovin, "Flow Around a Circular Cylinder—a Kaleidoscope of Challenging Fluid Phenomena," ASME Symposium on Fully Separated Flows, 1964, p. 104.

Measurement of Instantaneous Pressure and Velocity in Nonsteady Three-Dimensional Water Flow by Means of a Combined Five-Hole Probe

S. Matsunaga
Professor.

H. Ishibashi
Associate Professor.

M. Nishi
Associate Professor.

Department of Mechanical Engineering,
Kyushu Institute of Technology,
Tobata, Kitakyushu,
Japan

A new combined five-hole probe with hemispherical head of 2.0 mm diameter is developed for the measurement of nonsteady three-dimensional water flow. Each pressure hole is connected to a small semiconductor pressure transducer, which has a high frequency response, and the instantaneous pressure can be measured continuously by the probe. In the case of nonsteady flow, pressures detected by the probe are affected by the inertia due to flow unsteadiness. Therefore, in order to achieve an accurate nonsteady flow measurement, it is vital to reduce the inertial effects from the pressure reading. In the present study the inviscid flow analysis was carried out to evaluate the error due to the inertial effect, and the iterative correction procedure was examined by computer simulation.

Introduction

In order to achieve further improvement of the performance of hydraulic machinery, it is vital to understand the behavior of the turbulent flow inside the machine, where the flow has three-dimensional and nonsteady characteristics.

Hot-wire and hot-film velocimeters are commonly employed to measure the magnitude and the direction of a fluctuating velocity. These work well in the case of gas flow; however, these velocimeters are not suitable for velocity measurement in water flow because the sensing elements are very fragile and sensitive to dirt contamination. A laser-doppler velocimeter is a powerful tool [1] because of its distinguishing feature of not disturbing the flow field, although it cannot measure pressure and velocity simultaneously.

Since pressure-related data together with velocity data are required to evaluate the efficiency of turbomachines, various types of pitot tubes have been employed with electronic micro-pressure-transducers of high frequency response. Senoo, et al., [2] measured the two-dimensional periodic flow at the exit of a pump impeller with the cobra probe which was fixed to the pump casing. Castorph and Raabe [3] studied the unsteady three-dimensional flow field of a Kaplan runner by means of a 6-hole conical probe. Both authors demonstrated that combined multihole probe systems were well-established instruments for nonsteady water flow, providing that the influence of nonsteadiness on the pressure reading was negligible.

Regarding this assumption, as mentioned by Kovasznay, et al., [4], the surface pressure on a probe head in the nonsteady flow field is affected by the change in velocity. If this flow fluctuates rapidly, the inertial effect on the pressure readings can not be neglected. Significant errors will occur in the measured pressure and velocity data since the calibration curves are obtained in the steady or quasi-steady flow. Thus, it is necessary for accurate measurements to evaluate quantitatively the inertial effect on the pressure reading.

The present study is aimed toward establishing a procedure for reducing the inertial effect due to flow unsteadiness from the pressure reading, while the inertial effect due to the probe vibrations is excluded. To perform the objective, it is assumed that the reading of the probe is composed of the steady term and the inertial term, and the former is determined by the calibration test and the latter is approximated by inviscid theory. Since the instantaneous surface pressure at each pressure hole on the probe can be measured continuously, a method of successive approximation has been developed to calculate the inertial term from the time series data of the pressure readings. This iterative correction procedure for the inertial effect is examined by computer simulation.

Further, a new combined five-hole probe has been developed for the measurement of pressure and velocity in nonsteady three-dimensional water flow. A photograph of the present probe is shown in Fig. 1.

Combined Five-Hole Probe

To minimize the distortion of the flow field from the presence of a probe and also to reduce the effect of shear flow and the inertial effect on the pressure reading, the probe

Contributed by the Fluids Engineering Division for publication in the JOURNAL OF FLUIDS ENGINEERING. Manuscript received by the Fluids Engineering Division, February 22, 1979,

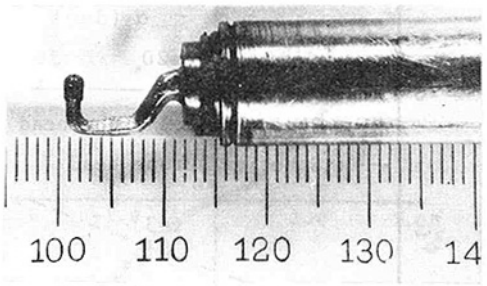

Fig. 1 A new combined five-hole probe

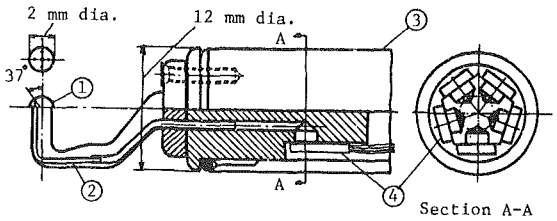

① Hemispherical probe head ② Pressure lead tube
③ Stem ④ Pressure transducer

Fig. 2 Construction of the designed probe

should be as small as possible. In the present study, attempts were made to reduce the size of probe head and to achieve the compact construction of the probe without introducing appreciable manufacturing difficulties. Figure 2 shows the details of the combined probe developed by the authors. The probe consists of a hemispherical head of 1 mm radius. On the surface of the hemispherical head are five pressure holes of 0.2 mm diameter arranged so that the four symmetrically spaced holes lie on a radius which makes an angle of 37 deg with the center hole. Five pressure lead tubes are individually connected to separate small semiconductor pressure transducers with a maximum pressure of 0.2 MPa and the natural frequency of 100 kHz. In order to secure quick response of the pressure sensing system of the probe, the length of each lead tube was made as short as possible. To eliminate the strong resonance peak via dampings, a silicon damping oil (kinematic viscosity, 20×10^{-6} m^2/s) was placed in these lead tubes using a vacuum pump.

Measurement of Frequency Response of the Probe. To examine the frequency response of the combined five-hole probe system, an apparatus, shown schematically in Fig. 3, was used. A 30 watts hydrospeaker was attached to one end of a closed pipe which was filled with water. A pressure transducer, which was used as the reference, was mounted on the pipe wall near the probe head. While varying the frequency of sound pressure signal from the hydrospeaker, all of the outputs of the five transducers for the probe and that of the reference transducer at the wall were recorded simultaneously. Figure 4 shows the measured frequency response of the pressure sensing system of the center pressure

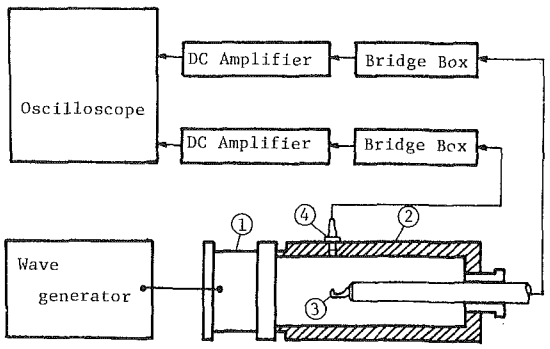

① Hydrospeaker ② Vessel
③ Combined five-hole probe
④ Pressure transducer

Fig. 3 Apparatus for measuring frequency response

hole. The dashed lines in the figure indicate the results predicted by the theory [5]. Table 1 shows relative frequency response referred to the system of the center pressure hole. It is seen that the differences among characteristics of five pressure sensing systems are considered negligible.

Theoretical Consideration. To analyze the behavior of a small probe placed in a three-dimensional nonsteady flow, a theory is developed assuming that the flow around the probe is incompressible and inviscid. According to the flow model

Nomenclature

a = radius of probe head
C_p = pressure recovery factor
f = frequency
f_i = function of α and δ (see equation (7))
f_α, f_δ = functions of X and Y (see equation (12), equation (13))
F_i, G_i, H_i = functions (see equation (16))
F_α = function (see equation (14))
$F_\delta, G_\delta, H_\delta$ = functions (see equation (15))
F_ϕ, G_ϕ, H_ϕ = functions (see equation (21))
G = gain
p = pressure
p_s = static pressure
r = radial distance
R = pipe radius
R_e = Reynolds number, $= 2aV/\nu$
V = magnitude of free-stream velocity
x, y, z = coordinate (see Fig. 5)
X, Y = ratios of pressure recovery factors
α = yaw angle
δ = pitch angle
γ = phase angle
θ = conical angle or the angle between the velocity vector and the probe axis z
θ_h = conical angle of pressure hole
ν = kinematic viscosity
ρ = density
ϕ = disturbance potential
ϕ^* = nondimensional disturbance potential, $= \phi/aV$

Subscript

i = ith pressure hole
The subscripts 1,2,3,4,5 refer to the five pressure holes: the center hole has the subscript 1, and the holes bearing the subscripts 2,1,3 lie in the equatorial plane and 5,1,4 lie in the meridional plane

Superscripts

$\rightarrow$ = vector
$'$ = steady term
$''$ = inertial term

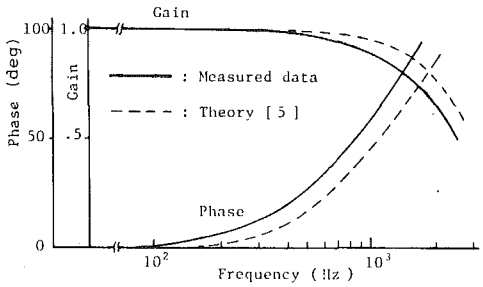

Fig. 4 Frequency response of the pressure sensing system of the center pressure hole on the probe

Table 1 Measured frequency response of the pressure sensing systems of the probe. Kinematic viscosity of a silicon damping oil is 20×10^{-6} m²/s. Uncertainty of G is within ±3 percent (odds of 20 to 1), and uncertainty interval of γ is within 5 deg (odds of 20 to 1).

Number of pressure hole	Measured gain G and phase angle γ (deg)			
	0.5 kHz		1.0 kHz	
	G/G_1	$\gamma-\gamma_1$	G/G_1	$\gamma-\gamma_1$
1	1.00	0.0	1.00	0.0
2	0.97	0.0	1.00	−3.0
3	1.00	2.0	1.00	−3.0
4	1.00	−1.0	0.99	−6.0
5	1.00	−1.0	1.10	−7.0

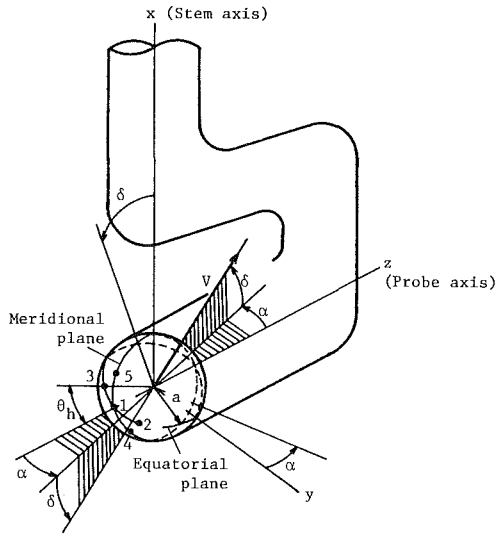

Fig. 5 Notation for a hemispherical probe head

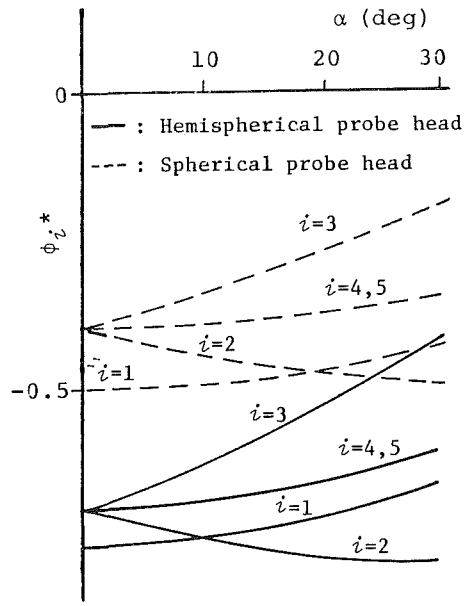

(a) δ = 0 (deg)

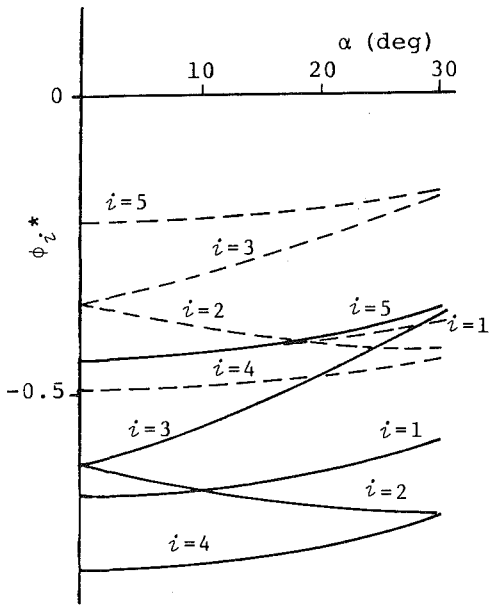

(b) δ = 28 (deg)

Fig. 6 Theoretical evaluation of the nondimensional disturbance potential

given in Fig. 5, where notation for the probe head is presented, x, y, and z components of free stream velocity **V** are defined as follows.

$$u = V\sin\delta,\ v = -V\sin\alpha\cos\delta,\ w = V\cos\alpha\cos\delta \qquad (1)$$

where V is the magnitude of the free-stream velocity.

Surface pressure p on the probe head is described using the pressure equation [6].

$$\frac{p}{\rho} = \frac{p_a}{\rho} - V\mathbf{e}\ (\text{grad}\ \phi) - \frac{1}{2}(\text{grad}\ \phi)^2 - \frac{\partial\phi}{\partial t} \qquad (2)$$

where ϕ is the disturbance potential and **e** is the unit vector of **V**.

A pressure-recovery factor C_p is defined by the following relation.

$$C_p = \frac{p-p_s}{\rho V^2/2} = C_p' + C_p'' \qquad (3)$$

where

$$C_p' = -\left\{V\mathbf{e}\ (\text{grad}\ \phi) + \frac{(\text{grad}\ \phi)^2}{2}\right\}\Big/\frac{V^2}{2} \qquad (4)$$

$$C_p'' = -\frac{\partial\phi}{\partial t}\Big/\frac{V^2}{2} = -\frac{2a}{V^2}\frac{\partial}{\partial t}(V\phi^*) \qquad (5)$$

C_p'' corresponds to the inertial term and is negligible in the case of steady or quasi-steady flow. If the shape of probe head is a sphere, the disturbance potential ϕ is obtained analytically, and C_p'' is expressed as in the next equation [4].

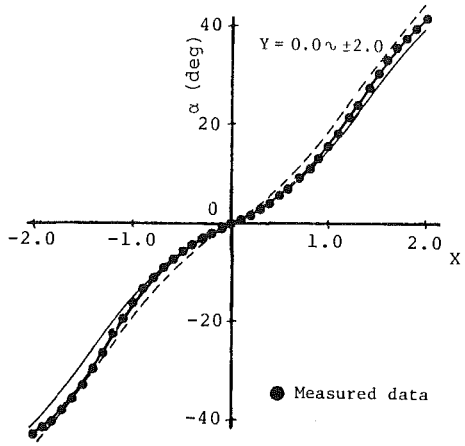

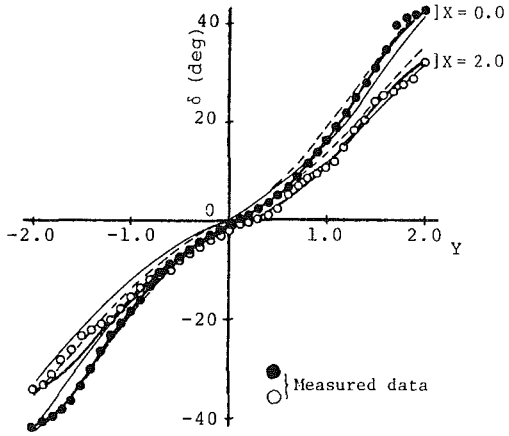

Fig. 7(a) Characteristics of angles, α and δ

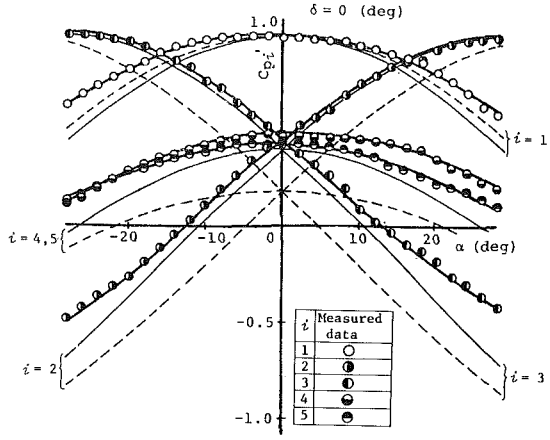

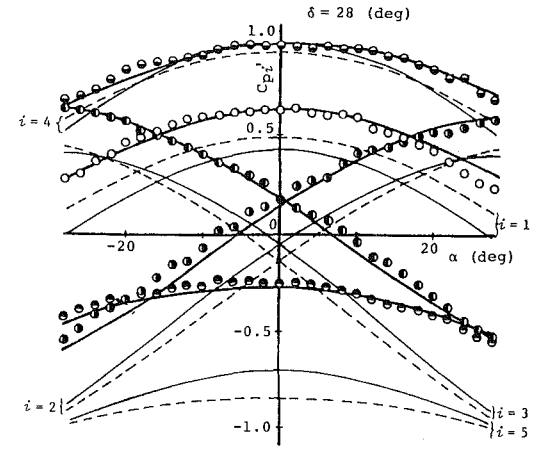

Fig. 7(b) Characteristics of pressure recovery factors, C_{pi}'

Fig. 7 Calibration curves for the five-hole probe. (▬▬ : experimental curve, ——: theoretical curve for a hemispherical probe head, - - -: theoretical curve for a spherical probe head. Uncertainty of C_{pi}' is within ±2 percent (odds of 20 to 1))

$$C_p'' = -\frac{a}{V^2}\frac{d}{dt}(V\cos\theta) \tag{6}$$

where a is the radius of sphere and θ is the conical angle which is defined as the angle between the velocity vector and the probe axis z.

As shown in equations (5) and (6), the inertial effect on the pressure reading is reduced by reducing the size of the probe head.

The disturbance potential ϕ for hemispherical probe head was numerically calculated by the singularity method [6], where the disturbance field was specified with three-dimensional doublets distributed along the axis of the body. Since the nondimensional disturbance potential, $\phi^* = \phi / (aV)$, is expressed as a function of two flow angles α and δ, the theoretical characteristics of ϕ^* with respect to the flow angles were developed beforehand to use for the correction of the inertial effect. Figure 6 shows some typical calculated results. The numbers in the figure indicate the corresponding pressure hole of the probe.

Three-Dimensional Calibration in Steady Water Jet. Characteristics of the steady term C_p' with respect to the angles α and δ must be determined experimentally because they deviate gradually from the theoretical characteristics when the angle between the velocity vector and the radial line through the pressure hole becomes large. Thus, C_{pi}' for the ith hole on the probe head is expressed as

$$C_{pi}' = f_i(\alpha, \delta) \tag{7}$$

For the influence of Reynolds number on the characteristics of C_p', it has been shown that the characteristics are practically independent for probe Reynolds number in the range between 4×10^3 and 1.5×10^5 [7], which corresponded to the range in the present experiments.

Considering various methods of presenting the calibration data for five-hole probe tested three-dimensionally in steady flow [7, 8, 9, 10], the ratios of recovery factors X and Y, which are defined as follows, are adopted.

$$X = (C_{p2}' - C_{p3}')/\Delta C_{pX} \tag{8}$$

$$Y = (C_{p4}' - C_{p5}')/\Delta C_{pY} \tag{9}$$

where

$$\left.\begin{aligned} \Delta C_{pX} &= C_{p1}' - C_{p3}' \quad (C_{p2}' \geqq C_{p3}') \\ \Delta C_{pX} &= C_{p1}' - C_{p2}' \quad (C_{p2}' < C_{p3}') \end{aligned}\right\} \tag{10}$$

$$\left.\begin{aligned} \Delta C_{pY} &= C_{p1}' - C_{p5}' \quad (C_{p4}' \geqq C_{p5}') \\ \Delta C_{pY} &= C_{p1}' - C_{p4}' \quad (C_{p4}' < C_{p5}') \end{aligned}\right\} \tag{11}$$

X and Y are determined by measuring the pressure difference

Table 2 R.M.S. deviation estimated for various ranges of measuring angle

	Order of polynomial			R.M.S. Deviation			
	G	H	F	$\theta = \pm 12°$	$\pm 20°$	$\pm 28°$	$\pm 40°$
α	0	0	5	0.51°	0.72°	1.00°	1.37°
δ	4	5	5	0.37°	0.36°	1.00°	2.45°
C_{p1}'	5	5	4	0.015	0.020	0.028	0.037
C_{p2}'	4	4	5	0.021	0.030	0.050	0.079
C_{p3}'	4	4	5	0.020	0.030	0.045	0.057
C_{p4}'	4	4	4	0.020	0.020	0.026	0.036
C_{p5}'	5	5	5	0.019	0.019	0.040	0.043

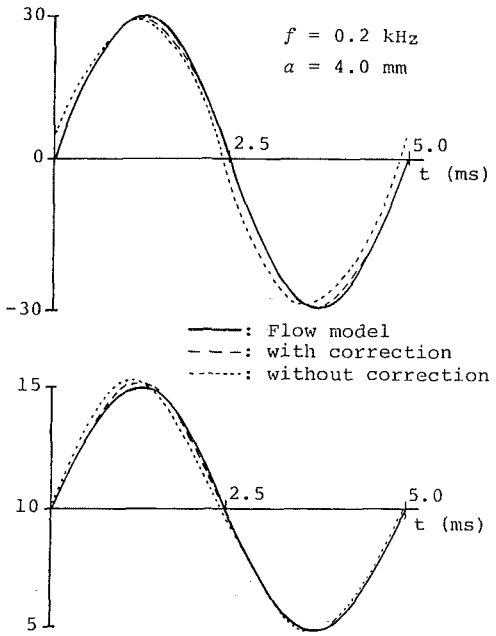

Fig. 8 Evaluation of the correction procedure. Solid lines correspond to the periodic flow model, where V_s = 10 m/s, V_0 = 5 m/s, α_s = 0 deg and α_0 = 30 deg are used in equation (25). Dotted lines indicate the results without correction of inertial effect, and dashed lines indicate those with correction of inertial effect. (α (deg): top, V(m/s): bottom)

between the corresponding holes on the probe head, if the orientation of the probe is prescribed with respect to the velocity vector. Thus, angles α and δ are expressed as the functions of X and Y.

$$\alpha = f_\alpha (X, Y) \tag{12}$$

$$\delta = f_\delta (X, Y) \tag{13}$$

To determine the functions f_i, f_α, and f_δ, the calibration tests in steady flow were performed using a circular water jet, taking care of the basic accuracy of the equipments. The probe was placed in a potential core of the jet, and the various pressures were obtained for the ranges of setting angles $-45 < \alpha < 45$ deg and $-45 < \delta < 45$ deg at a probe Reynolds number of 1.3×10^4. The angular position of the probe was measured within an accuracy of 0.5 deg.

Typical examples of the measured data are shown in Fig. 7 with circular marks. Figure 7(a) indicates the relationship between the angle and the ratio of recovery factors, and Fig. 7(b) indicates the variations of C_{pi}' with respect to the yaw angle α. As the yaw angle α was independent of the ratio of recovery factors Y, the functions f_α, f_δ, and f_i were approximated by the following relations.

$$\alpha = F_\alpha (X) \tag{14}$$

$$\delta = G_\delta (X)\, F_\delta (Y) + H_\delta (X) \tag{15}$$

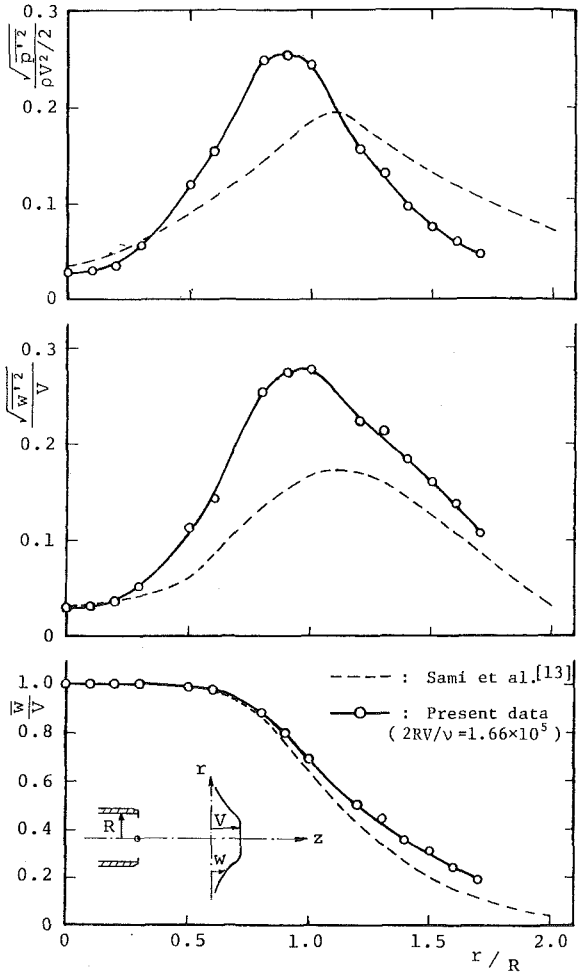

Fig. 9 Characteristics of the circular jet measured at the section of z/R = 6. '(prime) denotes fluctuations. (Uncertainty of $\bar{w}/V$ = ±0.03 (odds of 20 to 1))

$$C_{pi}' = G_i (\delta)\, F_i (\alpha) + H_i (\delta) \tag{16}$$

where F_α, F_δ, F_i, G_δ, G_i, H_δ, and H_i were represented in polynomial form, and all fits were obtained with a standard least squares technique.

Thick solid lines in Fig. 7 correspond to equations (14), (15), and (16), respectively, and these calibration curves agree well with the measured values. The r.m.s. deviations of polynomial form from experimental data are shown in Table 2 with respect to the measuring range of conical angle θ. From Fig. 7 and Table 2, it is suspected that 4th or 5th order polynomials may adequately describe the calibration data.

Correction of Interial Effect

In the experiments, analog outputs of the pressure trans-

ducers in the probe are recorded on a data recorder, and they are converted to digital values using a data acquisition system which continuously takes samples at certain time intervals and outputs paper tape or magnetic tape for data storage. Thus, for the compensating technique for the inertial effect, the following procedure based on a process of successive approximations using a digital computer is adopted, where it is assumed that the steady term p' in the pressure reading p at each instant is determined by the steady-state calibration curves (equation (16)).

Step 1: As a first approximation, pressures recorded as the time series data are assumed for steady state conditions so as to treat the inertial term being negligible, i.e., $p_i' = p_i$ ($i = 1$ to 5) at time t.

Step 2: The ratios X and Y at time t are obtained with the following relations.

$$X = (p_2' - p_3')/\Delta p_X \tag{17}$$

$$Y = (p_4' - p_5')/\Delta p_Y \tag{18}$$

where

$$\left.\begin{aligned} \Delta p_X &= p_1' - p_3' \quad (p_2' \geqq p_3') \\ \Delta p_X &= p_1' - p_2' \quad (p_2' < p_3') \end{aligned}\right\} \tag{19}$$

$$\left.\begin{aligned} \Delta p_Y &= p_1' - p_5' \quad (p_4' \geqq p_5') \\ \Delta p_Y &= p_1' - p_4' \quad (p_4' < p_5') \end{aligned}\right\} \tag{20}$$

Step 3: Using approximate values X and Y, the angles α and δ are determined with equations (14) and (15), respectively.

Step 4: With the knowledge of α and δ, five values of C_{pi}' are determined by polynomial equation (16), and five values of the nondimensional disturbance potential $\phi_i^* = \phi_i/(aV)$ are determined by the following relation which approximates theoretical results (see Fig. 6).

$$\phi_i^* = G_{\phi i}(\delta) F_{\phi i}(\alpha) + H_{\phi i}(\delta) \tag{21}$$

Step 5: V at time t is determined by the following equation.

$$V = \sqrt{2\ \Delta p_X/(\rho\ \Delta C_{pX})} \tag{22}$$

where Δp_x) is the pressure difference between two pressure holes corresponding to ΔC_{pX}.

Step 6: After V and ϕ_i^* are computed from the samples at all time levels repeating steps (2) through (5), five values of C_{pi}'' at time level t are calculated from the time derivatives of $V\phi_i^*$, which are computed numerically using a spline fit curve [11, 12].

Step 7: The static pressure p_s at time level t is calculated from equation (23).

$$p_s/\rho = p_1'/\rho - C_{p1}' V^2/2 \tag{23}$$

where p_1' is the steady term of pressure reading of the first hole.

Step 8: The pressure recovery factor C_{pi} is calculated from the relation $C_{pi} = (p_i - p_s)/\rho V^2/2$.

Step 9: The steady term C_{pi}' is determined by subtracting C_{pi}'' from C_{pi}.

Step 10: Five values of p_i' are calculated from the next equation.

$$p_i' = p_s + C_{pi}'\ \rho V^2/2 \tag{24}$$

Step 11: Each of them is compared with the corresponding assumed value of p_i'. If the differences between them are not within an allowable range, the assumed values of p_i' are corrected and steps (2) through (10) of the calculation are repeated. The process is mostly converged in several iterations.

Numerical Example. To examine how the procedure works, a computer simulation was conducted. A periodic flow model, where both the magnitude and the direction of velocity varied sinusoidally with respect to time, was adopted to represent the nonsteady flow.

$$\left.\begin{aligned} V &= V_s + V_0 \sin(2\pi ft) \\ \alpha &= \alpha_s + \alpha_0 \sin(2\pi ft) \\ \delta &= \delta_s + \delta_0 \sin(2\pi ft) \end{aligned}\right\} \tag{25}$$

where f is the frequency of the periodic flow.

Figure 8 shows the typical results for a spherical probe head of 8 mm diameter. Solid lines indicate the variation of yaw angle α and velocity V with respect to time given by equation (25) when the frequency f is set 0.2 kHz. The calculated results, given by dotted lines, were obtained neglecting the inertial effect. Dashed lines indicate the results obtained with the proposed correction procedure. From Fig. 8, it is seen that the procedure works well as the first order correction for the inertial effect.

In the case of the designed five-hole probe, since the head diameter is 2 mm, further reduction of inertial effect may be expected.

Applications

The combined five-hole hemispherical probe shown in Fig. 1 was used to measure the three-dimensional periodic flow downstream of mixed flow pump impeller [14] and to measure the fluctuating pressure and velocity in the developed region of a submerged circular water-jet. For example, Fig. 9 shows the distributions of the axial component of mean velocity $\overline{w}/V$, relative turbulence intensity $\sqrt{\overline{w'^2}}/V$ and r.m.s. pressure fluctuation $\sqrt{\overline{p'^2}}/\rho V^2/2$ in the jet measured at the section which is 6 times the nozzle radius from the nozzle exit. For comparison, air jet data in the literature [13] are reproduced in Fig. 9. The difference between them may be attributable to the difference of test conditions.

Conclusion

From the present study, the following conclusions are drawn:

1) A new combined five-hole probe with hemispherical head of 2 mm diameter has been developed. The probe is proving to be a handy instrument for measuring instantaneous pressure and velocity in nonsteady, three-dimensional water flow.

2) The correction procedure to reduce the inertial effect due to the change in flow velocity was established, which was needed to obtain the accurate measurement of nonsteady flow.

Acknowledgments

The authors would like to express their appreciation to Mr. Mitani and Mr. Uno, members of the Fluids Engineering Laboratory in the Kyushu Institute of Technology, for their assistance in the preparation of this paper.

References

1 Eckardt, D., "Detailed Flow Investigations Within a High-Speed Centrifugal Compressor Impeller," ASME JOURNAL OF FLUIDS ENGINEERING, Vol. 98, No. 3, 1976, pp. 390–402.

2 Senoo, Y., Kita, Y., and Ookuma, K., "Measurement of Two-Dimensional Periodic Flow With a Cobra Probe," ASME JOURNAL OF FLUIDS ENGINEERING, Vol. 95, No. 2, 1973, pp. 295–300.

3 Castorph, D., and Raabe, J., "Measurement of Unsteady Pressure, Unsteady Relative and Absolute Velocity Field of a Kaplan Runner by Means of an Electronic Multi-Miniature-Probe as a Basic Contribution to Research of Unsteady Runner Load," *Proceedings of the 7th IAHR Symposium,* Vienna, 1974.

4 Kovasznay, L. S. G., et al., "Instantaneous Pressure Distribution around a Sphere in Unsteady Flow," Technical Report, Dept. Mechanics, Johns Hopkins Univ., 1971.

5 Matsunaga, S., Nishi, M., and Takenaka, K., "The Dynamic Response of a Pressure Sensing System with Damping Tube," *Bulletin of Kyushu Institute of Tech.,* No. 32, 1976, pp. 47–52. (in Japanese)

6 Karamcheti, K., *Principles of Ideal-Fluid Aerodynamics,* John Wiley and Sons, Inc., New York, 1966.

7 Wright, M. A., "The Evaluation of a Simplified Form of Presentation for Five-Hole Spherical and Hemispherical Pitometer Calibration Data," *Journal of Physics,* E: Scientific Instruments, Vol. 3, 1970, pp. 356–362.

8 Lee, J. C. and Ash, J. E., "A Three-Dimensional Spherical Pitot Probe," *Trans.* ASME, Vol. 78, 1956, pp. 603–608.

9 Rubner, K. and Bohn, D., "Verfahren für die Auswertung der Meßergebnisse von Strömungssonden durch mehrdimensionale Approximation der Eichkurven und Eichflächen," *Zeitschrift für Flugwissenschaften,* Vol. 20, 1972, pp. 36–42.

10 Dudek, J. A., "A Calibration Procedure for Pressure Probes in Three-Dimensional Subsonic Flows," ASME Paper 73-WA/PTC-5.

11 Walsh, J. L., "The Best Approximation Properties of the Spline Fit," *J. Math. Mech.,* Vol. 7, 1962, p. 2.

12 Shaalan, M. R. A., and Daneshyar, H., "A Critical Assessment of Methods of Calculating Slope and Curvature of Streamlines in Fluid Flow Problems," *Proc. Instn. Mech. Engrs.,* Vol. 186, 1970/1972, pp. 891–896.

13 Sami, S., Carmody, T., and Rouse, H., "Jet Diffusion in the Region of Flow Establishment," *Journal of Fluid Mechanics,* Vol. 27, Part, 2, 1967, pp. 231–252.

14 Matsunaga, S., Ishibashi, H., and Nishi, M., "Accurate Measurement of Nonsteady Three-Dimensional Incompressible Flow by Means of a Combined Five-Hole Probe," *Nonsteady Fluid Dynamics,* ASME, 1978, p. 65–72.

E. B. Wylie
Professor of Civil Engineering.
Mem. ASME

V. L. Streeter
Professor Emeritus of Hydraulics.
Fellow ASME

University of Michigan,
Ann Arbor, Mich. 48109

Multidimensional Fluid Transients by Latticework

An evaluation of a discretized method of analysis for low-velocity two and three-dimensional transient fluid-flow problems is presented. The method assumes the continuum can be represented by a latticework of flow elements and that the physical response in the continuum can be determined by solving the one-dimensional transient flow equations in the line elements. The approach is explained, and validated by presenting comparisons between numerical and analytical hydrodynamic solutions.

Introduction

In 1968 Streeter and Wylie [1] proposed the use of a latticework of flow elements to simulate the continuum in the analysis of two and three-dimensional transients. The one-dimensional equations of motion and continuity were used, with no friction term, and the method of characteristics was used in the explicit solution procedure in such a way that the time increment to traverse each and every line element was the same. At that time the scaling parameter was not known, yielding results that lagged the actual continuum transient. Subsequently the authors applied the procedure to ground water flow in graduate course work, and determined the scaling parameter from continuity relationships when using a rectangular latticework of line elements with overlap. This work was reported in a paper by Wiggert and Wylie [2]. In 1975, Wylie [3] applied the method, with proper scaling, to a dam-reservoir hydroelastic problem, excited by seismic activity. He developed the scaling parameter from impedance considerations of lattice and continuum. In 1971 Fabic [4] developed the scaling parameter for square and cubic latticeworks by comparison of continuity and motion equations, using acoustical approximations. This work was extended into coding for solution of transient cases. In none of these works was the velocity at a point interpreted in a meaningful practical sense.

Since 1975 much work has been undertaken on the development of two-dimensional space transients by the characteristics method [7–11]. Rectangular grids are utilized and a potentially accurate scheme is generated. However, during implementation of the method, some form of numerical interpolation is required which results in numerical damping and dispersion of steep gradients. The general form of a transient response is modeled by the method [11].

When a continuum is replaced by a lattice of equal-length-flow elements, and a transient is imposed on the system at its boundaries, a "scattering" effect occurs at each node. This reduces the strength of the transmitted wave due to the multiple branching and effects a lag in the transient. By use of a scaling parameter, which modifies the acoustical wave speed, the lattice is able to accurately model the continuum, yielding the proper head-time relations at any node, and yielding the continuum velocity components at any node.

Since friction is not included in the lattice element equations, it may be shown that circulation around any closed circuit of the latticework is zero and, hence, a velocity potential exists. Due to discretization required by the lattice structure, there may be minor fluctuations in the results as compared with analytical solutions of high frequency excitations.

In this treatment the scaling concepts are developed, point velocities are defined, and the method then applied to one-dimensional flow through square and cubical grids. One-dimensional flow is then applied to equilateral triangular-lattice structures to demonstrate the use of grids other than square. Two-dimensional transients are studied with reference to square and triangular grid structures. Comparisons in each case are made with analytical continuum solutions.

The Method, Including Scaling Concepts

A multidimensional domain is represented by a grid of line elements as shown in Figs. 1(*a*), (*b*), and (*c*). In each line element the one-dimensional transient flow equations of motion and continuity are applied. At line-element intersections, which are visualized as points, a common pressure must exist and the mass conservation law must be satisfied at each instant of time. Irregularly-shaped boundaries may be described and allowed to interact with the line elements much as the physical boundary interacts with the continuum. Pressure waves and fluid particle velocities are transmitted and reflected within the latticework and at boundaries. Although the concept requires a finite discretization, in the limit as the line elements become shorter, the response from the grid approaches the physical response in the corresponding continuum.

The equations of motion for any direction in a continuum are identical to the equation of motion for a single line element, and hence do not need to be considered in deriving scaling relationships.

The continuity equation for three-dimensional flow is given by

$$(\rho u)_x + (\rho v)_y + (\rho w)_z + \rho_t = 0 \qquad (1)$$

Contributed by the Fluids Engineering Division for publication in the JOURNAL OF FLUIDS ENGINEERING. Manuscript received by the Fluids Engineering Division, December 26, 1978.

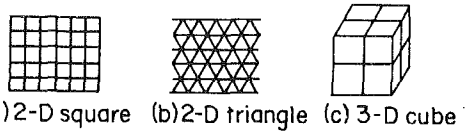

Fig. 1 Grid flow elements

in which u,v,w are velocity components in the x,y,z - directions, ρ is the mass density, t the time, and subscripts represent partial differentiation. If ρ_x, ρ_y, $\rho_z << \rho_t$, and the bulk modulus of elasticity is introduced, $K = \rho p_t/\rho_t$,

$$u_x + v_y + w_z = -\frac{\rho_t}{\rho} = -\frac{p_t}{K}$$

For two-dimensional flow $w_z = 0$, and for one-dimensional flow $v_y = w_z = 0$.

Considering any lattice of identical elements in three dimensional flow, with m lattice elements attached to a node, from divergence relationships

$$\frac{3}{m}(V_{1_{\xi 1}} + V_{2_{\xi 2}} + \ldots V_{m_{\xi m}}) = u_x + v_y + w_z = -\frac{p_t}{K} \quad (2)$$

V_1 is the velocity in lattice element 1 in the ξ_1 direction, and correspondingly for the other lattice elements. Since all lattice elements are identical and disturbances resulting from p_t are superimposed on existing flows, $V_{1_{\xi 1}} = V_{2_{\xi 2}} = \ldots V_{m_{\xi m}} = V_{\xi 1}$, yielding

$$3V_\xi = -\frac{p_t}{K}$$

For one-dimensional transient flow the continuity equation is

$$\rho a^2 V_\xi = -p_t$$

Since each lattice element is treated as a one-dimensional flow element, the last two equations must be the same, hence

$$a = (3K/\rho)^{1/2} = 3^{1/2} c \quad (3)$$

yielding the scaling relationship $(3)^{1/2}$ for any three-dimensional lattice of identical elements. By applying the same reasoning to two-dimensional flow $a = (2)^{1/2} c$ is the scaling relation between acoustic wave speed a in the element and acoustic velocity c in an infinite fluid.

Figure 2 illustrates a possible two-dimensional lattice, in that all elements have the same length and the same properties.

Another development of the use of the factor $(2)^{1/2}$ was presented in connection with a square grid used for reservoir modeling during seismic events [3]. In this case a criteria was sought that would provide the same response from the line element grid as from the continuum. An impedance of the latticework was determined so that it matched the characteristic impedance of the continuum. Again, for the two-dimensional square grid, the factor $(2)^{1/2}$ was needed as an elasticity multiplier.

By use of the acoustical equations, following the method of Fabic [4], the continuum equations of motion and continuity for a two-dimensional flow are

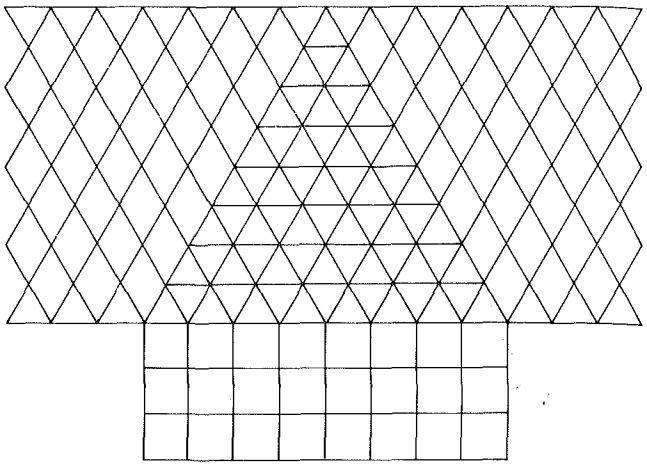

Fig. 2 Example of two-dimensional lattice

$$u_t + \frac{1}{\rho}p_x = 0, \quad v_t + \frac{1}{\rho}p_y = 0,$$
$$\rho_t + (\rho u)_x + (\rho v)_y = 0 \quad (4)$$

and for a square grid of elements:

Equations of Motion

$$u_t + \frac{1}{\rho}p_x = 0, \quad v_t + \frac{1}{\rho}p_y = 0 \quad (5)$$

Continuity Equations

$$\rho_t + (\rho u)_x = 0, \quad \rho_t + (\rho v)_y = 0$$

If we now consider a small transient fluctuation from rest

$$p = p_0 + p', \ \rho = \rho_0 + \rho', \ u = u', \ v = v'$$

$$\text{with } p' << p_0, \ \rho' << \rho_0, \ \rho' = p'/c^2 \quad (6)$$

then substitute into equations (4) and (5) and drop the primes, the following equations are found. For the continuum the equations are:

$$u_t + \frac{1}{\rho_0}p_x = 0, \quad v_t + \frac{1}{\rho_0}p_y = 0,$$
$$p_t + \rho_0 c^2(u_x + v_y) = 0 \quad (7)$$

and for the line elements, $\rho' = p'/a^2$:

Equations of Motion

$$u_t + \frac{1}{\rho_0}p_x = 0, \quad v_t + \frac{1}{\rho_0}p_y = 0 \quad (8)$$

Continuity

$$p_t + \rho_0 a^2 u_x = 0, \quad p_t + \rho_0 a^2 v_y = 0$$

In the square grid, at the intersection of elements, p_t is the same for each element, so the continuity equations (8) are added, yielding

Nomenclature

a = scaled acoustic velocity
c = acoustic velocity in infinite fluid
g = gravity
H = piezometric head
h = dimensionless pressure head
K = bulk modulus of elasticity
l = length of lattice element
m = number of attached lattice elements at a node
p = pressure
p_0 = static pressure
r = polar coordinate
t = time
u,v,w = velocity components
V = velocity in lattice element
x,y,z = coordinate directions
η = variable in analytic solution
θ = angle, polar coordinates
ξ = direction along a lattice element
ρ = mass density
ρ_0 = mass density at rest
τ = constant
ψ = variable in analytic solution
ω = angular velocity

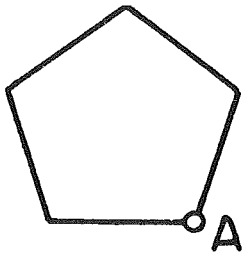

Fig. 3 Simple circuit of line elements

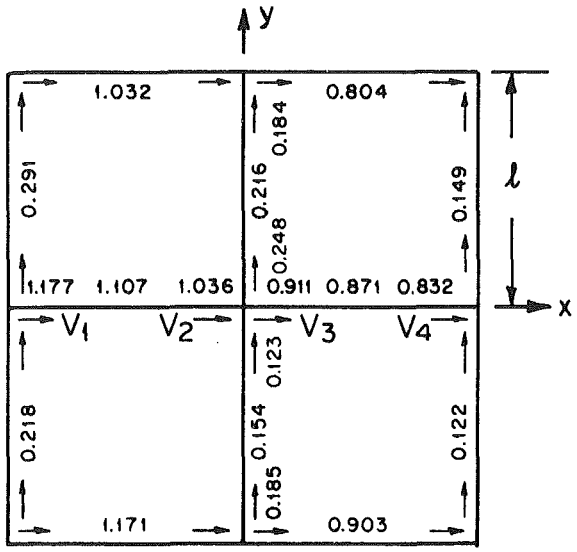

Fig. 4 Line element velocities, square grid

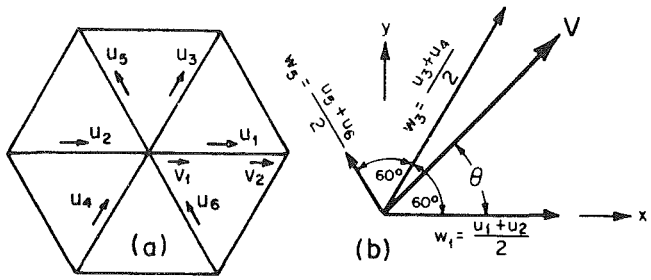

Fig. 5 Components of velocity vector, triangular grid

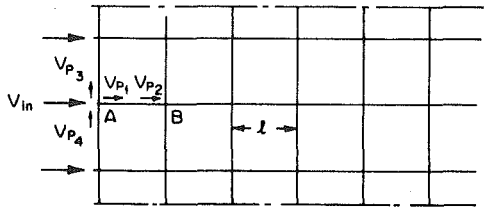

Fig. 6 Model for 1-D flow in 2- or 3-D grid

$$p_t + \frac{1}{2}\rho_0\ a^2(u_x + v_y) = 0 \tag{9}$$

This equation relates the pressure variation at the point to flow components in the two directions in the line elements. If the lattice line elements are visualized in the limit to be of differential size the continuity equations of (7) and (9) may be compared, and it is seen that the propagation velocity a in the lattice must be $(2)^{1/2}$ times the acoustic wave propagation velocity c in the continuum

$$a = (2)^{1/2}c \tag{10}$$

For the cubic latticework the same procedure may be applied to yield a scaling parameter of $(3)^{1/2}$. Comparisons between the equations of motion in (7) and (8) show them to be identical in the line elements and in the continuum.

Irrotational Flow and Velocity Definitions

The compatibility equations used in the method of characteristics, without friction, are [5]:

$$H_{P_B} = H_A - \frac{a}{g}\,(V_{P_B} - V_A) \tag{11}$$

$$H_{P_A} = H_B + \frac{a}{g}\,(V_{P_A} - V_B) \tag{12}$$

in which A and B designate the upstream and downstream ends of the line elements, variables with subscript P represent unknown values at the end of the time step, while variables H and V without P are used for the beginning of the time increment. In these equations the flow element has a length $l = a\,\Delta t$ with a the acoustic speed corrected for the scale factor, as shown in equation (10).

Application of these equations for each flow element at a junction, plus use of the continuity equation stating the net flow into the junction must be zero, permits solution for the variables at end of Δt if conditions are known at beginning of Δt. This is an *explicit* solution, in which each junction is solved independently of the other junctions. This provides an efficient procedure from a computer use viewpoint.

By starting from rest, and applying a small head change to a junction, as at A in Fig. 3, it may be noted that the same change in velocity is transmitted through the adjacent elements, thereby maintaining zero circulation around the circuit. With zero circulation throughout any simple circuit the concept of the velocity potential may be applied, and at any instant, the flow in each element (i.e., average of velocity at each end of the element) is the velocity component of the continuum in that direction. This defines an average velocity over the length of the element. To find the velocity at a node point, such as the center of Fig. 4, in the x-direction it is $(v_1 + v_2 + v_3 + v_4)/4$, and similarly for the y-direction. Figure 4 also shows line element velocities taken from computer output in the square grid. The condition of zero circulation is easily noted. In the equilateral triangular grid of Fig. 5(*a*), the average velocity of each line element is given as $u_1 = (v_1 + v_2)/2$. The circulation is zero, hence the velocities are components of the velocity vector for each triangle. To find velocity at a point, say the center, the three components, Fig. 5(*b*), are shown 60 deg apart. Any two may be used to find the magnitude and direction of the vector. Let the vector be shown, then

$$V\cos\theta = w_1$$
$$V\cos(60 - \theta) = w_3 \tag{13}$$

These are easily solved for V and θ the continuum vector for the point.

When inputting a velocity to the grid at the boundary the velocity vector at each boundary nodal point is known. The components may then be placed in the adjoining flow elements by use of the above procedure.

Applications

One-Dimensional Flow Through Square and Cubic Grids. As a simple demonstration of the procedures, one-dimensional flow through a square or a cubical grid parallel to a flow element is examined, Fig. 6. The velocity vector at the input boundary is given by $V = V_0 \sin \omega t$ for one-half

Table 1 Computed and continuum velocities

	2-D @ t = 0.017 s velocities, m/s		3-D @ t = 0.01380 s velocities, m/s	
distance, m	computed	analytical	computed	analytical
6	0.0	0.0	0.0001	0.0
7	0.0	0.0	0.0283	0.0290
8	0.0026	0.0006	0.0581	0.0585
9	0.0324	0.0332	0.0809	0.0814
10	0.0612	0.0621	0.0950	0.0950
11	0.0834	0.0839	0.0979	0.0977
12	0.0960	0.0970	0.0893	0.0892
13	0.0972	0.0972	0.0709	0.0704
14	0.0872	0.0872	0.0456	0.0436
15	0.0675	0.0672	0.0103	0.0119
16	0.0416	0.0395	0.0004	0.0
17	0.0075	0.0073	0.0	0.0
18	0.0002	0.0	0.0	0.0

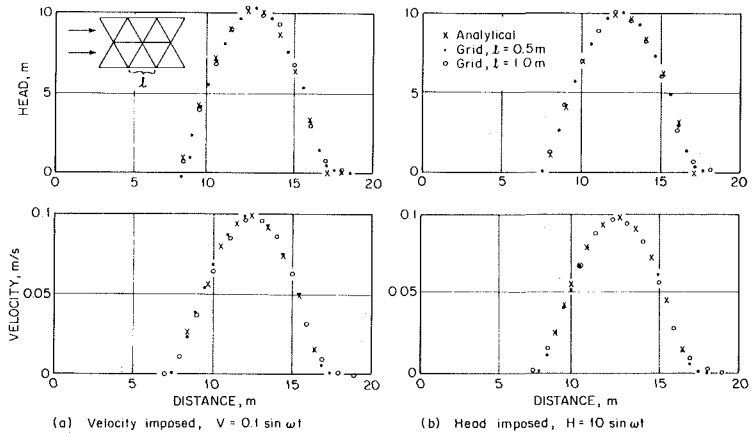

Fig. 7 Comparison; t = 0.017 s, flow parallel to side

period of excitation. From the definition of velocity at point A

$$(2\,V_{\text{in}} + V_{P_1} + V_{P_2})/4 = V \tag{14}$$

From continuity at node A, $V_{in} = V_{P_1} + (n\text{-}1)\,(V_{P_3} - V_{P_4})$, with $n = 2$ or 3 for two- or three-dimensional flow. These two equations plus the compatibility equations from the characteristics method, equations (11) and (12), provide five (seven) equations to solve for the five (seven) variables in the two (three) dimensional case. At any time step it is necessary to solve first for conditions at node B so that V_{P_2} is a known variable in equation (14).

A case study, using the following data, is presented: l = 0.25 m, c = 1000 m/s, ω = 340.087 rad/s, V_0 = 0.09806 m/s. After 96 time steps of calculation, the head and velocity was taken from computer output and compared with the analytical continuum solution, as shown in Table 1.

The computer output for head when velocity was input was equally good, and similarly head input at the boundary produced as satisfactory a comparison with analytical for both velocity and head.

One-Dimensional Flow Through Triangular Grid. Two cases are examined: first the case with flow direction parallel to a side, and second with flow normal to a side. Both head and velocity as a half sine wave are imposed at the boundary, and the resulting heads and velocities throughout the grid are compared with analytical continuum results.

The computer cases illustrated here have a coarser discretization than the previous cases, and some minor discrepancies may be seen in the plots. The excitations are the same as for the square grid, except for V_0 = 0.1 m/s. Figure 7 shows plots of numerical head and velocity versus distance from excitation point for flow parallel to a side for two discretizations. The analytic results in the continuum are also shown. The same basic agreement is achieved for flow normal to a side, i.e., at right angles through the same triangular grid.

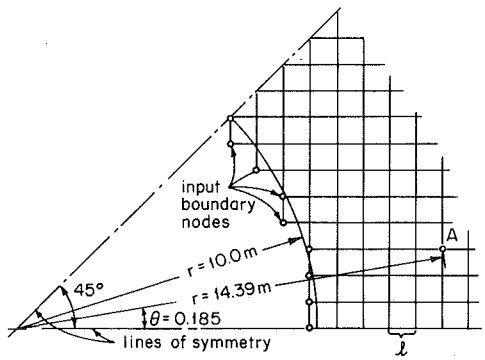

Fig. 8 Two-D example using square grid

Two-Dimensional Flow Through Square Grid. The transient pressures and velocities that develop in a continuum as a result of a line source can be calculated [6]. The theory assumes compressible potential flow with small velocities. The strength of the source at the origin is described as a function of time by the equation

$$f(t) = \frac{\tau}{t^2 + \tau^2} \tag{15}$$

in which τ is a constant. The dimensionless pressure head as a

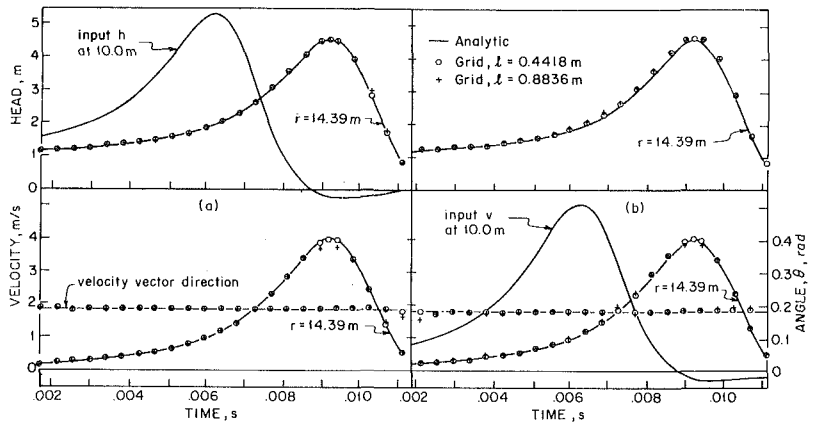

Fig. 9 Response as function of time, square grid

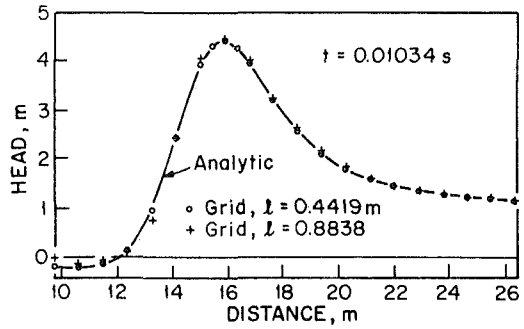

Fig. 10 Response at $t = 0.01034$ s, square grid

function of time, t, and distance, r, is given by:

$$h = 1 + \frac{1}{4gH_0}\left(\frac{c}{2r\tau^3}\right)^{1/2} \sin\left(\frac{\pi}{4} - \frac{3\eta}{2}\right)\cos^{3/2}\eta \qquad (16)$$

in which η is defined in the equation $t = r/c + \tau \tan \eta$. The dimensionless velocity is

$$v = \frac{1}{4V_0}\left(\frac{c\cos\eta}{2\tau r}\right)^{1/2}\left[\frac{1}{r}\cos\psi + \frac{c\tau}{c^2\tau^2 + (ct-r)^2}\right.$$
$$\left.(\sin\psi - \cos\psi\tan\eta)\right] \qquad (17)$$

in which $\psi = \pi/4 - \eta/2$. The quantities H_0 and V_0 are arbitrary heads and velocities used in nondimensionalizing the problem. Equations (16) and (17) are valid if $r >> c\tau$ and $t << 2r/c$.

A 45 deg sector of the two-dimensional space is modeled with the square grid, Fig. 8. Line element lengths of 0.8838 m are shown with the boundary approximated at $r = 10.0$ m. Input boundary nodes are shown, where either equation (16) or equation (17) was applied. Point A is identified at $r = 14.39$ m, $\theta = 0.185$ rad. Figure 9 shows the velocity and head at point A determined (a) analytically, (b) with $l = 0.8838$ m, and (c) with $l = 0.4419$ m. The input head, equation (16), used at the boundary nodal points is also shown. Figure 9(b) provides a similar comparison when velocity, as defined in equation (17), is used at the boundary nodes. Figure 10 shows a graph of pressure head versus distance at $t = 0.01034$ s, plotted using data along the x-axis. Figures 11(a) and (b) show contours of head and velocity as determined from the finer grid results. The arcs of circles show the analytic results as determined from equations (16) and (17). The velocity vector should be radial throughout the field and this proved to be the case in the numerical results.

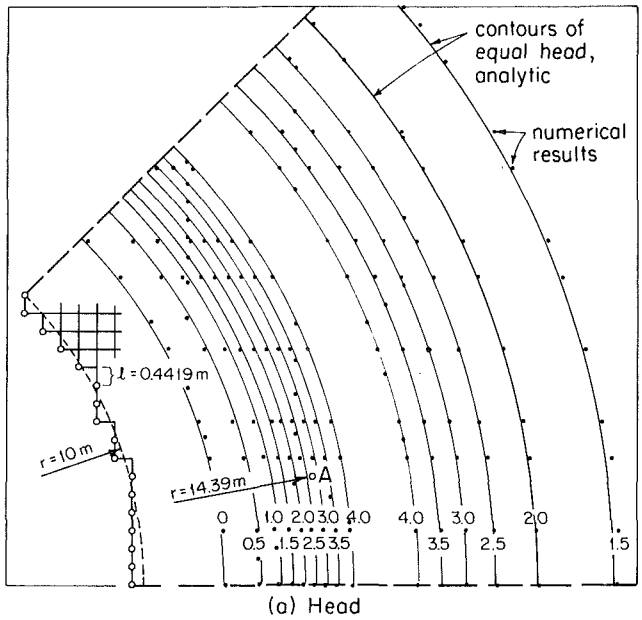

(a) Head

Fig. 11(a)

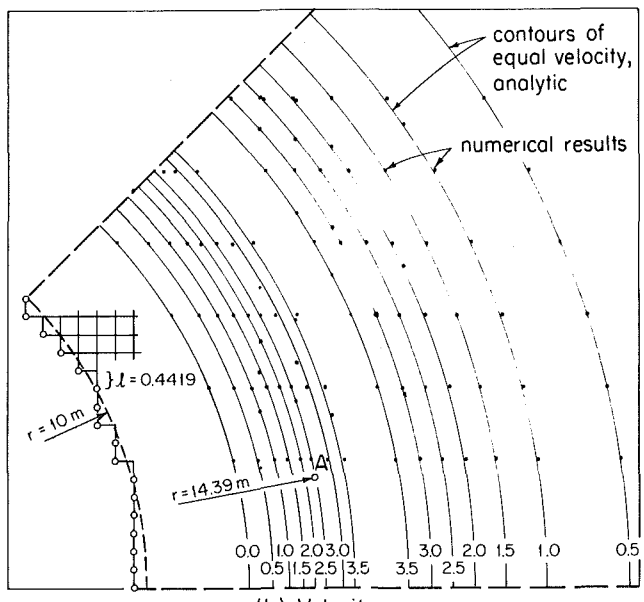

(b) Velocity

Fig. 11(b)

Fig. 11 Numerical versus analytic, square grid. $t = 0.01034$ s

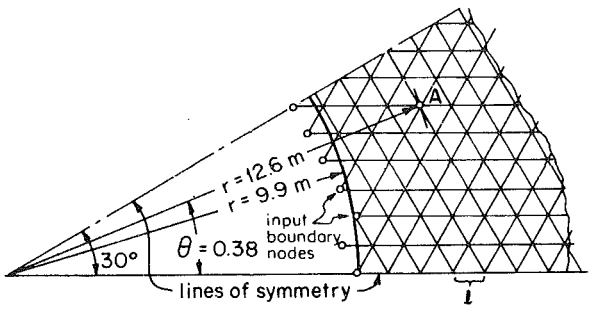

Fig. 12 Two-D example using triangular grid

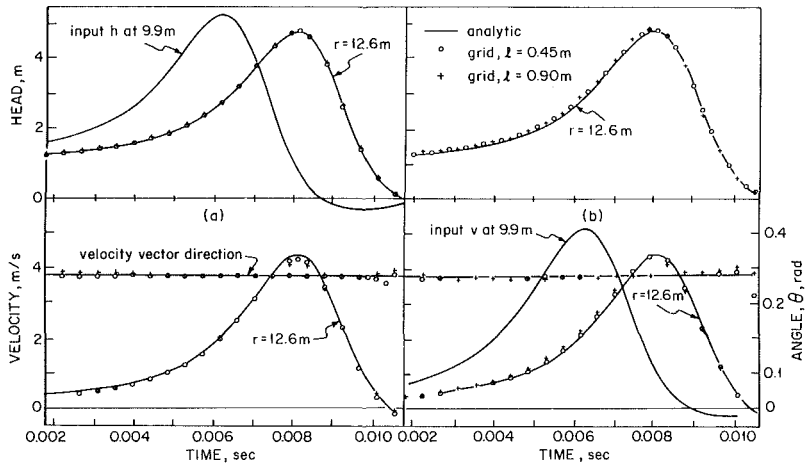

Fig. 13 Response as function of time, triangular grid

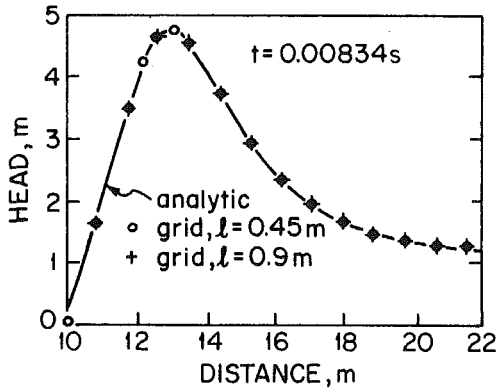

Fig. 14 Response at $t = 0.00834$ s, triangular grid

Two-Dimensional Flow Through Triangular Grid. The same problem was solved using the grid shown in Fig. 12. Line element lengths of 0.90 *m* are shown with the boundary nodes at approximately 10 m from the origin. In this case a 30 deg sector was used to model the flow case. Node A identifies a point at $r = 12.6$ *m*, $\theta = 0.38$ rad at which comparisons are made in Fig. 13. Figures 14 and 15 provide comparisons similar to the earlier example. Two discretizations of 0.90 and 0.45 *m* were used.

Conclusion

A latticework of line elements is utilized to model liquid transients in the continuum. Analytical solutions are used for comparison with numerical results to validate the model. The method is restricted to low Mach number applications. It offers the advantage of an explicit solution at nodes and at boundaries, provides guaranteed stability, and offers the opportunity to handle problems in the multidimensional domain with unusual and irregular boundaries. The boundary conditions may be fixed or moveable, or could be interactive as in the case of a hydroelastic problem.

This paper

(*a*) provides a validation of the method by use of comparisons with analytic solutions,

(*b*) provides a background for the need for the scaling factors and develops the numerical values for two and three-dimensional flow,

(*c*) provides a consistent velocity definition in the latticework,

(*d*) shows the numerical results to be essentially nondispersive,

(*e*) shows that the flow in the grid is irrotational,

(*f*) demonstrates that grids other than square can be effectively applied, and

(*g*) provides additional insight to the need for concern about discretization when modeling high frequency problems.

Acknowledgments

This study was supported by the National Science Foundation Research Grant No. PFR 77-22219 to the University of Michigan.

References

1 Streeter, V. L., and Wylie, E. B., "Two- and Three-Dimensional Transients," ASME *Journal of Basic Engineering*, Vol. 90, No. 4, Dec. 1968, pp. 501–510.

2 Wiggert, D. C., and Wylie, E. B., "Numerical Predictions of Two-Dimensional Transient Groundwater Flow by Method of Characteristics,"

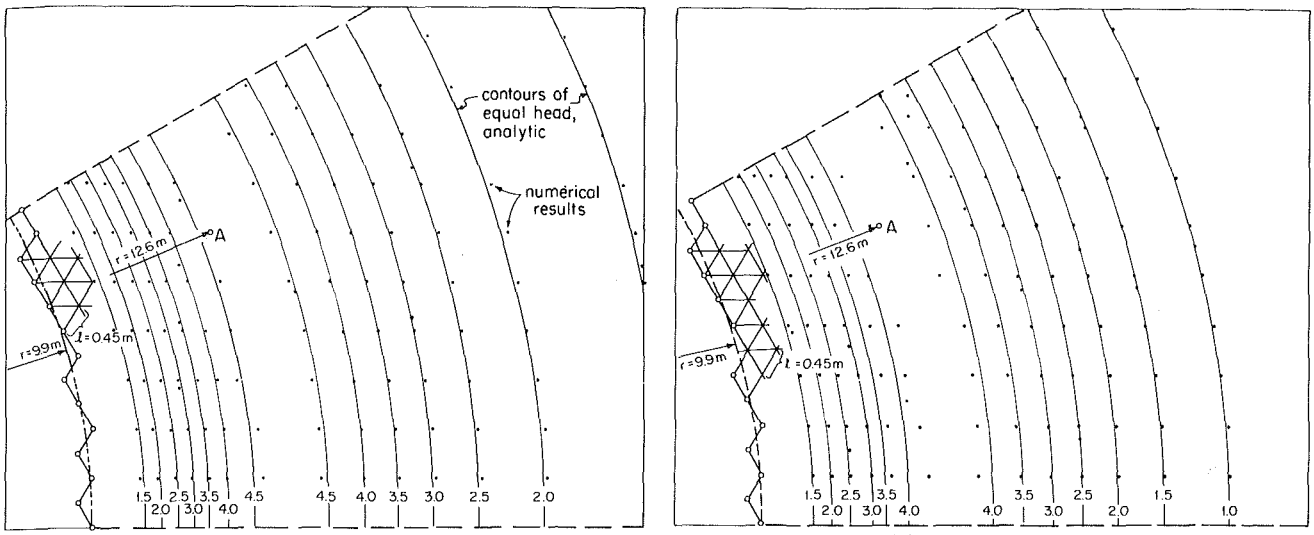

Fig. 15 Numerical versus analytic, triangular grid. $t = 0.00834$ s

Water Resources Research, Vol. 12, No. 5, Oct. 1976.

3 Wylie, E. B., "Seismic Response of Reservoir-Dam Systems," *J. Hydr. Div., ASCE,* Vol. 101, No. HY3, Mar. 1975, pp. 403–418.

4 Fabic, S., "Two- and Three-Dimensional Fluid Transients," *Trans., ANS,* Vol. 14, 1971, pp. 360–361.

5 Wylie, E. B., and Streeter, V. L., *Fluid Transients,* McGraw-Hill Advanced Book Division, New York, N. Y., 1978.

6 Lanb, H., *Hydrodynamics,* Dover Publications, 1945.

7 Shin, Y. W., and Kot, C. A., "Two-Dimensional Fluid-Hammer Analysis by the Method of Near Characteristics," Argonne National Laboratory, ANL 75-21, May 1975.

8 Shin, Y. W., and Valentin, R. A., "Numerical Analysis of Fluid-Hammer Waves by the Method of Characteristics," *Journal of Computational Physics,* 1976, pp. 20, 220–237.

9 Shin, Y. W., and Kot, C. A., "Two-Dimensional Fluid-Transient Analysis by the Method of Characteristics," *J. of Computational Physics,* Vol. 28, No. 2, Aug. 1978, pp. 211–231.

10 Shin, Y. W., and Valentin, R. A., "A Numerical Method Based on the Method of Characteristics for Two-Dimensional Fluid Transients," Joint ASME/CSME Pressure Vessels and Piping Conference, Montreal, Canada, June 25–30, 1978.

11 Shin, Y. W., "Two-Dimensional Fluid Transient Analysis by the Method of Characteristics," ASME, Fluid Transients and Acoustics in the Power Industry, Winter Annual Meeting, San Francisco, Calif., Dec. 10–15, 1978.

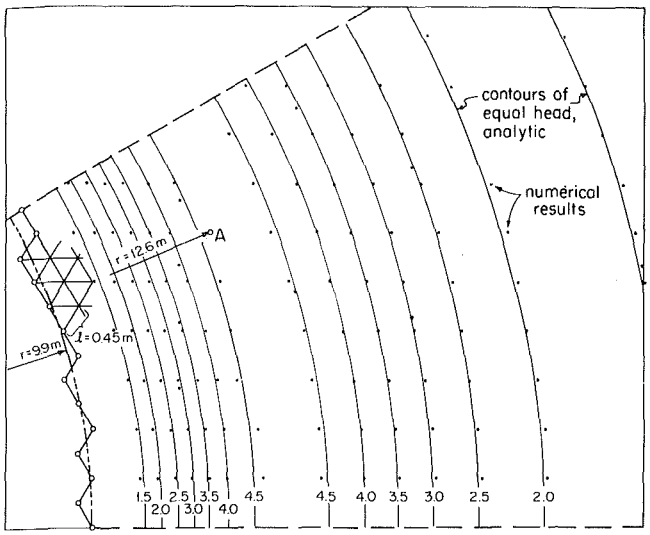

(a) Head

Fig. 15(a)

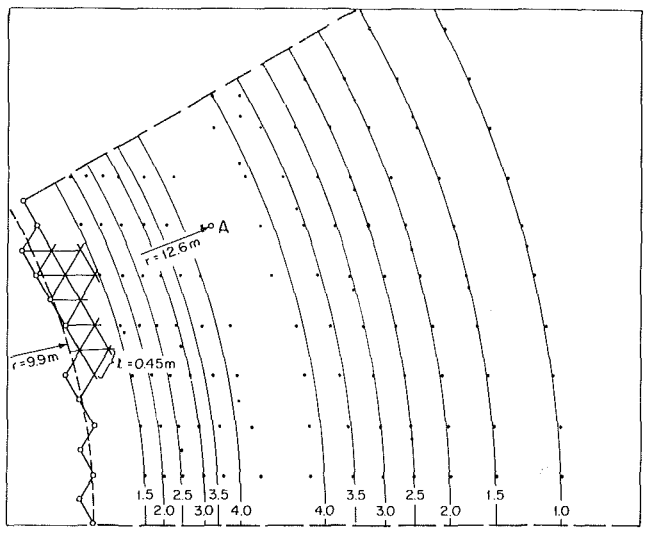

(b) Velocity

Fig. 15(b)

Fig. 15 Numerical versus analytic, triangular grid. $t = 0.00834$ s

Water Resources Research, Vol. 12, No. 5, Oct. 1976.

3 Wylie, E. B., "Seismic Response of Reservoir-Dam Systems," *J. Hydr. Div., ASCE,* Vol. 101, No. HY3, Mar. 1975, pp. 403-418.

4 Fabic, S., "Two- and Three-Dimensional Fluid Transients," *Trans., ANS,* Vol. 14, 1971, pp. 360-361.

5 Wylie, E. B., and Streeter, V. L., *Fluid Transients,* McGraw-Hill Advanced Book Division, New York, N. Y., 1978.

6 Lanb, H., *Hydrodynamics,* Dover Publications, 1945.

7 Shin, Y. W., and Kot, C. A., "Two-Dimensional Fluid-Hammer Analysis by the Method of Near Characteristics," Argonne National Laboratory, ANL 75-21, May 1975.

8 Shin, Y. W., and Valentin, R. A., "Numerical Analysis of Fluid-Hammer Waves by the Method of Characteristics," *Journal of Computational Physics,* 1976, pp. 20, 220-237.

9 Shin, Y. W., and Kot, C. A., "Two-Dimensional Fluid-Transient Analysis by the Method of Characteristics," *J. of Computational Physics,* Vol. 28, No. 2, Aug. 1978, pp. 211-231.

10 Shin, Y. W., and Valentin, R. A., "A Numerical Method Based on the Method of Characteristics for Two-Dimensional Fluid Transients," Joint ASME/CSME Pressure Vessels and Piping Conference, Montreal, Canada, June 25-30, 1978.

11 Shin, Y. W., "Two-Dimensional Fluid Transient Analysis by the Method of Characteristics," ASME, Fluid Transients and Acoustics in the Power Industry, Winter Annual Meeting, San Francisco, Calif., Dec. 10-15, 1978.

DISCUSSION

Y. W. Shin.[1] The paper discusses a method of treating multidimensional fluid transient problems by an equivalent latticework consisting of one-dimensional pipe segments. The authors prove the equivalence of the latticework to multidimensional transients by comparing the differential equations and scaling the characteristic fluid wave speeds. The method applies to the low velocity flows where the corresponding waves are constant. Hence, due to the whole time step ($\Delta t = \Delta x/a$), the maximum possible time step for the explicit numerical scheme, the method is subject to little numerical dispersion. This feature offers a great merit since methods based on multi-dimensional field equations all reveal some degree of dispersion errors resulting from the restrictive time steps required for numerical stability. For example, the Lax-Wendroff scheme requires reduction from full steps by factors $1/\sqrt{2}$ and $1/\sqrt{3}$ for two and three space dimensions, respectively. These are the amounts found in the method of Wylie and Streeter needed to scale the wave speeds for use of full Courant steps. The two-dimensional nearcharacteristic scheme (references [7 and 9]) and the scheme based on a bicharacteristic method (reference [8]) show a factor 1/2. An improved bicharacteristic scheme (references [10 and 11]) increases the factor to 3/4 so that $\Delta t = 3/4\ (\Delta x/c)$. No clear indication was found during the course of this work that further improvement can be made. Nor is available in open literature in the discusser's knowledge an explicit method based on field equations that allow a full time step.

The authors demonstrate the accuracy and workability of the method by considering essentially either a one-dimensional flow or otherwise uniform flow by changing grid orientation. Although the results serve the purpose well and appear quite convincing, the discusser finds it difficult to foresee how the method would perform for a multidimensional flow case. Analytical results are available for a two-dimensional corner diffraction problem (see references [7-11]) for use as a comparison basis. It would be also of interest to compare with experimental results and examine the neglected viscosity effects that become important in vortexing around obstacles. Experimental data are also available: White and Bleakney[2] for a two-dimensional case and Taylor[3] for a three-dimensional case.

Authors' Closure

In response to Dr. Shin's suggestion, the authors have modeled a two-dimensional corner diffraction problem with the latticework method. In this problem [12] a pulse is assumed to approach a right-angled wedge with its front parallel to one face of the wedge, and to hit it at $t = 0$. Part of the pulse continues past the wedge, part is reflected back by the wedge, and in addition a diffracted wave originates from

[1] Components Technology Division, Argonne National Laboratory, Argonne, Ill. 60439.

[2] White, D. R., and Bleakney, W., "Shock Loading of Rectangular Structure," Technical Report II-11, Dept. of Physics, Princeton University, 1952.

[3] Taylor, W. J., "A Method for Predicting Blast Loads During the Diffraction Phase," *The Shock and Vibration Bulletin,* Bulletin 42 (Part 4 of 5 Parts), Jan. 1972.

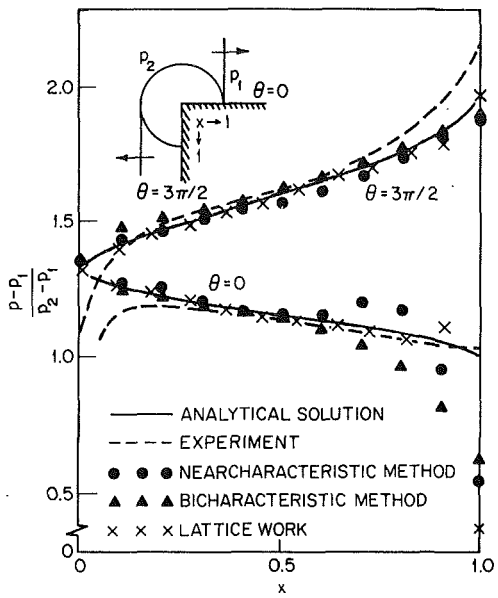

Fig. 16 Diffraction of plane acoustic wave from 90 deg sharp wedge (references [7, 14])

the vertex of the wedge. The diffracted wave is confined to a circle of radius ct at time *t*, with its center at the vertex of the wedge. The field within this circle is of interest and, in particular, comparisons are made along the top and front faces of the wedge to a distance equal to the radius.

The analytic solution assumes an instantaneous pulse, an impossible condition in any numerical method. The minimum pulse rise time is one time step in a numerical procedure. In the latticework method a significant disturbance is created at the wave front if the pulse is introduced as rapidly as one time step. In the results presented herein the pressure pulse was introduced at the left side of the grid over twelve time increments, with a cubic equation used to describe the shape of the front during the twelve increments. The pressure was then held constant at the pulse height.

Figure 16 superimposes the latticework results on the figure from reference [7], which shows theoretical and experimental results as well as results from two options using the two-dimensional method of characteristics. Although 66 data points were available from the latticework method along the two faces of the wedge only 12 were plotted. These illustrate the disturbance at the wave front.

The authors appreciate Dr. Shin's discussion and his suggestions.

Additional Reference

12 Keller, J., "Diffraction of a Shock or an Electromagnetic Pulse by a Right-Angled Wedge," *J. Applied Physics*, Vol. 23, 1952, pp. 1267–1268.

Angled Injection of Jets Into a Turbulent Boundary Layer

L. H. Y. Lee
Engineer,
Product Development,
Chiap Hua Comalco Limited,
Kowloon, Hong Kong

J. A. Clark
Senior Lecturer,
Department of Mechanical Engineering,
Univ. of Hong Kong,
Hong Kong

Inclined laminar submerged plane jets were injected from a 1 cm slot into a turbulent boundary layer developed on a sidewall of a water channel. Profiles of mean velocities and longitudinal fluctuations were measured to 64 slot widths downstream of the jet exit. Length and velocity similarity scales were obtained from mean velocity data, and local values of skin friction coefficient were determined. Two maxima in the longitudinal fluctuation profiles were established and found to follow precisely loci of vortex formations. The maxima grew exponentially in the downstream direction and peaked at a location where these transverse vortices were at their full strength before coalescence. Effects of different injection angles and velocity ratios were found. Further extension of a physical model to describe the flow is validated based on correlation of mean and fluctuating velocity data with visual information.

Introduction

This experimental investigation concerns angled injection of a submerged laminar plane jet into a well-developed thick turbulent boundary layer. The inclined jet on interaction with the boundary layer creates two additional shear layers giving asymmetric mean velocity profiles downstream of the jet exit. This external flow configuration is more complex than a wall-jet with velocity extrema, producing regions which resemble a flat plate boundary layer, a free mixing layer, and a wake layer. The ratio of jet velocity to free stream velocity, m, and the jet injection angle, ϕ, are varied and, where applicable, comparisons made with wall-jets and mixing layers.

Relevant areas of application of this study in fluids engineering are boundary layer control on aircraft wings, interaction of lifting jets of V/STOL aircraft and cross-winds, film cooling of turbine blades, dilution air injection in combustors, aerodynamic throttling of flow through nozzles in rockets and jet engines, fluid waste disposal, and control gate structures in open channels. Recently, Bradshaw [1] has classified merging of two or more shear layers as a category of complex turbulent flows. Few large scale definitive experimental investigations have been conducted in this area with most effort concentrated on the downstream fully developed region. However, LaRue and Libby [2] investigated slot injection of helium at zero angle into a turbulent boundary layer of air with a velocity ratio of 0.4 and also studied the immediate vicinity downstream of the jet exit. Related research on plane jets inclined to the free stream is limited to studies of reattachment phenomenon [3], spatial pressure variation in the separation bubble region [4], and the defining of boundaries of different flow regimes downstream of the jet exit [5].

With different velocity ratios and injection angles, profiles of mean velocity and rms values of longitudinal fluctuations normal to the wall were measured to 64 slot widths downstream of the jet exit. Wall shear stress variation in the streamwise direction was determined by the Clauser [6] "crossplot" method. These data were supplemented by flow visualization, and an already proposed physical model [7] to describe the interaction phenomena of this complex situation of merging shear flows is extended in the downstream direction. The information is useful for testing prediction procedures and provides deeper insight into the physics of this complex flow situation with a better understanding of transport phenomena and turbulence development.

Experimental Arrangement and Measuring Techniques

Experiments were performed in a recirculating water channel 5.8 m long, 38.1 cm wide, and 76.2 cm high. The depth of water was 56 cm giving an aspect ratio of 1.47 for the wetted cross-section. A trip wire of 0.3 cm diameter was fixed to the sidewall, across the depth at the channel entrance, to enduce laminar-turbulent transition of the test boundary layer. At a distance of 4 m downstream from the trip wire, with a fully established turbulent boundary layer and constant free stream velocity $U_0 = 7.92$ cm/s of uncertainty ± 0.12 cm/s, a laminar plane jet was injected from a 1 cm slot at angles of $\phi = 0$, 15 or 30 deg from the wall, as shown schematically in Fig. 1. Its spanwise location and aspect ratio of 20 ensured two-dimensionality, minimal corner effects from the open channel, and the middle two thirds of the jetspan free from end effects.

The nine physical cases studied are shown in Table 1 with the jet Reynolds numbers R_e calculated using the velocity of the jet at the exit center U_j and the width w of the jet slot. Variation in kinematic viscosity of water caused minor differences in R_e. The length Reynolds number based on the distance from the virtual origin of the boundary layer to the center of the jet exit was 460,000 and R_θ was 720.

Contributed by the Fluids Engineering Division and presented at the Fluids Engineering Conference, New Orleans, La., March 18-20, 1980, of THE AMERICAN SOCIETY OF MECHANICAL ENGINEERS. Manuscript received by the Fluids Engineering Division, July 19, 1978. Paper No. 80-FE-2.

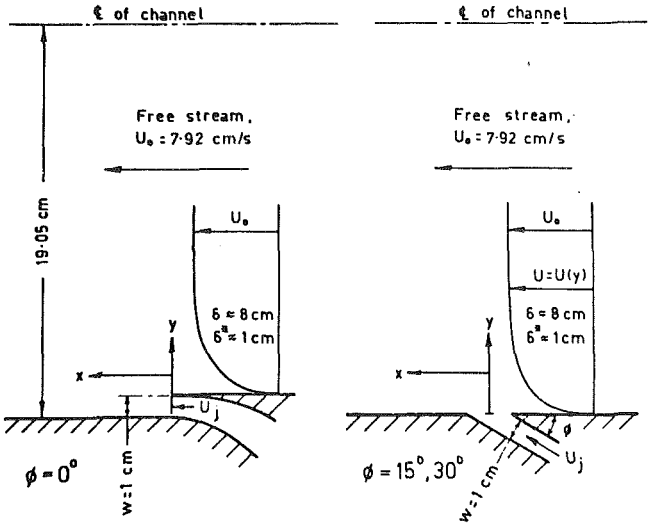

Fig. 1 Schematic diagram of angled injection of plane jet into a developed turbulent boundary layer

Mean velocity from Pitot tubes and turbulence intensity measurements using hot-film probes were made to 64 slot widths downstream of the jet exit and the respective uncertainty bands are indicated on the appropriate figures. As suggested by Ghosh and Roy [8], separate flattened Pitot and static tubes were used in conjunction with an optical micromanometer to determine mean velocities. This arrangement gave a pressure difference estimation of 0.02 mm WG accuracy. The Pitot and static tubes were tested according to NPL recommendations [9] and checked against velocity measurements using combined time-streak markers in the hydrogen bubble visualization technique. Turbulence intensity measurements were made employing a constant temperature DISA 55M anemometer with standard bridge and heavy quartz-coated DISA 55R42 conical hot-film probes using non-linearized signals. The Pitot tube and the hot-film probe are insensitive to small misalignment with the mean flow direction and this has been considered in the estimation of uncertainty bands. Details of calibrations using the water channel and all the measuring techniques employed are given in Lee [10].

Table 1 Physical properties of inclined submerged plane jet. (Uncertainty of m and R_e, with absolute values of 20:1 odds, is shown.)

Injection angle, ϕ, degrees	Velocity ratio, $m = U_j/U_0$	Reynolds number, $R_e = U_j w/\nu$
0	2.11	2,070
	1.62	1,580
	1.30 ± 0.03	1,280 ± 20
15	2.22	1,870
	1.76	1,490
	1.30	1,100
30	2.44 ± 0.04	2,590 ± 40
	1.84	1,940
	1.50	1,540

The Visual Picture

A platinum wire of 0.001 in. diameter (0.00254 cm) and insulated at 1 cm intervals was used in the hydrogen bubble flow visualization technique which provided a detailed overall picture of the flow field. Observations of the interaction of mixing layers of the plane jet and the boundary layer in the initial region immediately downstream of the jet exit were made and revealed important mechanisms in the generation of random small scale turbulence. Figure 2 is a typical photograph extracted from cine-film taken of a horizontal hydrogen bubble generating wire placed normal to the planes of shear. The jet leaving the slot deflects toward the wall and finally reattaches it, encompassing a region of recirculating fluid. The size of this recirculation bubble region increases with increasing injection angles. Two thin shear layers develop, oscillate, and roll up to form two-dimensional transverse vortex tubes. The mixing layer further from the wall is referred to as the outer mixing layer whereas the other shear layer, closer to the wall, the inner mixing layer.

The transverse vortices in the outer layer grow as they convect downstream entraining fluid from the jet and the initial turbulent boundary layer. These vortices interact dramatically with coalescing patterns, classified as either pairing or interlocking. In the former, two consecutive transverse vortices undergo coalescence by induction, revolving around each other and forming a single bigger vortex structure. In the latter, initiation of coalescence starts at various positions simultaneously, with many vortex tubes

Nomenclature

c_f = local skin friction coefficient, $\frac{1}{2}c_f = \tau_w/\frac{1}{2}\rho U_0^2$
m = velocity ratio, U_j/U_0
R_e = jet Reynolds number, $U_j w/\nu$
U = time-averaged mean velocity in x-direction
U_j = exit central velocity of plane jet
U_0 = free stream velocity, 7.92 cm/s
U_m = maximum value in normal mean velocity profile
U_t = minimum value in normal mean velocity profile
$U_{0.5}$ = mean velocity at mixing center where velocity has magnitude of $\frac{1}{2}(U_m + U_t)$.
U_τ = friction velocity, $\sqrt{\tau_w/\rho}$
ΔU = excess velocity, $(U_m - U_t)$
u' = rms value of longitudinal component of velocity fluctuation
u'_{max} = maximum values in normal u' fluctuation profile
w = slot width of plane jet, 1 cm
x = streamwise coordinate from center of jet exit, as defined in Fig. 1
y = lateral coordinate normal to wall
z = spanwise coordinate from center plane of jet exit
δ = boundary layer thickness of developed turbulent boundary layer at jet exit
δ^* = displacement thickness of developed turbulent boundary layer at jet exit
δ_m = distance from wall to maximum value in normal mean velocity profile
δ_t = distance from wall to minimum value in normal mean velocity profile
$\delta_{0.9}, \delta_{0.5}, \delta_{0.1}$ = respective distances from wall, as defined in Fig. 4
θ = momentum deficit thickness, defined by equation (1)
ϕ = injection angle of submerged plane jet

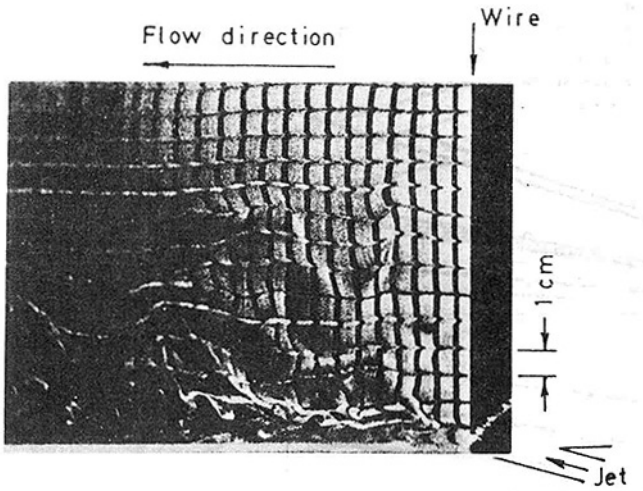

Fig. 2 Flow visualized with hydrogen bubble generating wire normal to the plane of shear at $x/w = 2$ for a submerged plane jet ($\phi = 15$ deg and $m = 1.30$)

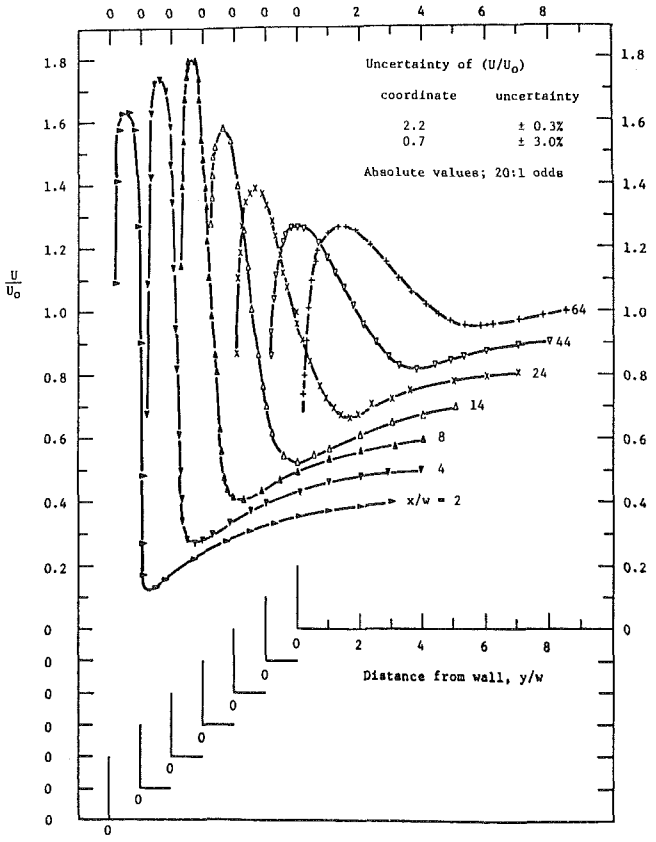

Fig. 3 Longitudinal distribution of mean velocity profiles for $2 < x/w < 64$ ($\phi = 15$ deg, $m = 2.22$)

interlocking with one another resembling a net arrangement. Weak secondary longitudinal vortex tubes are also observed in the outer layer and they help to bring about the interlocking process already described. The transverse vortices in the inner layer being more confined are of a smaller size entraining fluid from the jet and the recirculation bubble region. Details of all these mechanisms are given separately in Lee and Clark [7].

Greater injection angles result in greater entrainment rates and larger transverse vortices in both mixing layers. The size of the recirculation region resulting from separation is also larger particularly for $\phi = 30$ deg. Visualization further

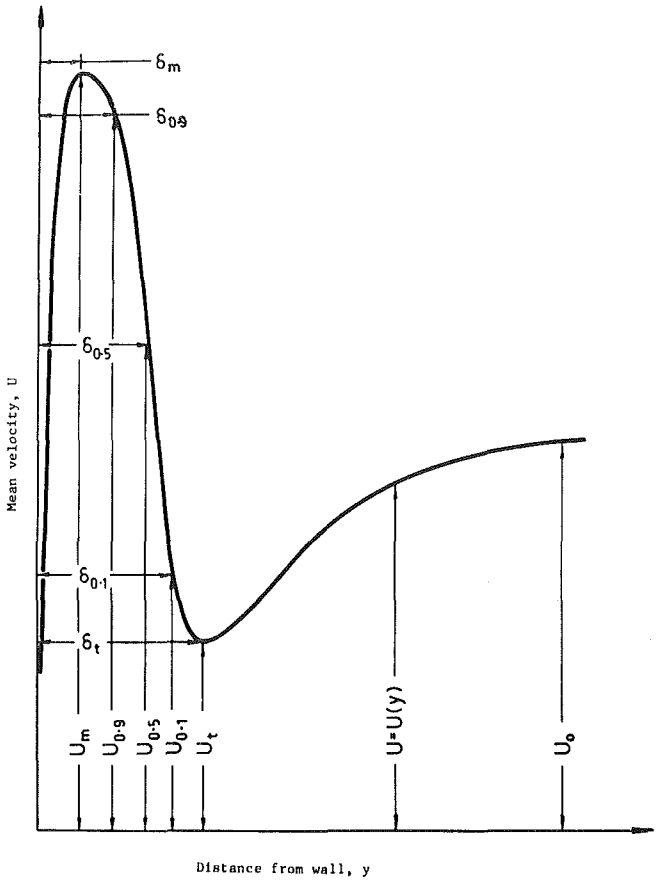

Fig. 4 Definition of velocity and ordinate length scales

reveals for larger m that the jet is more unstable and transition starts earlier with initiation of vortex formation closer to the jet exit. Eventually the coherent vortex structures in both layers breakdown forming random small scale turbulence, and farther downstream patches of turbulence eject intermittently from the wall.

Mean Velocity Measurements

Profiles of mean velocities normalized with the free stream velocity U_0 are plotted against distance y from the wall for various longitudinal stations, as is illustrated in Fig. 3 for $\phi = 15$ deg and $m = 2.22$. For each ϕ and m distinct velocity extrema were found, and the strong asymmetry of the profiles prevented the use of a single velocity and length scale to obtain similarity. At 64 slot widths downstream from the jet exit, velocity extrema are still apparent indicating that the flow development was still incomplete. Using the maximum velocity U_m and the minimum velocity U_t the profiles were divided into an inner or wall layer, an outer layer, and the wake layer adjacent to the free stream. The respective distances from the wall to the velocities U_m, $(U_t + 0.9\Delta U)$, $U_{0.5}$, $(U_t + 0.1\Delta U)$, and U_t are designated as δ_m, $\delta_{0.9}$, $\delta_{0.5}$, $\delta_{0.1}$, and δ_t as shown in Fig. 4 where the excess velocity $\Delta U = U_m - U_t$ and the velocity at the mixing center $U_{0.5} = \frac{1}{2}(U_m + U_t)$.

Length Scales. The ordinate scales δ_m, $\delta_{0.5}$, δ_t plotted as a function of the downstream distance x/w are shown in Figs. 5(*a-f*) and all indicate linearity in regions downstream. It is conjecture that this linearity is caused by the pressure gradient normal to the jet axis and the restriction on the jet development normal to the wall by the presence of the developed boundary layer. Comparisons are shown with various studies [11-14]. Upstream extrapolation for $\delta_{0.5}$ and δ_m does not produce coincidence along the x/w axis, indicating that the

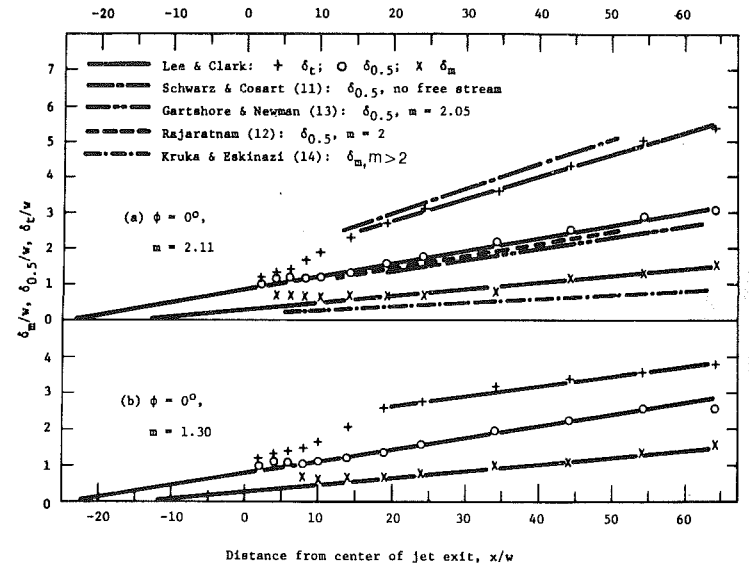

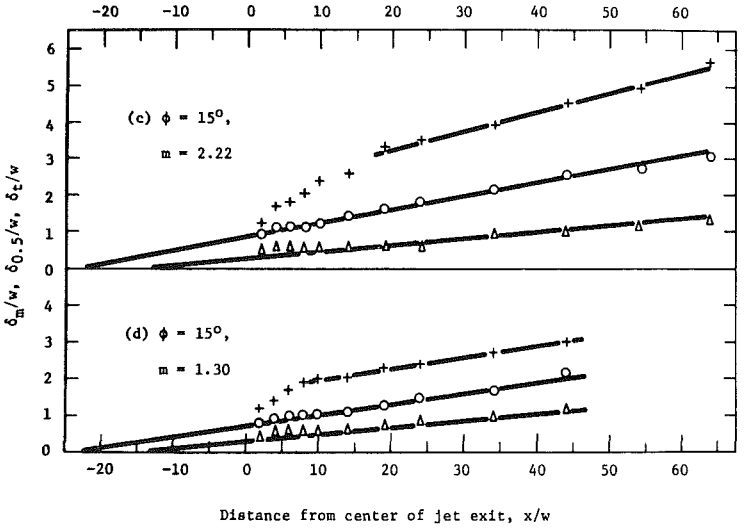

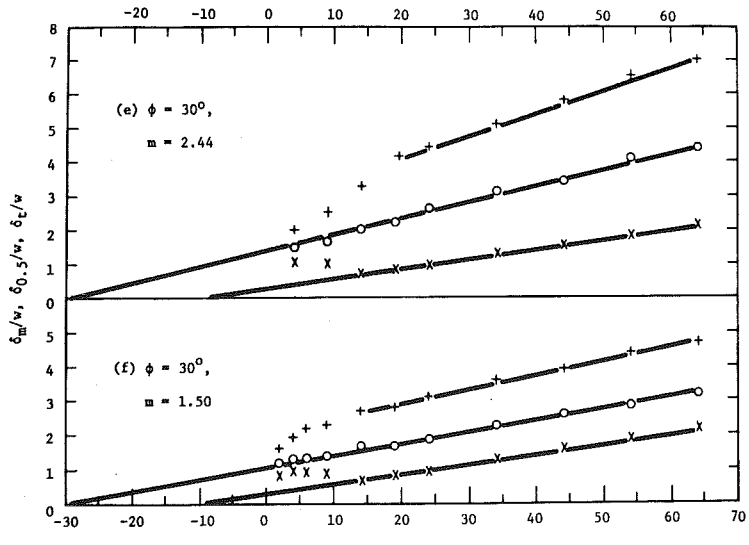

Fig. 5*(a-f)* **Longitudinal development of mixing layers for submerged plane jet**

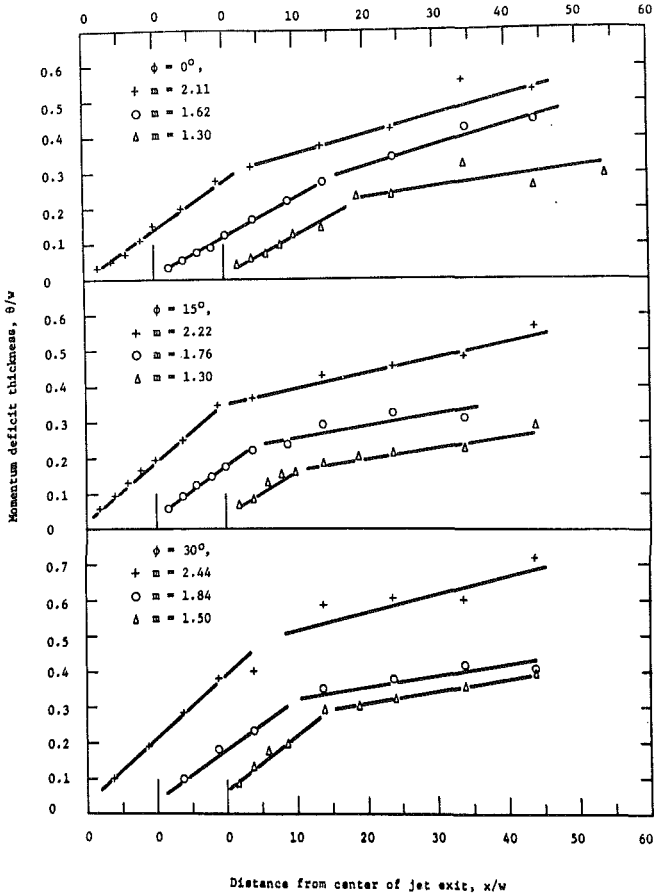

Fig. 6 Longitudinal distribution of momentum deficit thickness in the outer layer of the submerged plane jet

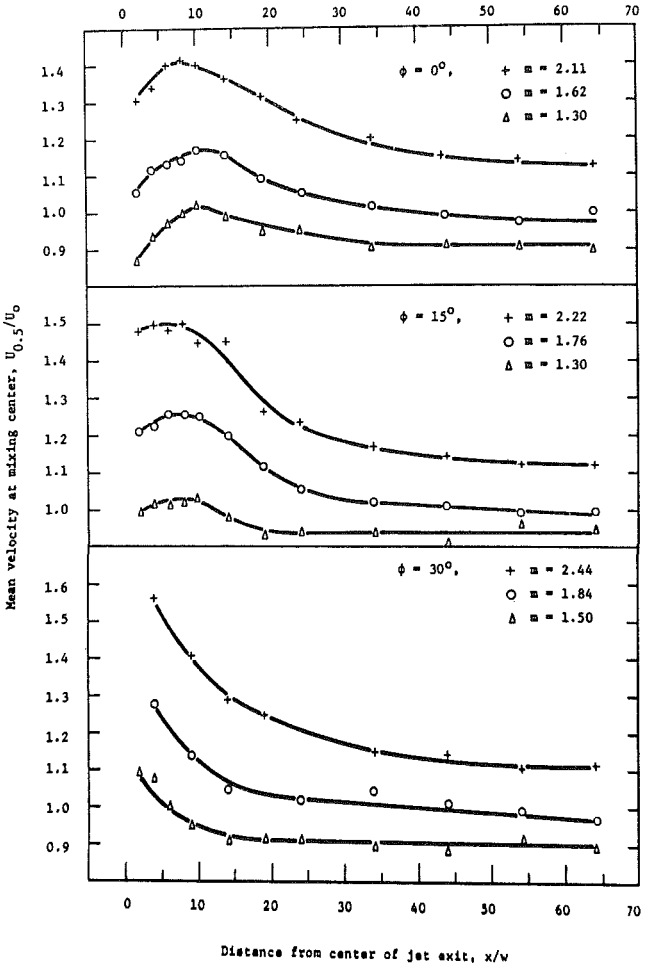

Fig. 8 Longitudinal distribution of mean velocity at the mixing center of the outer layer of the submerged plane jet

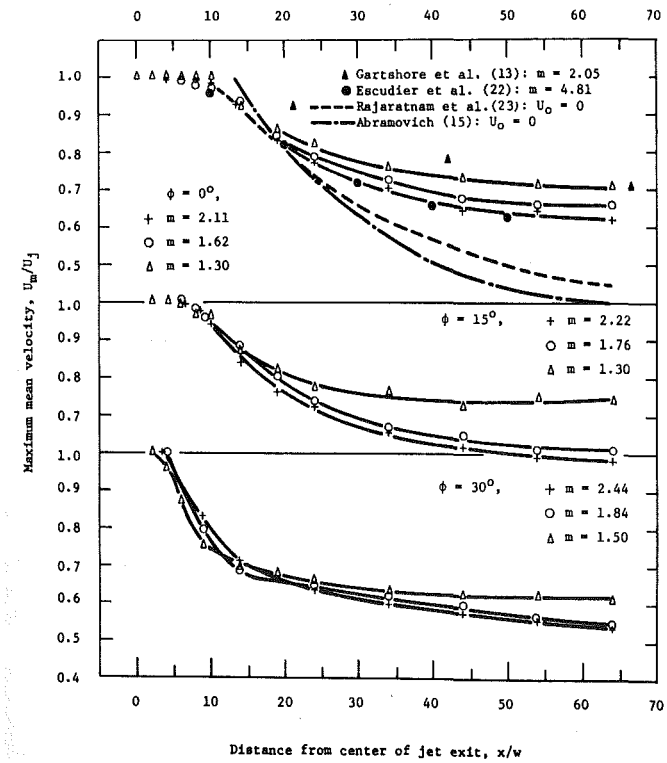

Fig. 7 Longitudinal decay of the maximum velocity

virtual origin of the jet must be defined accurately. For each ϕ, increasing m increases $\delta_{0.5}$ and δ_t, but δ_m remains constant. The former changes are caused by larger cross-stream components of jet velocity, while δ_m is more influenced by the relative magnitudes of the longitudinal and transverse components of velocity in the jet. The latter component results in, for $\phi = 30$ deg, increases in δ_m, $\delta_{0.5}$, δ_t and the virtual origin of δ_m shifting forward while that for $\delta_{0.5}$ shifts backwards.

A suitable length scale for the outer layer is $(\delta_{0.1} - \delta_{0.9})$, as used in plane coflowing jets by Abramovich [15] and in plane mixing layers by Rodi and Spalding [16]. This was found more appropriate than $(\delta_{0.5} - \delta_m)$ used by Kruka and Eskinazi [14] or δ_f used by Bradshaw and Gee [17], where $\delta_f = \Delta U/(\partial U/\partial y)_f$ and f refers to the point of inflexion in the free shear layer velocity profile. The other suitable length scale used for the outer layer was based on the momentum deficit thickness θ as used by Winant and Browand [18] in a two-stream mixing layer, where

$$\theta = \int_{\delta_m}^{\delta_t} \left[\tfrac{1}{4} - \left(\frac{U - U_{0.5}}{\Delta U} \right)^2 \right] dy. \quad (1)$$

Two distinct regions of linear growth in θ/w with downstream distance are indicated in Fig. 6. Browand [19] also noted two distinct linear regions for θ development in a two-dimensional free shear layer, whereas Freymuth [20] obtained a nearly constant value of θ for a separated laminar boundary layer. It

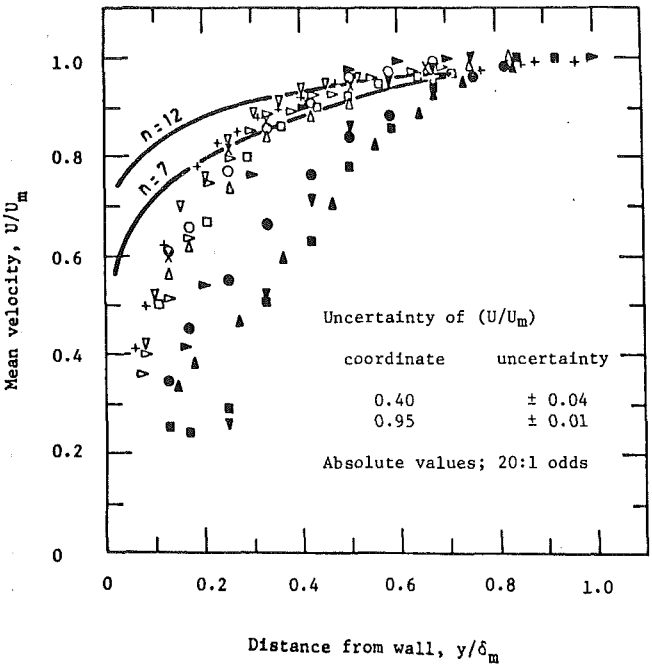

Fig. 9 Distribution of velocity in the inner layer for $2 < x/w < 64$ (ϕ = 15 deg, m = 2.22). Legends same as in Fig. 3

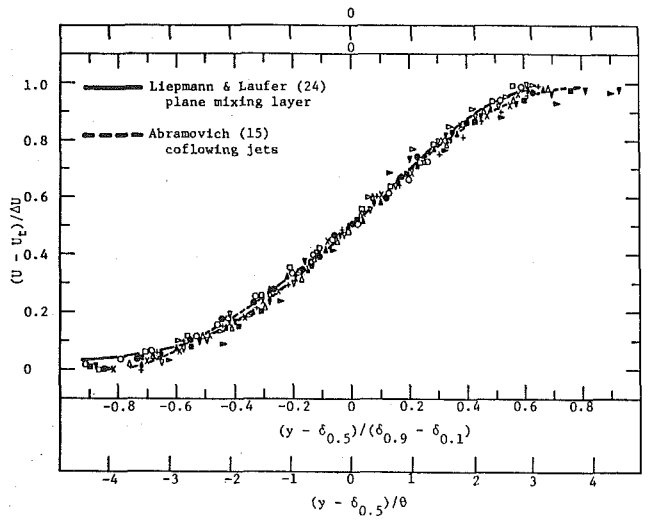

Fig. 10 Velocity similarity in the outer layer for $2 < x/w < 64$ (ϕ = 15 deg, m = 2.22). Legends same as in Fig. 3

is of interest to note that the ratio of θ to $(\delta_{0.1} - \delta_{0.9})$ had a constant value of 0.209, and Sato [21] determined for parabolic jets the ratio of momentum thickness to half breadth from 0.196 to 0.255.

Velocity Scales. Profiles of normalized maximum velocity U_m/U_j and normalized velocity at mixing center $U_{0.5}/U_0$ are plotted against distance from center of jet exit in Figs. 7 and 8, respectively. In the latter profiles, peaks occur in each curve at a particular longitudinal position although for ϕ = 30 deg it appears at or upstream of the first measuring station. Due to the ratio of U_m/U_t being small the growth rates are different from that of a wall jet without an external stream.

Velocity profiles in the inner layer normalized with U_m and δ_m are illustrated by Fig. 9. Close to the jet exit data is scattered indicating a region of rapid transformation, whereas farther downstream the data points aggregate showing similarity and two curves $U/U_m = (y/\delta_m)^{1/n}$ with n = 7 and 12 are drawn for comparison. Schwarz and Cosart [11] noted values for n of 14 ± 1, whereas Kruka and Eskinazi [14] reported n varying from 10.3 to 13.4 depending on the velocity ratio. From this study the effect on n of varying ϕ and m seems negligible and a range of n values difficult to ascertain, with increasing uncertainty near the wall. Velocity profiles in the outer layer are normalized with ΔU and $(\delta_{0.1} - \delta_{0.9})$ or θ, and shown in Fig. 10. Data fall on comparison curves [15, 24] showing a unique relationship regardless of x, m, and ϕ. The wake or outermost layer is progressively absorbed in the longitudinal direction.

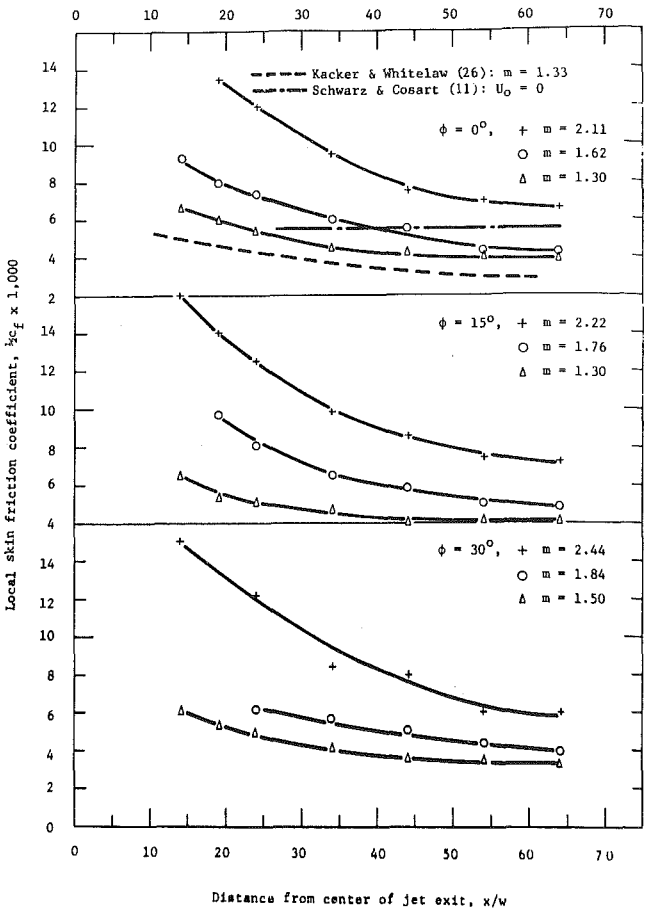

Fig. 11 Distribution of local skin friction coefficient in the longitudinal direction

Full comprehensive data relating to the above configuration for the complete range of velocity profiles, at numerous longitudinal stations for different injection angles and velocity ratios, is presented in Lee [10].

Local Skin Friction Coefficient, c_f. Local wall shear stress τ_w was determined by the "crossplot" method using velocity measurements close to the wall. For each ϕ and m, normal mean velocity profiles in the inner layer at each measuring station were drawn in graphs with U/U_0 and yU_0/ν as coordinates. Superimposed on these graphs known as Clauser charts were derived lines of constant ½ c_f calculated from the logarithmic law $U/U_\tau = (1/\kappa)\ln(yU_\tau/\nu) + B$, with κ = 0.4187 and B = 5.45 as recommended by Patel [25]. The appropriate value of c_f was thus obtained by cross-plotting from the charts, and its downstream distribution is shown in Fig. 11 for the fully developed region.

Turbulence Intensity Measurements

The streamwise development of the profiles of the rms value of longitudinal velocity fluctuation u' normalized with U_0 are illustrated in Fig. 12 for ϕ = 15 deg and m = 2.22. Two maxima u'_{max} exist in these turbulence profiles and their

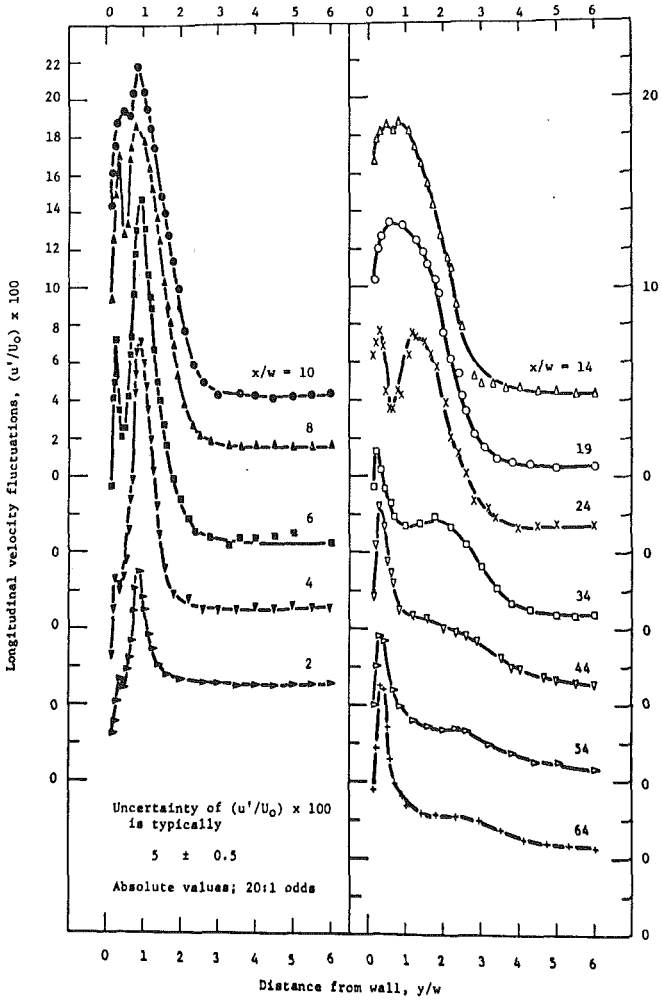

Fig. 12 Streamwise distribution of normal profiles of longitudinal component of velocity fluctuation (ϕ = 15 deg, m = 2.22)

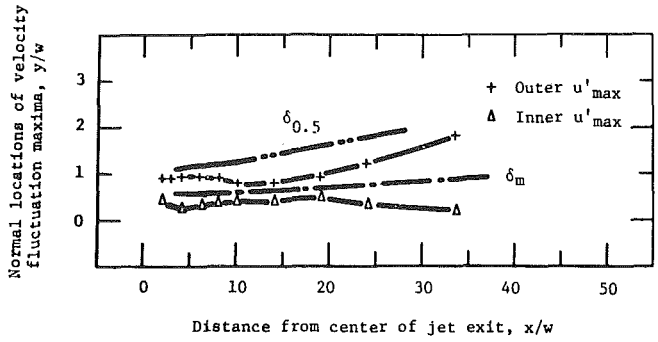

Fig. 13 Normal ordinate locations of the longitudinal velocity fluctuation maxima relative to positions of $\delta_{0.5}$ and δ_m (ϕ = 15°, m = 2.22)

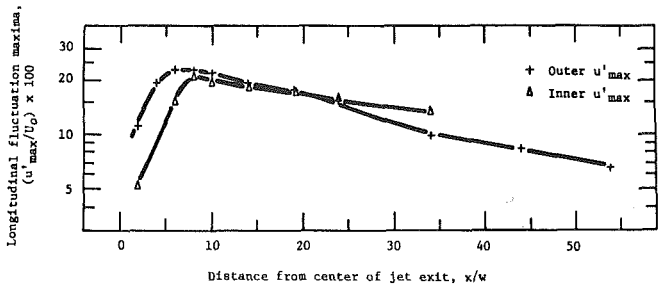

Fig. 14 Streamwise distribution of outer and inner longitudinal velocity fluctuation maxima (ϕ = 15 deg, m = 2.22)

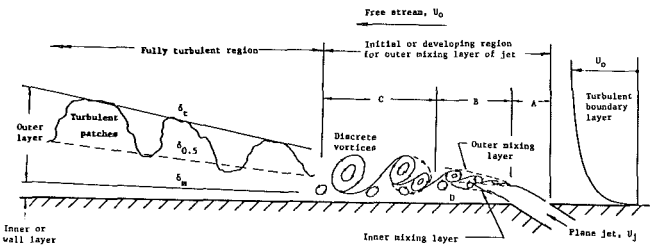

Fig. 15 Physical model illustrating transition mechanisms and turbulent development downstream of the jet exit
A - initial region of transformation;
B - region of discrete vortex tubes;
C - region of vortex interaction; and
D - recirculation bubble region.

locations are shown in Fig. 13 with experimental curves of δ_m and $\delta_{0.5}$ superimposed. For ϕ = 0 deg and 15 deg, the inner u'_{max} appear in the wall layer and the other u'_{max} in the outer layer. When ϕ = 30 deg, complicated mixing patterns in the initial region give peculiar locations of the u'_{max} for $x/w < 10$. Figure 14 shows in the streamwise development of these maxima, regions of exponential growth before relaxation with the peak values in the outer layer upstream of that in the inner layer. The rate of decay of u'_{max} in the inner layer is less than that for the outer layer, as the inner layer is fed continuously from turbulence generated near the wall. Turbulence fluctuation u' increases with increasing m due to the larger cross-stream component of jet velocity. However an increase in ϕ moves the outer u_{max} further from the wall but the inner u'_{max} is unaffected. Peak values of the maxima are comparable for ϕ = 0 deg and 15 deg whereas for ϕ = 30 deg the values are much larger.

Normal profiles of u' from Kacker and Whitelaw [26] for a wall jet with an external stream showed two maxima. Bajura and Szewczyk [27] also observed two maxima in the amplitude distribution of u' fluctuations resulting from the growth of natural disturbances in a plane wall jet, with the outer maximum of higher intensity than the inner maximum. From slot injection of helium into an air boundary layer with m = 0.4, LaRue and Libby [2] observed that intensities of velocity, concentration, and density fluctuations increased sharply downstream of the slot and peaked where the mixing region from the splitter plate impinged on the wall. In all the present studies exponential growth of u'_{max} to a peak is observed in the initial region immediately downstream of the jet exit.

Correlation of the Flow Measurement Data

An initial region of flow development and a fully turbulent region were established in the outer layer by observing two regions of linear growth in the momentum deficit thickness θ and by examining the variation in ordinate length scales δ_m, $\delta_{0.5}$, δ_t, and velocity excess ΔU, and the growth and decay of u'_{max}. In the initial region ($\delta_t - \delta_m$) represented the scale and size of the transverse vortices, whereas in the fully developed region δ_t served as the outer border of the bounding envelope for turbulent patches which eject intermittently from the wall. Also the change of slope in θ occurred at a location where the coalescence of discrete vortices was complete.

For ϕ = 0 deg and 15 deg, within initial region coincidence occurred in the distance from the wall of $\delta_{0.5}$, the outer u'_{max}, and the loci of the axes of transverse vortices for each velocity ratio. However for ϕ = 30 deg, coincidence of $\delta_{0.5}$ and the vortex loci in the outer mixing layer was good but the u'_{max} were found closer to the wall. This may be attributed to the separation and reattachment phenomenon, and the resulting unsteady behavior associated with the recirculation bubble

region. In general the streamwise position of the outer u'_{max} peak coincided with, in the outer mixing layer, the transverse vortices at full strength before interaction. The inner u'_{max} peak was found to occur immediately after vortex interaction. It is postulated that the outer u'_{max} correlates with the presence of transverse vortices in the outer mixing layer while the inner u'_{max} is more associated with shorter smaller transverse vortices found in the inner mixing layer. In the fully turbulent region, the outer u'_{max} occurred midway between the δ_m and $\delta_{0.5}$ ordinates and moved away from the wall in the downstream direction, whereas the inner u'_{max} remained close to the wall.

The physical model which has been described [7] is extended in the downstream direction into the fully turbulent region, supported by these mean velocity and turbulence measurements, as shown in Fig. 15. Here the asymmetric velocity profiles with linearity of length scales and similarity of velocity scales were obtained.

Conclusion

An extensive experimental investigation has been done in a complex flow situation involving angled injection of a submerged laminar plane jet into a well-developed turbulent boundary layer. The overall picture of the flow field with the associated mixing processes and turbulence development was described. The mean velocities, length scales, local skin friction coefficients and turbulence intensities were determined as part of the parametric study of the flow characteristics which were dependent on velocity ratio and injection angle. Linearity of length scales and similarity of velocity scales were obtained downstream of the jet exit.

Correlation of visual information and this quantitative data revealed that longitudinal velocity fluctuation maxima relate to the existence and loci of vortices and that their size before coalescence relates to the length scales obtained from the measured mean velocity profiles. A physical model describing the low frequency mixing processes from the jet exit into the turbulent region downstream has been enhanced and substantiated.

References

1 Bradshaw, P., "Review - Complex Turbulent Flows," ASME *Journal of Fluids Engineering,* Vol. 91, No. 1, 1975, pp. 146–154.

2 LaRue, J. C., and Libby, P. A., "Measurements in the Turbulent Boundary Layer with Slot Injection of Helium," *The Physics of Fluids,* Vol. 20, No. 2, 1977, pp. 192–202.

3 Wygnanski, I., and Newman, B. G., "The Reattachment of an Inclined Two-Dimensional Jet to a Flat Surface in Streaming Flow," *Canadian Aeronautics and Space Institute Transactions,* Vol. 1, No. 1, 1968, pp. 3–8.

4 Artt, D. W., "An Experimental Investigation of Film Cooling, with Reference to the Injection Region," Ph.D. thesis, Queen's University of Belfast, North Ireland, 1970.

5 Stek, J. B., and Brandt, H., "Aerodynamic Throttling of a Two-dimensional Flow by a Thick Jet," *The Aeronautical Quarterly,* Vol. 27, 1976, pp. 229–242.

6 Clauser, F. H., "Turbulent Boundary Layers in Adverse Pressure Gradients," *Journal of Aeronautic Sciences,* Vol. 21, 1954, pp. 91–108.

7 Lee, L. H. Y., and Clark, J. A., "Flow Visualization in Complex Turbulent Flows," *Journal of Hydraulics Division,* Proc. ASCE, Vol. 106, No. HY2, Feb. 1980, pp. 247–268.

8 Ghosh, S. N., and Roy, N., "Boundary Shear Distribution in Open Channel Flow," *Journal of Hydraulics Division,* Proceedings ASCE, Vol. 96, No. HY4, 1970, pp. 967–994.

9 Bryer, D. W., and Pankhurst, R. C., *Pressure-probe Methods for Determining Wind Speed and Flow Direction,* HMSO, London, 1971.

10 Lee, L. H. Y., "Visual Studies of Jets Injected into a Turbulent Boundary Layer," Ph.D. thesis, University of Hong Kong, Hong Kong, 1977.

11 Schwarz, W. H., and Cosart, W. P., "The Two-dimensional Turbulent Wall-jet," *Journal of Fluid Mechanics,* Vol. 10, Part 4, 1961, pp. 481–495.

12 Rajaratnam, N., "Plane Turbulent Compound Wall Jets," *Journal of Hydraulic Research,* Vol. 10, No. 2, 1972, pp. 189–203.

13 Gartshore, I. S., and Newman, B. G., "The Turbulent Wall Jet in an Arbitrary Pressure Gradient," *The Aeronautical Quarterly,* Vol. 20, 1969, pp. 25–56.

14 Kruka, V., and Eskinazi, S., "The Wall-jet in a Moving Stream," *Journal of Fluid Mechanics,* Vol. 20, Part 4, 1964, pp. 555–579.

15 Abramovich, G. N., *The Theory of Turbulent Jets,* MIT Press, Cambridge, Massachusetts, 1963.

16 Rodi, W., and Spalding, D. B., "A Two Parameter Model of Turbulence, and Its Application to Free Jet," BL/TN/B/12, Dept. of Mech. Engr., Imperial College, London, 1969.

17 Bradshaw, P., and Gee, M. T., "Turbulent Wall Jets with and without an External Stream," Aero. Research Council, R & M 3252, 1960.

18 Winant, C. D., and Browand, F. K., "Vortex Pairing: the Mechanism of Turbulent Mixing-layer Growth at Moderate Reynolds Number," *Journal of Fluid Mechanics,* Vol. 63, Part 2, 1974, pp. 237–255.

19 Freymuth, P., "On Transition in a Separated Laminar Boundary Layer," *Journal of Fluid Mechanics,* Vol. 25, Part 4, 1966, pp. 683–704.

20 Browand, F. K., "An Experimental Investigation of the Instability of an Incompressible, Separated Shear Layer," *Journal of Fluid Mechanics,* Vol. 26, Part 2, 1966, pp. 281–307.

21 Sato, H., "The Stability and Transition of a Two-dimensional Jet," *Journal of Fluid Mechanics,* Vol. 7, 1959, pp. 53–80.

22 Escudier, M. P., and Nicoll, W. B., "The Entrainment Function in Turbulent Boundary-layer and Wall-jet Calculations," *Journal of Fluid Mechanics,* Vol. 25, Part 2, 1966, pp. 337–366.

23 Rajaratnam, N., and Subramanya, K., "Diffusion of Rectangular Wall Jets in Wider Channels," *Journal of Hydraulic Research,* Vol. 5, 1967, pp. 281–294.

24 Liepmann, H. W., and Laufer, J., "Investigations of Free Turbulent Mixing," NACA TN 1257, 1947.

25 Patel, V. C., "Calibration of the Preston Tube and Limitation on its Use in Pressure Gradients," *Journal of Fluid Mechanics,* Vol. 23, Part 1, 1965, pp. 185–208.

26 Kacker, S. C., and Whitelaw, J. H., "Some Properties of the Two-dimensional, Turbulent Wall Jet in a Moving Stream," ASME *Journal of Applied Mechanics,* Vol. 35, Part 4, 1968, pp. 641–651.

27 Bajura, R. A., and Szewczyk, A. A., "Experimental Investigation of a Laminar Two-dimensional Plane Wall Jet," *The Physics of Fluids,* Vol. 13, No. 7, 1970, pp. 1653–1664.

J. A. Clark
Senior Lecturer,
Department of Mechanical Engineering,
University of Hong Kong,
Hong Kong

Lam Kit
Lecturer,
Department of Mechanical
& Marine Engineering,
Hong Kong Polytechnic,
Hong Kong

Shear Layer Transition and the Sharp-Edged Orifice

The present experiments provide information about free shear layer transition to turbulence and the associated three-dimensional behavior patterns of vortex growth and breakdown. The free shear layers of a submerged jet were generated from two-dimensional sharp-edged orifices. Two distinct types of growth patterns, namely, the twisting growth pattern and the interlocking growth pattern were observed. The interaction phenomena of these vortex tubes are hypothesized to be associated with mutual induction. Quantitative data of exit central velocity, pre-coalescent wavelength between consecutive vortices, and vortex shedding frequency were measured and the interrelationships of Strouhal number, Reynolds number and the dimensionless convection velocity of vortices are discussed.

Introduction

The investigation of free shear layer instability and transition is important in the understanding of a complicated process in turbulence generation. The formation of vortices due to the instability of free shear layers formed by different geometries of nozzles, orifices and splitter plates have been investigated by Sato [1], Wille [2], Michalke [3], Freymuth [4], Becker and Massaro [5], Beavers and Wilson [6], Rockwell and Niccolls [7], Clark and Markland [8], Winant and Browand [9].

Quantitative results of frequency of vortex occurrence, f, obtained using hot-wire anemonetry or directly from visualization methods illustrated that the relationship between Strouhal number and Reynolds number was different for various jet devices. The dimensionless vortex convection velocity, U_c/U_0, was found to have values between 0.5 and 0.6 and they are listed in Table 1.

Research also concentrated on the behavior mechanisms of vortex development and breakdown into turbulence. The two-dimensional vortex coalescent process or "vortex-pairing" is described by Beavers and Wilson [6], Rockwell and Nicolls [7] and Winant and Browand [9]. However, Miksad [11], Clark and Markland [8], Holdeman and Foss [12] and Rockwell [13] focus attention on three-dimensionality effects before the vortices break down into turbulence, but, as pointed out by Roshko [14], the precise role has yet to be determined.

The present research aims at obtaining a more detailed picture of the three-dimensional effects in the transverse vortex tubes, the mechanism of vortex growth, and their breakdown into turbulence. Quantitative data of Strouhal number, $S_t = fW/U_0$, dimensionless convection velocity for different Reynolds numbers, $R_e = U_0 W/\nu$, and slot widths of jet W were measured, where U_0 is the exit central velocity of jet.

Contributed by the Fluids Engineering Division and presented at the Fluids Engineering Conference, New Orleans, La., March 18-20, 1980, of THE AMERICAN SOCIETY OF MECHANICAL ENGINEERS. Manuscript received by the Fluids Engineering Division, September 18, 1978. Paper No. 80-FE-1.

Experimental System With Visualization Technique

Free shear layers generated from a sharp-edged two-dimensional orifice were chosen as they have steep transverse velocity profiles which are extremely unstable and readily roll up into vortices. Also, as pointed out by Becker and Massaro [5], these mixing layers with their complicated transition phenomena have only been fragmentarily studied and more work is needed for clarification. A large scale recirculating water tunnel, shown in Fig. 1, was designed to obtain Reynolds numbers R_e from 1,300 to 16,500 with laminar flow at the exit of the two-dimensional orifice. A 275 cm tall vertical duct was made with a perspex test section to facilitate flow visualization. Its cross-section is 43 cm × 43 cm and incorporates a sharp-edged orifice of slit widths: 7.6 cm, 5.1 cm, 3.8 cm, 2.5 cm, and 1.3 cm, respectively. The aspect ratio (AR) of the slits are 5.7, 8.5, 11.3, 17, and 34, respectively. The large scale device allowed relatively clear pictures of the vortex growth and breakdown processes, and the large aspect ratios would minimize the influence of the wall boundaries at both ends of the orifice outlet and ensure the development of two-dimensional shear layers. Writing ink as the tracer dye was entrained into the vortex core after it had slowly slid down one of the inclined edges of the orifice slit. Thus, colored vortex tubes were observed rolling up when viewed from the lateral direction, with the growth process and paths of the vortices clearly shown. Motion films of the phenomena were taken using an 8 mm movie camera with a speed of 54 frames/s.

In this context a vortex tube is the rolled-up region of dyed fluid which defines a collection of vortex lines. Such agglomerations of vorticity are joined to their neighbors by an umbilical cord of vorticity but this portion is excluded using this terminology. These studies concentrate on the life of these initially discrete vortical structures.

Vortex Formation, Growth Patterns, and Breakdown

Vortices generated at the slit exit were observed to convect downstream during which time they interact, coalesce and

Table 1 Experimental values of dimensionless convection velocities

Free shear layer devices	Experimental investigators	Convection velocity U_c/U_0
Plane nozzle (air)	Sato [1]	0.55
Separated shear layer (air)	Browand [10]	0.58
Round nozzle (air)	Becker and Massaro [5]	0.52
Splitter plate (air)	Miksad [11]	0.57
Plane nozzle (water)	Rockwell and Niccolls [7]	0.50 to 0.55
Plane wall jet (water)	Clark and Markland [8]	0.54 to 0.66
Plane orifice (water)	Present study	0.54

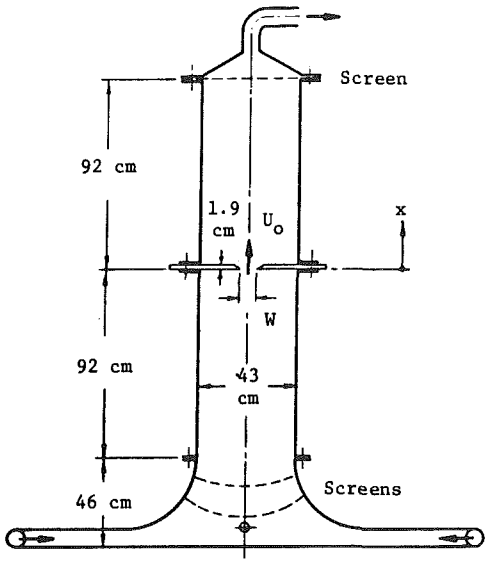

Fig. 1 Schematic diagram of test section for recirculating water tunnel (*W* not to scale)

develop with different growth patterns. These vortex tubes finally disintegrate completely into fully developed turbulence. The stages of this transition process are:

1) Vortex Formation ($0 < \times < 1.5\lambda_0$). Free shear layers generated from sharp-edged orifices are extremely unstable and roll up into circular transverse vortices at distances from 1 to 1.5 precoalescent wavelengths λ_0 from the sharp edge. the vortex tubes (initial diameter approximately 0.3 cm) were observed to extend to the side wall boundary layers (43 cm channel width). The field of detailed observations was taken from the central 7.6 cm to 10 cm region in which no systematic influence of finite span of test section occurred. The vortices on initiation were observed to be two-dimensional transverse vortices with axes parallel to the slit edge (Fig. 2). In its initial stage of development, the full length of the vortex tube convects downstream with the same speed and it behaves as a rectilinear vortex.

2) Patterns of Growth ($1.5\lambda_0 < \times < 12\lambda_0$).

Two-Dimensional Vortex Coalescent Region ($1.5\lambda_0 < \times < 5\lambda_0$): As newly generated consecutive vortices convect downstream, the leading vortex is caught by the trailing vortex and then they coalesce and become a single larger vortex. This uniting is relatively rapid and the process occurs without significant three-dimensional effects. Such coalescence usually occurs at $3\lambda_0$ to $5\lambda_0$ downstream from jet exit. The size of the resulting combined vortex after the first coalescence is approximately 1.5 times that of the initial vortex, while the new relative distance between consecutive vortices is doubled ($2\lambda_0$). Such coalescence may be similar to that of Rockwell and Niccolls' [7] "nascent stage" coalescence but in this case the size of the pre-coalescent vortices is bigger. The catching-up process continually occurs and the approach direction of the trailing vortex is compatible with the direction of rotation of the leading vortex.

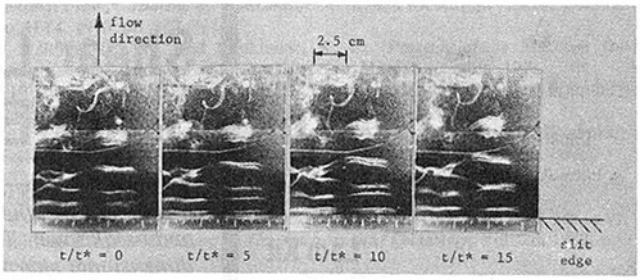

Fig. 2 Time history visualization of vortex initiation close to the slit edge and development of vortex growth patterns for $W = 2.5$ cm and $U_0 = 5.6$ cm/s with $f = 5.8$ Hz

Three-Dimensional Twisting and Interlocking Region ($5\lambda_0 < \times < 12\lambda_0$): Three-dimensional effects often initiate about $5\lambda_0$ from the jet exit. These result from induction present during coalescence producing spanwise variations. As the vortex tubes convect farther downstream from the two-dimensional region, their axes bend and deviate from the pure transverse direction. This change from the rectilinear, in some extreme cases, produces segments of the vortex tube aligned in the longitudinal streamwise direction as part of a horseshoe configuration. In this three-dimensional region, the vortices do not coalesce with each other along their entire length at the same instant. Instead, they twist, or interlock, resulting in either of the two distinct growth patterns, namely, the twisting pattern, or the interlocking pattern. Figs. 3A, B show diagramatically the two growth types which exist for each slit and Reynolds number investigated. In twisting or interlocking

Nomenclature

B_0 = breakdown distance of vortex tube from sharp-edge of orifice
d = diameter of vortex tube
f = average frequency of occurrence in vortex shedding
L = length of sharp edge of orifice, 43 cm
R_e = jet Reynolds number based on exit central velocity, $U_0 W/\nu$
S_t = jet Strouhal number based on exit central velocity, fW/U_0
t = time in seconds
t^* = a reference length of time, 0.0185 s
U_c = convection velocity of vortex tubes
U_0 = exit central velocity of jet
W = width of orifice or nozzle outlet for plane jet
x = streamwise coordinate from center of jet exit
y = lateral coordinate normal to shear layer
z = spanwise or transverse coordinate
Γ = circulation or strength of vortex, $U_0\lambda_0$
λ_0 = average precoalescent wavelength between consecutive vortices

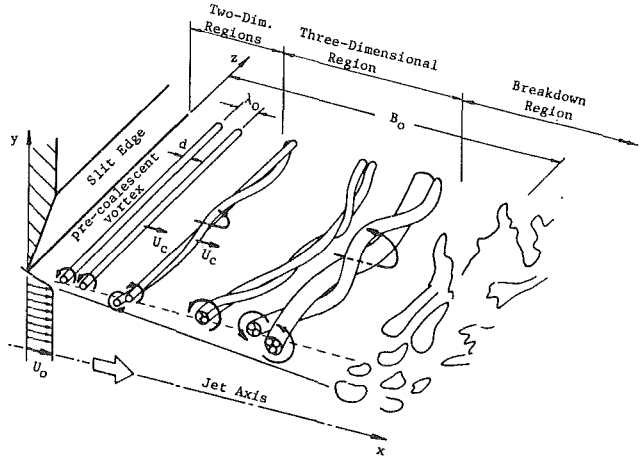

(A) TWISTING PATTERN

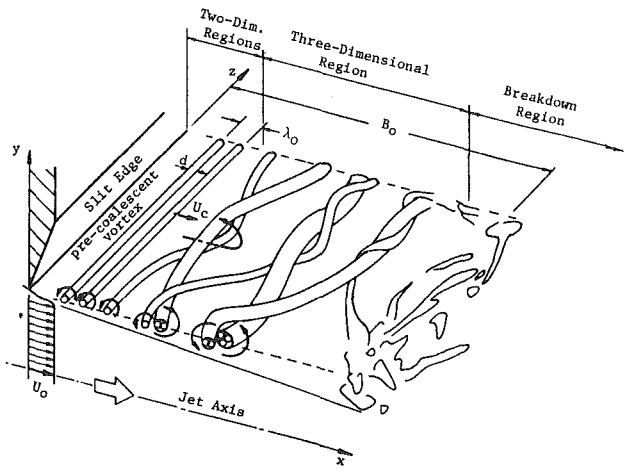

(B) INTERLOCKING PATTERN

Figs. 3A,B Diagrammatic representation of vortex behavior patterns from the initiation stage to vortex coalescence, twisting or interlocking and eventual breakdown into turbulence

as many as five original pre-coalescent vortices may eventually be intimately involved before eventual breakdown. Recent research by Chandrsuda, et al., [15], also illustrated similar twisting patterns known as "double helix." These patterns of growth result from induction between vortex tubes and the degree of twisting or interlocking depends on the relative induction effect. The extent of three-dimensionality in twisting growth patterns is not as strong as in the interlocking growth patterns. It was observed that even with the same jet speed and Reynolds number, the growth patterns always change. The more regular twisting growth pattern develops into the chaotic interlocking growth pattern. Over the full length of the vortex tubes, some sections may be involved in twisting while others in interlocking, thus the latter effect would spread in the spanwise direction due to induction.

3) Vortex Breakdown ($x > 12\lambda_0$). The vortices eventually break down with complete disintegration of their structure into incoherent turbulence, due initially to twisting or interlocking. No single vortex tube was observed to break down by itself in isolation. Vortex tubes usually disintegrate more rapidly by stretching and diffusion due to interlocking than twisting, which is consistent with Clark and Markland's [8] observations that the velocities induced by vortex elements with axes in the direction of motion often lead to a rapid three-dimensional breakdown of the ordered flow. Depending on the degree of three-dimensionality, even with the same slit configuration and Reynolds number, the breakdown distance

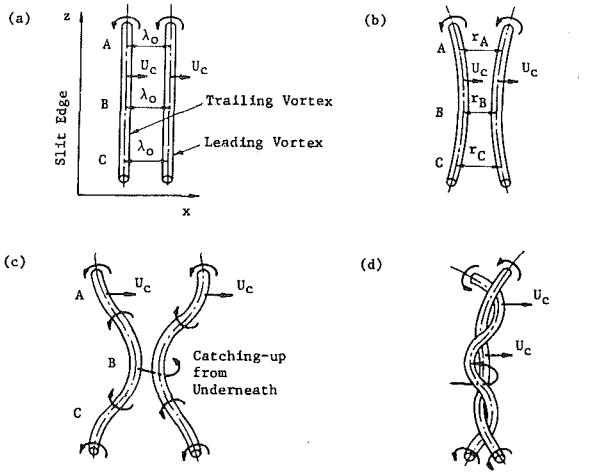

Fig. 4 The influence of mutual induction causing interaction effects between consecutive vortices with

- ***(a)* two rectilinear vortices initially parallel;**
- ***(b)* bending of the axes due to external influences;**
- ***(c)* stronger three-dimensional effects from mutual induction; and,**
- ***(d)* vortex tubes catching-up and twisting around each other.**

B_0 may differ by $4\lambda_0$ to $5\lambda_0$. Before the downstream formation of turbulence, the twisting patterns usually involve the interaction of more successive original vortices than the interlocking patterns. It is believed that a contributary affect to eventual breakdown is the stretching produced when the vortices twist or interlock with each other.

Qualitative Explanation of Vortex Growth Mechanisms in a Free Shear Layer

In these experiments, with large aspect ratio ($5.7 < AR < 34$) and Reynolds numbers of 1,200 to 17,000, the vortex interaction phenomena occur within $12\lambda_0$, namely, $x/W < 1.1$ for AR = 5.7 and $x/W < 5$ for AR = 34. Further support by Foss and Jones [16], Holdeman and Foss [12], and Rockwell [13] reveals that these observed flow regions are "safe" from systematic three-dimensional vortex stretching which occur in the neighborhood of the wall. Freymuth [4] postulated that the three-dimensional breakdown of the vortices is caused by their mutual interaction, i.e., by induction. The above detailed observations relate this mutual induction between vortices more specifically to the three-dimensionality of the growth patterns before breakdown.

When an initially discrete vortical structure is first generated, it moves downstram with convection velocity U_c with its axis parallel to the preceding vortex. Due to small external disturbances from either vortex breakdown phenomena or three-dimensional effects in the preceding vortex, the axes of the two consecutive vortex tubes (aspect ratio $L/d > 100$) easily bend and no longer remain parallel as indicated in Fig. 4. For two consecutive vortices under the influence of mutual induction, according to Biot - Savart's Induction Theorem [17], the effect of induction would depend on the relative distance between vortices. The segments of vortex tubes closer to each other would coalesce more quickly, giving rise to three-dimensionality. Bending of a vortex tube is amplified as the vortex convects downstream and the direction of its axis, along a limited length, may eventually change to a longitudinal direction with part of the vortex appearing as a "horseshoe" shape. Farther downstream the two vortex tubes twist around each other as part of the growth patterns of twisting or interlocking. More detailed descriptions of such mechanisms together with a theoretical model calculated by computer are given by Lam [18]. Also vortex induction playing a key role in the pairing process is modelled using discrete vortices by Acton [19].

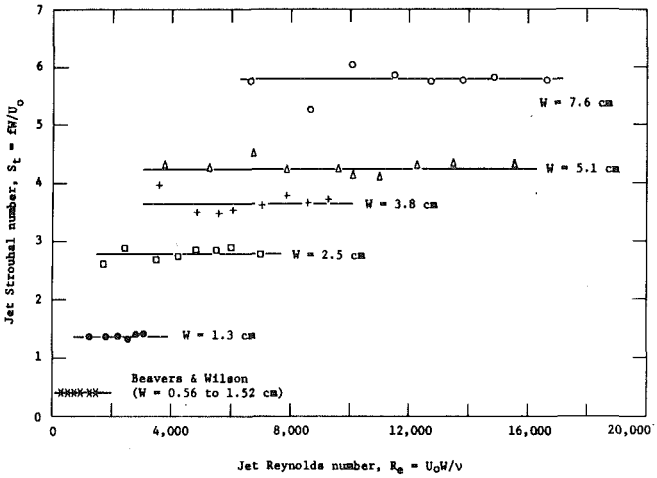

Fig. 5 Relationship between jet Strouhal number and jet Reynolds number for the free shear layer

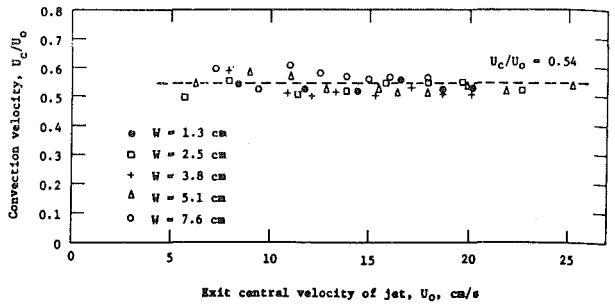

Fig. 6 Relationship between dimensionless convection velocity of the vortex tubes and the exit central velocity of jet

Experimental Results and Analysis

Strouhal Number S_t and Reynolds Number R_e. The number of precoalescent vortices shed per second was counted using cine film projected in slow motion. The frequency of vortex shedding f is not exactly periodic with a maximum uncertainty or deviation from the mean ranging from ± 10 percent at low frequencies (below 10 Hz) to ± 3 percent at high frequencies (above 16 Hz). The frequency f for each slit was found to be directly proportional to the jet central velocity U_0. Thus the relationship $f = k_w U_0$ was obtained, where k_w is a constant for a given slit width (W) of the experimental facility. It was observed that k_w increases with decreasing W until a maximum at $W = 2.5$ cm. As shown in Fig. 5, the Strouhal number S_t was plotted against the Reynolds number R_e for each slit and S_t was found to be constant in the range of $1{,}200 < R_e < 18{,}000$ and dependent on W. The uncertainty of (S_t, R_e), with absolute values of 20:1 odds, is for coordinates (6, 10,000) an uncertainty of (± 0.4, ± 200) and for coordinates (1.3, 2,000) an uncertainty of (± 0.1, ± 50).

These results are consistent with the findings of Beavers and Wilson [6] for two-dimensional sharp-edged orifices. The latter suggests that viscosity is not important in the generation of these vortices from two-dimensional orifices which are without a significant initial boundary layer condition, as is not the case for plane smooth nozzles.

Wavelength λ_0 and Convection Velocity U_c. In this research, the precoalescent wavelength λ_0 between vortices shed was measured and for each slit configuration, the average value of λ_0 is independent of U_0 within the R_e range. The results of U_c/U_0 or $f\lambda_0/U_0$ obtained in this experiment are shown in Fig. 6. All the values are within the limits 0.5 and 0.6 with a mean value $f\lambda_0/U_0 = 0.54$ of uncertainty ± 0.06. After coalescence, the wavelengths between consecutive vortices could not easily be determined and consequently quantitative information relating to vortex convection downstream of the two-dimensional region was not found.

Conclusions

Free shear layers developed from a submerged jet of water issuing from two-dimensional sharp-edged orifices have been visualized. Vortex formations, growth patterns and breakdown associated with transition were studied, the shear layer being sub-divided in the longitudinal direction. The vortex formation region (0 to $1.5\lambda_0$) is characterized by initiation of vortex tubes with axes parallel to the slit edge. The two-dimensional vortex coalescent region ($1.5\lambda_0$ to $5\lambda_0$) is dominated by the coalescence of vortex tubes by induction, with the vortices remaining parallel and rectilinear but of larger diameter and increased spacing. The three-dimensional twisting and interlocking retion ($5\lambda_0$ to $12\lambda_0$) displays either the twisting growth pattern or the interlocking growth pattern, with the vortices no longer rectilinear but having three-dimensional characteristics. Finally, the breakdown region ($> 12\lambda_0$) produces random turbulence after the vortices have undergone increased stretching due to the mutual induction effects.

Qualitative results showed that for each orifice, the jet Strouhal number is a constant independent of Reynolds number and the dimensionless convection velocity $U_c/U_0 = 0.54 \pm 0.06$ for all Reynolds numbers.

References

1 Sato, H., "The Stability and Transition of a Two-Dimensional Jet," *Journal of Fluid Mechanics,* Vol. 7, No. 1, 1960, pp. 53-80.

2 Wille, R., "Contribution a la Phénoménologie des Jets Libres," *Technique et Science Aeronautiques et Spatiales,* No. 6, 1962, pp. 422-432.

3 Michalke, A., "Vortex Formation in a Free Boundary Layer According to Stability Theory," *Journal of Fluid Mechanics,* Vol. 22, No. 2, 1965A, pp. 371-383; and Vol. 23, 1965B, pp. 521-544.

4 Freymuth, P., "On Transition in a Separated Laminar Boundary Layer," *Journal of Fluid Mechanics,* Vol. 25, No. 4, 1966, pp. 683-704.

5 Becker, H. A., and Massaro, T. A., "Vortex Evolution in a Round Jet," *Journal of Fluid Mechanics,* Vol. 31, No. 3, 1968, pp. 435-448.

6 Beavers, G. S., and Wilson, T. A., "Vortex Growth in Jets," *Journal of Fluid Mechanics,* Vol. 44, No. 1, 1970, pp. 97-112.

7 Rockwell, D. O. and Niccolls, W. O., "Natural Breakdown of Planar Jets," ASME *Journal of Basic Engineering,* Vol. 94, 1972, pp. 720-730.

8 Clark, J. A., and Markland, E., "Flow Visualization in Free Shear Layers," *Journal of Hydraulics Division,* Proc. ASCE, Vol. 99, No. HY11, Nov. 1973, pp. 1897-1913. Errata: Vol. 100, HY6, June 1974, pp. 832-833.

9 Winant, C. D., and Browand, F. K., "Vortex Pairing: The Mechanism of Turbulent Mixing-Layer Growth at Moderate Reynolds Number," *Journal of Fluid Mechanics,* Vol. 63, No. 2, 1974, pp. 237-255.

10 Browand, F. K., "An Experimental Investigation of the Instability of an Incompressible, Separated Shear Layer," *Journal of Fluid Mechanics,* Vol. 26, No. 2, 1966, pp. 281-307.

11 Miksad, R. W., "Experiments on the Non-Linear Stages of Free Shear Layer Transition," *Journal of Fluid Mechanics,* Vol. 56, No. 4, 1972, pp. 695-719.

12 Holdeman, J. D., and Foss, J. F., "The Initiation, Development, and Decay of the Secondary Flow in a Bounded Jet," ASME JOURNAL OF FLUIDS ENGINEERING, Vol. 97, 1975, pp. 342-352.

13 Rockwell, D. O. "Vortex Stretching Due to Shear Layer Instability," ASME JOURNAL OF FLUIDS ENGINEERING, Vol. 99, 1977, pp. 240-244.

14 Roshko, A., "Structure of Turbulent Shear Flow: A Newlook," *AIAA Journal,* Vol. 14, No. 10, 1976, pp. 1349-1357.

15 Chandrsuda, C., Mehta, R. D., Weir, A. D., and Bradshaw, P., "Effect of Free-stream Turbulence on Large Structure in Turbulent Mixing Layers," *Journal of Fluid Mechanics,* Vol. 85, Part 4, 1978, pp. 693-704.

16 Foss, J. F., and Jones, J. B., "Secondary Flow Effect in a Bounded Rectangular Jet," ASME *Journal of Basic Engineering,* Vol. 90, No. 2, 1968, pp. 241-248.

17 Batchelor, G. K., *An Introduction to Fluid Dynamics,* Cambridge University Press, 1967, p. 509 for "Biot-Savart's Induction Theorem."

18 Lam, K., "Visualization Study on Growth and Breakdown of Two-Dimensional Vortices from Sharp-Edged Slits," M.Phil. thesis, 1977, Dept. of Mechanical Engineering, University of Hong Kong, Hong Kong.

19 Acton, E., "The Modelling of Large Eddies in a Two-Dimensional Shear Layer," *Journal of Fluid Mechanics,* Vol. 76, Part 3, 1976, pp. 561-592.

DISCUSSION

J. F. Foss.[1] The author's observations of the twisting and the interlocking modes of vortex structure interactions provides a welcome contribution to the literature in free shear layer instabilities. As the authors note, the shear layer generated from a sharp-edge orifice has not been extensively studied; consequently it would be instructive to compare the present observations with those of flow visualization studies from the more common "parallel exit flow" conditions to ascertain if twisting and interlocking events are also observed for the latter. In particular, since it is now recognized that the authors' Strouhal number results are influenced by the apparatus, it will be of interest to determine if the two proposed modes are a "universal" feature of unstable shear layers.

The present discussion is focused upon the pre-interaction stage of the shear layer's evolution. Specifically, the author' $S_t = S_t(W, R_e)$ experimental results, which are in contrast with the results of the Beavers and Wilson study [6], have stimulated the development of a theoretical model to make rational the observations of the two studies. Apparently, the following observations have not been previously advanced in the published literature. The theoretical results of general interest are:

i) a rationale for the use of the nozzle width (W) as the appropriate scale length for the sharp-edge orifice; this is in contrast with the indirect role of W in the instability process associated with parallel flow nozzles.

ii) a rationale for the observed: $S_t \sim R^0{}_e$.

In addition to these general observations, the existance of apparatus dependent effects in the present study will be identified. The theoretical considerations, which lead to the observed: $S_t \sim (R^0{}_e)$ results for sharp-edge orifices, can be set in a context which also yields the familiar $S_t \sim R_e{}^{1/2}$ result for parallel flow nozzles. This general context will first be established.

Consider the shear layers which develop downstream of the separation lines in Figures 1 and 2. The dashed lines show the solution domains for the boundary value problems of interest; viz, the region in which the shear layer instability will create a series of vortices from the continuously shed vorticity of the approach boundary layer. This process of agglomerating the shed vorticity is not, in the unforced state, strictly periodic; see, for example, Freymuth [4]. However, an average period can be defined ($\equiv \pi$) and τ will be used as a time scale in the following considerations.

Since the Navier-Stokes and the conservation of mass equations constitute a complete set of equations for the description of the flow in the domain of interest, it is possible to use these equations to establish the parametric dependence of the period τ upon the other parametric factors involved in the problem description. As discussed, for example, by Potter and Foss (20), the non-dimensional velocity: $\vec{v}^*(=\vec{v}/U_0)$, and pressure: $p^*(=p/\rho U_0{}^2)$ will be a function of the non-dimensional position: $\vec{x}(=\vec{x}/L)$ and time: $t^*(t/\tau)$ for the given problem of interest; furthermore, the solution to the non-dimensional equations will be parametrically dependent upon the scaling parameters introduced by the equations and the boundary conditons. For the shear layer, the Strouhal number appears as the coefficient of the partial time derivative term and the Reynolds number as the coefficient of the viscous term in the Navier-Stokes equation (note, $\tau^{-1}=f$):

$$\left[\frac{Lf}{U_0}\right]\frac{\partial \vec{v}^*}{\partial t^*} + \vec{v}^* \cdot \nabla^* \vec{v}^* = -\nabla^* p^* + \left[\frac{\nu}{U_0 L}\right]\nabla^{*2}\vec{v}^*$$

Additional parameters may be introduced by the boundary conditions.

For the specific case of the shear layer as shown in Figure 1, and for $\theta/W << 1$, it is interesting to note that there is no intrinsic geometric length scale: L. That is, the evolution of the upper shear layer instability would be independent of the presence of the lower shear layer. Experimentally, the shear layer instability process would be unchanged if the dimension w were, for example, doubled. In spite of this, the S_t data from such experiments are often (properly) presented in terms of the width W; viz., $S_t\,(=fW/U_0) \sim R^{1/2}(=[U_0 W/\nu]^{1/2})$; see for example, Davies and Baxter (21). This is made rational by the observation that an appropriate length scale for the flow problem of Figure 1 can be based upon the initial boundary layer: e.g., $L=\theta(x=0)$.* Furthermore, since $\theta(x=0)$ is the result of the boundary layer growth on the approach nozzle wall and since this length scales upon *W for a given nozzle*

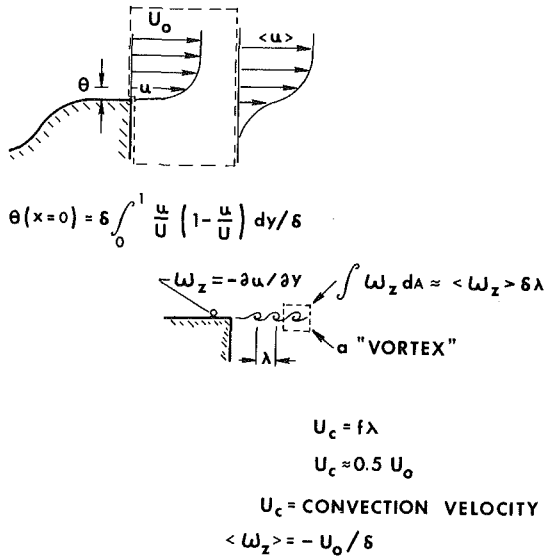

Fig. 1 Parallel flow nozzle

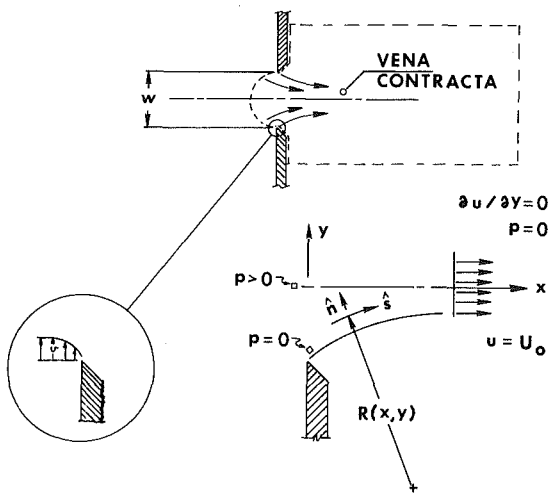

Fig. 2 Sharp-edge nozzle

[1] Mechanical Engineering Department, Michigan State University, East Lansing, Mich. 48824.

geometry, it is plausible that $\theta \sim \sqrt{U_0 W/\nu}$ for a laminar boundary layer on the nozzle wall. Numerous observations of this functional dependence have been made.

The above considerations, which represent a rephrasing of concepts available in the published literature (see, e.g., Michalke [22]), have been presented to emphasize the indirect role of W in the instability process of the shear layer depicted in Figure 1. This makes the parallel exit flow condition fundamentally different from that of the sharp-edge orifice instability problem.

The explicit role of W for the sharp-edge orifice, is most readily seen by considering the streamline pattern which exists from $x=0$ to $x=x_c$; x_c denotes the streamwise location of the vena contracta where, to first order, $p(x_c,y)=0$. The pressure field, in the domain: $0<x<x_c$, can be represented in terms of the solution to the Navier-Stokes equations for this region. If the Reynolds number is sufficiently large, it can be expected that the particular form:

$$\frac{\partial p}{\partial n} = \rho \frac{V^2}{R}; \qquad 8.11 \text{ of (20)}$$

will represent the govening equation for $p(x,y)$ where $n(x,y)$ is the "outward drawn" normal to the streamline and $R(x,y)$ is the radius of curvature of the streamline at the point (x,y). The minimum R value exists at the sharp edge of the nozzle surface where the flow separates; it is infinite at the centerline for all x (neutrally bouyant and symmetric conditions assumed) and it is infinite at x_c. The value of W represents a naturally defined geometric scale length for this problem; hence $n^*=n/W$, $R^*=R/W$ and p^*, $\vec{v}^*$ are as above. The Euler "n" equation is strictly valid for an inviscid flow situation; however, since $\theta(x=0)$ is expected to be quite small for moderately large Reynolds numbers (i.e., $\theta << W$) it is reasonable to assume that the (x_c/W) ratio will be quite insensitive to $[U_0 W/\nu]$. Note that as the R_e is increased, the above noted minimum R value is expected to be increased. This is the primary influence of the Reynolds number in the sharp-edge orifice configuration.

The above considerations show that the Strouhal number: $S_t = fW/U_0$, can be expected to depend upon the parameters of the problem as:

$$S_t = S_t\left(\frac{U_0 W}{\nu}, \frac{\theta(x=0)}{W}, \frac{\delta_d(x=0)}{\theta(x=0)}, \ldots\right)$$

The experimental observation, by Beavers and Wilson, that: $S_t \sim (R^0{}_e)$, suggests that the potentially more complex flow field: the sharp-edge orifice shear layer, is less complex than the shear layer which was created from the geometry of Figure 1. Their investigation, executed for a range of Reynolds numbers and nozzle exit widths, revealed that a universal value of the Strouhal number apparantly exists; viz., $S_t \cong 0.43$. The implication of their data is that the instability process is governed by the radius of curvature in the shear layer which exists between $x=0$ and $x=x_c$. This speculation is considered to be quite worthy of theoretical analysis.

The present author's results are now subject to proper interpretation. Specifically, the data of Figure 5 are similar to those of Beavers and Wilson in that $S_t \sim (R^0{}_e)$; however, the present results also show a systematic dependence between the constant of proportionality and the width of the nozzle. Since the tunnel width is equal to the nozzle length and since this length is constant for the authors' study, the W variation is equivalent to a variation in aspect ratio. Considering that the Beavers and Wilson data represent an infinite aspect ratio condition, i.e., one representative of a two-dimensional experiment, it is interesting to consider the possibility that the present results can be interpreted as an aspect ratio dependence: $S_t = S_t(W/L)$.

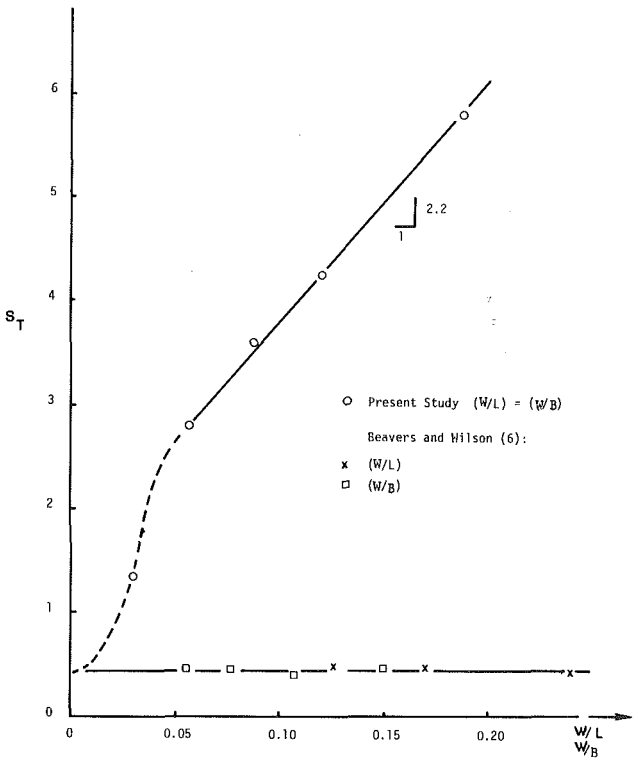

Fig. 3 Comparative evaluation: Strouhal number dependence upon geometric parameters

0 Present study *(W/L) = (W/B)*
x Beavers and Wilson [6] *(W/L)*
□ Beavers and Wilson [6] *(W/B)*

Figure 3 presents the authors' data, along with the "seemingly-infinite-aspect-ratio" data of Beavers and Wilson,[2] on $[S_t, W/L]$ coordinates. Note that the dashed line represents an interpolation which has the correct slope as W/L approaches zero. It is obvious that the observations do not support the interpretation that a systematic aspect ratio dependence exists. Furthermore, the ratio of slit width W to channel width B was also checked for its possible influence, the similar values of W/B for the two studies also reject this parameter as the source of a significant influence on the observed S_t values.

A plausible source of the apparatus dependent effects in the authors' study is provided by the internal flow pattern which must exist in the 43×43 cm channel downstream of the slit. Since only the original mass flux will exit the channel and since the "jet" will entrain "ambient" fluid during its passage to the end of the channel, there must be a recirculation pattern which delivers fluid to the shear layer and, in particular, to the neighborhood of $x=0$. It does not appear to be useful to further speculate about this feedback pattern, the internal flow patterns are sufficiently complex that it would be difficult to accurately predict them. Consequently, no attempt will be made to rationalize the $dS_t/d(W/L)$ slope of the present investigation. It can be noted, however, that the Beavers and Wilson study was carried out with a geometry that would not establish such a sharp distinction between the return flow and the through flow in the test section; this lends considerable credence to the interpretation that the feedback

[2] Neither the aspect ratio nor the W/B values of the Beavers and Wilson jets were not identified in the original paper. The writer hereby expresses appreciation to Prof. Beavers for supplying this supplementary information.

effect is the predominant cause for the authors' observations that the Strouhal number increased with W/L (or W/B). In conclusion, it is emphasized that this aspect of their results and their reference to. . . "large aspect ratio",. . ."two-dimensional" conditions must be properly interpreted. Experiments, stimulated by the above considerations, are being executed in the writer's laboratory.

Acknowledgment

The writer wishes to express appreciation to the Alexander von Humboldt Foundation, Federal Republic of Germany. The extended considerations presented above were developed during the writer's sabbatical leave. The Fellowship support, provided by the Foundation for this time period, is gratefully acknowledged.

Additional References

20 Potter, M. C., and Foss, J. F., *Fluid Mechanics,* Wiley, 1975.

21 Davies, P. O. A. L., and Baxter, D. R. J., "Transition in Free Shear Layers," *Structure and Mechanisms in Turbulence,* Vol. 1, Springer-Verlag, No. 75, Lecture Notes in Physics, 1978.

22 Michalke, A., "The Instability of Free Shear Layers," *Progress in Aerospace Sciences,* Pergamon Press, 1972, Oxford-New York, p. 213.

Authors' Closure

Flow visualization studies for the "parallel exit flow" conditions have already been completed by Clark and Markland [8]. However that study concerned in particular the free shear layer transition in two-dimensional wall jets but conformed to the specific condition of its shear layer, as shown in Fig. 1 of the discussion, that $\theta/W << 1$. Comparing those studies with the present observations show fundamental differences, namely; the twisting and interlocking growth patterns were not present and the transverse vortices, on initiation in the shear layer of the wall jet, were of relatively short length (not rectilinear) and grew exponentially as they convect downstream before breaking down three-dimensionally creating the onset of turbulence. Further, the Strouhal number and wave-length dependence on Reynolds number were given by $S_t = 0.0084\ R_e^{1/2}$ and $\lambda_0/W = 71.8\ R_e^{-1/2}$. Thus the two proposed growth pattern modes are not a "universal" feature of unstable shear layers.

To develop a theoretical model for the pre-interaction stage of the shear layer's evolution, it is relevant to select the appropriate length scale for the two-dimensional orifice situation. Although the present results indicate an influence of orifice width, albeit in the formation of the vena contracta as shown in Fig. 2 of the discussion, the applicable length scale may relate to shear layer dimensions immediately before its rolling-up due to its instability. The discusser has dealt in great length with apparatus dependent effects both for the orifice and nozzle but it is obvious that there is a need for further experiments to resolve a number of these questions.

The discusser's interpretation, that the feedback effect is the predominant cause for the authors' observations that the S_t increased with W/L, is not accepted due to what is observed of the re-circulation patterns in the channel downstream of the sharp-edged orifice. To resolve this would necessitate altering the exit conditions of the test section for the recirculating water tunnel. Nevertheless the twisting and interlocking growth patterns and interaction phenomena by mutual induction of the vortex tubes that are observed, are not influenced by the apparatus. These observations occur within 12 λ_0, namely, $x/W < 5$ for $W = 1.3$ cm to $x/W < 1.1$ for $W = 7.6$ cm. Thus with an orifice length (L) of 43 cm and a channel width of 43 cm, the conditions of "two-dimensionality" and "large aspect ratio (L/W)" can be understood and that the visualization studies were confined to a region free from systematic three-dimensional wall effects. Also it should be noted that the final breakdown to random turbulence occurred before 16 λ_0, independent of the type of growth pattern mode involved.

Additional Reference

8 Clark, J. A., and Markland, E., "Flow Visualization in Free Shear Layers," *Journal of Hydraulics Division, Proc. ASCE,* Vol. 99, No. HY11, Nov. 1973, pp. 1897–1913. Errata: Vol. 100, No. HY6, June 1974, pp. 832–833.

Experimental Studies of External Hygrocysts

J. P. Kovac[1]

R. T. Balmer

Rheology Laboratory,
College of Engineering and
Applied Science,
University of Wisconsin-Milwaukee,
Milwaukee, Wisc. 53201

The three-dimensional banding phenomenon that occurs on the outside of single horizontal rotating cylinders covered with a liquid film was experimentally studied. Over 400 data sets from a variety of cylinders and liquids produced an emperical correlation between the number of bands formed and the rotational Reynolds, Weber, and Froude numbers. The average film thickness on the top of the rotating cylinder was found to be independent of the physical properties of the liquid and the centrifugal acceleration of the cylinder. The surface velocity measured in the crown of the bands was found to be nearly the same as that predicted by the steady state unbanded velocity field solution of Moffatt.

Introduction

The observation of ripples, bands or stripes in the fluid on the surface of a horizontal rotating cylinder is not new (see Fig. 1), but serious attempts at their analysis is relatively recent. Theoretical solutions of this type of three-dimensional hygrocyst (Greek: fluid cell) [1] flow field is extremely difficult, but approximate solutions and/or experimental studies of special cases have recently been carried out by Pearson [2], Pitts and Greiller [3], Sone, et al. [4], Yih [5], and Moffatt [6].

Pearson [2] considers the banding formed in spreading or rolling a thin viscous film onto a flat horizontal plate. In this case the fluid is forced through the small gap between the spreader or roller and the flat plate. He utilizes the hydrodynamic theory of lubrication in which inertial and gravitational forces have been ignored. Pearson's theoretical results show that when the flow is governed by surface tension effects that the dominating factor is the dimensionless ratio of Reynold's to Weber number (in which the same characteristic length is used in both numbers, $\mathrm{Re/Wb} = \sigma/(\mu U)$ where σ is the surface tension, μ is the viscosity, and U is the characteristic velocity). Pearson's experimental data supported his theoretical results for $0.1 \leq \mathrm{Re/Wb} \leq 10.0$.

Pitts and Greiller [3], in dealing with the banding on the surface of counter-rotating horizontal cylinders submerged in liquid up to their centerline, focused their attention on the hydrodynamics in the nip region. Using the symmetry condition along the vertical line passing through the nip and a special coordinate system, they developed an approximate solution to the hydrodynamic equations of motion in which the inertial and gravitational terms were also neglected. Their solution requires that the meniscus shape at the nip be parabolic (a condition which resulted from their experimental observations). They were able to show theoretically that the term (Wb/Re) (α/R), where α is the nip half width and R is the cylinder radius, is an important parameter in the banding phenomenon. Their experimental results with glycerine and lactic acid appeared to show the onset of banding at a critical value of (Wb/Re) (α/R), though they noted that at times it was difficult to tell whether or not any bands were present. Their rollers were two inches in diameter (or less) and the nip gap was always in the range of 0.002 in. to 0.02 in. With such a small gap on the relatively small half submerged cylinders, the band height could not become very large (they refer to the bands as "ripples") and it would be difficult indeed to tell whether or not bands were present under certain conditions.

Sone, Fukushima and Fukada [4] carried out an experimental study with a double roller calendering system similar to that used by Pitts and Greiller [2] except that the rotating cylinders were not submerged at all in the test fluid. Their test fluids were butter, printing ink and silicone oil, all of which were measurably non-Newtonian and considerably more viscous ($0.006 \leq \mathrm{Re/Wb} \leq 0.2$) than those used by Pearson or Pitts and Greiller. Their qualitative results were generally in agreement with those of Pitts and Greiller except that they observed the additional influence of a fluid (Maxwell model) relaxation time. The found that as the test fluids relaxation time increases: (*a*) the distance between the band peaks decrease, (*b*) the band width decreases, and (*c*) the band height (defend as the peak to trough distance) increases to a maximum and then decreases.

Yih [5] has carried out a complex stability analysis of a rotating liquid film with a free surface and found that the critical wave number for flow stability depends predominantly on the surface tension (Weber number) and varies inversely with the Reynold's number. In Yih's analysis the equations of motion were linearized (thus eliminating viscosity), gravity was ignored, and the flow was assumed axisymmetric. Moffatt [6] noted that Yih's analysis is not universally applicable to horizontal rotating cylinder banding flows since gravity and viscous shear are often dominating forces in the equations of motion. Yih also performed a series of experiments on a 22 cm diameter lucite cylinder partially submerged in the test fluid (glycerine and a glycerine-water mixture). His data generally agreed with the main results of the stability analysis, but no general correlation for the banding phenomenon was produced.

[1] Present address: Motorola, Inc., Shaumburg, Ill. 60196.

Contributed by the Fluids Engineering Division for publication in the JOURNAL OF FLUIDS ENGINEERING. Manuscript received by the Fluids Engineering Division, September 25, 1978.

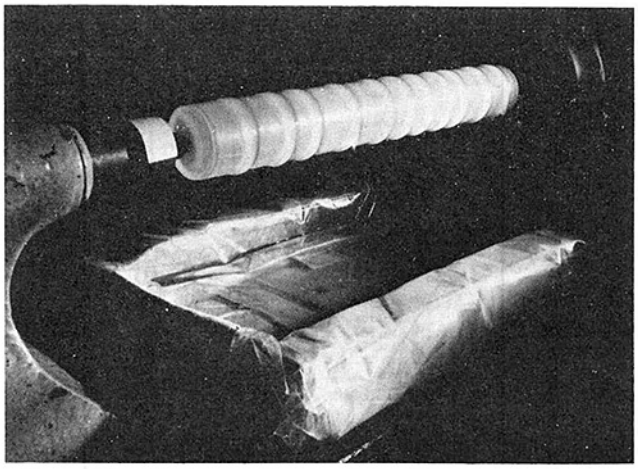

Fig. 1 Glycerine hygrocysts on a rotating 4.4 cm diameter cylinder

Moffatt [6] attempts to analyze the banding phenomenon by first developing a solution for the unbanded steady state velocity field in the liquid layer on the surface of a horizontal rotating cylinder. He develops this solution from the inertialess lubrication theory equations by assuming that the fluid film thickness is much less than cylinder radius. His result is:

$$u(r,\theta) = U - \frac{g \sin\theta}{2\nu}(y^2 - 2yh) \tag{1}$$

where $U = R\omega$ is the tangential surface velocity of the cylinder of radius R and angular velocity ω, y is the radial distance measured from the surface of the cylinder (i.e., $y = 0$ at $r = R$), θ is the angular displacement measured from the top of the cylinder in the direction of cylinder rotation, and $h = h(\theta)$ is the local film thickness. Moffatt then investigates the stability of this unbanded flow solution and concludes that it will inevitably be unstable. However, he does not predict any of the physical characteristics of the banded configuration from the stability analysis and performs only preliminary observational experiments on a nonsubmerged 4.08 cm diameter perspex cylinder using a very viscous (8 PaS) sucrose-water solution.

In view of the extreme difficulty in directly solving the complete hydrodynamic equations for this type of three-dimensional flow, additional experimental data should be of value in formulating improved analytical studies. The purpose of this paper is to present the results of a large experimental study on the formation of liquid bands on the outside of single horizontal nonsubmerged rotating cylinders.

Experimental Method

The experimental apparatus has been described elsewhere [7]. Three test cylinders (4.4, 7.6, and 10.8 cm diameter) were made of capped plexiglass or glass tubes. Glycerine-water mixtures were chosen for the test fluids because their viscosities and surface tensions could be varied over a wide range. The test fluid viscosity was inversely proportional to the amount of water in the mixtures, and the surface tension was varied through the addition of small amounts of surfactant (Kodak Photo Flo solution).

Unfortunately, gylcerine-water mixtures do not wet plexiglass well. Tests with bare plexiglass cylinders produced good results at high rotational speeds, but at low rotational speeds patches of unwetted plexiglass appeared. In order to maintain a consistent liquid layer on the cylinder a thin seamless nylon stocking was stretched over the entire cylinder. The capillary action of the weave of the stocking maintained a wetted surface. The thickness of the fluid film was always greater than the stocking thickness and it was assumed that the surface roughness of the stocking had no effect on the phenomenon being observed.

A liquid layer was applied to the rotating cylinder by raising a shallow pan containing the test liquid up into contact with the bottom of the rotation cylinder. This arrangement provided a uniform, thick, liquid layer on the cylinder's surface. When the cylinder was properly coated, the shallow pan was lowered out of contact with the cylinder but retained directly below the cylinder to catch the excess liquid which dripped off during the transient band formation period (see Fig. 1).

The development of the liquid bands from the thick liquid layer begins with the formation of drip sites located in the region $\pi \leq \theta \leq 3\pi/2$ (where $\theta = 0$ at the top of the cylinder, and where θ is measured in the direction of rotation). As the dripping continues, the fluid film between the drip sites flows axially towards the sites to replace the fluid being lost. Consequently, the film thickness between drip sites decreases significantly while the film thickness at the drip sites increases somewhat. This film thickness variation quickly develops into a banded structure, with one band occurring at each drip site. The dripping rate continually decreases and eventually stops, resulting in a loss of only about 15 percent of the initial band height over a period of two hours. When the dripping ceases an equilibrium state is reached where further liquid loss occurs only by evaporation. An equilibrium configuration was rotated continuously at constant speed for 24 hours without any change in the number of bands present. Since only an integer number of bands, N, can occur and since the final number of bands depends somewhat on the initial drip site distribution, then the reproducibility of number of bands formed with any one set of experimental conditions is $N \pm M$, where M is also an integer. The variation, M, depends primarily on the cylinder length since any two adjacent bands will merge into a single band if they are initially within a certain critical distance of each other. However, once all band mergers have occurred, the remaining bands distribute themselves uniformly along the length of the cylinder. For the results presented here it was observed that M was approximately equal to unity.

While the existence of steady state flow could be verified at medium to high rotational speeds, at low rotational speeds a very long transient process occurred. At low speed rotation, initially two bands consistently formed, one at each end of the cylinder. The gap between these bands remained covered with the thick liquid layer. These two end bands never stopped dripping, and continually, slowly, migrated towards each other until they eventually merged into a single stable (drip-free) band near the center of the cylinder.

Experiments were also carried out to measure liquid surface velocities in the steady state band-trough system. High speed (64 frames/sec.) 16 mm motion picture studies were made of dye traces applied to the surface of the liquid film. The procedure consisted of marking a fluid element with a drop of dye and then performing a frame by frame analysis of the motion of the dye relative to a grid of lines drawn on the cylinder's nylon covering. Values of liquid surface velocity at $\theta = 0$ and $\theta = \pi/2$ were obtained by placing a mirror at 45° above the cylinder and photographing both the cylinder and the mirror from a camera position of $\theta = \pi/2$. In this way both views were photographed simultaneously from a single camera location.

For a given cylinder (of length L and radius R) steady state band structure measurements included recording the liquid's properties (density ρ, viscosity μ-measured on a Weissenberg Rheogoniometer, and surface tension σ-measured with a du Nöuy apparatus), the rotational speed of the cylinder ω, and

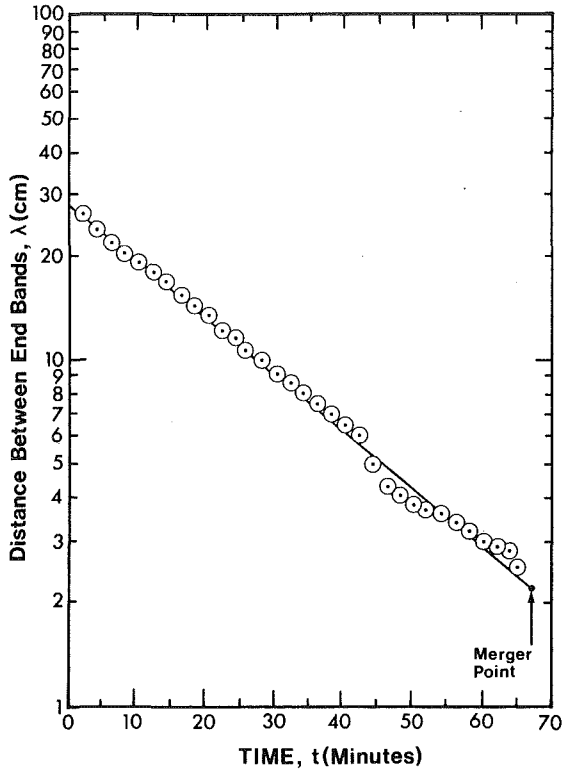

Fig. 2 Semilog plot of the distance between migrating end bands at low (ω = 0.79 RPS) rotational speed versus time. The test fluid was glycerine (μ = 2.78 poise, σ = 57.7 dyn/cm) on a 4.4 cm diameter, 34 cm long cylinder. The solid line is given by $\lambda = 28.7 \exp(-t/26.4)$, where λ is in cm and t is in minutes. Coordinate uncertainty (absolute, 20:1 odds): (λ,t) ($\pm$0.05, $\pm$0.10).

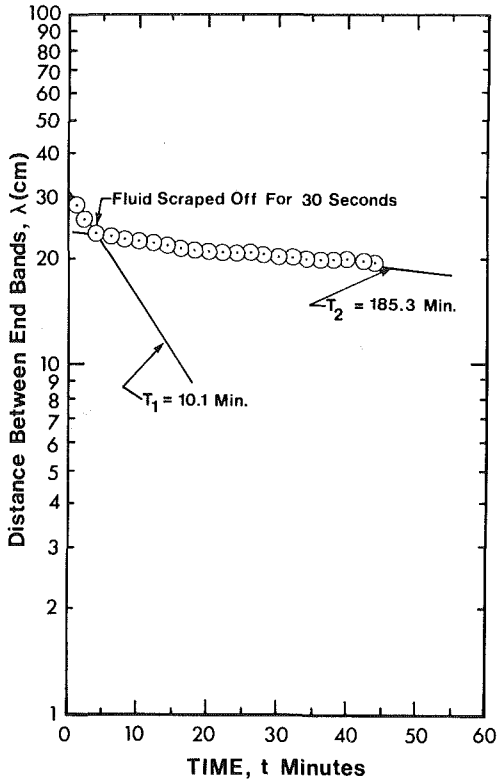

Fig. 3 Semilog plot of the distance between migrating end bands at low (ω = 0.80 RPS) rotational speed versus time when the liquid film was removed from the region between the bands. The test fluid and cylinder are the same as those used in Fig. 3. Coordinate uncertainty (absolute, 20:1 odds): (λ,t) ($\pm$0.05, $\pm$0.10).

the average film thickness at the top of the cylinder $h_{avg.}$ (defined as one half of the band crown to trough distance and measured using the same technique as Yih [5], see [8] for details).

Results

Figure 2 presents distance-time data for end-band migration towards the center of the cylinder at a low rotational speed. These data are accurately fit with an exponential relationship of the form:

$$\lambda = \lambda_0 \exp\left(-\frac{t}{T}\right) \tag{2}$$

where λ and λ_0 are the distance between the end-bands at time t and time zero respectively, and T is the time constant of the migration. Close inspection of these bands revealed that the film thickness on the cylinder-end side of each band was always significantly less than that in the inter-band region. Therefore, the wetting angle between the band and the inter-band region was approximately zero. However, the wetting angle on the relatively dry cylinder-end side of each band was finite. Therefore a net surface tension force difference existed across each band which would tend to pull the bands toward each other until they merged. Also, Moffatt [6] notes that since the pressure on the surface of the bands is atmospheric, then the pressure inside the bands must be less than atmospheric due to contrifugal force effects. Therefore each band would tend to draw fluid from the inter-band (trough) region via pressure forces. This meant that end-band migration could be stopped by removing a section of the inter-band liquid and thus equalizing the surface tension and pressure forces on each side of the band. Figure 3 presents the results of removing as much as possible of the inter-band liquid shortly after the end-bands had formed. Since not all

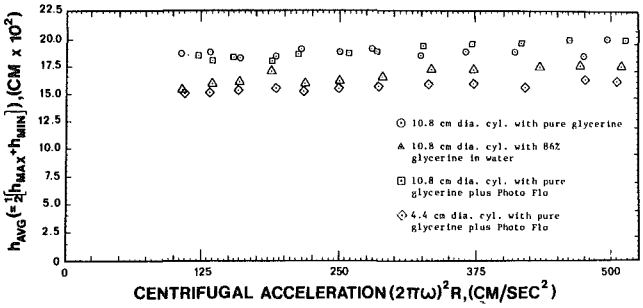

Fig. 4 Average film thickness at the top of the rotating cylinder versus centrifugal acceleration. Coordinate uncertainty (absolute, 20:1 odds): (h_{avg}, Acc.) ($\pm$0.01, $\pm$1.0).

the inter-band liquid could be removed without disturbing the system, the end-band migration was not completely stopped, but it was slowed considerably.

Using the high speed 16 mm photographic technique described earlier and a Vanguard Motion Analyzer the values of the relative surface velocities of the center (crown) of the bands were determined at $\theta = 0$ and $\theta = \pi/2$ on a 10.8 cm diameter cylinder. Adding these values to the bands' tangential velocity (35.33 cm/s) gave the following results:

$$u_s\Big|_0 = 35.33 \ cm/s = U \tag{3a}$$

$$u_s\Big|_{\pi/2} = 42.18 \ cm/s \tag{3b}$$

Thus there was no relative velocity of the liquid on the top of the cylinder, but the liquid led the cylinder at the $\theta = \pi/2$ position. An interesting comparison can be made between these measurements and the steady state unbanded velocity

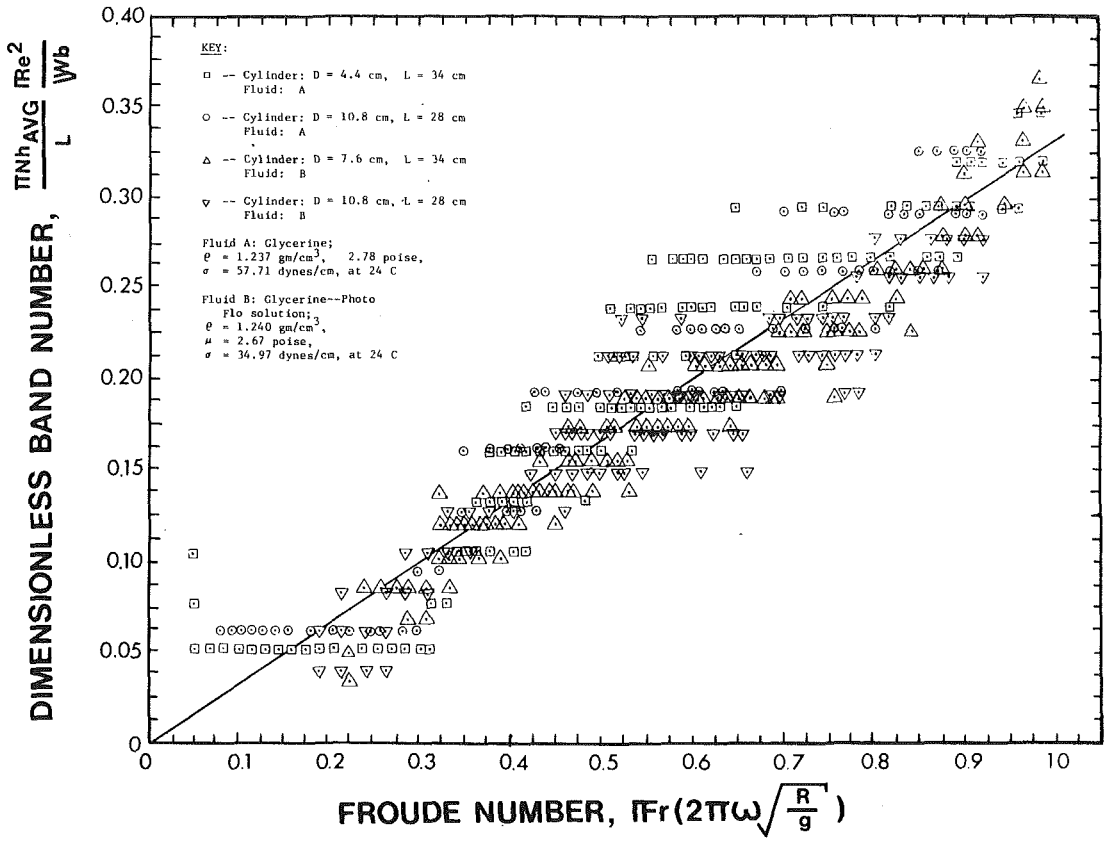

Fig. 5 The final correlation of $\phi Re^2/Wb$ versus for over 400 data points. Coordinate uncertainty (absolute, 20:1 odds): ($\phi Re^2/Wb$, Fr) (± 0.0025, ± 0.03).

field solution of Moffatt [6], equation (1). The liquid surface velocity is obtained by setting $y = h$, giving:

$$u_s = U + \frac{gh^2 \sin\theta}{2\nu} \cdot \tag{4}$$

At the top of the cylinder ($\theta = 0$) equation (4) predicts $u_s = U$ as was measured (equation 3*a* above). At the $\theta = \pi/2$ position equation (4) gives:

$$u_s\Big|_{\pi/2} = U + \frac{g}{2\nu}\left[h\left(\frac{\pi}{2}\right)\right]^2 \tag{5}$$

where $h(\pi/2)$ is the film thickness at $\theta = \pi/2$. At equilibrium (no fluid being lost from the cylinder) continuity dictates that the flow, Q, through any angular section must be constant, so that [6]:

$$Q = \int_0^h u\,dy = Uh + \frac{gh^3}{3\nu}\sin\theta = \text{constant} \tag{6}$$

Equating equation (6) evaluated at $\theta = 0$ and $\theta = \pi/2$ gives:

$$h(0) = h\left(\frac{\pi}{2}\right) + \frac{g}{3\nu U}\left[h\left(\frac{\pi}{2}\right)\right]^3 \tag{7}$$

In our experiments, $h(0) = 0.178$ cm and $\nu = 2.153$ cm^2/s. Using these values in equation (7) give $h\ (\pi/2) = 0.160$ cm, and using this value in equation (5) produces

$$u_s\Big|_{\pi/2} = 41.12 \text{ cm/s}\ , \tag{8}$$

which is quite close to the measured value of 42.18 cm/s (equation 3*b*).

Also, the steady gravity flow of a liquid film of thickness h down a vertical flat plate has a surface velocity given by [9]:

$$u_s\Big|_{fp} = \frac{gh^2}{2\nu}, \tag{9}$$

which is identical to the relative velocity part ($u_s - U$) of equation (5). This indicates that under the lubrication theory assumptions used by Moffatt [6] that the flow down the side of cylinder rotating into the gravity field is largely simple gravity flow. The measurements described above indicate that this is also true when the system is in the banded configuration.

Under steady state conditions the inter-band region had no measurable relative velocity.

Figure 4 presents the results of film thickness measurements along the top of the cylinder. The average band height there, perhaps because of the zero relative velocity at this point, was found to be independent of liquid surface tension (σ), liquid viscosity (μ), cylinder diameter (D) and centrifugal acceleration ($4\pi^2\omega^2 R$) over the following ranges:

$$35 \le \sigma \le 61 \text{ dyn/cm}$$

$$0.1 \le \mu \le 0.28 \text{ PaS}$$

$$4.4 \le D \le 10.8 \text{ cm}$$

$$100 \le 4\pi^2\omega^2 R \le 500 \text{ cm/s}^2$$

Because the average film thickness at the top of the cylinder was independent of the system variables, it was chosen as the characteristic length in the dimensionless Reynold's (Re), Weber (Wb), and band (ϕ) numbers:

$$\text{Re} = \frac{\rho V h_{\text{avg}}}{\mu} = \frac{2\pi\omega R \rho h_{\text{avg}}}{\mu} \tag{10}$$

$$\text{Wb} = \frac{\rho V^2 h_{\text{avg}}}{\sigma} = \frac{(2\pi R\omega)^2 \rho h_{\text{avg}}}{\sigma} \tag{11}$$

$$\phi = \frac{N h_{\text{avg}}}{L} \tag{12}$$

where ω is the angular velocity measured in revolutions per second. The cylinder's radius was used as the characteristic length in the dimensionless Froude number (Fr) because it was desirable to maintain the representation of this number as the square root of the ratio of the centrifugal acceleration at the surface of the cylinder to the local gravitational acceleration.

$$\mathrm{Fr} = \frac{V}{\sqrt{gR}} = 2\pi\omega\sqrt{\frac{R}{g}} \tag{13}$$

The correlation of the data cast in the form of the dimensionless parameters defined in equations (10)-(13) was done by a trial and error method which attempted to produce a relationship in which all the data fell along a single correlation line. After several trials it was found that the correlation of $\phi \mathrm{Re}^2/\mathrm{Wb}$ versus Fr produced satisfactory results, as shown in Fig. 5. The scatter in this figure is caused largely by the variability in number of bands possible in any rotational state ($\mathrm{N} \pm \mathrm{M}$) as discussed earlier, and not by the uncertainty in the precision of the measurement. The solid line in Fig. 5 is a least square fit to over 400 data points and corresponds to the equation:

$$\frac{\phi \mathrm{Re}^2}{\mathrm{WbFr}} = 0.1038, \tag{14}$$

which is similar to, but more complex than, the correlations of Pearson [2] and Pitts and Greiller [3].

Conclusions

Since a three-dimensional banded structure has been observed in liquids spread on a flat plate, in liquids on the outside of closely spaced horizontally counter rotating cylinders, in liquids on the outside of a single rotating horizontal cylinder, and in liquids inside a single partially filled horizontal rotating cylinder, it is not clear what the hygrocyst mechanism is, or that it is necessarily the same in each of these cases. Pearson [2] feels that the first two cases are driven by a balance between the pressure forces generated in the spreader gap or roller nip and the viscous forces, with the surface tension force exerting a stabilizing influence. We agree with Moffatt [6] that the case of external and internal hygrocyst formation with single horizontal rotating cylinders are driven by a balance between gravity, viscous and centrifugal forces. The surface tension force stabilizes the system at short disturbance wavelengths, but the system appears to be always unstable for long wave length disturbances. The measured surface velocity of the liquid in the crown of the bands was found to agree well with the steady state unbanded velocity field equations of Moffatt [6].

References

1 Balmer, R. T., "The Hygrocyst - A Stability Phenomenon in Continuum Mechanics," *Nature,* Vol. 227, 1970, pp. 600-601.

2 Pearson, J. R. A., "The Stability of Uniform Viscous Flows Under Rollers and Spreaders," *Journal of Fluid Mechanics,* Vol. 7, 1960, pp. 481-500.

3 Pitts, E., and Greiller, J., "The Flow of Thin Liquid Films Between Rollers," *Journal of Fluid Mechanics,* Vol. 11, 1962, pp. 33-50.

4 Sone, T., Fukushima, M., and Fukada, E., "An Anomalous Flow During Rolling of Viscous Materials," in the *Fourth International Congress on Rheology,* Part 3 (E. H. Lee, ed.), Interscience, 1965, pp. 227-239.

5 Yih, C. S., "Instability of a Rotating Liquid Film With a Free Surface," *Proc. Roy. Soc.,* Vol. A258, 1960, pp. 63-89.

6 Moffatt, H. K., "Behavior of a Viscous Film on the Outer Surface of a Rotating Cylinder," *Journal de Mecanique,* Vol. 16, 1977, pp. 651-673.

7 Balmer, R. T., and Wang, T. G., "An Experimental Study of Internal Hygrocysts," ASME JOURNAL OF FLUIDS ENGINEERING, Vol. 98, 1976, pp. 688-694.

8 Kovac, J. P., "Experimental Study of the External Hygrocyst Phenomenon with Modeling Applications for the Jovian Atmosphere," Master of Science thesis, University of Wisconsin-Milwaukee, 1976.

9 Bird, R. B., Stewart, W. E., and Lightfoot, E. N., *Transport Phenomena,* Wiley, New York, 1960, pp. 37-41.

Viscous Liquid Films in Nonradial Rotating Pipes[1]

J. T. Dakin

General Electric Company,
Corporate Research and Development,
Schenectady, N. Y. 12301

The dynamics of a thin liquid film flowing through a rotating pipe are studied. The flow is assumed to be fully developed and dominated by viscous forces. The fluid is drawn along the pipe by the centrifugal force. The pipe is tilted with respect to the radial direction so that the centrifugal force has a component perpendicular to the pipe axis. An approximate dynamic model is developed which describes the film surface shape, and which includes the effects of the Coriolis-induced secondary motion. Several simple, interesting solutions are presented.

Introduction

A potentially significant application of thin water films lies in the cooling of the rotating blading of a high-temperature gas turbine. Here, the film would be drawn by the centrifugal force through nearly radial cooling passages located beneath a turbine blade surface [2]. The large magnitude of the centrifugal force at the turbine blade can be expected to produce large film velocities, small film thicknesses, and large film heat-transfer coefficients. The values of these quantities are not readily calculated because the film will not, in general, distribute uniformly around the circumference of a cooling passage. In the plane perpendicular to the cooling passage axis, the film experiences a Coriolis force and an off-axis component of the centrifugal force, both of which influence the film's circumferential dynamics. The object of this paper is a description of the fluid film behavior under these circumstances.

There is a considerable amount of literature devoted to thin films in stationary environments. A review of this literature has been presented by Fulford [3]. While much of the phenomenology of these films may apply to the present case, there is one significant difference. The work on stationary films deals primarily with films of uniform thickness – either films traveling down vertical surfaces with no normal body forces or films traveling down tilted plates. Aside from occasional meniscus effects, such films can all be treated as two-dimensional. This study, however, deals with films that are inherently three-dimensional, because of non-uniform thickness and Coriolis-induced secondary motion.

The literature on fluids in rotating pipes all deals with the single-phase problem. The problem was first studied analytically by Barua [4], who dealt with fully developed laminar flow. He showed that in the presence of rotation the pipe flow will develop a two-celled secondary motion; this is due to the fact that high-velocity fluid in the core region experiences a larger Coriolis force than does slower liquid near the wall. Later, Trefethen [5] measured the rotation-induced increase of friction in pipe flow, and correlated the secondary flow effects observed in rotating, heated, and curved pipes. The two-celled secondary flow must also be present in the rotating thin films considered here.

There is some literature on centrifugal-driven films on rotating disks [6, 7]. In this work the film is essentially two-dimensional because of rotational symmetry. This literature is of interest here because it deals with high-shear thin films motivated by a body force rather than by a concurrent gas stream.

Dakin and So [8] developed an approximate theory for the flow of liquid films in radial rotating pipes. The flow was assumed to be viscous-dominated, although inertia effects were carried through the calculations. The effect of surface tension was included in that analysis.

In recent experiments Dakin [9] has studied the heat transfer to water films in radial and near-radial pipes. In those experiments the flow rates were sufficiently high that the films were expected to be turbulent. The films in the present analysis are assumed to be laminar.

In the analysis presented here, the rotating pipe is given a general nonradial orientation. Thus the circumferential dynamics of the film are influenced both by the Coriolis force considered by Dakin and So [8] and by the centrifugal force component which lies perpendicular to the pipe axis. In this analysis the previously considered inertia forces and surface tension are neglected. This simplifies the problem sufficiently to allow several interesting closed-form solutions. The nonmenclature and the method of analysis are similar to those of Dakin and So.

Governing Equations

A pipe of radius R rotating at angular velocity ω is considered. The fluid motion in the cross section of the pipe shown in Fig. 1, is a distance L from the axis of rotation. At this location the pipe is tilted by an angle ψ with respect to the radial direction; the orientation of the tilt with respect to the plane of rotation is arbitrary. It is assumed that ψ is small enough to allow the approximation $\sin \psi = \psi$, $\cos \psi = 1$.

A quasi-cylindrical coordinate system attached to the pipe axis is shown in Fig. 2. The z coordinate is along the pipe axis and away from the axis of rotation. The coordinate r is measured from the wall of the pipe toward the axis of the

Contributed by the Fluids Engineering Division for publication in the JOURNAL OF FLUIDS ENGINEERING. Manuscript received by the Fluids Engineering Division, March 27, 1979.

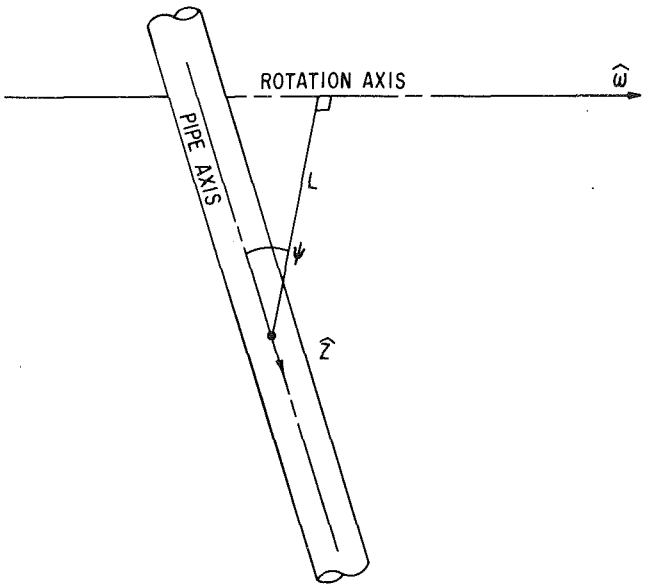

Fig. 1 Perspective drawing indicating the orientation of the pipe with respect to the axis of rotation

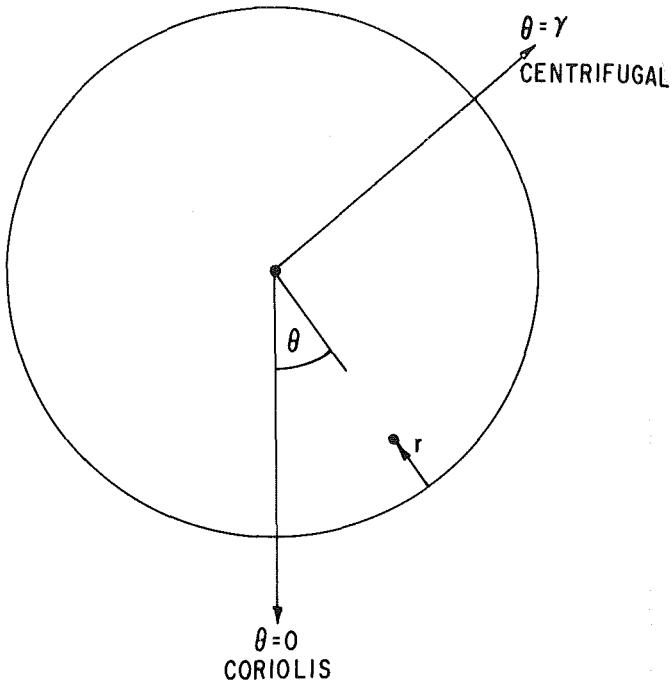

Fig. 2 A cross-section view of the pipe, indicating the coordinate system

pipe. The polar angle θ has its 0 value in the direction toward which the Coriolis force acts on a fluid particle traveling in the z direction. The off-axis component of the centrifugal force is directed toward $\theta = \gamma$. Thus, γ specifies the orientation of the pipe tilt with respect to the plane of rotation.

The fluid motion is assumed to be stable, without time variations. The fluid is assumed to be constant-propertied and without phase change. The static pressure in the gas core of the pipe, P_e, is assumed to be constant along the length of the pipe. Thus, the fluid film is driven in the z direction by the centrifugal force rather than by a static pressure gradient.

The fluid film flow is taken to be fully developed in the z-direction and viscous-dominated. This condition can never be exactly realized by a rotating fluid film, because the centrifugal force increases with z. However, the fully developed viscous approximation is justified whenever the Reynolds number $B = \omega\delta_0^2/\nu$ is less than unity. Justification for an analogous approximation is given by Sparrow and Gregg [6].

This analysis is restricted to the case in which the maximum film thickness, δ_0, is much less than R, which in turn is much less than L. With these qualifications, the dominant terms in the Navier-Stokes and continuity equations are [8]

$$0 = 2\omega \cos\theta v_z + \omega^2 L \cos(\theta-\gamma)\psi + \frac{1}{\rho}\frac{\partial p}{\partial r} \tag{1}$$

$$0 = 2\omega \sin\theta v_z + \omega^2 L \sin(\theta-\gamma)\psi + \frac{1}{R\rho}\frac{\partial p}{\partial \theta} - \nu\frac{\partial^2 v_\theta}{\partial r^2} \tag{2}$$

$$0 = \omega^2 L + \nu\frac{\partial^2 v_z}{\partial r^2} \tag{3}$$

$$0 = \frac{\partial v_r}{\partial r} + \frac{1}{R}\frac{\partial v_\theta}{\partial \theta} \tag{4}$$

It should be noted that equation (4) shows $v_r/v_\theta \approx \delta/R$. This in turn has permitted dropping lower-order viscous terms in equations (1) and (2). The remaining viscous term in equation (2) is a consequence of the Coriolis-induced secondary motion and a critical element in the circumferential force balance.

The boundary conditions which apply are no slip at the wall

Nomenclature

$B = \omega\delta_0^2/\nu$ = a Reynolds number
$D = \psi/B$ = centrifugal/Coriolis ratio
g,h,i,j,k = polynomials defined in Table 1
L = distance from rotation axis
p = static pressure inside film
p_e = static pressure in pipe core
Q_1, Q_2, Q_3 = constants defined in Table 2
r_1, θ, z = cylindrical polar coordinates
$r = R - r_1$ = transformed r_1 coordinate
R = radius of pipe
$\mathrm{Re} = v_z\,\delta/\nu$ = film Reynolds number
V_r = velocity component along r-direction
$\tilde{V}_r$ = typical value for V_r
V_θ = velocity component along θ-direction
$\tilde{V}_\theta$ = typical value for V_θ
$V_\theta^*(\theta)$ = velocity scale for V_θ
V_z = velocity component along z-direction
W = specified flow through liquid film
γ = θ angle between the Coriolis and the off-axis centrifugal force
$\delta(\theta)$ = film thickness
δ_0 = maximum film thickness
$\eta = \frac{r}{\delta}$ = nondimensional r coordinate
θ_c = angle at which $\delta = 0$
ν = fluid kinematic viscosity
ρ = fluid density
σ = surface tension
ϕ = contact angle of liquid film
ψ = pipe angle with respect to radial direction
ω = rotational speed of pipe

Subscripts

0 = first moment (Table 1, 2)
1 = second moment (Table 1, 2)

Table 1 Polynomials in η

Symbol	Polynomial	First moment	Second moment
g	$\eta - \frac{1}{2}\eta^2$	0.3333	0.2083
h	1	1.0000	0.5000
i	$\frac{1}{2}(1-\eta^2) - \frac{1}{6}(1-\eta^3)$	0.2083	0.0750
j	$\eta^2 - \frac{1}{2}\eta^3$	0.2080	0.1500
k	$-5 + 8\eta$	−1.0000	0.1666

($r = 0$), and no shear at the free surface ($r = \delta(\theta)$). It is further assumed that no mass leaves the free surface, and that the liquid has constant pressure at the free surface.

Method of Solution

Equations (1) through (4) have been simplified sufficiently that approximate closed-form solutions are readily obtained. The method of solution can be described briefly as follows.

Equation (4) is ignored as v_r is not of interest. Equation (3) is integrated directly to give v_z, which is then inserted into equations (1) and (2). Equation (1) is then integrated to give p, which in turn is inserted into the remaining equation (2). Equation (2) is then solved by introducing a velocity profile for v_θ. The first two r-integrated moments of equation (2) yield two simultaneous, linear, ordinary differential equations in $\delta(\theta)$ and the characteristic velocity $v_\theta^*(\theta)$. These are readily solved to give $\delta(\theta)$.

A direct integration of the z momentum equation, (3), with the appropriate boundary conditions gives

$$v_z = \frac{\omega^2 L \delta^2}{\nu}\left(\eta - \frac{1}{2}\eta^2\right) \tag{5}$$

where the dimensionless r variable $\eta = r/\delta$ has been introduced. Substituting (5) into (1) and integrating along r from the surface gives the pressure

$$p_{(\eta,\theta)} = \frac{\rho\omega^3 L\delta^3}{\nu}\cos\theta\left[\frac{1}{2}(1-\eta^2) - \frac{1}{6}(1-\eta^3)\right] + \rho\delta\omega^2 L\cos(\theta-\gamma)\,\psi(1-\eta) + p_e \tag{6}$$

The circumferential velocity, v_θ, must satisfy three boundary conditions. It must be zero at $\eta = 0$, must have zero r derivative at $\eta = 1$, and must integrate to zero between $\eta = 0$ and 1 so that there is no net transport of fluid in the θ direction. The simplest polynomial profile for v_θ which satisfies these requirements is

$$v_\theta = v_\theta^*(\theta)\quad(\eta - \frac{5}{2}\eta^2 + \frac{4}{3}\eta^3) \tag{7}$$

Here $v_\theta^*(\theta)$ is a yet-to-be-determined characteristic velocity.

Now equations (5) through (7) may be substituted into equation (2) to give, after much simplification,

$$\frac{\nu^2 k}{\delta_0^2\omega^3 L\delta^2} V_\theta^* = 2\sin\theta g\left(\frac{\delta}{\delta_0}\right)^2 + \frac{2}{R}\frac{d\delta}{d\theta}\cos\theta\,(3i+j)\left(\frac{\delta}{\delta_0}\right)^2 + D\sin(\theta-\gamma)h + D\frac{1}{R}\frac{d\delta}{d\theta}\cos(\theta-\gamma)h \tag{8}$$

The parameter D, which has been introduced, represents the ratio of off-axis-centrifugal to Coriolis force at the thickest part of the film,

Table 2 Numerical constants

Symbol	Represents	Value
Q_1	$2g_0k_1 - 2g_1k_0$	0.5276
Q_2	$h_0k_1 - h_1k_0$	0.6666
Q_3	$(6i_0 + 2j_0)k_1 - (6i_1 + 2j_1)k_0$	1.0276

$$D = \frac{\psi\nu}{\omega\delta_0^2} = \frac{\psi}{B} \tag{9}$$

The letters g, h, i, j, and k represent polynomials in η which are tabulated in Table 1.

Equation (8) involves two unknown functions: $V_\theta^*(\theta)$ and $\delta(\theta)$. To solve for these functions one takes the first two moments of equation (8), integrating over η from 0 to 1. The two simultaneous equations that result are then solved to give $v_\theta^*(\theta)$ and $d\delta/d\theta$. Only the latter is of interest, and it is found to be

$$\frac{d\delta}{d\theta} = -R\frac{\sin\theta\left(\frac{\delta}{\delta_0}\right)^2 Q_1 + D\sin(\theta-\gamma)Q_2}{\cos\theta\left(\frac{\delta}{\delta_0}\right)^2 Q_3 + D\cos(\theta-\gamma)Q_2} \tag{10}$$

Here $Q_1 - Q_3$ represents various combinations of the moments of the polynomials in Table 1. The values of $Q_1 - Q_3$ are presented in Table 2. Given values of δ_0, γ, and D, one may simply integrate equation (10) to obtain the shape of the film surface.

An important caution must be attached to equation (10). This equation is somewhat nonphysical near the edges of the film. There δ/δ_0 goes to zero, and equation (10) gives $d\delta/d\theta = -R\tan(\theta-\gamma)$. The equation is trying to make the film surface perpendicular to the centrifugal force, because that is the dominant force near the film edge in this model. This is because the ratio of centrifugal to Coriolis forces is proportional to $1/\delta^2$, as discussed earlier in relation to equation (9).

In a real film, however, one expects surface tension to play a crucial role near the film edge. There the film will have a meniscus in which the surface tension and centrifugal forces cancel without the requirement of $d\delta/d\theta = -R\tan(\theta-\gamma)$. The surface tension could have been included in this analysis, as it was in the analysis of Dakin and So [8]. This would have resulted in a more complex third-order differential equation in place of equation (10). The surface tension effect was omitted here in the interest of obtaining the simple closed-form solutions to be discussed next.

Simple Solutions

This section describes three simple solutions to equation (10).

A. Centrifugally Dominated Films. In very thin films having $D >> 1$, equation (10) reduces to

$$\frac{d\delta}{d\theta} = -R\tan(\theta-\gamma) \approx -R(\theta-\gamma) \tag{11}$$

Here, the small angle approximation is used because very thin films are usually also very narrow. The solution to equation (11) is simply

$$\delta = \delta_0 - \frac{1}{2}R(\theta-\gamma)^2 \tag{12}$$

This is the equation of a surface which is flat, and per-

pendicular to the direction of the off-axis centrifugal force. The behavior here is identical to that of a viscous fluid film flowing through an inclined pipe under gravity. The edge of this film, where $\delta = 0$, defines

$$\theta_c = \gamma \pm \sqrt{2\delta_0/R} \tag{13}$$

The volume flow through this film is given by

$$W = R \int d\theta \int_0^{\delta(\theta)} dr\ v_z \tag{14}$$

Substituting equations (5), (12), and (13) into (14) gives

$$W = 0.43 R^{1/2} \delta_0^{7/2} \omega^2 L \nu^{-1} \tag{15}$$

In general, a centrifugally dominated film can only support a very low flow. As W increases, so does δ_0, and eventually the condition $D >> 1$ breaks down.

When the centrifugally dominated solution $d\delta/d\theta$ is inserted into equation (8) for $D >> 1$, one obtains $v_\theta^* = 0$. In other words, the centrifugally dominated film has no secondary motion. This is to be expected, since the centrifugal force is conservative and can be balanced by pressure alone.

B. Coriolis-Dominated Films. For thicker films satisfying $D << 1$, equation (10) reduces to

$$\frac{d\delta}{d\theta} = -R \frac{Q_1}{Q_3} \tan\theta \approx -0.513\, R\theta \tag{16}$$

Again, the small-angle approximation has been applied. The solution to equation (16) is

$$\delta = \delta_0 - 0.257\ R\theta^2 \tag{17}$$

This is the equation of a surface that is perpendicular to the Coriolis force at $\theta = 0$ but concave outward. The behavior of this sort of film is uncertain at the edges because there the Coriolis force is no longer dominant and centrifugal-meniscus effects will take over. Ignoring this meniscus effect θ_c and W can be computed as before:

$$\theta_c = \sqrt{3.89\delta_0/R} \tag{18}$$

$$W = 0.60 R^{1/2} \delta_0^{7/2} \omega^2 L \nu^{-1} \tag{19}$$

As discussed earlier, a viscous-dominated film can only occur when $B<1$. Hence, the present case of $D<<1$ can only occur for extremely small values of the tilt angle ψ. This effectively limits the viscous, Coriolis-dominated solution above to the case of radial pipes. This is the case studied in more detail by Dakin and So [8], who did include the effects of surface tension.

C. Full-Wetting Films. A particularly interesting situation arises whenever the centrifugal and Coriolis forces oppose one another. For exact opposition, $\gamma = \pi$, equation (10) reduces to

$$\frac{d\delta}{d\theta} = -R \tan\theta \frac{\left(\frac{\delta}{\delta_0}\right)^2 Q_1 - DQ_2}{\left(\frac{\delta}{\delta_0}\right)^2 Q_3 - DQ_2} \tag{20}$$

This equation has an exact solution in which the film thickness is uniformly $\delta = \delta_0$, provided that

$$D = Q_1/Q_2 \tag{21}$$

Substituting from equation (9) and Table 2, it is seen that this occurs for

$$\delta_0 = \left(\frac{Q_2 \psi \nu}{Q_1 \omega}\right)^{1/2} = (1.26\ \psi\ \nu/\omega)^{1/2} \tag{22}$$

A computation of the flow through such a film gives

$$W = 2.96 \omega^{1/2} L R \nu^{1/2} \psi^{3/2} \tag{23}$$

The uniform wetting solution represented by equations (21) through (23) is fully consistent with surface tension forces, even though these have been neglected in this model. Because the uniform wetting film has no edges, the contact-angle aspect of surface tension does not enter here. Because the uniform wetting film surface has constant curvature, the liquid pressure at the free surface has no θ derivative whether or not there is surface tension.

Whether the uniform wetting film can occur stably in an appropriately oriented rotating pipe is not certain [1]. Nonetheless, it remains an intriguing solution to the approximate set of fluid equations considered.

Observations [9] of turbulent films in near-radial rotating pipes have shown some increase in film width (θc) for the case of $\gamma = \pi$. This increase is presumably due to the same opposition between Coriolis and centrifugal forces which allows the present fullwetting solution.

Discussion

An approximate analysis has been developed to describe the viscous flow of a liquid film through a rotating pipe with arbitrary near-radial orientation. The viscous approximation is valid when the Reynolds number B is less than 1. The analysis accounts for the effect of Coriolis-induced secondary motion upon the circumferential force balance by introducing a velocity profile for v_θ. The central result of the analysis is equation (10), which can be integrated to give the film thickness profile.

Three simple but interesting solutions to equation (10) are presented. For very thin films having $D >> 1$, a centrifugally dominated, flat-surfaced film is centered at $\theta = \gamma$. For thicker films having $D << 1$, a Coriolis-dominated, concave film is centered at $\theta = 0$. The solution given is valid only for near-radial pipes, because of the viscous requirement associated with B.

A very interesting third possibility arises when the pipe tilt is oriented so that the Coriolis and the off-axis centrifugal forces oppose ($\gamma = \pi$). Then, for $D = Q_1/Q_2$, the film is uniformly distributed about the entire circumference of the pipe. It is not clear whether this uniform wetting film is stable.

While the effects of surface tension were not included in the mathematical formalism, these effects were discussed. First, it was noted that surface tension is most important in the edge, or meniscus, region of the film, where in a real film the centrifugal and surface tension forces would balance. Second, surface tension considerations may cause the uniform wetting film discussed above to break up into a Coriolis-dominated rivulet.

This derivation is limited to the case of laminar films. Experience with stationary thin films [3] shows that laminar behavior is expected when the film Reynolds number based on surface velocity is of order 10^3 or smaller. For the films considered here this Reynolds number has its largest value at the thickest part of the film. There, using equation (5),

$$\mathrm{Re} \equiv \frac{v_z \delta}{\nu} = \frac{1}{2} \frac{L}{\delta_0} B^2 \tag{24}$$

Near the edges of the film, δ, v_z, and R_e all approach zero.

Acknowledgment

The author wishes to thank Lloyd Trefethen and Ronald So for a number of useful discussions in the course of this work.

References

1 An expanded version of this paper has been printed as Report No. 77CRD133, General Electric Technical Information Exchange, P.O. Box 43, Bldg. 5, Schenectady, New York 12301.

2 Kydd, P. H., and Day, W. H., "An Ultra High Temperature Turbine for Maximum Performance and Fuels Flexibility," ASME Paper 75-GT-81 (1975);

and Dakin, J. T., Horner, M. W., Peikarsky, A. J., and Triandafyllis, J., "Heat Transfer in the Rotating Blades of a Water Cooled Gas Turbine," in *Gas Turbine Heat Transfer* 1978, edited by J. L. Eriksen and H. L. Julien, ASME, 1978.

3 Fulford, George D., "The Flow of Liquids in Thin Films," *Advances in Chemical Engineering,* Vol. 5, 1964, p. 151.

4 Barua, S. N., "Secondary Flow in a Rotating Straight Pipe," *Proc. Roy. Soc.,* Vol. A227, 1954, p. 133.

5 Trefethen, L., "Fluid Flow in Radial Rotating Tubes," Actes, IX^{e} Congrès International de Mécanique Appliqué 2, 341, 1957.

6 Sparrow, E. M., and Gregg, J. L., "A Theory of Rotating Condensation," ASME JOURNAL OF HEAT TRANSFER, Vol. 81, 1959, p. 113.

7 Bromley, L. A., Humphreys, R. F., and Murray, W., "Condensation On and Evaporation From Radially Grooved Rotating Disks," ASME JOURNAL OF HEAT TRANSFER, Vol. 88, 1966, p. 80.

8 Dakin, J. T., and So, R. M. C., "The Dynamics of Thin Liquid Films in Rotating Tubes: Approximate Analysis," ASME JOURNAL OF FLUIDS ENGINEERING, Vol. 100, 1978, p. 187.

9 Dakin, J. T., "Vaporization of Water Films in Rotating Radial Pipes," *Int. J. Heat Mass Transfer,* Vol. 21, 1978, p. 1325.

10 Lezius, D. K., and Johnston, J. P., "Roll Cell Instabilities in Rotating Laminar and Turbulent Channel Flows," *J. Fluid Mech.,* Vol. 77, 1976, p. 153.

and Dakin, J. T., Horner, M. W., Peikarsky, A. J., and Triandafyllis, J., "Heat Transfer in the Rotating Blades of a Water Cooled Gas Turbine," in *Gas Turbine Heat Transfer* 1978, edited by J. L. Eriksen and H. L. Julien, ASME, 1978.

3 Fulford, George D., "The Flow of Liquids in Thin Films," *Advances in Chemical Engineering*, Vol. 5, 1964, p. 151.

4 Barua, S. N., "Secondary Flow in a Rotating Straight Pipe," *Proc. Roy. Soc.*, Vol. A227, 1954, p. 133.

5 Trefethen, L., "Fluid Flow in Radial Rotating Tubes," Actes, IX^{e} Congrès International de Mécanique Appliqué 2, 341, 1957.

6 Sparrow, E. M., and Gregg, J. L., "A Theory of Rotating Condensation," ASME JOURNAL OF HEAT TRANSFER, Vol. 81, 1959, p. 113.

7 Bromley, L. A., Humphreys, R. F., and Murray, W., "Condensation On and Evaporation From Radially Grooved Rotating Disks," ASME JOURNAL OF HEAT TRANSFER, Vol. 88, 1966, p. 80.

8 Dakin, J. T., and So, R. M. C., "The Dynamics of Thin Liquid Films in Rotating Tubes: Approximate Analysis," ASME JOURNAL OF FLUIDS ENGINEERING, Vol. 100, 1978, p. 187.

9 Dakin, J. T., "Vaporization of Water Films in Rotating Radial Pipes," *Int. J. Heat Mass Transfer*, Vol. 21, 1978, p. 1325.

10 Lezius, D. K., and Johnston, J. P., "Roll Cell Instabilities in Rotating Laminar and Turbulent Channel Flows," *J. Fluid Mech.*, Vol. 77, 1976, p. 153.

DISCUSSION

R. T. BALMER.[1] I believe that the developing class of flows in rotating containers currently lacks sufficient delineating subcategories for clear reader identification. The phrase "rotating pipe" connotes a pipe rotating about an axis coincident or parallel to its own axis, whereas flows in tubes rotating about an axis which is not parallel to the tube axis are difficult to describe verbally. Perhaps a phase such as "transversely rotating pipe" should be used for the latter, and then allow the simple phrase "rotating pipe" to default to the former case.

This paper appears to be motivated by pragmatic need in the area of turbine blade cooling, however, the results are sufficiently general to be of use in other areas (such as lubrication theory). A slight discrepancy occurs in equation (23) wherein W is referred to as the "mass" flow when it is defined elsewhere (e.g., the nomenclature) as the "volume" flow. Also, equation (23) does not have the dimensions of either a mass or volume flow. I suspect that there is an R missing from this equation. Also, I cannot but wonder about the ultimate validity of the assumed circumferential velocity profile given in equation (7), but I do not have an alternate method to suggest short of a complicated numerical solution technique of equations (1) - (4).

[1] Mechanical Engineering Department, University of Wisconsin - Milwaukee, Milwaukee, Wis.

Author's Closure

The author wishes to thank Professor Balmer for his comments. The issue of nomenclature in describing the orientation of rotating containers is indeed a potential source of confusion. There is, however, ample precedent (e.g. reference [4]) for using "rotating pipe" to refer to the case where the pipe and rotation axes are perpendicular to each other. Changes have been made in the sentence preceding equation (23) and in that equation to correct the discrepancies which Balmer notes. Equation (7) is admittedly an approximation, but one which satisfies the continuity and boundary conditions.

A. Klein

P. Pucher

M. Rohlffs

Motoren- und Turbinen-Union
München GmbH,
POB 50 06 40,
8000 München 50, W. Germany

The Effect of Blade-Wakes on the Performance of Short Dump-Diffuser Type Combustor Inlets

Experimental results are presented of the effects of flow distortions, generated by a compressor cascade, on the performance of a short annular dump-diffuser type combustor inlet. The distance between the cascade and the diffuser entrance plane was varied. The losses increase substantially when this distance becomes small. In most of the tests the losses turned out to be minimum at a distance of about two blade-chord lengths. When the cascade was removed, the losses were higher than this minimum value. Evidence is presented that the radial blockage factor rather than the total blockage factor determines the magnitude of the losses.

Introduction

Gas turbine combustor inlets serve the purpose of retarding the flow downstream of the compressor before it enters the flame tube. This is required to avoid high flow losses and to establish satisfactory conditions for combustion. In aircraft jet engines the flow must be decelerated within a particularly short distance, because axial length increases the engine weight, which should be kept as low as possible. This constraint adds to the difficulties of designing inlets with a good performance over a wide range of engine operating conditions and manufacturing tolerances. One possible solution to this problem is illustrated, for annular combustors, in Fig. 1. It essentially consists of a prediffuser and a dump zone, formed by a hemispherical flame tube head and two inclined (conical) walls joining the prediffuser exit and the inner and outer casing. Downstream of the prediffuser, a small portion of the flow is fed into the flame tube within the stagnation region of its head, while the major part proceeds to the two annuli which surround the flame tube, and enters via its ports.

A large number of parameters affects the performance of such a configuration. If the main geometric features are given, it is the mass flow split between the two annuli and the axial distance of the flame tube head from the prediffuser exit (the "dump gap") which essentially determine the losses. In addition to this, the wakes generated by the compressor may add to the complexity of the flow. Indeed, Klein, et al., [1] demonstrated that the existence of a cascade of blades at a short distance upstream of the prediffuser considerably increased the flow losses and also altered the manner in which they depended on the parameters of influence. Stevens, et al., [2], however, in measurements on a similar combustor inlet incorporating a cascade fitted either 0.05 or 3.0 blade chord lengths upstream, in both cases obtained the same losses as with a fully-developed boundary layer type flow entering the diffuser. The same researchers also tested a combustor inlet downstream of an axial compressor, which they operated at three different mass flows. The distance between the compressor and the inlet corresponded to two chord lengths of the exit guide vanes. For two off-design conditions, the losses were again the same as with fully developed flow. However, when the compressor operated close to its design point, the loss was nearly 25 percent lower.

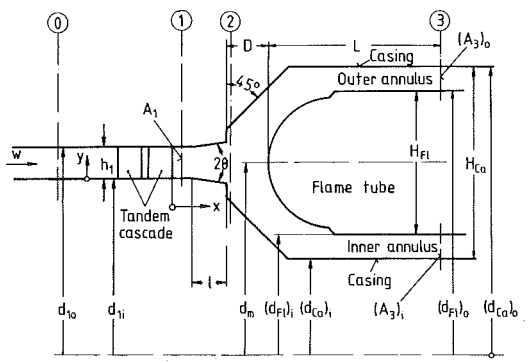

Fig. 1 Test model

The present paper reports on experimental results, which further clarify the effects of blade wakes on the flow in combustor inlets of the type shown in Fig. 1.

2 Test Facility

Air, delivered by a compressor, passed through a plenum chamber, a contraction, an annular flow development section with a length to radial height ratio of 22 and then entered the combustor inlet depicted in Fig. 1. This inlet had a short prediffuser with an included angle of $2\Theta = 14$ deg. One might expect a larger angle to give a better performance, but this was not confirmed by the tests reported in [1]. The conical walls were inclined by 45 deg toward the axis. They were so connected to the prediffuser, that in its exit plane radial steps

Contributed by the Fluids Engineering Division for publication in the JOURNAL OF FLUIDS ENGINEERING. Manuscript received by the Fluids Engineering Division, November 11, 1978.

Table 1 Main dimensions of test model

$\frac{l}{h_1}$	$\frac{(d_1)_i}{(d_1)_o}$	$\frac{2\,h_1}{d_m}$	$\frac{(d_{Fl})_o}{d_m}$	$\left(\frac{d_{Fl}}{d_{Ca}}\right)_o$	$\left(\frac{d_{Fl}}{d_{Ca}}\right)_i$	$\frac{2\,H_{Fl}}{dm}$
0.944	0.911	0.094	1.245	0.928	1.160	0.490
$\frac{L}{H_{Fl}}$	$\frac{H_{Fl}}{H_{Ca}}$	$\frac{(A_3)_o}{(A_3)_i}$	$\frac{(A_3)_o}{(A_3)_i}$	$\frac{(A_3)_o}{A_1}$	$\frac{(A_3)_o + (A_3)_i}{A_1}$	
1.50	0.707	1.773	1.353	0.773	2.135	

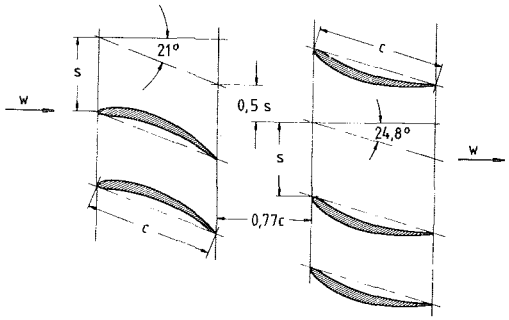

Fig. 2 Geometry of the tandem cascade

0.5 • h_1 wide were formed. The flame tube model had neither ports nor cooling rings, so that the entire flow passed along the two annuli surrounding it. The mass flow split could be varied with the help of throttles at the downstream ends of the annuli. The main dimensions of the model are given, in a nondimensional form, in Table 1.

An annular tandem compressor cascade of NACA 65-series blades could be fitted at a variety of distances upstream of the diffuser entry. The blade and cascade geometry is given in Fig. 2 and Table 2. It remained unchanged along the blade span. The cascade geometry was so chosen that, in a two-dimensional setup, the outlet flow direction would have been axial. However, owing to the small blade aspect ratio of 0.625, chosen to create large flow distortions, the secondary flows created at the hub and the casing extended to and joined at mid-span. Therefore the flow field was essentially three-dimensional. The blades were carefully adjusted, and axial symmetry was much better than in the tests reported in [1].

3 Test Program and Data Reduction

3.1 Cascade Loss Coefficient. Extreme care was taken to establish, in a separate test series, the cascade loss coefficient. To this end the combustor inlet was disconnected and the flow downstream of the cascade allowed to discharge to the surroundings. Various annuli were fitted behind the cascade, their length, normalized by the blade chord, ranging from $x/c = 0.01$ to $x/c = 2.40$. Thorough total pressure traverses were made at the end of each of these annuli (plane 1) across two blade spacings at 13 radial stations in four sectors, circumferentially displaced by 90 deg. Integrated mean values for these four sectors were found to differ little only. Their average value was subtracted from the mean total pressure in plane 0 upstream of the cascade, determined by a radial traverse, and this difference nondimensionalized by the mean dynamic pressure in plane 1:

Table 2 Blade and cascade geometry

Blade chord length [mm]	c	26.0
Blade height [mm]	h_1	16.2
Blade aspect ratio	h_1/c	0.625
Hub - tip ratio	d_i/d_o	0.911
Radial-clearance-chord ratio	C/c	
first blade row, at the hub		0.015
first blade row, at the casing		0
second blade row, at the hub		0.015
second blade row, at the casing		0.008
Solidity at mid-span	c/s	1.680
Thickness-chord ratio	t/c	0.080
Camber-chord ratio	f/c	0.111

$$\zeta_{\text{cascade}} = \frac{\bar{p}_{t0} - \bar{p}_{t1}}{\frac{\bar{\rho}1}{2}\bar{w}_1{}^2}. \qquad (1)$$

The static-pressure variation behind the cascade was not determined because of the great inaccuracies involved. Only wall pressures were obtained. Hence the value of p_{t1} will be increasingly at error as the distance of the measuring plane decreases. Therefore the values according to equation (1), determined at various distances behind the cascade, were plotted against x/c. They were found to change significantly

Nomenclature

A = cross-sectional area
B = blockage factor (equation (3))
C = radial clearance between blade and hub or casing
c = blade chord length
D = axial distance of the flame tube head from the prediffuser exit plane ("dump gap")
d = diameter
f = maximum blade camber
H_{Ca} = radial distance between the inner and outer casing
H_{Fl} = height of flame tube
h = radial height of annulus, blade height
L = location of downstream measurement plane (Fig. 1)
l = length of prediffuser
p_t = total pressure
s = blade spacing
t = maximum blade thickness
w = axial velocity
x = coordinate in axial direction, $x = 0$ in the trailing-edge plane of the second blade row
y = coordinate in radial direction, $y = 0$ at the hub
ρ = fluid density
Θ = diffuser semiangle
ζ = loss coefficient (equation (2))

Subscripts

Ca = casing
Fl = flame tube
i = inner
max = maximum value
0 = outer
rad = radial
tot = total
0,1,2,3 pertaining to measurement planes 0,1,2,3 (Fig. 1)

Superscript

$-$ = (bar) mean value

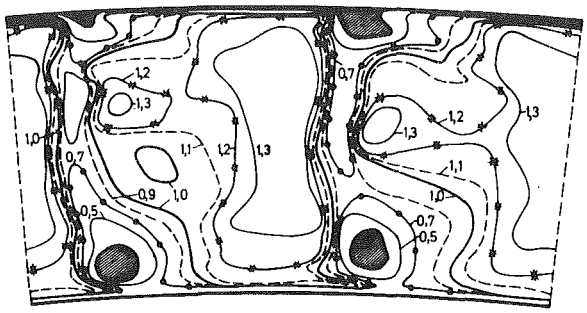

Fig. 3 Axial velocity contours at a nondimensional distance x/c = 0.06 downstream of the cascade

up to $x/c \approx 0.7$, while the change, at still larger distances, was comparable to that of a fully developed pipe flow. Hence, for determining the losses of the combustor inlet with $x/c = 2.40$, the cascade-loss coefficient obtained at that distance was used. For smaller values of x/c, the respective losses for developed pipe flow were subtracted.

The total pressures were corrected for shear according to [3]. The mass flows obtained from the integration of the data at $x/c \approx 0.7$ were within 0.5 percent of those measured by a standard orifice.

3.2 Main Program. In the main test program, where the configuration of Fig. 1 was investigated, the total pressures at the downstream end of the outer and inner annulus surrounding the flame tube (plane 3 in Fig. 1) were measured by three rakes displaced approximately by 120 deg around the circumference. Since the wakes of the blades were still felt in this plane, the circumferential variation of the total pressure was checked for a variety of mass flow splits and the position of the rakes so chosen, that the average of the readings equalled the true mean value. Wall pressures at the hub and casing were also taken in plane 3. Their values at the flame tube and the casing were equal. Also, total pressures behind the prediffuser (plane 2 in Fig. 1) were obtained from four rakes, displaced circumferentially by 90 deg, which were rotated over two blade spacings. The static pressures in plane 2 (see Fig. 1) were taken as the means from the extrapolations of the pressures recorded along the inner and outer walls of the prediffuser. Also, the total pressures in plane 0 (see Fig. 1) were measured by a rake and the wall pressures recorded. Integration of the distributions in each of these planes was made by "momentum weighting" according to [4], so that the mean values satisfy all the three conservation laws.[1]

The loss coefficient of the combustor inlet was then obtained separately for the inner and outer annulus from

$$\zeta = \frac{\bar{p}_{t0} - \bar{p}_{t3}}{\frac{\bar{\rho}_0}{2}\bar{w}_0^2} \cdot \frac{\bar{\rho}_0 \bar{w}_0^2}{\bar{\rho}_1 \bar{w}_1^2} - \zeta_{\text{cascade}}, \tag{2}$$

where the ratio $\bar{\rho}_0\ \bar{w}_0^2/\bar{\rho}_1\ \bar{w}_1^2$ had been determined in the preliminary test program. Both the "total" and "radial" blockage factors

$$B_{\text{tot}} = 1 - \frac{\bar{\rho}\bar{w}}{\rho_{\max}\ w_{\max}};\quad B_{\text{rad}} = 1 - \frac{(\bar{\rho}\bar{w})_{\text{rad}}}{(\rho_{\max}\ w_{\max})_{\text{rad}}} \tag{3}$$

were determined, in each of the planes 1,2,3, where subscript "max" refers to the maximum velocity of either the entire plane or the radial distribution.[2]

[1] The same procedure was also chosen when determining the cascade loss coefficient, equation (1).

[2] In plane 1, the blockage factors were determined during the preliminary test program.

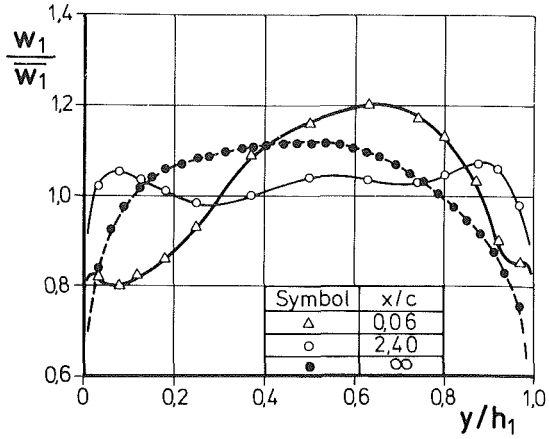

Fig. 4 Axial entry velocity profiles

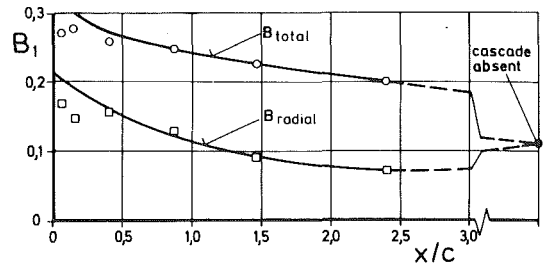

Fig. 5 Variation with x/c of the blockage factors at the prediffuser entry

Measurements were conducted with distances from the blade trailing edges ranging from $x/c = 0.06$ to 2.40 and "dump gaps" D (definition see Fig. 1), referred to entrance annulus height h_1, covering values from $D/h_1 = 0.7$ to 2.5, for outer-to-inner annulus mass flow splits of approximately $0.7 < M_0/M_i < 2.5$. Throughout the test program, the Mach number in the prediffuser entry plane was $\text{Ma}_1 \sim 0.25$, while the Reynolds number, defined by the annulus height h_1 and the mean velocity $\bar{w}_1$, was $\text{Re}_1 = 1.0 \cdot 10^5$.

In a separate test, the prediffuser had a free discharge, and its outlet was thoroughly traversed with $x/c = 0.06$ and 1.50 in order to obtain more accurate total pressure and velocity distributions than was possible by the rakes used in the main program.

An uncertainty assessment is made at the end of the paper.

4 Results and Discussion

4.1 Conditions at the Prediffuser Entrance and Exit. Figure 3 shows the axial velocity contours $w/\bar{w}$ = const. in a section comprising two blade spacings of the flow entering the prediffuser, when the distance from the cascade is $x/c = 0.06$. The secondary-flow vortices, located in the corners between the blade suction surfaces and the hub or casing, are clearly seen. They are more pronounced at the hub. The flow field is nowhere two-dimensional. Figure 4 depicts the mean axial velocity profiles at $x/c = 0.06$ and 2.40, obtained from integrating circumferentially and averaging the results for the four sectors in which traverses were made. At $x/c = 0.06$ the profile is highly distorted. It peaks at 65 percent of the annulus height and exhibits minima close to the hub and the casing indicating the locations of the secondary-flow vortices. Even at $x/c = 2.40$ these vortices are still present, but they have moved farther inward into the flow field. It is interesting to note that in the center portion of the annulus the velocity distribution at $x/c = 2.40$ is flatter than the one measured in [1] when the cascade was absent, which has been included in Fig. 4. As a consequence, the "radial" blockage factor,

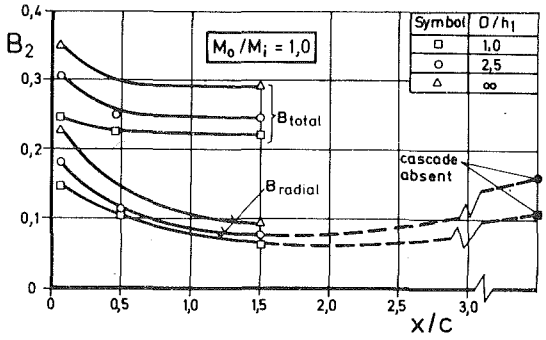

Fig. 6 Variation with x/c of the blockage factors at the prediffuser exit

presented in Fig. 5, at $x/c = 2.40$ has a value $B_{1\,rad} = 0.07$ only as compared with 0.107 without the cascade ($x/c = \infty$). This is due to the energy transfer owing to the vigorous mixing as the flow proceeds downstream. It makes the "radial" blockage already at a distance $x/c = 1.0$ attain the value measured in the absence factor decreases at a far lower rate when the distance increases (Fig. 5). At $x/c = 2.40$ it has still a value of $B_{1\,tot} = 0.20$.

The scatter in Fig. 5 of the data at small values of x/c is due to the experimental inaccuracy at these distances described in the previous section. Owing to it, the true axial velocity profile at $x/c = 0.06$ will be somewhat more distorted than shown in Fig. 4.

Figure 6 depicts the change with x/c of the blockage factor in the prediffuser exit plane. Because of the acceleration effected by the flame tube head, the blockages become smaller as the "dump gap" decreases. For $D/h_1 = \infty$ (free discharge), the "radial" blockage factors have the same values as in the entrance plane, small differences at short distances x/c being due to the greater inaccuracies of the data in that plane. Also, the velocity profile still peaks at 65 percent of the channel height (not shown here). The "total" blockage factors, however, are larger than at entry and also decrease at a slower rate when x/c increases.

4.2 Combustor-Inlet Losses. In the following figures, the loss coefficients according to equation (2) are presented separately for the inner and outer annulus. Figure 7 depicts their variation with the normalized "dump gap" D/h_1 for mass flow splits $M_0/M_i = 0.7$ and 1.8 when the entrance plane is at a small ($x/c = 0.06$) and at a large ($x/c = 2.40$) distance from the cascade. Figure 8 shows the respective variation for all the distances x/c tested, including the results obtained in the absence of the cascade, with $M_0/M_i = 1.0$.

The existence of an optimum "damp gap", displayed by these figures, has been explained already in [1] and [5]. The new finding here is the striking increase of the losses when the distance x/c decreases, which may amount to as much as 100 percent (Fig. 7(a), $M_0/M_i = 1.8$). It is also worth noting, that the larger distances x/c give smaller losses than obtained in the absence of the cascade. This is particularly true for ζ_0 (Fig. 8(b)).

Figure 9 presents, for a fixed "dump gap" $D/h_1 = 1.0$, the variation of the losses with mass flow split. It reveals an additional remarkable feature: While at the larger distances x/c the losses comparatively little only depend on M_0/M_i, they become very sensitive to the mass flow split when the distance from the cascade is small, especially at the smaller "dump gaps."

Finally, Fig. 10 illustrates, for different "dump gaps" with a constant mass flow split ($M_0/M_i = 1.0$), the decrease of the losses when the distance x/c increases, and Fig. 11 shows this variation for a constant "dump gap" of $D/h_1 = 1.0$ for

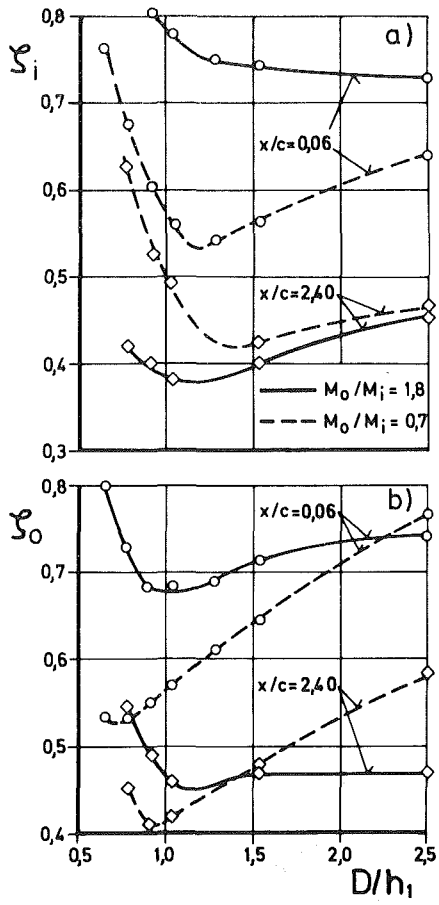

Fig. 7(a and b) Variation of loss coefficients with D/h_1 for mass flow splits $M_0/M_i = 0.7$ and 1.8

different mass flow splits. Most of these curves have minima, with the exception of ζ_i at the smaller "dump gaps." They are especially pronounced in Fig. 10(b) where the loss without a cascade exceeds the minimum loss at $x/c = 2.0$ by up to 30 percent. This is surprising, because the total flow distortion at the prediffuser outlet at $x/c = 2.0$ is far higher than when the cascade is absent (Fig. 6). However, the radial blockage factor in both the prediffuser entrance and exit planes (Figs. 5 and 6) behaves essentially in the same way as the losses in Fig. 10. One must conclude, therefore, that the radial distortion rather than the total distortion is the parameter of influence.

In this context it is interesting to note that Stevens, et al., [2] in their compressor experiments could not believe the much higher losses for off-design operation relative to design conditions to be due to the small increase in blockage factor (0.11 to 0.12) measured. However, they only evaluated "total" blockage. The difference in "radial" blockage may in fact have been much larger. Also, their 30 percent higher losses with a fully developed flow than with compressor design conditions can be explained in this way: Since $B_{1\,rad}$ in their experiments must have similarly depended on the distance from the compressor as shown in Fig. 5 and since they employed the optimum distance of $x/c = 2.0$ from the outlet guide vanes, the compressor profile must have had a considerably lower "radial" blockage than the boundary layer profile. This is a much more likely explanation than differences in turbulence, suggested in [2].

Adenubi's [6] experiments with a compressor mounted upstream of cylindrical-hub annular diffusers had led to the conclusion that the diffuser losses were unaffected by the existence of the compressor. This would contradict the ex-

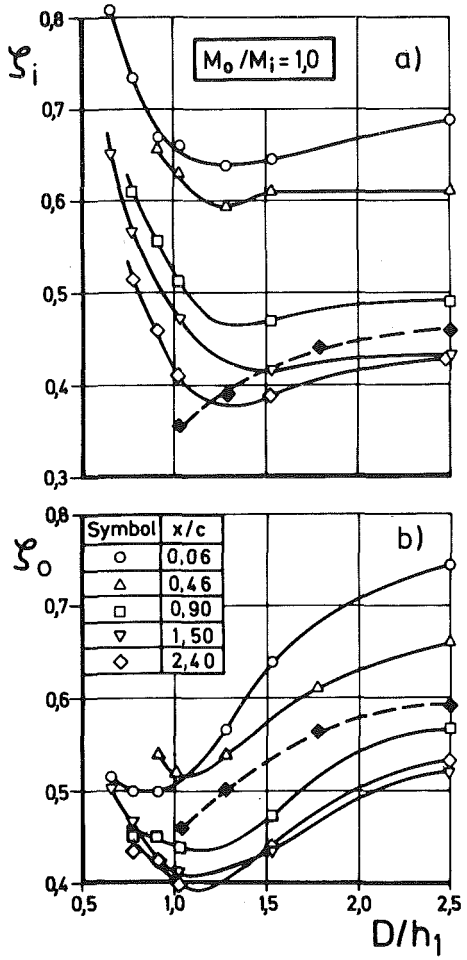

Fig. 8(*a* and *b*) Variation of loss coefficients with D/h_1 for a mass flow split $M_0/M_i = 1.0$ / Full symbols: Cascade removed

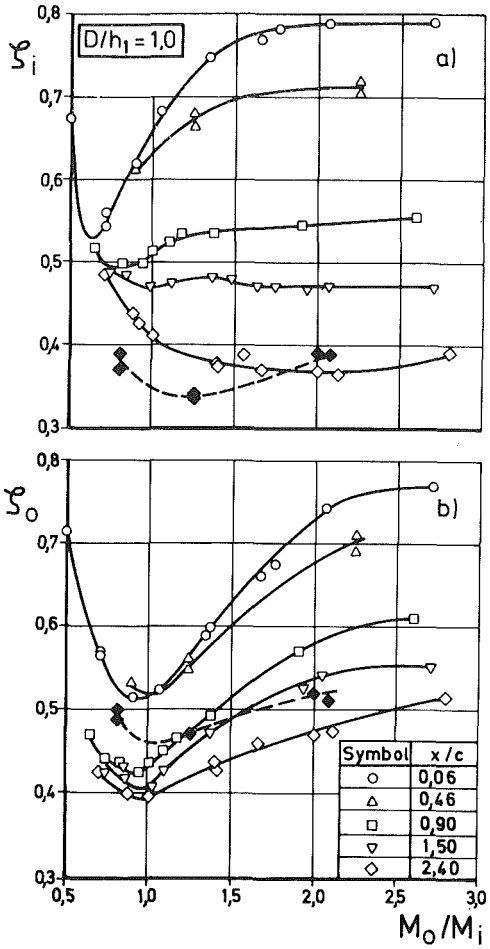

Fig. 9(*a* and *b*) Variation of loss coefficients with mass flow split/Full symbols: Cascade removed

planation just given since [2] states the distance between the exit guide vanes and the diffuser entry to have been also $x/c = 2.0$. However, Adenubi in his paper [6] does in fact not give this distance. From the schematic of his test set-up it would rather appear to have been about $x/c = 5$, and in that case the effects of the compressor may indeed have subsided.

There is still the conflicting evidence from the cascade experiments reported in [2], where the same losses were obtained with $x/c = 0.05$ and 3.0. One explanation, which appears likely from the experiences made during the present investigation, are experimental errors in establishing the mean total pressure in the entrance plane at a distance as short as $x/c = 0.05$. Another possibility is that the finding of Stevens, et al., [2] is due to the prediffuser length in their cascade experiments having been 60 percent larger than that in their compressor experiments and four times the one used in the present investigation. Indeed, the distortions at prediffuser exit were smaller with $x/c = 0.05$, due to the mixing process, than with $x/c = 3.0$. Thus, prediffuser length is certainly very important.

Apart from geometrical parameters, according to Fishenden and Stevens [5], it is mainly the amounts of diffusion and flow curvature which determine the losses of a dump-diffuser type combustor inlet. In the presence of a cascade, conditions are much more complex. As an example, Fig. 11(*a*) for $x/c = \infty$ (no cascade fitted) shows the inner annulus losses to increase as the diffusion decreases (i.e., when M_0/M_i decreases), but with a cascade fitted immediately upstream, just the opposite is true. This leads to the situation, that with $x/c = \infty$ one may have $\zeta_0 > \zeta_i$, while $\zeta_i > \zeta_0$ when x/c is small (see Fig. 11). The orientation of the distortions with respect to the plane, in which the diffusion takes place, is certainly of importance. This was demonstrated by Viets [7], is quite straightforward from the vortex-stretching hypothesis described e.g. by Quinn [8] and was suggested in [2] to be responsible for different developments in the outer and inner annulus flow paths. However, conditions in the present investigation are even more complicated by the existence of the strong secondary-flow vortices with vorticity in a plane normal to that of the ordinary blade wakes.

5 Uncertainty Assessment

The uncertainty of the results, determined by the well-known method of Kline and McClintock [9], with 20: 1 odds, is given in Table 3. Possible fixed errors are included in Table 3, except those of measurements at distances behind the cascade smaller than $x/c \approx 0.5$. Therefore, in addition to the uncertainty, a fixed error for the results at $x/c = 0.06$ in Figs. 3 and 4 has to be taken into account: $w_1/\overline{w}_1 \approx 1.0 - 0.04$. The maximum additional fixed error occurs at $x/c = 0.01$, and the blockage factors in Fig. 5 at $x/c = 0.01$ are:

$$B_{1\ \text{total}} = 0.36 - 0.08,$$
$$B_{1\ \text{radial}} = 0.22 - 0.05.$$

6 Conclusions

An experimental investigation has been carried out to determine the effects of blade wakes on the performance of a short annular dump-diffuser type combustor inlet. To this

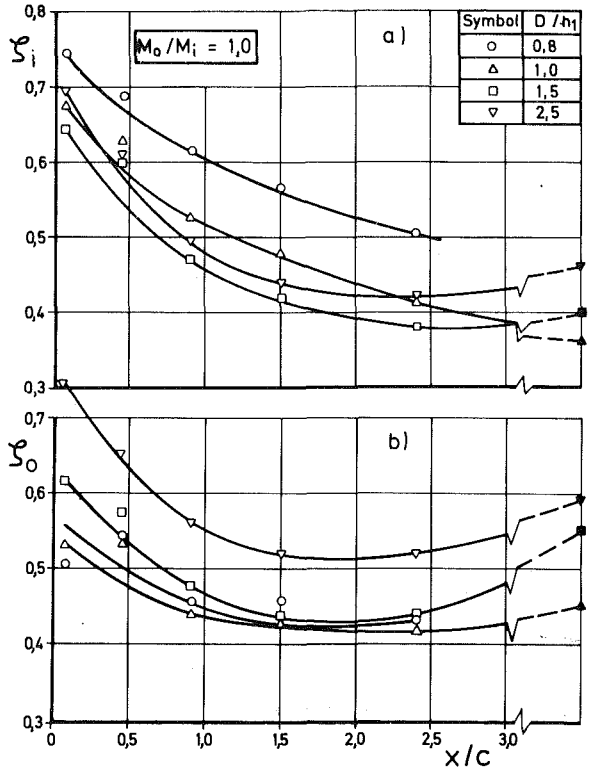

Fig. 10(*a* and *b*) Variation of loss coefficients with x/c for M_0/M_i = 1.0 / Full symbols: Cascade removed

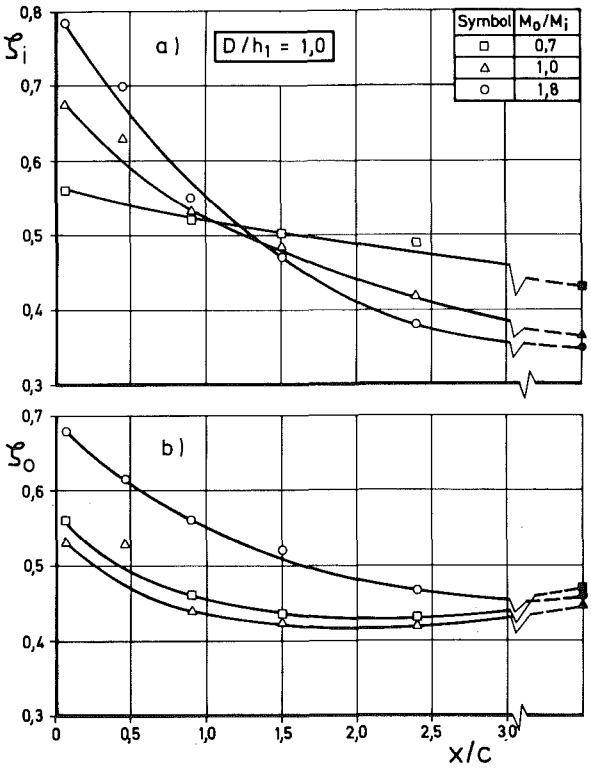

Fig. 11(*a* and *b*) Variation of loss coefficients with x/c for D/h_1 = 1.0 / Full symbols: Cascade removed

end, the losses of the system were measured when a compressor tandem cascade with a blade aspect ratio of 0.625 was fitted at different distances upstream of the entrance plane. They were compared with results obtained when the cascade was absent. The following conclusions are drawn:

Table 3 Uncertainty estimation

Loss coefficients of annuli of cascade	0.8 ± 0.045 0.995 ± 0.01	0.4 ± 0.028
Mass flow split	0.5 ± 0.025	3.0 ± 0.15
Blockage factor "total" "radial"	 0.25 ± 0.010 0.13 ± 0.005	 0.20 ± 0.004 0.07 ± 0.002
Axial velocity profile	1.2 ± 0.01	0.6 ± 0.05

1 Distortions of the type created by low-aspect ratio blades have a highly adverse effect on the performance when the blades are immediately upstream of the combustor inlet entrance plane. Within the range of distances tested, the loss in the inner annulus varied up to 100 percent and in the outer annulus up to 50 percent.

2 While the losses of the combustor inlet depend little on changes in mass flow split when it is at a large distance downstream of a cascade, they are sensitive to such changes when the distance is small.

3 A plot of the losses against the distance between the cascade and the entrance plane shows a minimum at about two blade chord lengths for most configurations. The loss, obtained when the cascade was not fitted, was up to 30 percent higher than this minimum.

4 It appears that the radial distortion rather than the total distortion at entry is responsible for the effects described, because it shows exactly the same variation with cascade distance as the losses. Loss changes described in the literature at a nearly constant "total" blockage may thus be explained by differences in "radial" blockage having been present.

Acknowledgment

The work was sponsored by the Bundesministerium der Verteidigung (German MOD) under contract of the Komponenten-Programm (German Engine Development Program). This support is gratefully acknowledged.

References

1 Klein, A., Katheder, K., and Rohlffs, M., "Experimental Investigation of the Performance of Short Annular Combustor-Dump Diffusers," *Proceedings,* 2nd International Symp. on Airbreathing Engines, Paper No. 23, University of Sheffield, England, Mar. 1974.

2 Stevens, S. J., Nayak, U. S. L., Preston, J. F., Robinson, P. J., and Scivener, C. T. J., "The Influence of Compressor Exit Conditions on the Performance of Combustor-Dump Diffusers," Paper No. 76-726, AIAA, 1976.

3 McMillan, F. A., "Viscous Effects on Pitot Tubes at Low Speeds," *Journal of the Royal Aeronautical Society,* Vol. 58, No. 8, 1954, pp. 570-572.

4 DeWyatt, M. D., "Analysis of Errors Introduced by Several Methods of Weighting Non-Uniform Duct Flows," NACA Techn. Note 3400, 1955.

5 Fishenden, C. R., and Stevens, S. J., "The Performance of Annular Combustor-Dump Diffusers," *Journal of Aircraft,* Vol. 10, No. 1, 1977, pp. 60-67.

6 Adenubi, S. O., "Performance and Flow Regime of Annular Diffusers With Axial Turbomachine Discharge Inlet Conditions," ASME JOURNAL OF FLUIDS ENGINEERING, Vol. 98, No. 2, 1976, pp. 236-243.

7 Viets, H., "Directional Effects in 3-D Diffusers," *AIAA-Journal,* Vol. 13, No. 6, 1976, pp. 823-825.

8 Quinn, B., "The Decay of Highly Skewed Flows in Ducts," ASME *Journal of Engineering for Power,* Vol. 97, No. 1, 1975, pp. 85-92.

9 Kline, S. J., and McClintock, F. A., "Describing Uncertainties in Single-Sample Experiments," *Mechanical Engineering,* Vol. 75, No. 1, 1953, pp. 3-8.

Journal of Fluids Engineering

Discussion

Investigations of Pulsating Turbulent Pipe Flow[1]

P. D. RICHARDSON.[2] Investigations of turbulent pipe flow with pulsations superimposed, which were not mentioned in this paper, were carried out by Jackson and Purdy [D1] in connection with studies being made quite widely at that time on the influence of sound and vibrations on flow and heat transfer [D2]. It was apparent from flow visualizations and heat transfer measurements that the flow in the pipe was modified by the presence of the sound or vibration field, the modifications being associated to some degree with the Reynolds stresses induced by the forced oscillations in the flow. Speaking more strictly, it appeared that circumstances which produced spatial gradients of Reynolds stresses were effective in changing the mean flow. With standing or progressive waves in airflow in pipes, the wavelengths could be as small as a few pipe diameters and the effects of spatial gradients could be seen quite easily. The higher speed of sound in water compared with air makes the wavelength corresponding to any frequency longer, and spatial gradient effects of induced Reynolds stresses tend not to be so well seen then, although they can still be present. Has the author of this paper observed any features in his results which could be associated with gradient effects of induced Reynolds stresses?

The author has two particular advantages compared with Jackson and Purdy. The first is the use of laser-Doppler velocimetry, and the second is that observation of large-scale structures in turbulent shear flows has been reported frequently since the time of the earlier work. The first allows observation of the flow undisturbed by a probe, and the second invites the question of whether any sort of coupling has been observed between flow structures associated with the pulsations and flow structures in the turbulent motion itself. Has the author found any such coupling?

Additional References

D1 Jackson, T. W., and Purdy, K. R., "Resonating Pulsating Flow and Heat Transfer," ASME *Journal of Heat Transfer,* Vol. 87, 1965, p. 507.

D2 Richardson, P. D., "Effects of Sound and Vibrations on Heat Transfer," *Appl. Mech. Rev.,* Vol. 20, 1967, pp. 201-217.

[1] By R. E. Kirmse, published in the December, 1979, issue of the ASME JOURNAL OF FLUIDS ENGINEERING, Vol. 101, No. 4, p. 436.

[2] Professor of Engineering, Brown University, Providence, R.I. 02912. Mem. ASME.

Authors' Closure

The comments of Professor Richardson are appreciated. The smallest wavelength of sound waves under the conditions of low frequent pulsations in the present investigation was more than 7000 pipe diameters. Hence the effects of spatial gradients mentioned by Prof. Richardson are not expected to be significant. Since the turbulent fluctuation velocities have not been measured in the present investigation, except for the case of the turbulent flow without pulsation, no coupling could be observed between flow structures of the pulsation and flow structures in the turbulent motion itself.

At the moment the test bed and the measuring systems are being modified by a colleague of the author (Erich Hartner). Instead of ordinary tap water a mixture of organic solvent and water, which exhibits the same optical refractive index as the surrounding glass pipe, will allow measurements of velocities arbitrarily near to the pipe wall. A two-dimensional LDA together with a specially tailored data acquisition system shall make possible simultaneous measurements of turbulent Reynolds stress and the kinetic energy of axial, radial, and circumferential fluctuations. These data shall be used to establish a relationship for the eddy viscosity in pulsating turbulent flow. These data also have the potential to answer the interesting questions raised by Professor Richardson.

A Fundemantal Criterion for the Application of Rotor Casing Treatment[1]

J. FABRI.[2] Various casing wall treatments have been tested in several laboratories for over ten years. Some of the configurations give improvement of the performance some other give alossin efficiency or in mass flow.

It is the merit of E. Greitzer and his co-authors to give some guidelines for the prediction of the effectiveness or the lack of effectiveness of casing wall treatments.

Greitzer's approach corresponds to the long lasting discussion whether the flow in a blade row should be

[1] By E. M. Greitzer, et al., published in the June, 1979, issue of the ASME JOURNAL OF FLUIDS ENGINEERING, Vol. 101, No. 2, p. 237.

[2] Director ONERA, 92320 Chatillon, France.

Griffith Diffusers[1]

A. KLEIN.[2] It has been known for some considerable time that, in the absence of special means of flow control, optimum diffusers have bell-shaped walls. Contours of this type follow from a variety of boundary-layer optimization principles, notably from the postulation that the flow should produce vanishing wall shear stress (for example Fernholz, reference [1] and Hackeschmidt, reference [2]), from a modification of this concept attributable to Huo (reference [3]) and from application of a special deceleration parameter proposed by Senoo and Nishi, reference [4]. In spite of the deficiencies of the boundary-layer methods used in these analyses, the neglect of the effect of turbulence level on flow behavior and of the effects of wall curvature on turbulence structure, the overall conclusion of these investigations is certainly correct: bell-shaped walls are optimum.

If one considers the gain in performance of such contoured-wall diffusers relative to rectilinear configurations, however, the result is disappointing. Although experiments conducted in reference [2] were claimed to have shown that a 50 percent shorter contoured-wall design would provide the same performance as an optimum conical diffuser, this was not confirmed in more recent investigations. The misleading statement in reference [2] is obviously due to insufficient knowledge at that time of optimum straight-wall diffuser performance. In fact, the results of references [3], [4], and [5] indicate such small performance gains of optimum vs. straight-wall configurations, that wall shaping must be considered an unnecessary design complication.

Bell-shaped walls, in order to be attractive in practical applications, must therefore be used together with reasonable flow control methods. Out of these, "passive" flow control devices such as screens are known to permit considerable reductions of unseparated-flow diffuser length for a given area ratio, and to produce a high degree of flow uniformity at the diffuser exit, but at the expense of very low performances (reference [6]). The high effectivenesses obtained by Yang and Nelson by "active" flow control at comparatively small suction rates are therefore worthy of note. The actual merits of their design can, however, only be appreciated when compared with the results for corresponding straight-wall diffusers and, in a more comprehensive way than the authors did, with the performance of Adkins' configurations (Yang and Nelson's reference [4]). Such a comparison has been attempted by this writer. It is presented in Table 1 for tubular configurations with Miller's (reference [7]) results for an optimum conical diffuser of the same non-dimensional length, and in Table 2 for annular and two-dimensional configurations with Sovran and Klomp's (reference [8]) and Reneau, et al.'s (reference [9]) results for corresponding straight-wall diffusers. Adkins' correlations were used to deduce effectivenesses and bleed requirements to be expected if the authors' geometries (either the same area ratio or the same non-dimensional length) were built as Adkins instead of as Griffith diffusers.

In establishing the data, a number of difficulties were encountered:

1. For the results of tubular and annular diffusers the authors cite reference [5]. However, they are in fact not available there. They were found in the additional reference [10], and the entrance dimensions required for applying Adkins' correlations have been taken from there.

2. Although the values for η_3 given by the authors coincide with those in reference [10] (if the last digit is rounded off), the definition of η_3 in reference [10] differs from that of the authors in that $\kappa_i = \kappa_e = 1$.

3. C_p-values when calculated from η_3 as defined by the authors with κ_i and κ_e as stated by them, are so high that effectivenesses $\eta_1 > 100$ percent result, and this is even true with $\kappa_i = \kappa_e = 1$. On the other hand, the authors claim values of $\eta_1 = 98$ percent to 99 percent.

4. $\kappa_i = 1.025$, stated by the authors, appears to be too high for the very short entrance length (and small inlet blockage) used. A more likely value $\kappa_i = 1.010$ has been chosen for determining the performance of the equivalent Adkins diffusers.

A comment by the authors on these remarks would be appreciated. In order to circumvent the difficulties stated, in the tables two differently obtained values of C_p and, in addition to the authors' η_3-data, two more values for η_3 have been given for the Griffith diffusers. For all the other diffusers η_3 is for $\kappa_i = \kappa_e = 1$; for diffusers without suction $\eta_3 = \eta_1$.

The data of Table 1 and 2 show the superiority of the Griffith diffusers over diffusers without flow control. Although this superiority is hardly apparent when effectiveness is compared, it is clearly demonstrated by the much higher pressure recoveries, a consequence of the considerably larger area ratios to be achieved at a given non-dimensional length. In addition to this, credit must also be given to the good uniformity of the exit flow, while on the other hand the energy required for suction should be considered.

Comparison with Adkins' diffusers is of particular interest. It can be seen that the effectiveness of only 80 percent for an area ratio 3.2, quoted by the authors, is somewhat misleading. In fact, Griffith and Adkins diffusers appear to have approximately equal performance when the entrance conditions are comparable. Exit flow uniformity cannot be assessed since Adkins does not mention it. On the other hand, contrary to the authors, he also presents performances measured with thicker inlet boundary layers, as would be common in practical applications. Such additional information for Griffith diffusers would be very valuable.

Additional References

1 Fernholz, H., "Eine grenzschichttheoretische Untersuchung optimaler Unterschalldiffusoren," *Ingenieur-Archiv*, Vol. 35, No. 3, 1966, pp. 192–201.

2 Hackeschmidt, M., and Vogelsang, E., "Über den Entwurf spezieller rotationssymmetrischer, gerader Grenzleistungsdiffusoren," *Wissenschaftliche Zeitschrift der Technischen Universität* Dresden, Vol. 15, 1966, No. 1, pp. 101–113.

3 Shuang Huo, "Optimization Based on Boundary Layer Concept for Compressible Flows," ASME *Journal of Engineering for Power*, Vol. 97, 1975, No. 2, pp. 195–206.

4 Senoo, Y., and Nishi, M., "Deceleration Rate Parameter and Algebraic Prediction of Turbulent Boundary Layer," ASME JOURNAL OF FLUIDS ENGINEERING, Vol. 99, 1977, No. 2, pp. 390–394.

5 Shuang Huo, "Generalized Comparison between Optimized and Conventional Diffusers," *Journal of Aircraft*, Vol. 13, 1976, No. 7, pp. 541–542.

6 Kachhara, N. L., Livesey, J. L., and Wilcox, P. L., "An Initial Approach to the Design of Very Wide Angle Axisymmetric Diffusers with Gauzes to Achieve Uniform Outlet Velocity Profiles," ASME JOURNAL OF FLUIDS ENGINEERING, Vol. 99, 1977, No. 2, pp. 357–364.

7 Miller, D., "Performance of Straight Diffusers," "Internal Flow. A Guide to Losses in Pipe and Duct Systems," Part II. B.H.R.A.-Fluid Engineering, Cranfield/Bedford, 1971.

8 Sovran, G., and Klomp, E., "Experimentally Determined Optimum Geometries for Rectilinear Diffusers with Rectangular, Conical or Annular Cross Section," In: *Fluid Mechanics of Internal Flow* (ed.: G. Sovran), Elsevier Publishing Company, Amsterdam - London - New York, 1967.

[1] By Tah-teh Yang and C. D. Nelson, published in the December, 1979, issue of the ASME JOURNAL OF FLUIDS ENGINEERING, Vol. 101, No. 4, p. 473.

[2] Motoren- und Turbinen-Union (MTU) München GmbH, Postfach 50 06 40, 8000 Munich, W. Germany.

Table 1

	Yang and Nelson	Adkins (reference [4] of paper)	Hacke-schmidt (reference [2])	Miller (reference [7])
L/R_{in}	3.5	2.7 3.5	3.5	3.5
AR	3.0	3.0 3.75	1.9	2.1
$2\,\delta^*/R_{in}$	0.012- 0.016	0.012	0.012	≈ 0.010
Q_S/Q	6.1 %[1]	5.3 % 6.5 %	0	0
C_p	0.88[2] 0.90[3]	0.86 0.88	0.70	0.67
η_3	0.92[4] 0.90[2] 0.936[5]	0.90 0.88	0.97	0.87

Table 2

	Annular			Two-dimensional	
	Yang and Nelson	Sovran and Klomp (reference [8])	Adkins (reference [4] of paper)	Yang and Nelson	Reneau, et al. (reference [9])
L/h_{in}	3.9	3.9	3.7	4.0	4.0
AR	3.0	1.8	3.0	3.0	2.0
$2\,\delta^*/h_{in}$	0.012- 0.016	0.02	0.012	?	0.007
Q_S/Q	9.0 %[1]	0	8.0 %	14 %	0
C_p	0.88[2] 0.91[3]	0.55	0.86	0.88	0.63
η_3	0.88[4] 0.86[2] 0.909[5]	0.80	0.88	0.83	0.84

Table 1 and 2: Comparison of diffuser performances
Table 1: Tubular diffusers, Table 2: Annular and two-dimensional diffusers

1) from reference [10]
2) from $\eta_1 = 0.99$ with $\kappa_i = 1.025$; $\kappa_e = 1.011$
3) from η_3 with $\kappa_i = \kappa_e = 1$
4) from $\eta_1 = 0.99$ with $\kappa_i = \kappa_e = 1$
5) as given in paper
h_{in} is the diffuser height at the inlet

9 Reneau, L. R., Johnston, J. P., and Kline, S. J., "Performance and Design of Straight, Two-Dimensional Diffusers," ASME *Journal of Basic Engineering*, Vol. 89, 1967, No. 1, pp. 141-150.

10 Nelson, C. D., Jr., Hudson, W. G., and Yang, T., "The Design and Performance of Axially Symmetrical Contoured Wall Diffusers Employing Suction Boundary Layer Control," ASME-Paper 74-GT-152, 1974.

P. S. BARNA.[3] To those who have been puzzled by the mysteries of boundary layer control in diffusers, it is refreshing news to learn of such a successful approach to both diffuser design and flow control as the Griffith diffuser. To this reviewer it was even a gratifying experience to personally observe the flow attachment to the walls of a test diffuser shown in an impressive movie film prepared by Professor T. Yang and his associates and presented at the meeting of the Colorado Joint Symposium of Fluid Machinery in June 1978.

It is now a well-established fact that diffuser performance depends on both the design proportions of the diffuser and the flow conditions at the inlet to the diffuser. This means that for a given specified geometry, performance entirely depends on the inlet flow conditions, so that manipulations for varying the velocity distribution (and Reynolds number) *at inlet* lead to results which are found to be more satisfactory if the distribution is uniform and the blockage is small. Tests have shown that this can be achieved successfully by employing boundary layer control at inlet, by removing *small* amounts of fluid relative to the total flow.

To employ boundary layer control *downstream* from the inlet is another matter, and the question then arises how far downstream should the control be applied and how much fluid needs to be removed? If, for example, one employs suction halfway along the length of a diffuser with straight walls, the experiments conducted by this reviewer show high rate requirements with only a limited amount of improvement in performance. To the best of my knowledge the question pertaining to straight diffusers apparently remains unanswered – where should control be applied to the best advantage?

It is this question which may be answered by employing curved walls as is the case of the Griffith diffuser. Although it is specific only for a certain curved wall geometry, nevertheless the theory locates the suction slot by using the "in-

[3] School of Engineering, Old Dominion University, Norfolk, Va. 23508.

verse" method that specifies the velocity distribution. Assuming incompressible and irrotational flow theory as the basis for the calculations, the method developed in the paper under review furnishes an answer to the wall geometry. Additional attraction is the shorter length and high area ratio attainable.

While the reviewer finds the paper commendable and thinks that Griffith diffusers may well have an application in the future, much of their acceptance will depend on practical considerations, such as the willingness to expend energy for boundary layer control. This will especially apply in large diffusers where the machinery required to provide the necessary suction may add to the already higher costs of producing the curved walls as compared to the simpler straight-walled diffuser design. In addition, there is some evidence that the suction rates in practice were found higher than predicted from theory and successful operation was limited to a narrow range of inlet conditions.

To the designer of diffusers it would come in handy to have a *Griffith Diffuser Data Book,* including charts for various area ratios and blockage factors, similar to that now existing for straight-walled diffuser design.

Authors' Closure

I would like to thank Professor Barna for his kind words about our work and agree with him on the comments that the required suction rates were often found to be higher than predicted. I believe there are two reasons to account for these differences.

First, we do not often predict the boundary layer profile accurately enough. It is the profile, not the momentum thickness or displacmeent thickness, that was used in Taylor's criterion to predict the minimum suction rate. The second source contributing to the difference in suction rate is that in actual flow systems there is always some disturbance, and the boundary layer can be momentarily and locally thickened to require higher overall suction rate to meet the local requirement. Flow separation could take place if the diffuser is operated with a minimum suction rate predicted by Taylor's criterion. Therefore, in practice one must provide a suction rate somewhat higher in order to have a margin for stability.

As far as a *Griffith Diffuser Data Book,* we have no plan for one at this time. However, I will welcome the opportunity to publish such a data book as Professor Barna suggested when circumstances permit.

I would like to thank Dr. A. Klein for his interest in our work. I appreciate his providing two tables to compare performances among diffusers, particularly between the Griffith type and the ones using vortex-fences. (Dr. Adkins' work at Cranfield.)

Because of Dr. Klein's comments relative to the values of K_i used in our paper, I have recomputed values for several test runs of our study. These of course depend upon the inlet velocity profiles. Unfortunately, our recorded profile data do not include measurements near the diffuser wall which would reflect the boundary layer development (or indicate inlet length.) Consequently we assumed a few additional non-dimensional velocity values near the wall to complete the profile for each K_i computation. Our results show that K_i vary from 1.001 to 1.01 instead of 1.025 as stated in NASA CR 2209 and several other publications. Apparently it was a computational error that led to our misquoting of a significant flow parameter; I wish to apologize for the error. On the other hand, we stated that "It is apparent that the gain from enhancement of pressure recovery of the diffuser may be eroded rapidly when the required suction flow rate is high. . . . . it is equally apparent that a Griffith type diffuser is not the choice when the upstream already has a thick boundary layer." Therefore the authors' feeling about the applicability of such diffusers to long inlet sections should be apparent; stating $K_i = 1.025$ by no means implies a long inlet was involved in our test set-up.

It also should be pointed out that the deviation of K_i value from 1.0 can be attributed to the nonuniformity of the potential core due to wall curvature as well as to the boundary layer, and inlet length is not the only contributing factor on the value of K_i.

Now I wish to respond to Dr. Klein's specific comments No. 1 and 2. ". . . . Table 1 of reference [5] . . . ." of the last paragraph, 1st column on page 476 should read ". . . . Table 1 of reference [6] . . . ." The definitions of η_2 and η_3 of "Griffith Diffusers" are identical to those used in reference [6]. With regard to both of Dr. Klein's comments 1 and 2, a typographical error in reference number has caused this confusion. With regard to his comments 3 and 4. I recomputed ϵ and η values of table 1 of NASA CR 2209 with $K_i = 1.01$ and $K_e = 1.0$. (K_e is only of secondary importance to the accuracy of ϵ and η.) We stated in CR 2209 that

$$\epsilon = \frac{(1.0 - FS)\,(P_{s,e} - P_{s,i})}{P_{d,i}\left[\kappa_i - \kappa_e \left(\frac{1.0 - FS}{AR}\right)^2\right]}$$

and

$$\eta = \frac{(P_{s,e} - P_{s,i})}{P_{d,i}\left[\kappa_i - \kappa_e \left(\frac{1.0 - FS}{AR}\right)^2\right]}$$

With $K_i = 1.01$ and $K_e = 1.0$, our η values ranged from 0.97 to 1.01. Allowing 1 percent error in η, one may state that η ranged from 0.96 to 1.00 instead of 0.97 to 0.99. The η used in CR 2209 is η_3 of the December 1979 paper entitled "Griffith Diffuser." It should be evident from the above expressions of ϵ and η that a smaller value of K_i will lead to a higher value of ϵ and, therefore, to a higher value of η. Taking K_i to be one would lead to a result of $\eta = 1.02$ for test run No. 12 of Table 1 CR 2209. I believe this value of η suggests that $K_i = 1$ is not a reasonable value for the measured values of suction flow rate and Δp. Cp values of Table 1 were computed from Δp. If boundary layer is the sole cause of K_i being greater than 1, then it follows that $K_i = 1$ yields zero boundary layer thickness and no suction requirement, certainly not the case that we investigated.

I have stated in the introduction that limited publications will be discussed for the purpose of suggesting that "perhaps the combined effect of using curved walls to control the pressure and boundary layer suction to maintain the designed pressure distribution is a more effective approach in achieving a high degree of pressure recovery than by either effect alone." It was along these lines that our discussion on several types of diffusers was made. Again the paper states that the peformances were reported in *different forms,* and they are not directly comparable. As long as we are discussing the difficulties in comparing various sets of diffuser data, perhaps it should be pointed out that the fine work reported by Adkins was with a diffuser havng a constant area section following the last pressure tap. Generally a downstream constant area section has a stabilizing effect over the upstream diffuser, and one should expect the same diffuser may have a slightly lower performance when the downstream constant area section is removed.

Pressure Pulse Propagation in Two-Component Slug Flow[1]

D. R. H. BEATTIE.[2] The work of Professors Martin and Padmanabhan should help dispel the widely held but erroneous belief, stemming from the work of Henry, et al., [2, 3], that pressure pulse behavior in two-phase slug flow is fundamentally different from that in bubble flow. The theory of Henry, et al., assumes no mechanical coupling between the phases, a condition which was simulated in their somewhat artificial "slug flow" experiments performed to confirm their theory. The theory of Martin and Padmanabhan takes account of this mechanical coupling between the phases, which in reality is almost complete, as is the case for bubble flow. Thus slug flow pressure pulse characteristics should be similar to those expected from bubble flow. This is verified by the experimental data of Martin and Padmanabhan.

If thermal coupling between the phases is considered, a minor flow regime effect might be expected. The low thermal coupling expected for slug flow is such that the isentropic temperature change occurring during the pulse passage might reasonably be expected to be confined to the gas phase, with the result that, as supposed by Martin and Padmanabhan, the specific heat ratio γ in the theory is that for the gas, C_{gp}/C_{gv}. On the other hand, the more uniform dispersion of the phases in bubble flow is such that an assumption of thermal equilibrium is more reasonable. In this case, as shown by Miyazahi et al., [7], the value of γ then becomes

$$\frac{x\ C_{gp}+(1-x)\ C_l}{x\ C_{gv}+(1-x)\ C_l}$$

where x is the mass fraction of gas, and C_l the liquid specific heat. For the small gas mass fractions occurring in the described air-water slug flow experiments, γ might be expected to be closer to unity if bubble flow had occurred. However, this dependence of pressure pulse velocity on flow regime, which is not taken into account in the theory of Martin and Padmanabhan, is small and of the order of normal data scatter. As expected, then, the experiments of Miyazahi, et al., [6], which covered both bubble and slug flow, did not indicate any discernible influence of flow regime on pressure pulse velocity characteristics.

Martin and Padmanabhan's treatment of the drift flux model is such that the distribution parameter, C_0, is assumed to be unity. Their conclusion that the pressure pulse velocity is that given by the homogeneous model with respect to the mixture center of mass velocity applies only if the "slip" between the phases is caused only by a drift velocity v_{gj} and is not general. Distribution parameter effects are considered in [19] and its supplement [22] which give the result

$$a \simeq \sqrt{\frac{\gamma p}{\alpha(1-C_0\alpha)\rho_l}}$$

(which reduces to equation (15) for $C_0 = 1$) with respect not to the center of mass velocity but, if $j >> v_{gj}$, to $j(C_0 + (1 - C_0\rho_l/\bar{\rho})$ where $\bar{\rho}$ is the homogeneous mixture density, and C_0 is as calculated in [19].

The theory of [19] applies for developed flows and, as such, is not strictly applicable to the experiments of Martin and Padmanabhan where the experimental distribution parameters, which are less than unity because of the skewed voidage profiles, indicate non-developed conditions. Nevertheless, the theory of [19], as indicated in the accompanying table, predicts the pressure pulse velocity data of Martin and Padmanabhan better than the homogeneous model does, even though the developed flow void fractions predicted by the method of [19] are clearly inappropriate. This suggests that, for pressure pulse velocity prediction, the theory of [19] can be extended to nondeveloped conditions, at least when the nondevelopment is characterized by skewed voidage profiles.

Table 1 Error statistics for pressure pulse velocity data of Martin and Padmanabhan. Errors are (calculated velocity - measurement velocity)/(measured velocity)

	Mean error	R.M.S. error
Homogeneous model	−17.4%	18.1%
Method of [19]	− 3.2%	6.7%

Additional Reference

22 Beattie, D. R. H., and Thompson, J. J., "The Effect of Flow Velocity on Two-Phase Propagation Phenomena," *Proceedings, Second International Conference on Pressure Surges,* London, Sept. 1976, supplement to paper D3.

Authors' Closure

The authors wish to thank Mr. Beattie for his comments and enhancement to the paper.

The effect of flow regime on degree of thermal coupling is an important, but not necessarily well understood, consideration. As clearly stated by Mr. Beattie we implicitly assumed that slug flow is associated with an isentropic temperature change, or a low thermal coupling. It is interesting, however, to note that Miyazahi, et al., [6] were not able to discern any effect of flow regime (bubbly and slug) on pressure pulse velocity. Uncertainties in the accurate knowledge of the void fraction and in the precise measurement of the wave speed must also be kept in mind. Using the same apparatus the authors found that the pressure pulse velocity in bubbly flow was generally better predicted by isentropic behavior than by isothermal, notwithstanding the difficulty in the actual determination of the sonic velocity with a reasonable degree of confidence.

The authors agree that their model is not necessarily general for any two-phase flow system. We neglect the distribution parameter, but not the drift velocity; whereas Mr. Beattie neglects the drift velocity, but not the distribution parameter. Although it is encouraging that the inclusion of C_0 in equation (15) yields an improvement over the homogeneous model ($C_0 = 1$), it is somewhat surprising that the method of [19] yields incorrect developed void fraction values for our system. The authors contend that caution should be exercised in claiming that the theory of Beattie [19] can be extended to nondeveloped conditions.

Because of uncertainties associated with the measurement of α and a in any pressure pulse propagation study the separation of such effects as (1) thermal coupling and (2) effect of voidage distribution in extremely difficult. The results of this investigation do demonstrate, however, that mechanical coupling must be considered in the analysis of pressure pulse propagation in slug flow.

[1] By C. Samuel Martin and M. Padmanabhan, published in the March, 1979, issue of the ASME JOURNAL OF FLUIDS ENGINEERING, Vol. 101, No. 1, pp. 44–52.

[2] Senior Research Scientist, Australian Atomic Energy Commission, N.S.W. Australia

On Vortex Wind Power[1]

G. L. MELLOR.[2] Dr. So has developed a viscous, vortex solution to the Navier-Stokes equations in cylindrical coordinates for axisymmetric flow. The solution is,

$$u = -ar \tag{1}$$

$$w = \begin{cases} \dfrac{A}{2a}\dfrac{R_1^2 - r^2}{2\nu/a + R_1^2} + 2az, & r \le R_1 \\ 2az, & r > R_1 \end{cases} \tag{2}$$

$$v = \frac{\Gamma\infty}{2\pi}(1 - e^{-ar^2/2\nu}) \tag{3}$$

He also obtained the static pressure distribution.

While the solution is interesting from the point of view of fundamental fluid mechanics, So's subsequent application to Yen's vortex tower, wind turbine system is incorrect since the solution can only be applied to a low Reynolds flow whereas the vortex wind turbine is an obviously large Reynolds application. We put aside the worrisome question of whether or not the flow is turbulent or laminar and assume, as So did, that the laminar equations of motion do apply.

Where So went wrong was in his choice of one of the free parameters of the solution, R_1, $\Gamma\infty$, A, and a. He chose R_1 to be the turbine outlet radius and later Johnston and Eaton [1] identified

$$\Gamma\infty \propto V_\infty R \tag{4}$$

where R is the tower's outer radius and V_∞ is the exterior free stream velocity and the (design dependent) constant of proportionality is of order one. He further argued that

$$A \propto \Gamma_\infty \, a \sqrt{\frac{a}{\nu}} \tag{5}$$

where the constant of proportionality is also of order one (and also design dependent; see discussion by Johnston and Eaton). Finally So chose

$$a = \frac{Z\nu}{R_1^2} \tag{6}$$

which seems to be in error. While (4), (5), and (6) together with (2) yield a vertical velocity of order V_∞ when $r < R_1$, the vertical velocity when $r > R$ is $4\nu Z/R_1^2$ and is, therefore, very small. The radial velocity in (1) is, of course, directly related to the vertical velocity through continuity and is similarly small.

The vortex tower, wind turbine system is a complicated, three-dimensional, fluid dynamic problem. However, I believe that one principle can be enunciated and that is this: for the vortex to exist in a tower of finite height, then the vertical velocity in the vortex at the top of the tower must be of order V_∞; otherwise, the vortex will not penetrate the atmospheric free stream at the top of the tower and, in fact, the morphology of the vortex system as observed in model tower tests and as assumed in every analysis to date would exist. Clearly, then, instead of (6) one has $a = \tilde{a} V_\infty/R$ where $\tilde{a}$ is a (design dependent) constant of order one. Then $u/V\infty = -\tilde{a}r/R$ and $w/V\infty = 2\tilde{a}Z/R$ for $r > R$. If, say, the tower height is $2R$, then $\tilde{a}$ must be 0.25 or larger for $w(H)/V_\infty$ to be 1.0 or larger.

We now have a very different fluid dynamical problem and one that is more closely related to a real vortex wind tower.

A recent – and very simple – analysis by Hsu, Mellor, and Yen [2] is a zero order, high Reynolds number analysis and yields a maximum power output of

$$\Gamma = \frac{1}{3\sqrt{3}} \rho V_\infty^3 \frac{\pi R^3}{R_1} \tag{7}$$

in the present nomenclature and assuming that $v(R) = V_\infty$. The coefficient in (7) is about four times larger than the result obtained by Johnston and Eaton. Actually, the correspondence is surprisingly close since it was based – erroneously it now appears – on So's solution.

[1] By Ronald M. C. So, published in the March 1978 issue of the ASME JOURNAL OF FLUIDS ENGINEERING, Vol. 100, No. 1, pp. 79–82.

[2] Professor, Department of Mechanical and Aerospace Engineering, Princeton University and Consultant to Grumman Aerospace Corporation, Bethpage, N. Y.

Additional References

1 Johnston, J. P., and Eaton, J., "Commentary on 'On Vortex Wind Power,'" ASME JOURNAL OF FLUIDS ENGINEERING, Vol. 100, 1978, pp. 252–253.

2 Hsu, C. T., Mellor, G. L., and Yen, J. T., "Some Flow Analyses for Tornado-Type Wind Turbines," *Proceedings of the Symposium on Fluids Engineering in Advanced Energy Systems*, San Francisco, Calif., Published by ASME, 1978, pp. 59–71.

Author's Closure

The author wishes to thank Professor Mellor for pointing out a very important principle in the modeling of Yen's vortex wind power generator. That is, the vertical exit velocity from the tower has to be of the same order of magnitude as the external stream, V_∞.

Professor Mellor argued that So has violated this principle in his modeling of Yen's vortex wind power generator through his suggestion that "a" should be determined from $a = 2\nu/R_1^2$. Therefore, this renders So's model incorrect. In as much as $a = 2\nu/R_1^2$ was suggested in So's paper, the power developed by the wind turbine as derived by So was actually independent of a. This can be seen from equations (16) and (17) of So's paper. If Γ_∞ is taken to be determined by the mass flow through the turbine and R_1, the outlet radius of the turbine is assumed specified, then the power P is given by

$$P = \frac{1}{8\pi^2} \frac{\rho}{R_1^4} \left(\frac{\dot{m}}{\rho}\right)^3$$

and is independent of a.

Professor Mellor's suggestion that $a = \tilde{a} V_\infty/R$ can still be applied to So's model without affecting the results for P. In this case, then, the vertical exit velocity from the tower will be of $0(V_\infty)$ everywhere within the tower. Therefore, So's model is again correct.

The author admits that the suggestion $a = 2\nu/R_1^2$ should not have been made. It is not a necessary part of the model and simply confuses the argument to extend the viscous, vortex solution of the Navier-Stokes equation to model Yen's vortex wind power generator.

Once again, the author wishes to thank Professor Mellor for pointing out this very important principle.

Turbulent Flow Measurements by Laser-Doppler Anemometry in Motored Piston-Cylinder Assemblies[1]

P. D. RICHARDSON.[2] It is excellent to see a study made of the flow in piston-cylinder assemblies by this distinguished laboratory. There are some basic questions in reciprocating engine design which should be answered by extension of this work.

One extension that would be useful is the development of display of the mean motion in terms of streaklines, as well as in terms of streamlines as portrayed here. This may require the acquistion of data at closer spacings of crank angle than used so far. To provide streaklines it is necessary to follow the trajectories of individual particles, and in the computations necessary to do this one can determine the locations in the cylinder reached by particles which have crossed the valve throat at particular crank angles. One particular result of this method of representation is that it would provide an experimental fluid-mechanical examination of the concept of stratified charge. This concept, of course, proposes that a fuel-lean region can be provided in a gasoline engine near the walls (which thermally quench reactions in a thin contact layer) and in regions otherwise susceptible to detonation, while a fuel-richer, roughly stoichiometric region can be established in the main part of the combustion chamber. One method proposed to achieve stratified charges is to vary the fuel-air mixture strength with crank angle during induction. With streakline data, it would be possible to determine what range of crank angles should be most suitable for admission of the lean air, and how well the leanness of the mixture would be maintained after induction and compression.

One other extension that I would be particularly interested to see is a comparison between the flows induced by straight inlet valves (as described in this paper) and inclined inlet valves. There is a long history of high-performance piston engines in which the inlet have their axes inclined to that of the cylinder. One possible contribution to the high performance, which does not appear to have been explored experimentally before, is the influence of the induction proces on vorticity production. In the air flow through the annular orifice formed by the valve and its seat one expects that there will be two sheets of vortex lines (in rings), of mutually opposite rotational sense, fed continuously into the cylinder during the induction stroke. With straight inlet valves one would expect these to feed into vortices as illustrated in Fig. 12 of the paper. However, with inclined inlet valves the vortex lines that form the rings will be inclined to the direction of mean motion imposed by the piston displacement, and there is an opportunity for vorticity amplification by vortex line stretching as the piston moves away from the valve. It might be argued that this will be reversed during the compression stroke which necessarily precedes ignition but in a turbulent flow there can be rapid development towards isotropy, and some of the additional vorticity gained by vortex line stretching be retained. The authors themselves note in their concluding remarks that certain regions of the flow should have an increase in small-scale turbulence and therefore be an appropriate region for combustion. The authors have an excellent opportunity to investigate whether this possible mechanism for enhancing small-scale turbulence does indeed contribute to the high performance of inclined overhead-valve engines.

[1] By A. P. Morse, J. H. Whitelaw, and M. Yianneskis, published in the June, 1979, issue of the JOURNAL OF FLUIDS ENGINEERING, Vol. 101, No. 2, pp. 208–216.

[2] Professor of Engineering, Brown University, Providence, R.I. 02912.

Authors' Closure

Professor Richardson's interest in the engine-oriented work at Imperial College is greatly appreciated and we have found his comments useful in considering guidelines for future studies.

His remarks concerning the concept of stratified charge are correct and the course of action which he suggests to determine the streakline patterns is possible but would involve a considerable amount of practical effort, particularly in an asymmetric flow configuration. Profile measurements of all three orthogonal velocity components would have to be made at very small crank-angle spacings and very small 'windows' around each crank angle of interest, in addition to small spacings geometrically. Such an investigation would require the continuous storage of data over the engine cycle on magnetic tape and, although such an acquisition system is in use at Imperial College, even a superficial examination of the type suggested would be very time-consuming in view of the amount of information required. It can be done and, in certain points of the cylinder and for certain crank angles (for example, close to an inlet value and around top-dead-center), may prove to be very desirable. In particular, it may prove to be well worthwhile when testing real valve configurations superimposed on plexiglass piston-cylinder assemblies and we do have it in mind for this type of application.

Professor Richardson's remarks about the use of inclined valves to provide an increase in small-scale turbulence by means of vortex amplification are interesting and warrant examination. For the near future, however, investigations at Imperial College are likely to be restricted to non-inclined valves, symmetrically and asymmetrically located, and with compression. We have now measured flow patterns for several valve geometries and with swirl, for an off-center valve and for a range of piston speeds, two piston-crown geometries and as a function of clearance volume and stroke. One immediate priority is to determine the influence of compression with similar arrangements. Thereafter, and with a knowledge of these various influences, angled valves, directed ports etc., will be examined.

Two Dimensional Lateral Flow Past a Barrier[1]

J. S. McNOWN.[2] Divided flow of the type described by the authors has one complication they did not include in their analysis. The calculations they refer to but do not present contain a mathematical oddity which can make the theoretical pattern of flow rather different both from the flows indicated in the figures and from real flows. The differences depend upon the characteristics of the streamline which divides the continuing flow from the lateral flow.

Only for a single point on each of the curves presented in Figs. 6 and 8 does the flow divide in the familiar form indicated by the line BD in Fig. A. For all other values of the governing parameters, the dividing streamline follows a line like BG_1D or BG_2D. In the latter cases, the analysis includes an artificial partial barrier extending along one of the walls into the flow passage. In the extreme case for which $\eta \rightarrow 0$ (Fig. 7), both the left hand boundary and the artificial barrier

[1] By A. S. Ramamurthy and B. L. Carballada, published in the December, 1979, issue of the JOURNAL OF FLUIDS ENGINEERING, Vol. 101, No. 4, p. 449.

[2] Department of Civil Engineering, University of Kansas, Lawrence, Kansas 66045.

The available information thus indicates that the authors' results may well prove useful in predicting real flows as have the results of others.

Minor points are worth mention. (1) F should coincide with E in the lower part of Fig. 5(b). (2) The authors should be consistent in setting $V_j = 1$ or not. Equations (1) and (2) differ in this respect; and, if $V_j = 1$, then $\eta = V_1$. (3) They also use radians and degrees interchangeably; if $K = 4/3$, then π/K is $3\pi/4$ not 135 deg (caption to Fig. 6). (4) The authors' Table 1 contains several inconsistencies and errors in the light of the foregoing discussion. Configurations 3, 4, and 5 are not alike, nor can all small angles be solved in closed form. (5) Reference [7] should be to Michell, not Mitchell.

Additional References

21 Mises, R. V., "Berechnung von Ausfluss und Ueberfallzahlen," *VDI Zeitschrift*, 1917, pp. 447-462.

22 Toch, A., and Moorman, R. W., "Manifold Efflux," *Free-Streamline Analyses of Transition Flow and Jet Deflection*, Ed. J. S. McNown and C. S. Yih, Univ. of Iowa, Studies in Engrg, Bull. 35, 1953, pp. 63-72.

23 McNown, J. S., and McCaig, I. W., "Complexities of Manifold Flow," *Proc. II Hydraulics Conf.*, Wash. State Univ., 1960, pp. 131-159.

Authors' Closure

For lateral flow past a conduit fitted with a barrier (Fig. A), Prof. McNown has stated that the heavy broken lines indicate two possible streamline positions characterizing the asymmetric case. However, in an earlier publication [23] it is stated that either case "has no counterpart in real flow, and sizeable departures from ideal (or locally symmetric) divisions would doubtless lead to pronounced separation." In the discussion of the present paper too, this fact is implied since he states that "in real flows, the jet would surely separate from the boundary as the authors indicate in Fig. 8" ($\alpha > \pi/K$). The present results for cases (Fig. 8) in which the barrier does not guide the flow, agree with existing solutions for the free jet [7] in the entire range of variables presented ($\alpha > \pi/K$, Fig. 8). It is interesting to note that specific cases of configurations presented (Fig. 1) can be viewed as a form of Von Mises flow [21] and that the present value of C_{co} agrees with earlier results when proper scaling factors are used. In view of the explanations provided, it can be stated that configurations 3, 4 and 5(a) provide results which agree with the corresponding free jet model for which closed form solutions have been obtained.

In the present analysis, D is forced to be the stagnation point and the stagnation streamline reaches D in all cases. In the more general case, stagnation may occur on DE or on DC with a lip cavity downstream of D. The hodograph drawn was not intended to include the formation of a lip cavity especially since this study was undertaken essentially to supplement existing simple cavity free models for lateral flow past barriers [1, 22]. The formation of a lip cavity can be accommodated in a more complex model. The analysis suggested by McNown which includes the artificial barrier does not account for the lip cavity.

The main thrust of th argument in the discussion appears to be that the flow is always guided by the barriers "no matter what." This thesis is flawed as one can easily conceive a barrier which is redundant for the cases where the free jet angle exceeds the barrier angle (Fig. 8). In Figs. 5(a) and 5(b), we are dealing with finite barriers and hence E need not coincide with F.

The authors wish to thank Prof. McNown for providing additional valuable information related to this theoretical analysis. An experimental program is underway to verify some of the assumptions made in the analysis of lateral flow past a two dimensional conduit fitted with a barrier.

Predicted and Measured Pressure Drop in Parallel Plate Rotary Regenerators[1]

A. L. LONDON.[2]

This paper describes an interesting rotary regenerator incorporating a unique rectangular passage geometry heat and mass transfer surface. The following listing summarizes the parameters relating to this discussion.

Mean aspect ratio of the rectangular passages (Fig. 2) = 1/121
Hydraulic diameter, $D_h = 1.764 \times 10^{-3}$ m (0.0694 inches)
through flow porosity, $\sigma = 0.796$
area density, $\beta = 4\sigma/D_h = 1805\ m^2/m^3$ (550 ft^2/ft^3)
passage length to hydraulic diameter ratio, $L/D_h = 57.6$
Reynolds No. test range 160 to 370

The area density of this surface is about twice that of the air-side of a modern automobile radiator (12 fins/in.).

This small aspect ratio geometry, approximating infinite parallel plates, has excellent characteristics with respect to both small fontal area and small volume requirements when operating with fully developed laminar flow [a]. The inherent advantages, however, are not realized unless manufacturing tolerances are closely controlled [b]. The effect of passage-to-passage nonuniformities is to produce a relatively small reduction of pressure drop and, unfortunately, a relatively large reduction of heat transfer. Are the authors planning to present the predicted and measured heat transfer performance for the regenerator?

There is virtually a one-to-one correspondence between the author's treatment of overall exchanger pressure drop and the methodology proposed in [5], as noted in Section 2.3. One point of difference is the use of a factor K of equations (1, 6, 7), termed a "pressure drop coefficient" in the paper and the "incremental pressure drop number" in [a], in place of K_c of [5], termed the "contraction loss coefficient." It is noted in Section 2.3 that $K_c = 0.55$ while $K = 0.686$. Both of these factors include the pressure drop effect required to produce a flow velocity profile typical of fully developed laminar flow in the small passage. Additionally, K_c includes flow irreversibility effects associated with the flow contraction, $C_c = 0.73$ for $\sigma = 0.796$, Fig. 3 of [c], followed by the reexpansion of the flow downstream from the vena contracta (Fig. 2 of [c]). No such effect is included in K. The authors' flow model, Fig. 3 of the paper, specifies loss free flow between Sections 1 and 2; that is, $C_c = 1.00$. However, K does include the effect of higher wall shear associated with the higher wall velocity gradient downstream from Section 2. There is no allowance for incremental wall friction in K_c in the entrance length region. This is consistent with the flow model Fig. 2 of [c], as the wall velocity gradients are small in the entrance length region when C_c is less than unity. As noted by the authors, the test data experimental uncertainty is of the order of ± 2.35 percent and the influence of a 0.55 (K_c) slope on the equation (1) line of Fig. 6, instead of 0.686 (K), shows as less than -1 percent at the highest test Reynolds number. Thus, the best flow model, Fig. 3 of this paper or Fig. 2 of Kays work [c], remains in doubt. The discrepancy in questions, however, varies inversely with Reynolds number and thus would be important at Re = 1000.

As a concluding comment, in view of the fact that Kay's pioneer paper [c] is 30 years old and is based on contraction

[1] By I. L. Maclain-Cross and C. W. Ambrose, published in the March, 1980, issue of the JOURNAL OF FLUIDS ENGINEERING, Vol. 102, No. 1, pp. 59-63.

[2] Professor (Emeritus), Mechanical Engineering, Stanford University, Stanford, Calif.

coefficient data that is almost 100 years old, it would be worthwhile to update the data base, the flow modeling, and the analysis for the entrance effects for abrupt changes in flow cross-section with low Reynolds number flow.

Additional References

a Shah, R. K., and London, A. L., *Laminar Flow Forced Convection in Ducts,* Academic Press, New York, 1978, pp. 383–397, 42.

b Shah, R. K., and London, A. L., "Effects of Nonuniform Passages on Compact Heat Exchanger Performance," ASME Paper 79-WA/GT-9 (to be published in the ASME *J. of Eng. for Power).*

c Kays, W. M., "Loss Coefficients for Abrupt Changes in Flow Cross Section with Low Reynolds Number Flow in Single and Multiple-Tube Systems," Trans. ASME, 1950, pp. 1067–1074.

Authors' Closure

Professor London's warning on manufacturing tolerances [b] is appropriate. Uniform plate spacing with the wound parallel plate regenerator requires a correct choice of the winding tension and careful manufacturing control of both winding tension and spacer uniformity.

The predicted fully developed heat transfer coefficient [a] for the sensible heat regenerator tested is $123 W/m^2 K$ for dry air at 300 K away from the spokes. All heat transfer coefficient values calculated from the authors measurements [1 Chap. 4, 3] for practical operating conditions are within ± 20 percent of this. The authors are planning to report on predicted and measured heat transfer performance after revising their predictions using [a] and making more careful measurements.

The differences between Kays [c] and the authors entrance loss predictions are important in other applications [3, d].

Finite difference solutions of the complete Navier-Stokes equations with the Boussinesq approximation for buoyancy forces have recently been obtained for constant temperature horizontal parallel plates including the region far upstream of the entrance as well as the flow development length [9, e, f]. For $20 \leqslant Re \leqslant 1000$, $0.7 \leqslant \sigma \leqslant 1$, $Pr = 0.7$ and Rayleigh number $Ra < 10\,Re^2$ no vena contracta or separation bubble occurs at the entrance as proposed by Kays [c] but incremental total pressure loss does decrease as σ increases. This incremental loss is above either Kays or the authors but decreases as Re increases. Incremental pressure drop number K, local Nusselt number and incremental heat transfer number [a] for constant heat flux calculated using this or similar solutions to four significant figures with $Ra = 0$, $Pr = 0.7$, $20 < Re < 2000$ and $0 < \sigma < 1$ would be useful and interesting but costly.

Additional References

d Sparrow, E. M., and Liu, C. H., "Heat-Transfer, Pressure-Drop and Performance Relationships For In-Line, Staggered, and Continuous Plate Heat Exchangers," *International Journal of Heat and Mass Transfer,* Vol. 22, 1979, pp. 1613–1625.

e Nguyen, T. V., Maclain-cross, I. L., and deVahl Davis, G., "Combined Forced and Free Convecton between Parallel Plates," International Conference on Numerical Methods in Thermal Problems, Swansea, July 2nd–6th, 1979.

f deVahl Davis, G., Maclain-cross, I. L., and Nguyen, T. V., "The Effect of Free Convection on Entry Flow Between Horizontal Parallel Plates," *Numerical Methods in Thermal Problems,* ed., Lewis, R. W., Morgan, K., and Zienkiewicz, O. C., Wiley, New York, 1980 (in press).

A Note on the Phase Relationships Involved in the Whirling Instability in Tube Arrays[1]

R. D. GIBSON,[2] N. TONKS[2] and T. S. WILKINSON.[3]

The author has examined and extended the earlier attempts by Connors [1] and Blevins [2] to model the self-induced whirling vibrations of tube arrays, such as are found in heat exchangers. All such attempts have been based on the premise that the vibrations are due to the mechanical cross-coupling of quasi-static forces, the force on a tube being dependent upon the relative displacements of the nearest neighboring tubes. Connors and Blevins considered the coupling between longitudinal and transverse bending modes for a single row of tubes in cross-flow assuming the phase of the nearest neighbors to be 180 degrees. The author considers the coupling between torsional and bending modes of neighboring tubes allowing for arbitrary phase relationships between nearest neighbors. The results obtained by the author can be applied to the motion considered by Connors and Blevins by a simple notational reinterpretation.

The author draws the conclusion that the Connors/Blevins quasi-static modelling does not lead to a vibratory instability but rather to a zero frequency divergent instability. We point out an error in the author's argument and show that the instability is vibratory, the frequency being the natural frequency of the system.

The author derives a fourth order homogeneous differential equation (5) for the transient displacement response of tube i. In order to examine the stability he defines the displacement in exponential vibration form

$$z_i = z e^{(\lambda + j\omega)t}, \qquad j = \sqrt{-1},$$

unstable vibrations corresponding to $\lambda > 0$ and the neutral stability curve corresponding to $\lambda = 0$. Substituting into the differential equation and equating real and imaginary parts he obtains (8a) and (8b). He then investigates the neutral stability curve by putting $\lambda = 0$ in (8b) and solving the resulting cubic in ω (8c) for the case when the phase of the nearest neighbors is 180 degrees as in the Blevins model. He shows that for the symmetric case of equal damping and stiffness in both motions there are two roots one of which is zero and the other the undamped natural frequency ω_0. He then attempts to examine the stability of the system by applying the Hurwitz criterion to (8a) obtaining an expression for the critical minimum velocity for the onset of instability. He observes that in order to reproduce the corresponding expression given by Blevins it is necessary to put $\omega = 0$ and he thus deduces that the neutral stability curve for the Connors/Blevins case corresponds to a zero frequency or divergent instability. The error arises from the fact that the Hurwitz criterion determines whether *all* the roots of a polynomial equation have negative real parts whereas the author has attempted to use it to investigate the sign of the real roots in isolation.

[1] By S. D. Savkar, published in the December, 1977, issue of the ASME JOURNAL OF FLUIDS ENGINEERING, Vol. 99, No. 4, pp. 727–731.

[2] Head of Department and Senior Lecturer, respectively, Department of Mathematics, Statistics and Computing, Newcastle upon Tyne Polytechnic, Newcastle upon Tyne, England.

[3] Head of Mathematical Services, NEI Parsons Limited, Newcastle upon Tyne, England.

coefficient data that is almost 100 years old, it would be worthwhile to update the data base, the flow modeling, and the analysis for the entrance effects for abrupt changes in flow cross-section with low Reynolds number flow.

Additional References

a Shah, R. K., and London, A. L., *Laminar Flow Forced Convection in Ducts,* Academic Press, New York, 1978, pp. 383–397, 42.

b Shah, R. K., and London, A. L., "Effects of Nonuniform Passages on Compact Heat Exchanger Performance," ASME Paper 79-WA/GT-9 (to be published in the ASME *J. of Eng. for Power).*

c Kays, W. M., "Loss Coefficients for Abrupt Changes in Flow Cross Section with Low Reynolds Number Flow in Single and Multiple-Tube Systems," Trans. ASME, 1950, pp. 1067–1074.

Authors' Closure

Professor London's warning on manufacturing tolerances [b] is appropriate. Uniform plate spacing with the wound parallel plate regenerator requires a correct choice of the winding tension and careful manufacturing control of both winding tension and spacer uniformity.

The predicted fully developed heat transfer coefficient [a] for the sensible heat regenerator tested is $123 W/m^2 K$ for dry air at 300 K away from the spokes. All heat transfer coefficient values calculated from the authors measurements [1 Chap. 4, 3] for practical operating conditions are within ± 20 percent of this. The authors are planning to report on predicted and measured heat transfer performance after revising their predictions using [a] and making more careful measurements.

The differences between Kays [c] and the authors entrance loss predictions are important in other applications [3, d].

Finite difference solutions of the complete Navier-Stokes equations with the Boussinesq approximation for buoyancy forces have recently been obtained for constant temperature horizontal parallel plates including the region far upstream of the entrance as well as the flow development length [9, e, f]. For $20 \leqslant Re \leqslant 1000$, $0.7 \leqslant \sigma \leqslant 1$, $Pr = 0.7$ and Rayleigh number $Ra < 10\,Re^2$ no vena contracta or separation bubble occurs at the entrance as proposed by Kays [c] but incremental total pressure loss does decrease as σ increases. This incremental loss is above either Kays or the authors but decreases as Re increases. Incremental pressure drop number K, local Nusselt number and incremental heat transfer number [a] for constant heat flux calculated using this or similar solutions to four significant figures with $Ra = 0$, $Pr = 0.7$, $20 < Re < 2000$ and $0 < \sigma < 1$ would be useful and interesting but costly.

Additional References

d Sparrow, E. M., and Liu, C. H., "Heat-Transfer, Pressure-Drop and Performance Relationships For In-Line, Staggered, and Continuous Plate Heat Exchangers," *International Journal of Heat and Mass Transfer,* Vol. 22, 1979, pp. 1613–1625.

e Nguyen, T. V., Maclain-cross, I. L., and deVahl Davis, G., "Combined Forced and Free Convecton between Parallel Plates," International Conference on Numerical Methods in Thermal Problems, Swansea, July 2nd–6th, 1979.

f deVahl Davis, G., Maclain-cross, I. L., and Nguyen, T. V., "The Effect of Free Convection on Entry Flow Between Horizontal Parallel Plates," *Numerical Methods in Thermal Problems,* ed., Lewis, R. W., Morgan, K., and Zienkiewicz, O. C., Wiley, New York, 1980 (in press).

A Note on the Phase Relationships Involved in the Whirling Instability in Tube Arrays[1]

R. D. GIBSON,[2] N. TONKS[2] and T. S. WILKINSON.[3]

The author has examined and extended the earlier attempts by Connors [1] and Blevins [2] to model the self-induced whirling vibrations of tube arrays, such as are found in heat exchangers. All such attempts have been based on the premise that the vibrations are due to the mechanical cross-coupling of quasi-static forces, the force on a tube being dependent upon the relative displacements of the nearest neighboring tubes. Connors and Blevins considered the coupling between longitudinal and transverse bending modes for a single row of tubes in cross-flow assuming the phase of the nearest neighbors to be 180 degrees. The author considers the coupling between torsional and bending modes of neighboring tubes allowing for arbitrary phase relationships between nearest neighbors. The results obtained by the author can be applied to the motion considered by Connors and Blevins by a simple notational reinterpretation.

The author draws the conclusion that the Connors/Blevins quasi-static modelling does not lead to a vibratory instability but rather to a zero frequency divergent instability. We point out an error in the author's argument and show that the instability is vibratory, the frequency being the natural frequency of the system.

The author derives a fourth order homogeneous differential equation (5) for the transient displacement response of tube i. In order to examine the stability he defines the displacement in exponential vibration form

$$z_i = z e^{(\lambda + j\omega)t}, \qquad j = \sqrt{-1},$$

unstable vibrations corresponding to $\lambda > 0$ and the neutral stability curve corresponding to $\lambda = 0$. Substituting into the differential equation and equating real and imaginary parts he obtains (8a) and (8b). He then investigates the neutral stability curve by putting $\lambda = 0$ in (8b) and solving the resulting cubic in ω (8c) for the case when the phase of the nearest neighbors is 180 degrees as in the Blevins model. He shows that for the symmetric case of equal damping and stiffness in both motions there are two roots one of which is zero and the other the undamped natural frequency ω_0. He then attempts to examine the stability of the system by applying the Hurwitz criterion to (8a) obtaining an expression for the critical minimum velocity for the onset of instability. He observes that in order to reproduce the corresponding expression given by Blevins it is necessary to put $\omega = 0$ and he thus deduces that the neutral stability curve for the Connors/Blevins case corresponds to a zero frequency or divergent instability. The error arises from the fact that the Hurwitz criterion determines whether *all* the roots of a polynomial equation have negative real parts whereas the author has attempted to use it to investigate the sign of the real roots in isolation.

[1] By S. D. Savkar, published in the December, 1977, issue of the ASME JOURNAL OF FLUIDS ENGINEERING, Vol. 99, No. 4, pp. 727–731.

[2] Head of Department and Senior Lecturer, respectively, Department of Mathematics, Statistics and Computing, Newcastle upon Tyne Polytechnic, Newcastle upon Tyne, England.

[3] Head of Mathematical Services, NEI Parsons Limited, Newcastle upon Tyne, England.

We now consider the correct interpretation of the analysis. Since the frequencies $\omega = 0$ and $\omega = \omega_0$ are roots of (8*b*) with $\lambda = 0$ they must also satisfy the corresponding form of (8*a*) viz.

$$\omega_0^4 + \frac{cAB}{mI}\rho^2 \; U^4 - 2\omega_0^2(1+2\xi^2)\omega^2 + \omega^4 = 0$$

where $cAB/mI > 0$. We see that $\omega = 0$ is not a solution of this equation and thus the neutral stability curve *cannot* correspond to a divergent instability. Substitution of $\omega = \omega_0$ yields the critical minimum velocity corresponding to that obtained by Blevins for the symmetric case. The same expression is obtained when the stability of the system is examined by applying the Hurwitz criterion to the quartic in s obtained from the homogeneous differential equation (5) by assuming $z_i = ze^{st}$ where s is complex. Hence the Connors/Blevins quasi-static modelling *does* lead to a vibratory instability, the frequency being the natural frequency of the system.

Journal of Fluids Engineering

Book Reviews

Flow Visualization, Edited by Tsuyoshi Asanuma, Hemisphere Publishing Corporation, 1979, approx. $70.

REVIEWED BY RICHARD A. BAJURA

This book is a report of the proceedings of the International Symposium on Flow Visualization held in Tokyo, Japan, on October 12–14, 1977. The Symposium consisted of 4 invited lectures on flow visualization techniques and 50 contributed papers. Flow visualization techniques were separated into five categories with the number of papers in each category as follows: Direct Injection Methods – 18; Tuft and Wall Tracing Methods – 3; Chemical Reaction and Electrical Control Methods – 10; Optical Methods – 16; and, Cavitation – 3. Papers were limited in length such that the main text, including an author and subject index, is 413 pages. The book contains numerous flow visualization photographs and is well-prepared publication-wise in agreement with the standards applied to other texts in the Hemisphere Publishing Corporation Series in Thermal and Fluids Engineering. The volume was produced from author-prepared mats typed single-spaced on regular typing paper.

The four review lectures were presented by Professors T. Asanuma (Japan), R. Reznicek (Czechoslovakia), W. Merzkirch (West Germany), and W. J. Yang (United States). These lectures were summary reports of different techniques considered popular in their respective regions. The papers by Merzkirch and Yang provide a substantial listing of relevant papers and reports on the various techniques and their application.

Generally speaking, the contributed papers were written primarily to describe the authors' flow visualization techniques/applications as opposed to the presentation of detailed results and analysis of fundamental new information in fluids engineering. However, the breadth of topics covered in the presentations makes the book an interesting review of many aspects of fluid mechanics from low Reynolds number flows in pipes to shockwaves in supersonic boundary layers.

Although the symposium was not intended to be a tutorial session on the various flow visualization techniques, several authors have described their facilities and methods sufficiently to enable the novice to develop similar capabilities on their own. Personally, this reviewer would appreciate detailed reporting of the practical aspects of developing such systems.

The majority of the papers in the Direct Injection Methods section of the book deal with the use of particulate tracers in air flows, such as generated by oil or tobacco smoke, DOP, and ammonium chloride. One or two papers each were presented which featured methods such as floating particles and liquid tracers in water flows, helium bubbles, optically active tracers, strobophotographic techniques and stereoscopic studies.

Papers in the Tuft and Wall Tracing Methods grouping were mainly centered on the use of tufts and surface oil tracings. One paper was presented describing computer-aided approaches to flow visualization.

Papers in the Chemical Reaction and Electrical Control Methods Section were heavily oriented toward the use of the smoke wire and spark tracing techniques. Two papers featured the use of hydrogen bubbles and one paper described an electrolytic precipitation method in studies of separation from cylinders.

In the Optical Methods section, the papers were almost equally divided among the following techniques: shadowgraph, schlieren, interferrometry, holography, birefringence and the use of various photographic methods.

While the selection and use of a given flow visualization technique depends upon the problem at hand, the statistical breakdown of papers leads one to believe that: (1) Japanese researchers are more involved with electrical control and tuft methods; (2) the participants from the other countries employ optical methods more frequently than their Japanese counterparts; and, (3) all researchers favor the use of direct injection methods.

This reviewer found the book and subject material quite interesting and feels that the book should definitely be acquired as part of an institutional library holding. With regard to one's personal library, the price of the book will probably limit its interest to those persons involved with flow visualization studies as part of their research programs. The next International Symposium on Flow Visualization is scheduled for September 9–12, 1980 at Ruhr-Universitat, Bochum, Germany.

Laminar Flow Forced Convection in Ducts, by R. K. Shah and A. L. London, Academic Press, New York, 1978, 477 pages. Price: $49.50

REVIEWED BY FRANK M. WHITE

This monograph, which is subtitled "A Source Book for Compact Heat Exchanger Analytical Data," contains an amazing number of analytical solutions for laminar velocity and temperature, both developing and developed, in ducts of practically every conceivable cross-section. No matter how much you know about "laminar flow in ducts," you will probably be astounded by the wealth of material collected by the authors in this book. The reviewer was thoroughly humbled by reading it and had his list of known analytical solutions more than tripled by the 536 references discussed by the authors.

Beginning with three introductory chapters on analytical techniques and dimensionless formulations, the authors then proceed through a systematic treatment of various duct shapes. Most discussions include velocity and thermal development, with constant wall temperature and constant heat flux conditions, and often with peripheral temperature variations around the cross-section. First of course is the circular duct, followed by separate chapters on parallel plates, rectangular, triangular, and elliptical ducts. Chapter 10 then treats "other singly-connected ducts": sine shapes, trapezoids, various quadrilateral and sector shapes, corrugations, cusps, and even the cardioid. In teaching laminar flow, it has traditionally been a little joke of mine to work out the circular and, say, the rectangular duct in class and then to tell the students they are assigned the cardioid for homework. Well, in the present monograph, the cardioid and Booth's lemniscate and many other mysterious duct shapes are discussed with utter solemnity, with figures and references.

After a short chapter on an approximate solution for small aspect ratio ducts, the book moves to annular ducts, both concentric and eccentric, plus a variety of other doubly-connected geometries. The authors then conclude with a chapter on longitudinal flow in rod bundles, solutions for finned and twisted-tape ducts, and an overview for the designer and the applied mathematician. In all these subjects, the wealth of detail and background is outstanding. The authors have succeeded admirably in producing a most comprehensive monograph on laminar flow in ducts. I highly recommend it as a source book for this specialized area of flow and heat transfer analysis.

Flow Meters: A Basic Guide and Source-Book for Users, by Alan T. J. Hayward, Halsted Press, New York, 1980, 197 pages. Price: $24.95

REVIEWED BY RODGER B. DOWDELL

Alan Hayward's objective, as stated in the Preface, was to prepare a book which would answer 90 percent of the questions about flow measurement that a man in the works office might ask, and to advise him where to find the answers for nine of the remaining ten questions.

The book is well written and concise with an adequate number of illustrations to make his presentations easily understandable to a man in the works office with a limited technical background. I particularly like his definitions, which are all referenced to the latest international documents and accompanied by effective diagrams. He has also described just about every meter that has seen service during the last 100 years and also has not slighted the newer, more sophisticated devices such as the Cross Correlation and Doppler Effect Ultrasonic meters or the Ion Deflection meter. However, these descriptions are rather brief and lacking in technical depth. I do not believe this book was written for a graduate, practicing engineer specializing in the area of flow measurement but rather for someone who has come across his first problem in flow measurement and doesn't know where to turn.

In my opinion, the best part of the book are his sections on "Where to Learn More" and the accompanying references. These are quite complete and up to date, and are reason enough for an engineer to add this book to his collection.